3D Printing for Optical Fibre Applications

Michal Grzegorz Zubel

Doctor of Philosophy

Aston University

September 2019

Aston University

3D Printing for Optical Fibre Applications

Michal Grzegorz Zubel

Doctor of Philosophy

2019

Thesis summary

The objective of this thesis is to combine the technology of silica and polymer fibre Bragg (FBG) gratings with fused deposition modelling (FDM), which is an additive layer manufacturing (3D printing) technique. The research into optimising transparency of the printouts allowed the printing of solid-core and hollow-core preforms of poly(methyl methacrylate) (PMMA) and polycarbonate. The first microstructured polymer optical fibre was then fabricated from the 3D-printed solid-core polycarbonate preform. This was the first fibre drawn from a 3D-printed preform to show single-mode operation (at a wavelength of 870 and 1550 nm). Moreover, the fibre displayed the lowest attenuation of all the fibres drawn from 3D-printed preforms reported so far, with a lowest attenuation figure of ~0.27 dB/cm in a few spectral regions (780-785 nm, 820-825 nm, 953-956 nm, 1070-1090 nm). Also, FBGs were inscribed in the fibre using three different laser systems: a 248-nm nanosecond krypton-fluoride laser, a 517-nm femtosecond laser, and a 325-nm continuous-wave helium-cadmium laser. The temperature sensitivity of the latter FBG was measured to be -21.3±1.9 pm/°C. Finally, the linear coefficient of thermal expansion and the thermo-optic coefficient of the fibre were measured to yield the values as low as $7.34\pm0.53\times10^{-7}$ °C^{-1} and $-39.4\pm3.7\times10^{-6}$ °C^{-1}, respectively. FDM was also used to embed polymer and silica FBGs into 3D printed protective housings. The printing process was paused midway to introduce the fibre. Such sensing patches were found to provide good mechanical protection while the measured strain sensitivity amounted to 92% of this for the unembedded grating. Furthermore, embedded silica FBGs yielded a temperature sensitivity 103±14 pm/°C. This figure is over 12 times higher compared to unembedded silica gratings and two times higher compared to polymer FBGs of the highest temperature sensitivity. Finally, embedded silica FBGs were capable of gauging humidity, its sensitivity value being measured as 13.8±1.1 pm/%RH.

Keywords: polymer optical fibres, optical fibre sensors, fibre Bragg gratings, fused deposition modelling, fibre embedding

To my wonderful wife.

Acknowledgements

The first word that comes to my mind when thinking of the years spent on that work is gratitude. This thesis has a single author, but without the help of others, you would not be reading it. I would like to gratefully acknowledge invaluable support of my supervisors, Professor Kate Sugden and Professor David Webb, who has always been for me a source of advice and encouragement. Many thanks to my friends and colleagues associated in the TRIPOD consortium for creating a friendly and collaborative research environment: Andreas Pospori, Andrea Fasano, Getinet Woyessa, Christian Broadway, Carlos Marques, Wei Zhang, Amédée Lacraz, Denis Ganziy, Ivan-Lazar Bundalo, Antreas Theodosiou, Onur Cetinkaya, Gökhan Demirci, Pavol Stajanca and Hafeez ul Hassan. I also owe thanks to Christiane Döring-Saad, Helen Yard and Andy Abbot from Aston University for the administrative and technical support.

Moreover, it is proudly acknowledged that this thesis contains collaborative work, which was done in cooperation with the following partners:

- Andrea Fasano (supervisor: Henrik K. Rasmussen) from Department of Mechanical Engineering, Technical University of Denmark (DTU)
- Getinet Woyessa (supervisor: Ole Bang) from Department of Photonics Engineering, Technical University of Denmark (DTU)
- Rui Min (supervisor: Beatriz Ortega and Carlos A. F. Marques) from ITEAM Research Institute, Universitat Politècnica de València, Valencia, Spain
- Arnaldo Leal-Junior (supervisors: Anselmo Frizera-Neto, Carlos A. F. Marques, and Maria José Pontes) from Telecommunications Laboratory (LABTEL), Electrical Engineering Department, Federal University of Espírito Santo, Brazil
- Antreas Theodosiou (supervisor: Kyriacos Kalli) from Photonics and Optical Sensors Research Laboratory, Cyprus University of Technology
- Carlos A. F. Marques from Instituto de Telecomunicações, University of Aveiro, Portugal

The sections containing the results of the collaborative work comprise collaboration statements, which detail the contribution of each researcher.

Funding from the People Programme (Marie Curie Actions) of the European Union's Seventh Framework Programme FP7/2007-2013/ under REA grant agreement No. 608382 is also thankfully acknowledged.

Most importantly though, I am hugely indebted to my family and especially to my wonderful wife, whom I cannot thank enough for all the sacrifices she made to help me get where I am.

Contents

List of abbreviations

1D	one dimension, one dimensional
2D	two dimensions, two dimensional
3D	three dimensions, three dimensional
ABS	acrylonitrile butadiene styrene
ALM	additive layer manufacturing
ANF	anti-resonant nodeless fibre
AR	anti-resonant, anti-resonance
ARF	anti-resonant fibre
BBS	broadband source
BDK	benzyl dimethyl ketal
CTE	coefficient of thermal expansion
DMA	dynamic mechanical analysis
DTU	Technical University of Denmark
ESM	endlessly single-mode
FBG	fibre Bragg grating
FDM	fused deposition modelling
FWHM	full width at half maximum
GI	graded-index
HC	hollow-core
HOM	higher order modes
IPA	isopropyl alcohol
LCTE	linear coefficient of thermal expansion
L-L	Lorentz-Lorenz
MM	multi-mode
mOF	microstructured optical fibre
mPOF	microstructured polymer optical fibres
NANF	nested anti-resonant nodeless fibre
NCF	negative curvature fibre
OFS	optical fibre sensor
PBG	photonic band gap
PBGF	photonic bandgap fibre

PC	polycarbonate
PCF	photonic crystal fibre
PLA	polylactic acid
PM	phase mask
PMMA	poly(methyl methacrylate)
POF	polymer optical fibre
POFBG	polymer optical fibre Bragg grating
RI	refractive index
SC	solid-core
SI	step-index
SM	single-mode
SOF	silica optical fibre
SOFBG	silica optical fibre Bragg grating
TIR	total internal reflection
TOC	thermo-optic coefficient
VCTE	volumetric coefficient of thermal expansion

List of figures

List of tables

Chapter 1 Introduction

1.1 Motivation

The motivation behind this thesis is to combine the capabilities and advantages of the following three technologies, which are introduced in the following sections:

- fused deposition modelling technology, which is a 3D printing method
- optical fibre technology
- fibre Bragg grating technology.

The focus of the thesis lies on using fused deposition modelling to:

- advance the fabrication technology of polymer optical fibres
- and expand the use of fibre Bragg gratings for sensing by integrating them with other materials.

1.1.1 3D printing

Widespread use of 3D printing, also known under the umbrella name additive layer manufacturing (ALM), constitutes one of the most prominent recent breakthroughs in the field of manufacturing [1, 2]. Among multiple advantages of these techniques count:

- relatively low price and, hence, high accessibility
- growing number of 3D-printing methods and available materials
- capability of reproducing complex shapes, sometimes lying beyond the reach of other manufacturing techniques
- ease of customisability

- much shortened delay between design and manufacturing phases.

Owing to these qualities, ALM is often considered the manufacturing technique of the future.

Fused deposition modelling (FDM), used in this work, is currently the most popular 3D-printing approach. It relies on using thermoplastic filaments to fabricate random structures made of polymer. Among the assets of this technique are:

- very low cost
- ability to mix materials within a single printout
- ease of fabrication of various functional elements (empty cavities, beams, channels, membranes etc.)
- a broad range of available materials having different mechanical, chemical, and thermal properties (including refractive index, transparency, chemical composition, flexibility, biodegradability, coefficient of thermal expansion, affinity to water etc.)
- ability to pause printing to insert into the printout items to be embedded.

All of these can be used to the benefit of the field of optical fibres. This will be discussed further in the following part of this chapter.

1.1.2 Silica and polymer optical fibres

The 20th century has seen great advances in various branches of electronics, including telecommunications, sensing and visual technologies. Since at least 1990s, they have been revolutionising our way of thinking and the way that the society functions. However, the most eminent example of achievements in telecommunication, the Internet, would not have come to life without long-haul optical-fibre telecommunication systems, which are an indispensable part of the digital revolution of the last years.

As the technology of optical fibre telecommunication was advancing, it was recognised as potentially the only one capable of providing high-throughput data links throughout the world, and thus holding a significant advantage over electronic communication. Substantial funding directed into optical fibre telecommunication over the last few decades have made it a mature branch of science and engineering and has brought its cost down.

Nowadays, the material of choice for long-haul telecommunication fibres is silica glass. With its low light attenuation [3], it has proven to be an excellent (though not perfect) transmission medium. However, it is not the only material used for fibre fabrication, the enormous family of polymers being a very interesting alternative. Although they are not able to outperform silica's low transmission loss, their important characteristics encompass [4]:

- flexibility in modification of their chemical and optical properties
- higher elasticity and failure strain than silica's
- biocompatibility

- biodegradability.

All these properties open a broad range of possible uses of polymer optical fibres (POFs), e.g., for:

- local area networks (e.g., in cars), benefiting from large-core fibres which would be impossible to fabricate in silica due to its stiffness [5]
- enhancement of non-linear properties [6]
- optical amplification [7]
- in-vivo biomedical applications [8]
- sensing applications [9] (including nuclear radiation, sparks, X-ray, pH, CO, O_2, ammonia, humidity, temperature, thickness, gas concentration, various chemical species, displacement, liquid level, particle concentration, flow, refractive index, gas leakage, stress, radial rotation, wind speed, acid concentration).

The range of sensing applications can be broadened even more with the use of fibre Bragg gratings, which will be introduced later.

1.1.3 Photonic crystal fibres

Classically, both polymer and silica optical fibres (SOFs) are entirely made of solid material and guide light by means of total internal reflection. The year 1999 [10] marked the emergence of fibres relying on another guidance mechanism, namely photonic bandgap. Photonic crystal fibres (PCFs), as they are called, normally rely on arrangement of empty holes in fibre cladding rather than refractive index contrast, with the fibre core being either solid or hollow. This concept allows unprecedented freedom in designing various fibre properties, the most prominent examples for solid-core (SC) PCFs being [11]:

- endlessly single-mode behaviour (i.e., fibre guiding one mode at maximum, irrespective of the wavelength of light)
- endlessly single-mode fibres of extremely large cores
- enormous flexibility in tuning group velocity dispersion
- possibility of enhancement or reduction of Kerr non-linear effects.

These qualities were soon turned into various applications, including:

- transmission of high energy in single mode [12]
- use of PCFs in lasers and amplifiers due to large cores and flexibility in designing their parameters [13-15]
- supercontinuum generation (due to use of Kerr-related non-linear effects) [16, 17]
- parametric amplifiers and oscillators (also due to use of Kerr-related non-linear effects) [18-20]
- dispersion compensation [21]
- dispersion-flattened fibres [22]

Hollow-core (HC) PCFs, which were neglected in the previous discussion, can also offer multiple advantages. Conventional optical fibres made from silica have turned out the be hugely successful both from scientific and technological viewpoints owing, among other things, to silica glass being used as the transmission medium. However, silica has some inherent limitations, which entail [23-27]:

- Rayleigh scattering, which dominates propagation loss at short wavelength
- glass absorption, binding propagation loss at long wavelength
- bandwidth limited to high transparency windows
- Raman and Kerr non-linear effects
- added latency to data transmission due to decrease in speed of light propagation
- dependence of fibre properties on temperature
- photodarkening effect.

All these issues disappear if light is guided in vacuum and are of much smaller extent in air, which is one of the main motivations to develop hollow-core fibres (HCFs). Two families of HCFs can be differentiated, depending on the guidance mechanism on which they rely: photonic band gap fibres and anti-resonant fibres. Negative curvature fibre is a particular example from the latter group and has recently proven to provide a very low transmission loss of 1.3 dB/km at ~1450 nm [28], less than an order of magnitude higher than this of state-of-the-art conventional silica fibres. Despite still being a relatively young field of technology, HCFs has been shown to offer [23-27]:

- extremely wide bandwidth
- decreased latency
- low nonlinearities
- very high damage threshold
- insensitivity to external stimuli (e.g., radiation, environmental changes)
- long interaction path with gases
- potential for extremely low loss.

Applications of HCFs include [23-27]:

- delivery of pulses of high energy
- delivery of radiation in the mid infra-red region
- recompression of high energy pulses
- nonlinear optics
- gas sensing
- generation of higher harmonics
- data transmission.

As with conventional fibres, there is no inherent limitation regarding material of which photonic crystal fibres (or microstructured fibres) are to be fabricated, besides material transparency. This

stimulated development of microstructured polymer optical fibres (mPOFs), with the first one being reported in 2001 [29]. mPOFs combine all advantages of POFs and PCFs mentioned above, and – when compared to conventional polymer fibres – mPOFs are composed of a single material. This avoids some complications during fibre manufacturing and use from the different material properties of the two polymers making part of conventional fibres (e.g., related to differences in glass transition temperature or thermal expansivity). Moreover, mPOF preforms can be fabricated more easily than preforms of silica PCFs. The latter are usually produced by the capillary stacking technique [26], which – while versatile in many ways – does involve some limitations. In contrast, mPOF preforms can also be fabricated by the drilling, extrusion, and casting methods [26].

In addition to these established fabrication technologies, fibre preforms can be 3D-printed using the FDM approach, as the basic material requirement, thermoplasticity, is common for polymers used in both POF manufacturing and FDM. Both solid-core and hollow-core fibres drawn from 3D-printed preforms have recently been reported [30-34]. These preliminary results seem promising but also leave much room for improvement, which is discussed further in Section 1.2.

1.1.4 Fibre Bragg gratings

A fibre Bragg grating (FBG) is a rather simple yet extremely useful device created in the core of an optical fibre. It consists of periodic modulation of refractive index of the core along the fibre axis, resulting in selective reflection of a (usually narrow) part of the light spectrum (Bragg reflection). Change of the modulation strength and period results in a different part of the spectrum being reflected, affecting its wavelength range and spectral shape. The first FBG was manufactured (inscribed) in a silica fibre in 1978 [35]. The development of the side inscription method in 1989 [36] paved the way to many variations of inscription techniques and grating parameters, leading to numerous applications in telecommunication and sensing. The former normally involve silica FBGs (SOFBGs) and encompass:

- dispersion compensation in telecommunication systems [37, 38]
- pulse compression [39-41]
- noise reduction [42]
- flattening gain in amplifiers based on erbium fibres [43, 44]
- reflectors in tuneable lasers [45-48]
- linewidth narrowing in semiconductor lasers [49]
- wavelength-division multiplexing [50, 51]
- Raman amplifiers [52, 53].

The use of FBGs for sensing was supported by maturing of the technology of the optical fibres for telecommunications and by certain limitations to electronic sensors discovered with advances in the field. FBGs make part of the family of optical fibre sensors (OFSs) [54-58], sharing their common advantages [58, 59]:

- lightweight, small and potentially cheap sensor structure
- possibility of integration with existing fibre optic networks
- many potential applications for which electronic sensors are intrinsically unsuitable
- ability to work in harsh, flammable, and explosive environment
- ease of multiplexing
- immunity to electromagnetic interference
- remote interrogation ability.

FBGs, classically made in silica fibres, are a particularly interesting group of OFSs because of the wide variety of measurands that they can sense, including strain [60], temperature [61], flow rate [62, 63], vibration [64], structural damage [65], and pressure [66]. Moreover, particular benefits of FBGs that are not shared by all OFSs entail no need for on-site calibration and signal being encoded in the wavelength of light and not its intensity, the latter making them independent of the amount of loss in the system.

FBGs have also been inscribed in polymer fibres (polymer optical fibre Bragg gratings, POFBGs). Interestingly, photosensitivity of poly(methyl methacrylate) (PMMA) was discovered as early as 1970 [67], (i.e., before silica's), but the first demonstration of a POFBG was not until 1999 [68], in a conventional optical fibre, while the first POFBG made in a microstructured fibre was reported in 2005 [69]. This long delay was surely influenced by a high loss of polymer optical fibres and the huge success of SOFBGs, stemming from the potential to fabricate devices that were directly applicable by integrating them with existing fibre optic networks. Nevertheless, the combined benefits of FBGs and POFs make polymer gratings outperform their silica counterparts in certain cases and, moreover, allow POFBGs to be implemented in applications lying completely beyond the reach of SOFBGs. Some examples of these encompass:

- capability of sensing relative humidity due to affinity to water shown by some polymers [70]
- higher temperature sensitivity than in SOFBGs due to large negative thermo-optic coefficient [71, 72]
- applications stemming from higher fibre elasticity compared to silica:
    - sensors of higher force and pressure sensitivity [73]
    - more accurate monitoring of compliant structures thanks to avoiding stiffening them [74] (if the fibre is less elastic than the structure to be monitored, the readout is falsified)
    - higher sensitivity to acoustic wave due to lower acoustic impedance [75]
    - increased sensor strain range [76]
- capability of post-inscription tuning of reflected wavelength by fibre annealing [77] of straining at elevated temperatures [78], resulting in a simple way to multiplex POFBGs [79].

The range of applications of both silica and polymer FBGs can be greatly broadened using the FDM 3D-printing technique, which the next section discusses in detail.

1.2 Challenges and objectives

Despite numerous advantages and applications of photonic crystal fibres and the FBG technology presented above, there remain some challenges and research gaps, which could potentially be addressed with the FDM technique. This section presents the motivation behind the proposed directions of development of POF manufacturing and sensing applications.

1.2.1 Polymer optical fibre applications

Advanced POFs are usually produced by drawing from a preform, which can be manufactured by means of various methods (see Section 2.6 for details). Their combined capabilities allow for the production of an extremely broad range of fibres. This involves mPOFs and conventional POFs of step-index, graded-index and more complex refractive index profiles. Other fibre characteristics of both SC and HC fibres can also be varied (including number of cores and their shape, size, and arrangement), resulting, e.g., in highly birefringent fibres and multicore fibres of various properties. Even more exotic examples of fibre designs entail SC fibres optimised for in-core microfluidics, Bragg and Omniguide fibres, and suspended-core fibres. However, among the conventional fibre manufacturing methods (Section 2.6.2), there is no single one permitting fabrication of all these different fibre types. FDM displays great potential to be such a method, combining advantages of all the conventional ones. This is due to its immense flexibility to reproduce different shapes, wide variety of available materials, and ability to mix them within one printout (multi-extruder printers).

Hollow-core polymer optical fibres

Preforms for the most advanced hollow-core fibres (i.e., photonic bandgap fibres, PBGFs, and anti-resonant fibres, ARFs) are most often fabricated by the capillary stacking method (see Section 2.6 for details). They are usually made of silica, although, in principle, POFs can also be produced this way. Despite having led to stunningly low fibre loss recently (Section 2.5.3), capillary stacking has also got some shortcomings, which hinder decreasing fibre attenuation further. First, it is a tedious and time-consuming manual technique, requiring much human involvement. It is then prone to human errors and difficult to transfer to industrial setting. Conversely, FDM is mostly an automated process requiring minimal human attendance. It can be optimised to yield repeatable results, which makes it easy to apply in industry. Secondly, in the capillary stacking used for PBGFs, usually circular capillaries are stacked together and then further transformed by pressure during drawing. This way, the microstructure of PBGFs achieves its final form, which is usually very different from this resulting from capillary stacking itself. However, FDM printouts can represent the desired structure of PBGFs or be very close to it. Hence, pressure work can be either avoided completely, which would simplify the drawing process, or applied to fine-tune fibre properties. Thirdly, capillary stacking is not flexible enough to realise certain PBGF designs, for instance, the triangular lattice of rods (hexagonal lattice of holes). The most widely

used structure of photonic crystal cladding is based on the triangular lattice of holes (hexagonal lattice of rods). It was shown experimentally to yield bandgaps of up to 33% [80] (bandgap width divided by centre wavelength). However, numerical simulations showed that other cladding designs can bring even wider bandgaps [81-83]. The square lattice, realised experimentally, yielded a bandgap of 44% [82]. According to the simulations, photonic crystal cladding based on the triangular lattice of holes (hexagonal lattice of rods) can bring bandgap as high as 66%. Yet, it has not been demonstrated experimentally so far due to limitations of the current preform fabrication methods. However, such design could be realised using FDM. This would require printing preforms of somewhat larger diameter than 20-30 mm usually used for PBGFs [24] due to limited 3D-printing resolution. The latter would not be a blocking factor though and could also be partly addressed by applying smoothing and thinning techniques typical of FDM. Fourthly, capillary stacking makes it rather difficult to fabricate preforms for anti-resonant fibres, which is the most promising type of photonic crystal fibre from the viewpoint of loss minimisation. The face of the nested anti-resonant nodeless fibre currently holding the record for the lowest transmission loss [28] still reveals some manufacturing imperfections. This is due to manual stacking process and only a single point of contact between the nested capillaries and the external tube. Yet, the attenuation of this fibre, compared to silica, was only 2 times higher at 950 nm and 8 times higher at 1450 nm, the latter being close to the range most widely used in the telecommunications (1500–1600 nm). Simulations suggest that the overall attenuation at 1450 nm is still limited by the confinement loss, which can be further minimised by optimising geometrical structure of anti-resonant elements. To tackle this issue, multiple complex fibre designs resulting from numerical studies were proposed in the literature (see Section 2.5.3). However, they all go beyond nested circular elements and rely on using shapes that are very difficult to reliably and repeatably fabricate by capillary stacking (e.g., ellipses and half-ellipses, also nested within other components). By contrast, FDM could reproduce all these advanced designs rather easily, all the more so as they contain much less detail than those of PBGFs.

As discussed above, 3D printing seems to be the key enabling technology to advance fabrication of photonic crystal fibre preforms. However, it must be underlined that state-of-the-art PBGFs and ARFs are made solely of silica and not polymers. A few techniques to 3D print transparent glass objects have emerged recently, which can be divided into direct and indirect 3D printing [84]. The former family entails molten glass extrusion [85] and selective laser melting of glass wire [86]. However, the resolution provided by both techniques (>1 mm) is far too coarse to be used for fibre preform printing. Moreover, these approaches rely on direct deposition of molten glass and, hence, require operating at very high temperatures (~1000 °C). This involves additional expensive equipment and hinders handling. The second group of techniques to 3D print transparent glass provides much better printing resolution: ~200 μm for direct ink writing of colloidal sol [87], ~600 μm for stereolithography of sol-gel precursor [88], and 60 μm for stereolithography of glass nanocomposites [89]. They all involve complex three-step thermal treatment after printing:

1) solvent evaporation (50-150 °C)
2) burning organic binder (150-800 °C)
3) sintering silica to form bulk glass (800-1500 °C).

Every step requires a particular temperature profile in time, exact temperatures varying among the techniques. Post-treatment processing time ranges from 46 h (for stereolithography of glass nanocomposites) to over 7 days (for stereolithography of sol-gel precursor). Moreover, all these methods result in printout linear shrinkage by 16-58% after sintering, depending on the technique. In the case of stereolithography of sol-gel precursor, the shrinkage can be anisotropic. Out of the three techniques, stereolithography of glass nanocomposites [89] seems potentially best-suited for 3D printing fibre preforms due to the best printing resolution, lowest and isotropic shrinkage, shortest post-treatment time, very high optical, mechanical, thermal, and chemical quality of the final printout (equivalent to this of glass). In addition, it is compatible with standard stereolithography process, which could facilitate its adoption.

Despite the advantages of stereolithography of glass nanocomposites, there also are multiple issues regarding this technique. First, this is a relatively new process (first published in 2016 [90]) and it seems not to have been adopted outside the research group of origin, according to the publication record. By contrast, FDM is a well-developed technique and is used very widely in a range of industries. Secondly, although various characteristics of glass fabricated by stereolithography of nanocomposites are claimed to be identical with these of bulk glass, there have been no reports on drawability of glass created by this process. While it can be expected to have similar drawing characteristics to bulk glass, this still awaits experimental demonstration. Contrastingly, various types of optical fibres (including step-index, solid- and hollow-core mPOFs) have been successfully manufactured from preforms made of a range of materials by FDM 3D printing (see Section 2.6.3). Thirdly, development of printouts in stereolithography of nanocomposites is based on projection of rectangular pixels to form consecutive layers (digital light processing approach [2]). This leads to curved surfaces in fibre preform – designed to be smooth – having sharp edges in *x*-*y* plane after printing. Even despite an *x*-*y* resolution of 60 μm, which is very fine for 3D printing, the surface roughness can adversely impact fibre transmission. This could be potentially mitigated using some smoothing techniques, which would further complicate the process though. Although the minimum line thickness in FDM cannot go below ~300 μm (assuming a nozzle diameter of 150 μm), its edge is expected to be much smoother than in stereolithography. Fine resolution can also be expected not to be the primary concern for ARFs, the more promising type of HC PCFs. Fourthly, the price of the nanocomposite used in the stereolithography process (trade name Glassomer [91]) is still quite high (€700 per 500 g). By contrast, FDM uses standardised, commercially available 3D printing filaments, which are much cheaper (€20-50 per 1 kg) due to wide adoption of this method. Lastly, producing transparent glass by the use of stereolithography of nanocomposites is a complex process and involves various steps of high temperature treatment (up to ~1000 °C), which also

contributes to the overall cost of the process. By contrast, objects manufactured by FDM also require annealing to increase transparency [30], but it is performed at a much lower temperature (90-170 °C) than when sintering glass nanoparticles.

For all the reasons enumerated above, plastic fibre preforms fabricated by means of the FDM technology are considered more promising than glass ones manufactured by stereolithography of nanocomposites. The aim of this thesis is then to 3D print hollow-core preforms for fibre drawing using the settings resulting from transparency optimisation of the FDM process.

Solid-core polymer optical fibres

The most widely used approach to produce plastic solid-core PCF preforms relies on the drilling technique (see Section 2.6.2), i.e., drilling an array of holes into bulk polymeric cylinder according to the desired design. While simple and automatable, this technique possesses certain limitation, which can be addresses by FDM. Namely, the holes resulting from drilling can be virtually only circular in shape. Enlarging the openings by moving the drill sideways during machining could give some more flexibility, the smallest reproduced details being limited by the diameter of the drill though. Such approach is industrially used in thin sheets of material, but it would be more cumbersome in thick blocks of plastic like fibre preforms. This is due to, e.g., difficulties in assuring the drill is exactly perpendicular to the preform surface. The drill becoming skew would, in turn, adversely affect the consistency of the preform pattern along the preform length, lowering the controllability of the fibre production process. By contrast, shapes reproduced by 3D printing can be extremely complex, of better resolution compared to drilling, and reliably reproduced along the preform length.

In 2015, a solid-core air-structured fibre fabricated (i.e., drawn) from a POF preform produced by FDM has been demonstrated [30]. The air structure of the reported fibre was almost above the micrometric range (both core and air structure holes of ~200 μm), but this approach should equally permit obtaining microstructured POFs with a core and air structure holes of single microns, which is the usual size for single mode guidance. To achieve this, further development of the fibre manufacturing process is required. This involves, first, using a more complex air structure pattern than a single ring of holes implemented in [30] because it can provide very limited light confinement conditions. Using two or more rings of holes would help decreasing the confinement loss further. Achieving a finer microstructure can be also facilitated by the use of a preform of higher diameter combined with an appropriately sized draw tower. Secondly, bringing the size of the air structure down can be achieved by using the two-step drawing process instead of drawing fibre directly from the preform in [30], which limited scaling the air structure of the fibre down. The two-step process involves drawing preform first into an intermediate cane and, subsequently, sleeving it with an outer tube before drawing into fibre. Thirdly, geometrical quality of the 3D-printed preform needs further optimisation so that the finer microstructure pattern can be reliably reproduced. Moreover, further increase of optical quality of the

preform is required to minimise fibre absorption loss. Finally, following all these steps can result in the fibre being single mode, which has not been the case for any fibre drawn from 3D-printed preform so far (i.e., not only solid-core mPOFs, but also solid-core step-index POFs and hollow-core POFs) [30-34]. The aims of this thesis are to optimise printout transparency, 3D print an SC mPOF preform and draw it into a single-mode fibre.

1.2.2 Sensing applications

Furthermore, inscription of a fibre Bragg grating in an mPOF drawn from 3D-printed preform would be another milestone in the application of FDM to fibre manufacturing and is one of the aims of this thesis. This has not been presented so far [30-32], presumably due to a too low overall fibre quality. First, the FBG inscription would prove the fibre is of good quality and that no undesired characteristics are introduced by using 3D printed preform. Secondly, inscription by standard techniques would be a proof of the fibre being ready to use with existing fibre technologies. Lastly, this would make the fibre available to use in real-world sensing applications.

Embedding FBGs in 3D-printed structures can be beneficial due to the advantages of ALM in general and FDM in particular. A noteworthy quality of the latter is the possibility of pausing printing at any time to insert a fibre sensor, which can extend its range of applications. First, an FBG can be embedded in a customisable protective housing or a sensing patch to be attached to the structure to be monitored. Materials and designs can be tailor-made for the planned use, and embedding can be made on-site utilising a portable desktop 3D printer. Secondly, the FBG embedding can be used to manufacture stand-alone sensors, whose sensing mechanism relies on integration with some functional parts (e.g., beams or membranes, which can allow gauging temperature, pressure, relative humidity, strain, bend etc.). Different types of them can be included in a single printout, facilitating manufacturing of complex and highly customised sensors. Thirdly, sensing capabilities of FBGs can be decidedly extended by the embedding due to decoupling light guiding element (optical fibre) from the sensing one (fibre housing structure) and optimising each one separately. For example, benefits can be derived from embedding FBGs in some non-transparent thermoplastics and utilising their particular characteristics for sensing since drawing POFs from them would not be possible. Furthermore, a silica FBG, which is more robust than POFBG but intrinsically insensitive to water at the same time, can be embedded in highly water-absorbing polymer to create a humidity sensor. Finally, all the discussed properties can be combined, resulting, e.g., in a 3D-printed SOFBG-based sensor attached to the structure to be monitored, capable of gauging strain in one part, while being strain-isolated in another. The latter part could host temperature- and humidity-sensing FBGs, which could also be used to compensate the readout of the strain-gauging one. The aim of this thesis is then to demonstrate embedding multiple FBGs in one housing structure for temperature-compensated strain sensing. Another aim is to characterise the response of embedded FBGs to strain, temperature, and relative humidity.

Apart from directly embedding FBGs in 3D printouts, FDM can also be used to manufacture moulds for fibre embedding by casting. They could be customised to a high degree, considering desired dimensions and shape of the cast along with appropriate fibre inlets. Such an approach can benefit from using complex 3D-printed spatial structures while not being confined to embedding fibres in thermoplastic spooled filament materials used in FDM. This can lead to, e.g., FBG embedding in thermoset plastics or silicones of elasticity much higher than this of 3D-printing filaments. Moreover, the moulds can be manufactured of soluble materials, facilitating cast removal by dissolving the mould away. Furthermore, FDM can potentially enable production of much smaller moulds of the size just enough to cover a fibre grating. Embedding a POFBG made of highly water-absorbing PMMA in a small water-resistant bead formed around it can help isolate it from interference with humidity for a long enough time to perform measurements in which cross-sensitivity to water is expected. One aim of this thesis is then to manufacture moulds for fibre embedding by casting to integrate the fibre with the cast and to protect PMMA POFBGs from the influence of humidity during measurements.

Finally, FDM can find its use in other parts of sensor manufacturing process. A further aim of this thesis is to demonstrate 3D-printed application-specific FBG holders that can facilitate FBG handling, with the application, e.g., in ultrasound sensing. Moreover, a grating inscription set-up can be customised by the use of 3D-printed parts, for instance, a tailor-made protective phase mask holder with an integrated feedback screen for FBG inscription.

1.2.3 Summary of the thesis objective

The objective of this thesis is to combine the technology of silica and polymer FBGs with FDM 3D printing to achieve the following aims:

- optimising FDM 3D printing process in terms of printout transparency
- 3D printing solid-core and hollow-core polymer optical fibre preforms
- drawing the 3D-printed POF preforms into fibre
- embedding silica and polymer FBGs in 3D-printed protective housings to be used for strain sensing
- embedding multiple FBGs in 3D-printed sensing patches for temperature-compensated strain sensing
- embedding silica and polymer FBGs in 3D-printed sensing patches to enhance their temperature and humidity sensing capabilities.
- manufacturing moulds for fibre embedding by casting to integrate the fibre with the cast and to protect PMMA POFBGs from the influence of humidity during measurements
- demonstrating 3D-printed application-specific FBG holders that can facilitate FBG handling, with the application in ultrasound sensing

- demonstrating a tailor-made protective phase mask holder with an integrated feedback screen for FBG inscription

1.3 Thesis outline

As this work aims to combine different areas of fibre optics with fused deposition modelling, the background of this thesis is extensive and encompasses various topics. They are presented in Chapter 2 and include, first, basics of conventional optical fibres, and secondly, optical fibre materials and the influence they have on performance of optical fibres. Anisotropic properties of polymers, which are paramount to understanding behaviour of POF, are also reviewed. Furthermore, photonic crystals and photonic crystal fibres are introduced, highlighting the mechanism of their operation and their advantages over conventional fibres. In addition, fabrication techniques of polymer optical fibres are presented, including the use of 3D printing. Finally, this chapter discusses various aspects related to FBGs, entailing grating theory, photosensitivity mechanisms of silica and polymer fibres, FBG fabrications techniques and their sensitivity to measurands.

Chapter 3 presents the experimental set-ups applied in this work. This includes the 3D printer used in this research, the draw tower which was utilised to draw the manufactured preforms into fibres, and the FBG inscription systems. Regarding the latter, the chapter discusses the construction and use of the inscription set-ups and procedures involves in grating fabrication. Moreover, results of grating inscription are shown and reviewed. This chapter also presents the techniques used for FBG tuning and multiplexing.

The results of 3D printing POF preforms are described in Chapter 4, including both solid-core and hollow-core preforms made of two polymers: PMMA and polycarbonate (PC). This chapter discusses various preform designs, fabrication challenges and steps followed to resolve them. The most successful preform, which is the solid-core PC one, was successfully drawn to fibre, which is detailed in Chapter 5. The fibre displayed the lowest ever reported attenuation for a POF drawn from a 3D-printed perform. Apart from fibre drawing, this chapter also presents results of extensive fibre characterisation, involving numerical simulations of modal structure and loss figure and cut-back attenuation measurement, along with calculation and discussion of coefficient of thermal expansion and thermo-optic coefficient of the fibre. Finally, Chapter 5 describes the first successful inscriptions of FBG in a fibre drawing from a 3D-printed preform, which was achieved using three different laser systems.

Chapter 6 presents the work performed by the author on embedding silica and polymer FBGs in 3D-printed sensing patches. This includes rationale behind the design of the structures, challenges posed by the embedding process and the ways they were addressed. Response of the patches to strain, temperature, and humidity is also presented and discussed, which includes strain, temperature, and

humidity sensitivity, hysteresis, temporal stability of grating response and its repeatability, fibre slippage in the sample and spectral evolution of the embedded FBGs.

Summary and conclusions of the work presented in this thesis are contained in Chapter 7. It also proposes direction of future work that can be performed based on the achieved results. Finally, Chapter 8 lists the publications made in the course of this research.

Chapter 2 Background

This chapter reviews background literature information on which this thesis is built. This has been split into conventional optical fibres, material properties of optical fibres, anisotropic properties of POFs, photonic crystals, microstructured fibres, techniques to fabricate POFs, and fibre Bragg gratings.

2.1 Conventional optical fibres

This section presents basic theoretical concepts behind conventional optical fibres. These include definition and geometry of the fibre, refractive index profile, and requirements for guidance based on total internal reflection. Fibre modes, including their naming convention, and fibre dispersion are also briefly described. Notation introduced in this section is used in the remaining part of the thesis.

2.1.1 Basic concepts

Optical fibre is a key component of every fibre-based system for telecommunication, sensing or imaging. The basic property of a conventional optical fibre is capability of guiding light by means of total internal reflection (TIR). Conventional optical fibre is composed of a long cylindrical axially symmetric element of two dielectric regions of different optical properties. The refractive index (RI) of the inner region (n_{co}), called core, is slightly bigger than the RI of the outer one (n_{cl}), called cladding. For non-magnetic media, normally used to fabricate optical fibres, RI is defined as the square root of the relative permittivity [25]. Using ray optics, the simplest image of light guidance can be constructed based on Snell law. If $n_{co} > n_{cl}$, light propagating in the core is totally internally reflected from the core-cladding

interface, provided the angle between the core-cladding interface and the direction of propagation is small enough. If a fibre of perfect geometry, homogeneity and transparency could be realised, TIR would allow lossless light transmission.

More accurately, we can consider the core to be an infinitely long cylinder of circular cross-section and radius ρ, see Figure 2-1 [25]. Light propagates along the axis of the fibre (z axis) and is characterised by the free-space wavelength λ and the wavenumber $k_0 = 2\pi/\lambda_0$. The wave equation for each electromagnetic mode depends of the term $exp(i\beta z)$ along the fibre axis, β being the propagation constant. Wave vectors both in the core and in the cladding have β as their z components. The length (norm) of the core wave vector is $n_{co}k_0$, and of the cladding wave vector, $n_{cl}k_0$. In order to propagate in the core, β must be $\leq n_{co}k_0$, and to propagate in the cladding, β must be $\leq n_{cl}k_0$. If these inequalities are not fulfilled, β is evanescent in the core or cladding, respectively. For light to be trapped in the core, i.e., to be only able to propagate in the core and not in the cladding, the following relation must be conserved: $n_{cl} < \beta/k_0 < n_{co}$. The term β/k_0 is often referred to as the effective refractive index (n_{eff}).

Figure 2-1. Schematic of a conventional step-index fibre [25].

In the system described above, transverse wavenumber $k_\perp$ can be defined as [25]:

$$k_\perp^2 + \beta^2 = n^2 k_0^2, \tag{2-1}$$

where n denotes local refractive index. In conventional step-index fibres having $n_{co} > n_{cl}$, β is real, so $k_\perp = \sqrt{n^2 k_0^2 - \beta^2}$. Consequently, effective transverse wavelength equals [11]

$$\lambda_{eff} = \frac{2\pi}{\sqrt{n^2 k_0^2 - \beta^2}}. \tag{2-2}$$

Figure 2-1 shows the simplest case of fibre structure, in which the value of RI changes abruptly at the distance ρ going along the fibre radius. Such an RI profile is called step-index, and a fibre of such profile is referred to as a step-index (SI) fibre (Figure 2-2(b)). Alternatively, RI profile of a fibre can change gradually, resulting in a graded-index (GI) profile and a GI fibre (Figure 2-2(b)). In principle, as long as the condition $n_{co} > n_{cl}$ is met, various RI profiles are possible, each resulting in different fibre

properties. The details of RI profiles of conventional fibres and their consequences are out of the scope of this thesis and can be found in the literature [26, 92].

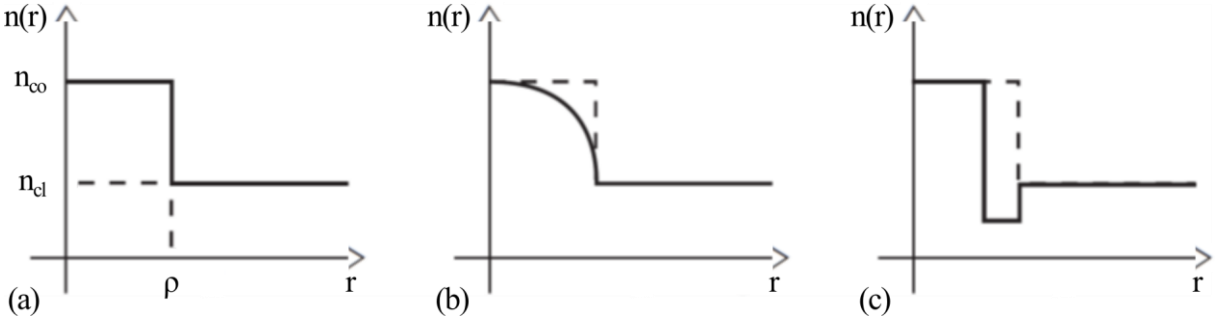

Figure 2-2. Examples of various RI profiles of a conventional optical fibre: (a) step-index (SI), (b) graded-index (GI), (c) depressed-index [26].

2.1.2 Fibre modes

The light propagating in the fibre core ($n_{cl}k_0 < \beta < n_{co}k_0$) is not free to take an arbitrary field distribution. This is due to the resonance condition (TIR) on the core-cladding boundary, which can be met only by a discrete set of transverse field distributions and their corresponding β values. The latter are eigenvalues of the propagation equation, while the transverse field distributions are their associated eigenfunctions [92]. The two quantities together form a fibre mode. For $n_{cl}k_0 < \beta < n_{co}k_0$, they are called guided modes, and there is a finite number of them.

The number of modes that the fibre can guide can be quantified by the so-called V parameter (also referred to as normalised frequency), taking the following form [92]:

$$V = k_0 \rho \sqrt{(n_{co}^2 - n_{cl}^2)}. \tag{2-3}$$

The smaller the parameter is, the lower the number of modes that are supported. For $V < 2.405$, the fibre supports only a single pair of modes that are degenerate (i.e., having the same β value) and is then said to be single-mode (SM, see Figure 2-3). Either of the pair of the degenerate guided modes is referred to as a fundamental mode (labelled HE_{11} in Figure 2-3). For $V > 2.405$, the fibre can support a higher number of modes, and is then said to be multi-mode (MM). In this case, the fundamental mode has the highest value of β of all supported modes. Modes other than the fundamental one are called higher order modes (HOM). As can be seen from Equation (2-3), a fibre of a given radius and RI difference between the core and cladding can be single-mode or multi-mode, depending on the wavelength of light, i.e., it is single-mode for a sufficiently large wavelength. Note that, for any set of ρ and λ, the fibre will always support at least one mode (see Figure 2-3).

Figure 2-3. Plot of the effective refractive index ($n_{eff} = \beta/k_0$) as a function of V for a few lowest order modes of a convectional optical fibre [93].

The electric ($\vec{E}$) and magnetic ($\vec{H}$) field vectors of a plane electromagnetic wave propagating in free space are always orthogonal to each other. They are also orthogonal, or transverse, to the direction of wave propagation, i.e, axial components of $\vec{E}$ and $\vec{H}$ (E_z and H_z, respectively) equal to 0. Such wave would be denoted as transverse electric magnetic, TEM. This picture changes in optical fibres due to boundary conditions imposed on an electromagnetic wave propagating in the fibre core. In this case, either $\vec{E}$ or $\vec{H}$, or both deviate slightly from the orthogonal arrangement with respect to the propagation direction (while still being orthogonal to each other). A mode in which $E_z = 0$ and $H_z \neq 0$ is called transverse electric, TE. In the opposite case (i.e., $E_z \neq 0$ and $H_z = 0$), a mode is referred to as transverse magnetic, TM. If neither E_z nor H_z equals 0, corresponding modes are called hybrid modes and labelled as HE or EH. The difference between HE and EH modes is based on relative strengths of E_z and H_z: in HE modes, E_z is relatively strong, while, in EH modes, H_z is relatively strong [94]. Furthermore, fibre modes are labelled with two subscripts (e.g., HE_{12}), which represent mode order in azimuthal and radial direction, respectively. For TE and TM modes, the first subscript is always equal to 0 due to azimuthal symmetry. Practically speaking, the first subscript multiplied by 2 equals the number of transverse field nodes in the azimuthal direction (e.g., going along core circumference). Similarly, the second subscript denotes the number of nodes the transverse field has in the radial direction, i.e., going along radius of the fibre core (see upper rows in Figure 2-4). More mathematically precise description of the fibre modes can be found in the literature [92, 94].

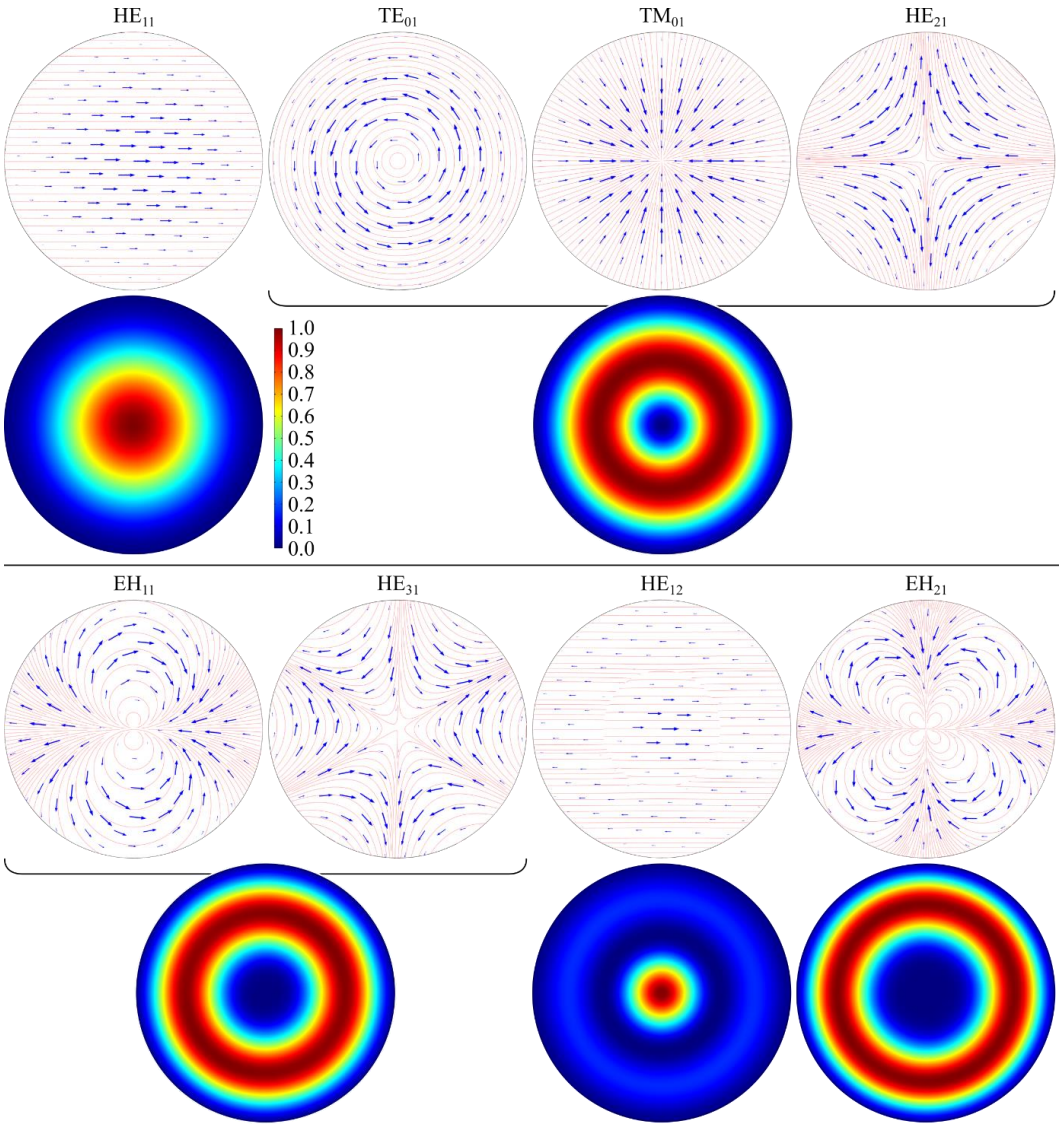

Figure 2-4. (Up) transverse electric field lines (in red) and field vectors (in blue) and (down) normalised time-averaged axial power flow intensity (Poynting vector) for the first eight modes of a conventional optical fibre. The length of the vector field arrows on the upper plots corresponds to field intensity. The plots were generated in the programme Comsol Multiphysics [95].

Power flow direction in non-absorbing waveguides is parallel to the fibre direction (z axis). Power density (or intensity) carried by the i-th mode is described by the time-averaged Poynting vector $\overrightarrow{S_i}$ [92]:

$$\overrightarrow{S_i} = \frac{1}{2}\mathrm{Re}\left\{\overrightarrow{E_i} \times \overrightarrow{H_i^*} \cdot \vec{z}\right\}, \tag{2-4}$$

where *Re* denotes real part, $\overrightarrow{E_i}$ and $\overrightarrow{H_i}$ – respectively, electric and magnetic field vectors of the i-th mode, * – complex conjugate, $\vec{z}$ – unitary z axis vector. $\overrightarrow{S_i}$ of the eight lowest-order modes of a conventional optical fibre is shown in the lower rows of Figure 2-4.

2.1.3 Dispersion

As it was stated, each non-degenerate mode has a different value of propagation constant (or a different effective refractive index; see also Figure 2-3). This leads to light in each mode propagating with different velocity [ ]:

$$v = \frac{c}{n_{eff}} = \frac{c\,k_0}{\beta}. \tag{2-5}$$

As it is difficult to precisely control which mode the light takes, it can effectively travel at a set of different velocities. This is called intermodal dispersion and makes a large difference after a long transmission distance. Other common sources of dispersion entail chromatic dispersion (due to dependence of β on λ) and polarisation mode dispersion (due to dependence of β on polarisation of light) [96]. However, in conventional optical fibres, their influence is usually much smaller. Dispersion is normally detrimental for optical communications, leading to pulse spreading and limiting maximum transmission distance and speed [92]. In addition, intermodal dispersion often hinders signal readout in fibre-optic sensing (e.g., when using fibre Bragg gratings [97]). Hence, for many applications, it is desirable that a fibre be single-mode.

2.2 Material properties of optical fibres

This section tackles the topic of optical fibre materials, including silica and various types of polymers. Their mechanical, chemical, optical, and thermal properties are discussed and compared from the viewpoint of their use in optical fibres.

The material used most widely to manufacture optical fibres is silica. Conventional optical fibres made of it constitute the largest and most mature branch of optical fibre technology. However, in principle, many materials can be used, including polymers, which are the focus of this dissertation.

This section gives an overview of mechanical, chemical, optical, and thermal properties of both silica and polymer optical fibres (SOFs and POFs, respectively). Major issues with POFs and limitations thereof are also addressed. Among POFs, the section focuses on poly(methyl methacrylate) (PMMA, trade name Perspex [98] or Plexiglass [ ]) and polycarbonates (PC, trade name Lexan [99]), the former being most widely used to fabricate POFs. This is because fibres fabricated of both PMMA and PC are presented in the experimental section of the thesis. Referral to any other polymer material is mentioned explicitly.

It must be noted that properties of POFs found in the literature vary substantially. This can be attributed to significant changes in these properties depending on many factors: details of polymerisation process (e.g., presence of initiators, plasticisers and chain transfer agents) and fibre drawing conditions.

2.2.1 Mechanical properties

One of the simplest yet very informative technique of mechanical characterisation is determining the relationship between stress and strain in a material (stress-strain curve). At low strains, the response of the material to stress is, to a good approximation, linear. It can then be described with the Hooke's law [100]:

$$\sigma = E\,\epsilon \tag{2-6}$$

where σ (Nm^{-2} or Pa) is stress, ϵ – strain, and E – Young's or elastic modulus (Nm^{-2} or Pa). The latter is then the slope of the stress-strain curve at low strain values.

There are important differences in the mechanical properties of silica and polymers, resulting from their physical and chemical nature. Silica, an isotropic elastic material, has a Young's modulus value of 73 GPa [101] at room temperature. The polymers used to fabricate POFs are viscoelastic materials, whose Young's modulus values for bulk samples at room temperature range from 1.6 to 3.4 GPa in the literature (see Table 2-1).

The Young's modulus of silica and polymers depends on temperature. Counterintuitively, for fused silica, it increases with temperature, contrary to almost all other glasses and polymers [102, 103]. Due to polymers being much more complex materials than inorganic glasses, they can display very different behaviour depending on the temperature at which they are used. This pertains not only to Young's modulus itself, but to the entire shape of the stress-strain curve (see Figure 2-5). More details can be found in the literature [100].

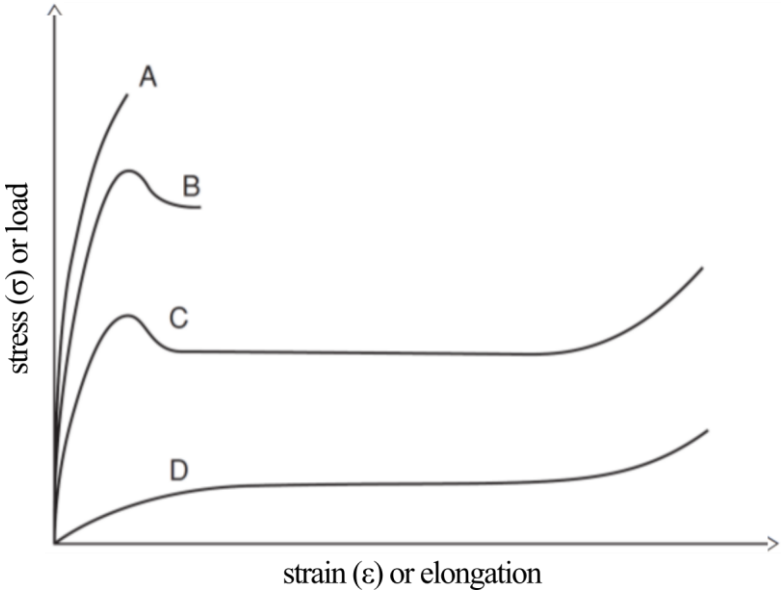

Figure 2-5. Stress-strain (or load-elongation) curves for a polymer at different temperatures (rising from A to D): (A) brittle fracture, (B) ductile failure, (C) cold drawing, (D) rubber-like behaviour [100].

Unlike bulk polymer, a POF drawn from it is often an anisotropic material. This impacts multiple characteristics of POFs, including the axial Young's modulus of the fibre, which is normally higher than in bulk [104] (see Table 2-1). Discussion of the anisotropic nature of POFs is given in Section 2.3.

Table 2-1. Comparison of mechanical properties and fibre loss for various polymers used for POF manufacturing.

Material	Glass transition temperature T_g (°C)	Highest reported operational temperature (°C)	Young's modulus in bulk (GPa)	Axial Young's modulus in fibre (GPa)	Minimum reported fibre loss (dB/m)
PMMA	106 [105]	92 [105, 106]	1.6-3.4 [4]	4.32 [107]	0.14[a] at ~650 nm [108] 10 at ~850 nm [109] ~100 at ~1550 nm [4]
MMA-*co*-PFPMA[b]	118 [108]	-	-	-	0.1 at ~650 nm [108]
Polycarbonate (PC)	145 [105]	125 [107]	2.00-2.44 [110]	2.70-3.03 [107, 111, 112]	4.06 at ~850 nm [105]
Topas 8007S-04	78 [113]	32.6 [114]	2.6 [113]	2.78-3.30 [107, 111]	-
Topas 5013S-04	134 [115]	110 [116]	3.2 [115]	3.10-3.27 [111]	3.67 at ~850 nm [116] 4.2[c] at ~850 nm [117]
Cytop	108 [118]	72 [119]	-	-	0.25 at ~1550 [120]
Zeonex 480R	138 [121]	100 [122]	2.1 [121]	2.41-2.71 [111]	2.34 at ~650 nm [122] <3.2 at ~850 nm [122]

[a] large core graded-index fibre

[b] a copolymer of methyl methacrylate and pentafluorophenyl methacrylate [108]

[c] core of Topas 5013S-04, cladding of Zeonex 480R

A huge difference can be observed in the failure strain of SOFs and POFs. The former typically ranges from 5-10% [123], although it may be decreased by scratches on the surface of glass [124] and repetitive loading [4]. Failure strain of POF can exceed 100% [76], though the exact value depends on the details of polymerisation, drawing [4], and the temperature at which it is measured (see Figure 2-5). Annealing has been reported to improve the performance of POFs, lowering the Young's modulus, yield point and tensile strength, while increasing the failure strain after a several-day-long treatment at 95 °C [125].

Hysteresis is another factor stemming from viscoelastic nature of polymers, which represents a substantial complication in fibre behaviour [4]. Figure 2-6 shows the result of cyclic strain applied to a PMMA fibre. Consecutive strains cycles represent the same strain increment and start after stress from previous cycle decreases to zero. After being left in a relaxed state, the fibre returned to its original length after several hours, the exact time being a function of the strain change induced previously [126].

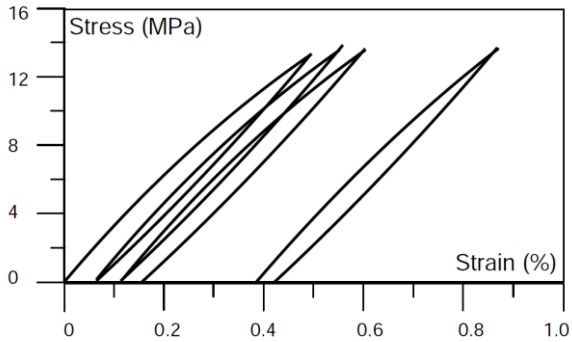

Figure 2-6. 1st, 2nd, 3rd and 10th cycles from repetitive tensile testing of PMMA fibre [126].

2.2.2 Chemical properties

From a chemical point of view, PMMA and PC, being organic materials, differ significantly from silica (SiO_2), which is an inorganic compound. Silica glass is made exclusively of covalent bonds, while the molecular structure of polymer is much more complex. Polymers are composed of long and primarily linear molecules linked with covalent bonds. Intermolecular interactions between different polymer molecules are governed by secondary (or weak) bonds. PC is the name of a group of compounds, of whom the most often used is bisphenol-A polycarbonate. Molecular structures of monomers of PMMA and PC are shown in Figure 2-7.

Organic chemistry has proven its flexibility in meeting various material requirements, giving much freedom in changing composition, structure and hence properties of polymers. The polymerisation process can be influenced changing substrates taking part in the reaction. Various types of chemical species can be introduced to the material structure, either as copolymers, or dopants, or main chain additives [4]. This has been reported to lead to improvement of photosensitivity [127], enhancement of nonlinear properties [128], sensitisation to chemical species [129] or optical amplification [130].

Figure 2-7. Molecular structure of repeating units of (a) PMMA [98] and (b) various kinds of PC [131].

2.2.3 Optical properties

In an idealised case of light propagation in an optical fibre made of homogenous lossless medium, TIR would assure that the light is perfectly confined to the core and, hence, can propagate infinitely far. In real conventional optical fibres, light propagates in a lossy medium (e.g., silica, polymer). Such losses can be divided into scattering losses and absorption losses (Figure 2-8) [96]. The former, also known as Rayleigh scattering, comes from RI of the fibre not being perfectly homogenous along the fibre axis. Optical fibres are made of amorphous materials, characterised by a random arrangement of atoms. This gives rise to nanoscopic fluctuations of RI (at the order of $\lambda/10$ or less), which act as sources of scattering. Rayleigh scattering is present both in silica and polymers.

Absorption loss in silica results from the presence of impurities, mainly hydroxyl ions (OH^-) and transition metal ions (e.g., Fe^{3+}, Cu^{2+}). Control over the latter gave the largest improvement in silica fibre attenuation since its invention. At $\lambda > 1.6$ μm, vibrational states of the atomic lattice (phonons) are the main source of losses. Although the main phonon absorption peak is at 9 μm for SiO_2, combination and overtone absorption bands appear also at higher wavelengths. This is due to anharmonic nature of interatomic forces (Figure 2-8).

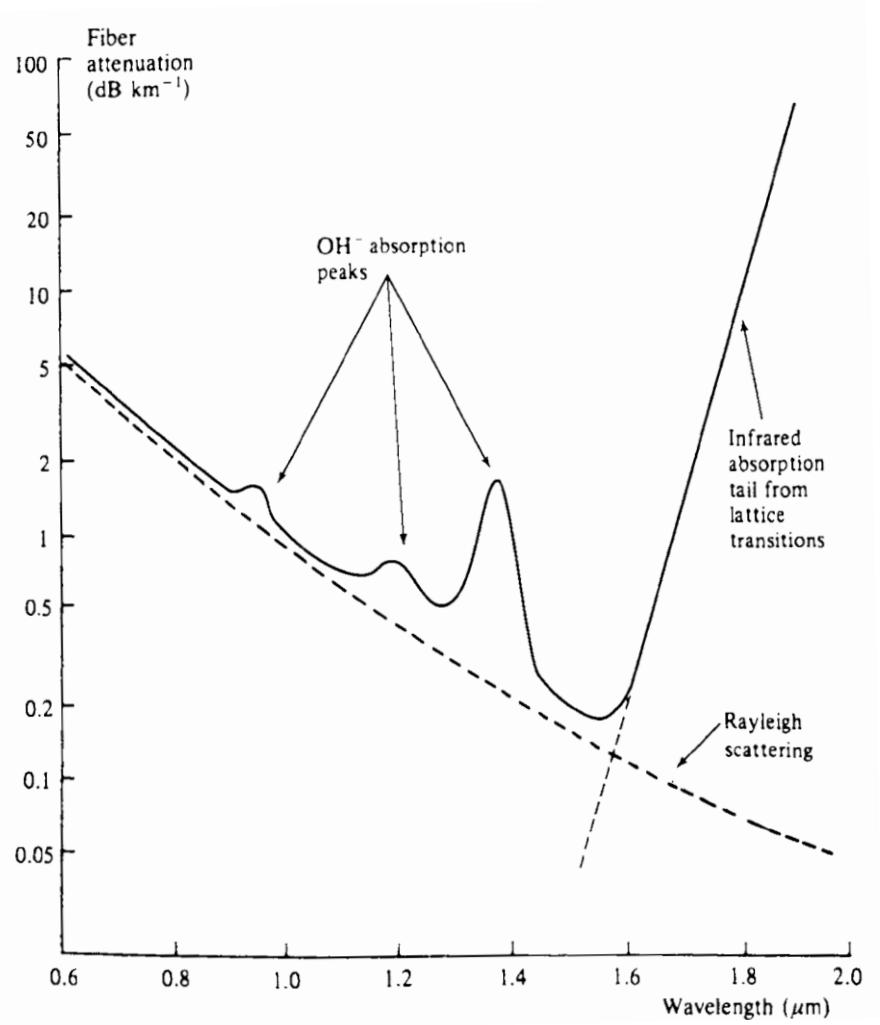

Figure 2-8. Attenuation vs wavelength for a typical conventional silica fibre. The main loss mechanisms are marked (see text for details) [96].

In polymers, absorption losses also manifest themselves at longer wavelengths. They result mainly from vibrational resonances of hydrogen bonds in polymer (C-H and O-H). This can be addressed by replacing hydrogen atoms, which are relatively light, with heavier one. Two species commonly used for that purpose are the deuterium isotope of hydrogen (leading to deuterated polymers) and fluorine (resulting in perfluorinated compounds).

The overall attenuation of SOFs is much smaller compared to POFs in the entire optical telecommunication spectrum, typically reaching 5 dB/km at 600 nm, 1 dB/km at 800 nm [4], and being much smaller at longer wavelengths. The lowest attenuation of silica fibre reported so far is 0.1419 dB/km at 1560 nm [3]. Long haul telecommunication systems are thus operated at 1300 nm or 1550 nm (2nd or 3rd telecommunication window, respectively). PMMA exhibit the opposite behaviour at these wavelength ranges, with enormous losses attaining 1 dB/cm (100,000 dB/km). On the contrary, the region of lowest losses falls around 650 nm (commercially available large core POFs can reach 0.1 dB/m (100 dB/km) [108]). Deuteration (i.e., substituting hydrogens of the polymer with deuterium)

has been reported to reduce the loss of a multi-mode fibre to less than 30 dB/km (in the region of 600-700 nm) [4], whereas the loss in the range of 1300 nm and 1500 nm has been reduced to around 10 dB/km using perfluorinated polymer (Cytop) [132] (Figure 2-9). The lowest reported loss figures for a range of polymers used to manufacture POFs are collated in Table 2-1.

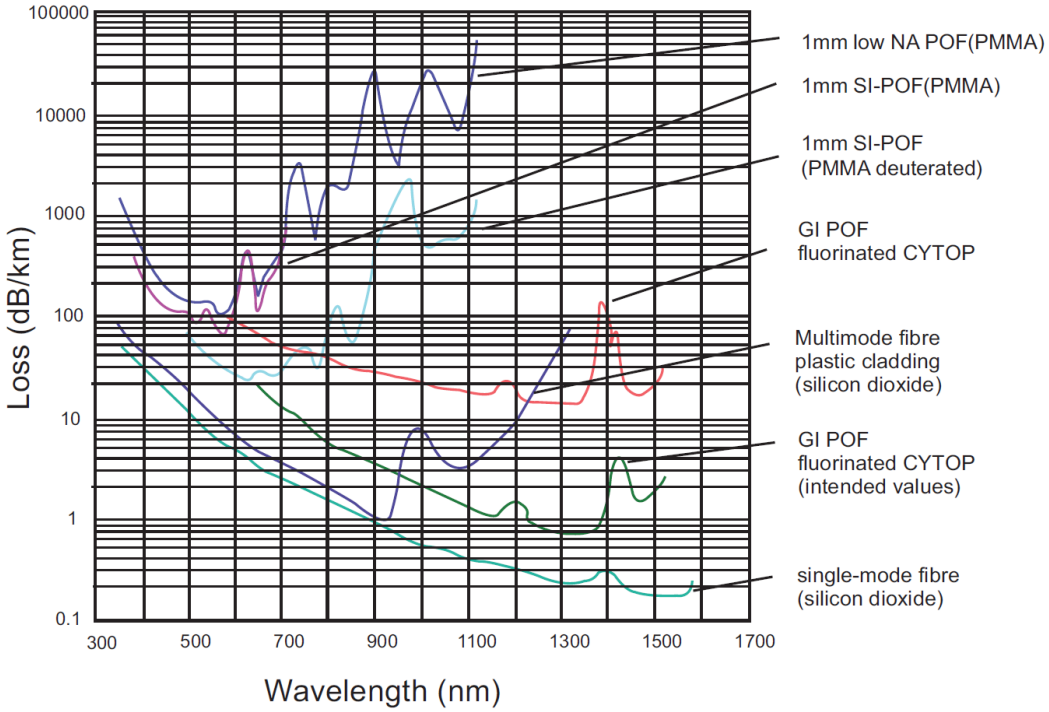

Figure 2-9. Comparison of the absorption spectra of a standard SOF and different types of POFs [126]. Low numerical aperture means a low light acceptance angle measured with respect to the fibre axis. Numbers in the legend correspond to fibre core diameter.

2.2.4 Thermal properties

Optical fibres are composed of silica or polymer in the amorphous phase (i.e., not crystalline). In solid state, silica can form both crystalline and amorphous phases, while polymers can be semi-crystalline, depending on their composition. However, when a material solidifies, in general a slow cooling rate is required so that it forms a crystalline phase. This condition is not met during both silica and polymer fibre drawing, which results in fibre being composed of amorphous materials.

When crystallisation does not occur despite the temperature falling below the melting temperature (T_m) on material cooling from the melt, the liquid is said to be supercooled (see Figure 2-10) [133]. In this instance, molecules of the liquid move more and more slowly. However, a coefficient describing the dependence of specific volume on temperature (or a coefficient of thermal expansion, CTE), which is the slope of the curve in Figure 2-10, is still the same as for a liquid. As the temperature falls, the rate of molecular movement becomes too small to be observed at the timescale of the experiment. The positions of the molecules become essentially "frozen", and the liquid is referred to as a glass. Moreover,

a change (normally a decrease) in CTE can be observed, and its value is now similar to this in the crystalline phase. In the glassy state, thermal expansion is dominated by atomic vibrations, which are very similar in both crystal and glass. The range of the temperature values over which the CTE changes is called the transformation range.

In order to quantify this transformation, a parameter called the glass transition temperature (T_g) is used. It can be defined in different ways. The simplest one is to extrapolate the specific heat line in the glass state until it crosses with this in the liquid state (see Figure 2-10), the temperature at the crossing point being T_g. Alternatively, it can be defined using a value of viscosity, which is nearly 10^{13} Pa for silica [133]. It must be underlined that glass transition is not a first-order phase transition and may be not any kind of phase transition at all [133]. Glass is not the crystalline or liquid crystalline phase. There is no single glass transition temperature for a given polymer. Rather, its thermal history determines T_g – glass 1 in Figure 2-10 was formed during a quicker cooling than glass 2.

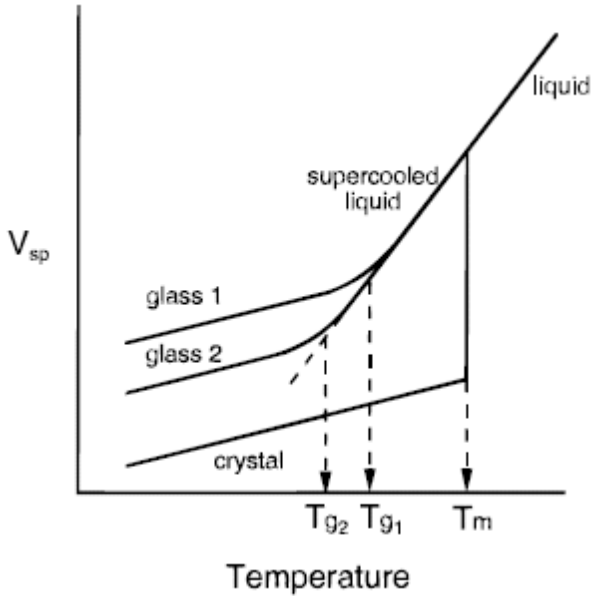

Figure 2-10. Specific volume (V_{sp}) as a function of temperature for a liquid capable of both crystallising and forming a glass. T_m – melting temperature, T_g – glass transition temperature [133].

Polymers, being much more complex materials than silica, exhibit more than one transition temperature [100]. These are called viscoelastic relaxation transitions and, starting from the one occurring at the highest temperature, are labelled as α, β, γ, δ etc. The first one is associated with T_g of the polymer. In PMMA, β relaxation is associated with side-chain movement of the ester group. Further relaxation transitions in PMMA are not important, because they appear at too low temperatures to be of practical interest for the scope of this work. For each POF, temperature values of the relaxation transitions vary and are a function of multiple parameters, including chemical and molecular

composition, presence of impurities and plasticisers, humidity, and fibre drawing conditions [77, 134, 135].

Normally, adjacent polymer molecules are only linked with each other by means of secondary bonds. This means that they are thermoplastic, i.e., they can transition between molten and glassy state multiple times on appropriate temperature changes. In some polymers under special conditions, adjacent polymer molecules can link to each other with covalent bonds when in the glassy state, forming a cross-linked molecular network. In this case, polymers are called thermoset and cannot transition to the molten state anymore. Thermoplasticity is one of the basic molecular requirements for polymers to be used for POF drawing.

The thermal expansion of a material can be quantified using a CTE. As it was mentioned, it can be defined as a change of volume with temperature (volumetric CTE, VCTE) or, alternatively, negative change of density with temperature:

$$\beta = \frac{1}{V}\left(\frac{dV}{dT}\right), \beta = -\frac{1}{\rho}\left(\frac{d\rho}{dT}\right), \tag{2-7}$$

where β (°C^{-1}) is the VCTE, V (m^3) – volume, ρ (kg/m^3), T (°C) – temperature. Analogously, the linear CTE (LCTE) can be defined as a change of length with temperature:

$$\alpha = \frac{1}{L}\left(\frac{dL}{dT}\right). \tag{2-8}$$

where α (°C^{-1}) is the LCTE, L (m) – length. For isotropic materials, the following relationship holds:

$$\beta = 3\alpha. \tag{2-9}$$

The refractive index is normally dependent on temperature too. The most widely used relationship between the RI and other physical quantities is the Lorentz-Lorenz (L-L) equation [136, 137]:

$$\frac{n^2 - 1}{n^2 + 2} = \frac{4\pi}{3}\frac{\rho N_a}{M}P, \tag{2-10}$$

where n is the RI, ρ – density, N_a – Avogadro's number, M – molecular mass, P – mean polarizability. There are other similar equations describing the same relationship [137], of which the Drude equation is also sometimes applied in the field of polymers. In this thesis, the L-L relationship will be used though. First, it is the most widely accepted and applicable for a broad range of materials. Furthermore, no clear benefits can be derived from using different relationships of polarisability as none of them prove decisively more accurate for polymers than the L-L equation.

Dependence of the RI on temperature (i.e., thermo-optic coefficient, TOC) can described with the following equation, consisting of two terms:

$$\frac{\mathrm{dn}}{\mathrm{dT}} = \left(\frac{\delta \mathrm{n}}{\delta \rho}\right)_{\mathrm{T}} \left(\frac{\delta \rho}{\delta \mathrm{T}}\right) + \left(\frac{\delta \mathrm{n}}{\delta \mathrm{T}}\right)_{\rho}. \tag{2-11}$$

The first one $\left(\left(\frac{\delta n}{\delta \rho}\right)_T \left(\frac{\delta \rho}{\delta T}\right)\right)$ represents a change of the RI due to a change in density at constant temperature $\left(\left(\frac{\delta n}{\delta \rho}\right)_T\right)$, density itself being dependent on temperature $\left(\frac{\delta \rho}{\delta T}\right)$. The second one $\left(\left(\frac{\delta n}{\delta T}\right)_\rho\right)$ corresponds to a change of the RI at constant density, i.e., solely due to temperature. Equation (2-11) can be rewritten, using Equation (2-7), into:

$$\frac{\mathrm{dn}}{\mathrm{dT}} = -\left(\frac{\rho \delta \mathrm{n}}{\delta \rho}\right)_{\mathrm{T}} \beta + \left(\frac{\delta \mathrm{n}}{\delta \mathrm{T}}\right)_{\rho}. \tag{2-12}$$

Differentiating the L-L equation, the term $\left(\frac{\rho \delta n}{\delta \rho}\right)_T$ can be written as:

$$\left(\frac{\rho \delta \mathrm{n}}{\delta \rho}\right)_{\mathrm{T}} = (1 - \Lambda_0) \frac{(\mathrm{n}^2 - 1)(\mathrm{n}^2 + 2)}{6\mathrm{n}}. \tag{2-13}$$

The parameter Λ_0, the strain polarisability constant, is not present in the result of the differentiation. It was added by Müller [138] to take into account the effect of a change in density on the atomic polarizability of a material. Applying Equation (2-13), Equation (2-12) can be expressed as:

$$\frac{\mathrm{dn}}{\mathrm{dT}} = \frac{(\mathrm{n}^2 - 1)(\mathrm{n}^2 + 2)}{6\mathrm{n}} (-\beta + \Lambda_0 \beta + \phi), \tag{2-14}$$

where $\phi = \frac{1}{P}\frac{dP}{dT}$ is the temperature dependence of polarisability. The values of the parameters β, Λ_0, and ϕ have been collated in Table 2-2. The values of ϕ for both polymers could not be found in the literature, but $\left(\frac{\delta \mathrm{n}}{\delta \mathrm{T}}\right)_{\rho}$ was given in [99]. From this, ϕ was calculated according to Equations (2-12) and (2-13) using the appropriate RIs, yielding slightly different values at different wavelengths. The value of ϕ for silica was corrected considering the parameter Λ_0, which was omitted in the calculations presented in the source paper [139].

As can be seen from Table 2-2, the TOC of polymers is dominated by β, which is over one order of magnitude higher than ϕ. For PMMA, the term $-\frac{(n^2-1)(n^2+2)}{6n}(1 - \Lambda_0)\beta$ gives the values from -86 to

-160×10^{-6} °C^{-1}, compared to $\frac{(n^2-1)(n^2+2)}{6n}\phi$ yielding -4.0×10^{-6} °C^{-1}. The results for PC are from -76 to -131×10^{-6} °C^{-1} and 8.7×10^{-6} °C^{-1}, respectively. The relative contribution of the two terms to the TOC looks just the opposite for silica due to ϕ being over one order of magnitude higher than β. The term $\frac{(n^2-1)(n^2+2)}{6n}\phi$ dominates the TOC with the contribution of ~8.4×10^{-6} °C^{-1}, whereas the term $-\frac{(n^2-1)(n^2+2)}{6n}(1-\Lambda_0)\beta$ only yields ~-0.51×10^{-6} °C^{-1}. Hence, the simplified variant of Equation (2-14) for polymers looks as follows:

$$\frac{dn}{dT} = \frac{(n^2-1)(n^2+2)}{6n}(-\beta + \Lambda_0\beta), \tag{2-15}$$

whereas for silica it can be rewritten as:

$$\frac{dn}{dT} = \frac{(n^2-1)(n^2+2)}{6n}\phi. \tag{2-16}$$

Table 2-2. The parameters β, Λ_0, and φ for isotropic PMMA, PC, and silica (at room temperature).

Parameter	PMMA	PC	Silica
Λ_0	0.15 [99]	0.18 [99]	0.4 [140]
β (× 10^{-6} °C^{-1})	180-330 [71, 99, 141-143]	150-243 [71, 99, 141, 142, 144-146]	~1.65 [139]
ϕ (× 10^{-6} °C^{-1})			16.2 [139]
at 850 nm	-7.0 [99] (RI = 1.4859 [147])	12.4 [99] (RI = 1.576 [107])	
at 1550 nm	-7.1 [99] (RI = 1.4809 [147])	12.6 [99] (RI = 1.567 [107])	

Equation (2-15) without the parameter Λ_0 is known under the Prod'homme theory [148]. An alternative yet equivalent notation, considering the three terms described by Equation (2-14), has been developed by Rachmachandran [149], who started from the Drude equation [137] instead of L-L. The equation by Ramachandran is also used to study TOC of polymers [72, 150]

2.3 Anisotropic properties of POFs

This section gives an overview of anisotropic material properties of POFs. After a general introduction to anisotropy, the following characteristics are covered: anisotropic Young's modulus, anisotropic thermal expansion, orientation and stress birefringence, and the dependence of orientation birefringence on temperature.

2.3.1 Introduction

When in bulk, both silica and polymers are isotropic materials. However, difference in their atomic structures results in polymers showing orientational anisotropy, which influences many of its properties. Generally speaking, molecular properties along a polymer molecule result from covalent bonds of the main molecular chain. However, material properties between the polymer molecules arise from secondary (or weak) intermolecular bonds. At random orientation of the polymer molecules, these molecular differences do not translate to variations of macroscopic material properties, and the material can be considered isotropic. When polymers are drawn or extruded, their molecules tend to be preferentially oriented along the draw or extrusion direction. Materials exhibiting such behaviour were thus named oriented polymers. Those characterised by one direction (axis) of deformation (i.e., drawing or extrusion) are called uniaxially oriented polymers. They also have one symmetry axis along the direction of deformation, and hence anisotropic behaviour of such materials manifests itself between the direction parallel and perpendicular to the direction of deformation. POFs make part of uniaxially oriented polymers, and so other types of molecular orientation in polymers are out of the scope of this thesis. As a result of anisotropic molecular orientation, macroscopic material properties of oriented polymers are also anisotropic. These include anisotropic Young's modulus, anisotropic thermal expansion, birefringence, and anisotropic thermo-optic coefficient among other material characteristics [151].

The process of drawing (or extrusion) of polymers can be described with the parameter called draw (or extrusion) ratio. It is defined as the ratio of the length of the sample in the draw direction after drawing to the length before drawing. When the measurements of length are difficult to perform (e.g., for POFs, due to their high length), the draw ratio can be defined using cross-sectional areas of the fibre or fibre diameters (assuming volume conservation on drawing) [152]:

$$\lambda_{\mathrm{d}} = \frac{\mathrm{l_f}}{\mathrm{l_i}} = \frac{\mathrm{A_i}}{\mathrm{A_f}} = \frac{\mathrm{d_i^2}}{\mathrm{d_f^2}}, \tag{2-17}$$

where λ_d is the draw ratio, l_i and l_f (m) are the initial and final lengths, respectively, of the polymer sample, A_i and A_f (m^2) are the initial and final areas, respectively, and d_i and d_f (m) are the initial and final diameters, respectively. POFs are characterised by a very high value of draw ratio, which is often at order of magnitude of 1000 [153].

Some properties of polymers (e.g., birefringence, thermal expansion) can be analysed by means of the aggregate model. Using this approach, an isotropic polymer can be considered to be an aggregate of axially symmetric intrinsic units of random orientation, i.e., the properties of the intrinsic unit (such as birefringence, thermal expansivity) are the same as those of the fully orientated material. As the polymer becomes oriented (e.g., due to drawing), axes of the intrinsic units rotate towards the drawing direction. This can be quantified by the orientation function. For uniaxially drawn transversely symmetric

polymers, the orientation function (f_{or}), sometimes referred to as the Hermans-Stein orientation function, takes the following form [151]:

$$f_{or} = \frac{1}{2}\left(3\,\overline{\cos^2\theta} - 1\right), \tag{2-18}$$

where θ denotes the angle between the draw direction (i.e., the fibre axis) and the intrinsic unit of the polymer (i.e., the molecular axis of a single segment of the molecular chain of the polymer). Bar over $cos^2\theta$ denotes the average over the polymer aggregate. For highly oriented polymers (often including POFs), $\theta \approx 0°$, hence $f_{or} \approx 1$.

2.3.2 Anisotropic Young's modulus

For uniaxially oriented polymers, the value of Young's modulus is usually higher in the draw direction (the fibre axis in POFs) than perpendicularly to it (Figure 2-11). This is due to the material behaviour in the draw direction being dominated by covalent bonds, which are much stronger than the secondary bonds and, hence, cause the material to be stiffer in the axial direction. Much weaker secondary bonds, which are at the origin of higher material flexibility, are responsible for the material properties perpendicular to the draw direction. The higher the degree of molecular orientation, the higher the anisotropy of Young's modulus (see Figure 2-12). Anisotropy in Young's modulus is also reflected in Table 2-1, in which its values in the axial direction are higher than the corresponding values in bulk for all polymers.

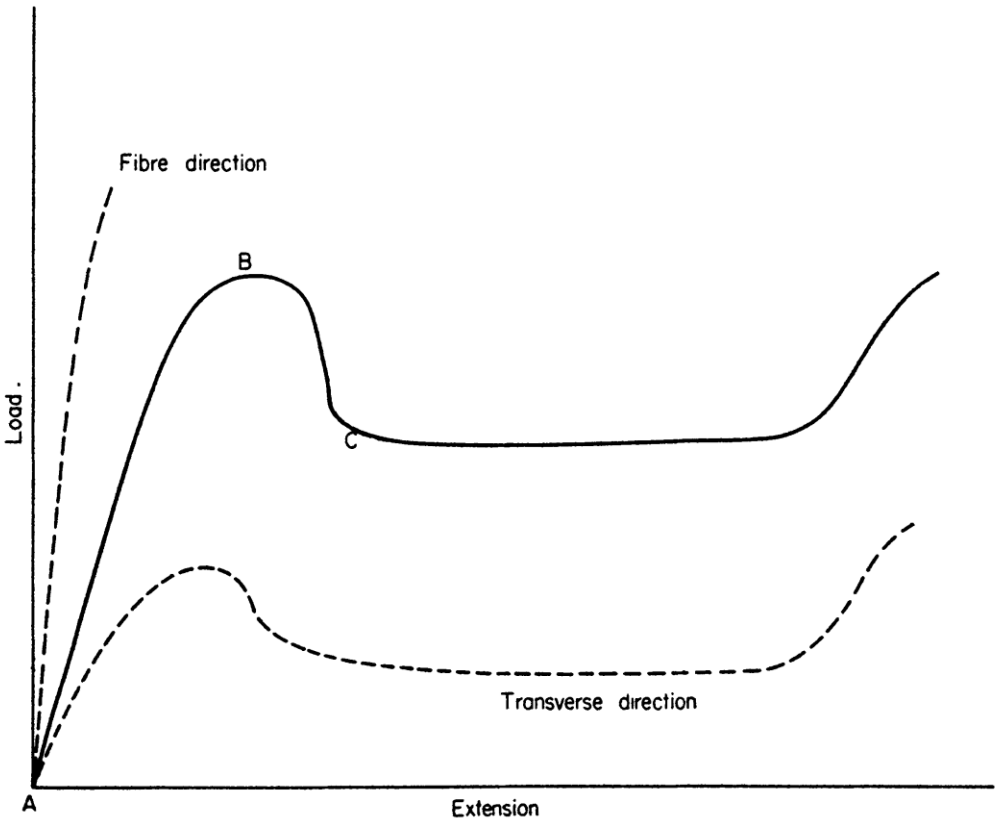

Figure 2-11. Typical stress-strain curve for (solid line) isotropic polymer and (dashed lines) oriented polymer, the latter showing different Young's modulus values for axial and transverse directions [151].

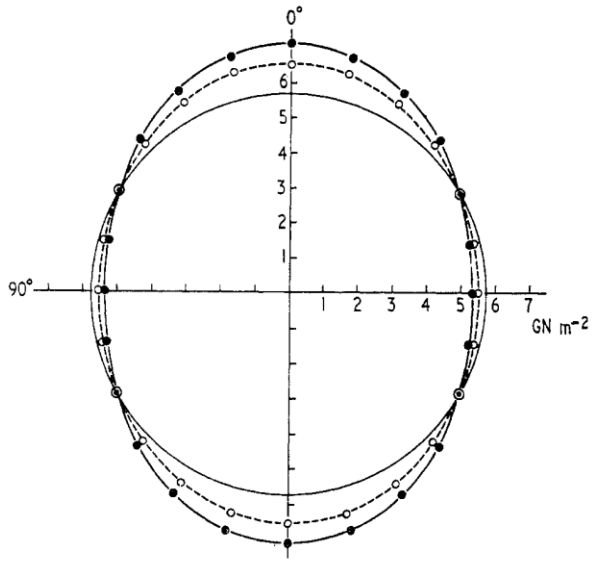

Figure 2-12. Polar diagram showing increasing anisotropy of Young's modulus of PMMA with growing degree of molecular orientation: (solid line) isotropic, (open circles) lower degree of orientation, (solid circles) higher degree of orientation. Angles on the axes are measured with respect to the draw direction [154].

2.3.3 Anisotropic thermal expansion

Thermal expansion is another material property that is anisotropic in oriented polymers [155-158] (including POFs [155]). In uniaxially oriented polymers, thermal expansion is usually lower in the axial direction than in the transverse one. Normally, the higher the draw or extrusion ratio, the higher the degree of anisotropy (see Figure 2-13).

In principle, VCTE of oriented polymers should be equal to this of the isotropic material. For uniaxially oriented polymers, VCTE takes the following form:

$$\beta = \alpha_{\parallel} + 2\alpha_{\perp}, \tag{2-19}$$

where $\alpha_{//}$ and $\alpha_{\perp}$ are LCTEs parallel and perpendicular, respectively, to the draw direction. Consequently, average LCTE (α_{av}) of uniaxially oriented polymers should also equal this of the isotropic material (α_{iso}). Since $\beta = 3\alpha_{iso}$ (Equation (2-9)), the following equation holds true:

$$\alpha_{\mathrm{iso}} = \alpha_{\mathrm{av}} = \frac{\beta}{3} = \frac{\alpha_{\parallel} + 2\alpha_{\perp}}{3}. \tag{2-20}$$

In the framework of the aggregate model, the relation of $\alpha_{\parallel}$ and $\alpha_{\perp}$ can be also approximated using the orientation function f_{or} defined earlier (see Equation (2-18)) [159, 160] [161]:

$$\frac{\alpha_{\perp} - \alpha_{\parallel}}{\alpha_{\perp}^{0} - \alpha_{\parallel}^{0}} = \mathrm{f_{or}}, \tag{2-21}$$

where $\alpha_{\parallel}^{0}$, $\alpha_{\perp}^{0}$ are intrinsic LCTEs parallel and perpendicular, respectively, to the axis of the intrinsic unit, i.e., to the axis of an ideally oriented polymer. For such polymers, $\alpha_{\parallel}^{0}$ is normally of the order of LCTEs of low molecular mass materials with covalent bonds only (e.g., silica glass, whose LCTE ≈ 0.55×10^{-6} °C^{-1}) [161]. On the other hand, $\alpha_{\perp}^{0}$ is normally much bigger than α_{iso}. Hence, $\alpha_{\parallel}^{0}$ can be safely assumed to equal to 0 [161]. In this case, Equation (2-21) can be reformulated using Equation (2-20) into:

$$\mathrm{f_{or}} \approx \frac{\alpha_{\perp} - \alpha_{\parallel}}{\alpha_{\perp}^{0}} = \frac{3}{2} \cdot \frac{\alpha_{\perp} - \alpha_{\parallel}}{\alpha_{\mathrm{iso}}} = 1 - \frac{\alpha_{\parallel}}{\alpha_{\mathrm{iso}}}. \tag{2-22}$$

For polymers of very high orientation ratio ($f_{or} \approx 1$), which is typical of POFs [153], $\alpha_{\parallel}$ can be negligibly small compared to $\alpha_{\perp}$. Despite the aggregate model having been used to assess CTEs of PMMA and PC [162-164], it was found that both PMMA and PC do not follow Equation (2-22) exactly. The CTE anisotropy of PMMA is smaller and that of PC, much larger than predicted by Equation (2-22) [163]. Hence, Equation (2-22) cannot be considered quantitatively accurate and should rather be treated as an indication of direction of changes.

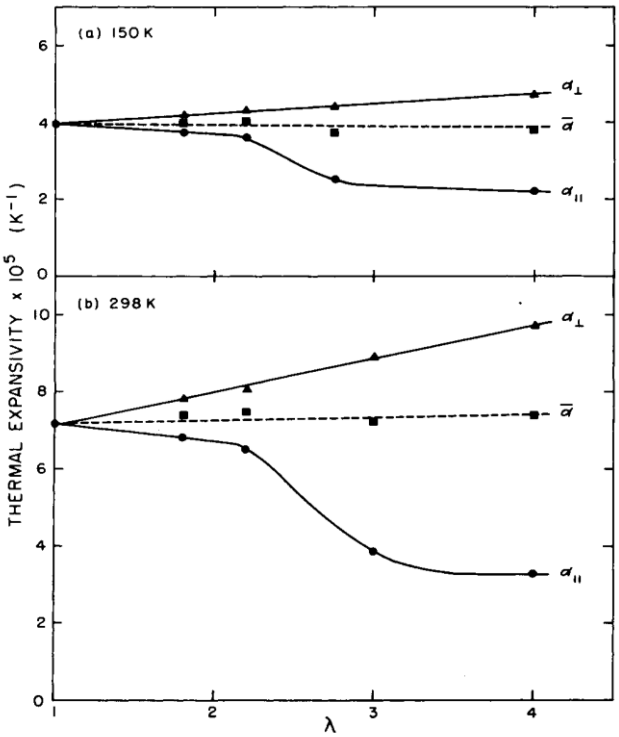

Figure 2-13. Dependence of LCTEs in the axial ($\alpha_{//}$) and transverse ($\alpha_{\perp}$) directions and average LCTE (α_{av}) on extrusion ratio of PMMA at (a) 150 K and (b) 298 K [159].

2.3.4 Introduction to birefringence

Birefringence, also called optical anisotropy, is an important characteristic of various materials [165] and is normally present in POFs too. It is a phenomenon where light propagating in a material experiencing different RI depending on the direction of propagation and the polarisation of the light [166]. In the simplest case, a birefringent material has one optic axis (e.g., *z* axis – see Figure 2-1) and is called a uniaxial material. The polarisation of light propagating along this axis is always perpendicular to it (i.e., is in *x*-*y* plane), and it experiences an ordinary refractive index n_o. Light propagating perpendicularly to the optic axis, e.g., along *x* axis, and being polarised along *y* axis, i.e., also perpendicularly to the optic axis (*z* axis in this case), experiences the ordinary RI n_o as well. However, light propagating in the same direction, i.e., along *x* axis, but being polarised along *z* axis (i.e., along the optic axis), experiences an extraordinary RI n_e. In a general case, light propagating in a random direction, described by the electric field vector $\vec{E} = [E_x, E_y, E_z]$, experiences a RI laying between n_o and n_e. The actual experienced RI value depends on relative contribution to $\vec{E}$ made by field components along (E_z) and transversely (E_x, E_y) to the optic axis. The higher the relative contribution of E_z, the closer the experienced RI is to n_e. Birefringence (Δn) described the range in which the RI experienced by light changes and, thus, is defined as the difference between the RI along extraordinary (n_e) and ordinary (n_o) directions [165]:

$$\Delta n = n_e - n_o. \tag{2-23}$$

In the case of POFs, birefringence can split into transverse and longitudinal. The former is visible when looking at the fibre from the side, i.e., it is birefringence between polarisations along *z* and *x* axes or *z* and *y* axes in Figure 2-1. Longitudinal birefringence is experienced by light travelling in a fibre core, i.e., it is birefringence between polarisations along *x* and *y* axes in Figure 2-1.

There are several causes of optical anisotropy [165]. Longitudinal birefringence can be caused by intended or accidental non-circularity of fibre core, by intended stress coming from stress-induced elements incorporated in the fibre structure, or by accidental stress due to fibre bending. These factors can also cause longitudinal birefringence in SOFs. However, this type of birefringence is not important for the scope of this thesis and, hence, is not expanded on, more information being available in the literature [25, 26, 92, 94, 167]. The origins of transverse birefringence of POFs include orientation birefringence [152, 153] and residual stress birefringence [98, 153]. These are both described.

2.3.5 Orientation birefringence

The orientation birefringence is caused by orientation of polymer molecules. POFs, having one axis of molecular orientation, have also one optic axis. Biaxial materials (i.e., having two optical axes) are thus out of the scope of this thesis. In the case of POFs, the optic axis coincides with the fibre axis, and hence RI for the extraordinary direction is parallel to the fibre axis ($n_e = n_\parallel$), and RI for the ordinary direction – perpendicular ($n_o = n_\perp$).

As with anisotropy in CTE, orientation birefringence can be analysed based on the aggregate model. In this case, the intrinsic unit displays different values of RI for polarisations parallel ($n_\parallel^0$) and perpendicular ($n_\perp^0$) to its axis (the superscript *0* denoting intrinsic RI values). According to Equation (2-23), intrinsic birefringence Δn^0 (i.e., birefringence of a fully oriented polymer) is defined as:

$$\Delta n^0 = n_\parallel^0 - n_\perp^0. \tag{2-24}$$

Similarly to Equation (2-21) describing anisotropic LCTEs by means of the orientation function f_{or}, orientation birefringence can be expressed as follows:

$$f_{or} = \frac{\Delta n}{\Delta n^0}, \tag{2-25}$$

which gives a good approximation coming from the pseudo-affine model for polymers in glassy state [100, 151]. It follows that:

$$\Delta n = \Delta n^0 \cdot f_{or}. \tag{2-26}$$

Similarly to CTE of oriented polymers (see Equation (2-21)), the higher the degree of molecular orientation (induced, e.g., by drawing or extrusion), the higher the birefringence (Figure 2-14).

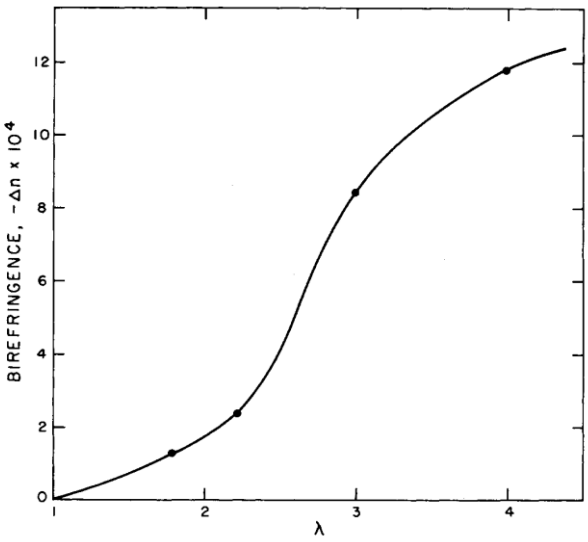

Figure 2-14. Dependence of birefringence on extrusion ratio for PMMA [159].

For small values of birefringence, the derivative of the Lorentz-Lorentz could be used to quantify intrinsic birefringence. However, it would only be valid for small values of birefringence, which is not the case for POFs [168]. The Lorentz-Lorenz equation (Equation (2-10)) does not take polarisation of light into account. Hence, the Vuks equations [169-171] are often used instead in the description of birefringent materials. They constitute a semi-empirical modification to the L-L equation and take the following form:

$$\frac{\mathrm{n_{e,o}^2}-1}{\mathrm{n_{av}^2}+2}=\frac{4\pi}{3}\frac{\rho \mathrm{N_a}}{\mathrm{M}}\mathrm{P_{e,o}}, \tag{2-27}$$

where n_e, n_o are RIs for along extraordinary and ordinary directions, respectively, P_e, P_o – polarisabilities along extraordinary and ordinary directions, respectively, and n_{av} is average RI. The other symbols are consistent with these in the L-L equation (Equation (2-10)).

As in uniaxially symmetric materials $n_e = n_\parallel$ and $n_o = n_\perp$, the Vuks equations can be reformulated as follows:

$$\frac{n_\parallel^2-1}{n_{av}^2+2}=\frac{4\pi}{3}\frac{\rho N_a}{M}P_\parallel, \tag{2-28}$$

$$\frac{n_\perp^2-1}{n_{av}^2+2}=\frac{4\pi}{3}\frac{\rho N_a}{M}P_\perp. \tag{2-29}$$

Average RI for materials with uniaxial symmetry is defined as:

$$n_{av}=\sqrt{\frac{n_\parallel^2+2n_\perp^2}{3}}. \tag{2-30}$$

The value of intrinsic birefringence (Δn^0) can be both positive ($n_{\parallel}^0 > n_{\perp}^0$) or negative ($n_{\parallel}^0 < n_{\perp}^0$). From the Vuks equations (Equations (2-28) and (2-29)), it can be seen that $n_{//}$ and $n_{\perp}$ are linked to their respective values of polarisation: the bigger the polarisation in a given direction, the bigger the corresponding RI. Thus, positive birefringence can be observed for materials whose $P_{//}$ is bigger than $P_{\perp}$, in the opposite case birefringence being negative. The latter is the case for PMMA: high polarisability of the side chain oxygens makes $P_{\perp}$ bigger than $P_{//}$ [153, 159, 172-174]. Oppositely, PC exhibits positive birefringence due to high polarisability of the main molecular chain [174, 175].

2.3.6 Stress birefringence

Residual stress birefringence is the second factor contributing to transverse birefringence of POFs. Two causes of stress in the fibres have been identified [153]: thermal quench stress and CTE mismatch stress. The former stems from temperature gradient along the fibre radius when the fibre is cooled down during fibre drawing, which normally is a very rapid process. The temperature outside the fibre is lower than inside it, and the outer layer of the fibre is the first to solidify (i.e., to cool down below T_g and increase in density). At this point, the temperature of the inner part of the fibre is still above T_g., making it have lower density than the inner part. After the entire POF cools down, these differences in density result in residual stress in the fibre [174]. The highest value of thermal quench stress is displayed at the outer surface of the fibre [153].

The second cause of residual stress in a POF, namely CTE mismatch stress, is due to difference in CTEs of the core and cladding materials. This only concerns fibres made of two materials having different CTEs (e.g., conventional step-index POFs). When the temperature of the POF is above T_g, all stress resulting from the CTE mismatch can relax, as polymer molecules are free to move past each other. This is no longer possible when temperature falls below T_g. From this point down to room temperature (or operational temperature), unrelaxed stress starts to build up. The bigger the CTE mismatch and the difference between T_g and the operational temperature, the bigger the residual stress. The highest value of CTE mismatch stress is found at the core-cladding interface [153].

Birefringence induced by stress can be described using the stress-optic law [98]:

$$\Delta n = C \cdot t, \tag{2-31}$$

where Δn is birefringence, t – true stress (i.e., considering the change of the cross-sectional area of the sample upon straining), C – stress-optic coefficient, which is independent of strain. The latter is defined as:

$$C = \frac{2\pi}{45kT}\frac{(n_{av}^2 + 2)^2}{n_{av}}(P_1 - P_2), \tag{2-32}$$

where k is the Boltzmann constant ($k \approx 1.38 \times 10^{-23}$ J/K), T (K) – temperature, n_{av} – average RI, and $P_{//}$, $P_{\perp}$ are polarisabilities along and perpendicularly to the axis of the intrinsic unit. The value of the stress-

optic coefficient for PMMA POFs (in the glassy state) was reported to lie between -1.5 and -4.4 × 10^{-12} Pa^{-1}, the actual value being influenced by fibre drawing stress and fibre annealing [172, 173]. The values measured for glassy PMMA samples other than POFs vary from +5.5 × 10^{-10} Pa^{-1} [176], through -1.08 × 10^{-10} Pa^{-1} [177] and -3.3 × 10^{-12} Pa^{-1} [178], to -2.4 × 10^{-12} [99, 172, 173]. No value for the stress-optic coefficient for PC POF was found in the literature. For other types of PC samples (in the glassy state), the following values were reported: 8.9 × 10^{-11} Pa^{-1} [175], 7.2 × 10^{-11} Pa^{-1} (for Bisphenol-A PC) [131], and 2.2-7.2 × 10^{-11} Pa^{-1} (for various types of PC) [131].

2.3.7 Dependence of orientation birefringence on temperature

Birefringence can also depend on temperature, corresponding to a non-zero $\frac{d(\Delta n)}{dT}$. Consequently, the TOC value $\left(\frac{dn}{dT}\right)$ can be different in every direction. For uniaxially symmetric materials, this results in TOC parallel to the fibre axis ($TOC_{\parallel}$, $\frac{dn_{\parallel}}{dT}$) being different from TOC perpendicular to it ($TOC_{\perp}$, $\frac{dn_{\perp}}{dT}$). According to the temperature derivative of Equation (2-26), dependence of birefringence on temperature can be expressed as:

$$\frac{\mathrm{d}(\Delta \mathrm{n})}{\mathrm{dT}} = \frac{\mathrm{d}(\Delta \mathrm{n}^0)}{\mathrm{dT}} \mathrm{f_{or}} + \Delta \mathrm{n}^0 \frac{\mathrm{df_{or}}}{\mathrm{dT}} \tag{2-33}$$

The term $\frac{d(\Delta n^0)}{dT}$ can be determined from $TOC_{\parallel}$ and $TOC_{\perp}$, which can be calculated as temperature derivatives of the Vuks equations (Equations (2-28) and (2-29)). Assuming that temperature dependence of polarisability (ϕ) can be neglected and including the parameter Λ_0 (see Equation (2-15)), temperature derivatives of the Vuks equations look as follows [171]:

$$\frac{2\mathrm{n}_{\parallel}}{n_{\parallel}^2 - 1} \frac{\mathrm{dn}_{\parallel}}{\mathrm{dT}} - \frac{2\mathrm{n_{av}}}{\mathrm{n_{av}^2} + 2} \frac{\mathrm{dn}_{av}}{\mathrm{dT}} = -\beta + \Lambda_0 \beta, \tag{2-34}$$

$$\frac{2\mathrm{n}_{\perp}}{n_{\perp}^2 - 1} \frac{\mathrm{dn}_{\perp}}{\mathrm{dT}} - \frac{2\mathrm{n_{av}}}{\mathrm{n_{av}^2} + 2} \frac{\mathrm{dn}_{av}}{\mathrm{dT}} = -\beta + \Lambda_0 \beta, \tag{2-35}$$

hence:

$$\frac{\mathrm{dn}_{\parallel}}{\mathrm{dT}} = \frac{n_{\parallel}^2 - 1}{2\mathrm{n}_{\parallel}} \left(-\beta + \Lambda_0 \beta + \frac{2\mathrm{n_{av}}}{\mathrm{n_{av}^2} + 2} \frac{\mathrm{dn}_{av}}{\mathrm{dT}} \right), \tag{2-36}$$

$$\frac{\mathrm{dn}_{\perp}}{\mathrm{dT}} = \frac{n_{\perp}^2 - 1}{2\mathrm{n}_{\perp}} \left(-\beta + \Lambda_0 \beta + \frac{2\mathrm{n_{av}}}{\mathrm{n_{av}^2} + 2} \frac{\mathrm{dn}_{av}}{\mathrm{dT}} \right). \tag{2-37}$$

From these equations and Equation (2-27), it follows that temperature derivative of intrinsic birefringence can be formulated as [171]:

$$\frac{d(\Delta n^0)}{dT} = \frac{dn_{\parallel}^0}{dT} - \frac{dn_{\perp}^0}{dT} = \left(1 + \frac{1}{n_{\perp}^0 n_{\parallel}^0}\right)\frac{n_{av}\Delta n^0}{n_{av}^2 - 1}\frac{dn_{av}}{dT}. \quad (2\text{-}38)$$

The term $\frac{df_{or}}{dT}$ describes thermal dependence of the orientation function and is the last term of Equation (2-33). Due to anisotropy in thermal expansion ($\Delta\alpha$), the angle θ between the intrinsic unit axis and the fibre axis changes. The term $\frac{df_{or}}{dT}$ can be expressed as [171]:

$$\frac{df_{or}}{dT} \approx 3\Delta\alpha\left(\overline{\cos^2\theta} - \overline{\cos^2\theta}^2\right), \quad (2\text{-}39)$$

where $\Delta\alpha = \alpha_{\parallel} - \alpha_{\perp}$. Equations (2-38) and (2-39) allow calculating dependence of birefringence on temperature (Equation (2-33)).

2.4 Photonic crystals

This section briefly described the concept of photonic crystals and defines terms which will be used in the following sections of this chapter.

A photonic crystal [25] is a material in which light propagation is suppressed at certain wavelengths due to periodically arranged regions of alternating high and low relative permittivity (or refractive index). Absorption is not involved in the inhibition of light propagation. Rather, this is due to density of possible states for light vanishing at certain frequency range, which means that light propagation becomes impossible. This frequency range is called the photonic band gap (PBG), hence photonic crystals are also referred to as photonic band gap materials. For PBG to be observed, the periodicity of the regions of different relative permittivity must be at the size of the wavelength of light. The term crystal in the name of photonic crystals underlines the fact that it is the periodicity that gives rise to the peculiar properties of this material.

The simplest case of a photonic crystal is a Bragg mirror (or a Bragg reflector) [25]. It is composed of a stack of alternating dielectric layers of different RIs. Light propagating normal to the interface of the layers undergoes subsequent transmission and reflection at each interface. When the layer thicknesses and the RIs are tuned appropriately, the conditions for constructive interference for the reflected light and destructive interference for transmitted light are met. This would result in the light being totally internally reflected from a Bragg mirror in an idealised case of an infinite stack of dielectric layers. Such approach is often used theoretically, as it allows applying the Bloch theorem to analyse a photonic crystal [25]. The number of layers in real-world photonic crystals is always finite, resulting in reflection of light not being total, but often almost total or big enough to be of practical interest. The reflection strength grows with increasing number of layers, increasing difference of RIs between the layers, and increasing uniformity of the stack [26]

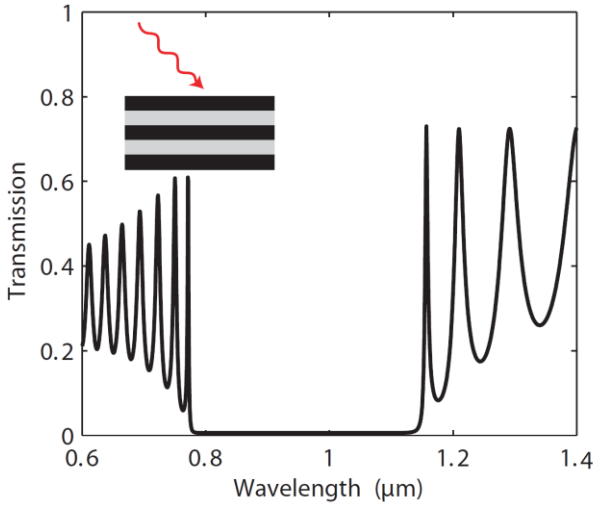

Figure 2-15. Example of the transmission spectrum of a Bragg mirror. The Bragg mirror structure is shown in the inset [26].

In the case of a Bragg mirror, periodicity is observed in one direction (normal to the interface of the layers). Such material is called a one-dimensional (1D) photonic crystal. In this case, PBG only appears for a rather narrow range of angles of incidence. Moreover, light propagation parallel to the interface layers cannot be inhibited. Two- or three-dimensional photonic crystals (2D or 3D, respectively) can be regarded as a generalisation of a 1D periodicity of Bragg mirrors to two or three dimensions. In the former case, light propagation is prohibited in the plane of periodicity, while in the latter case, an omnidirectional (or total) PBG exists. Photonic crystals of all types of periodicity are abundant in nature and are responsible, among other things, for the bright and colourful reflections in opals and structural coloration of butterflies, beetles, birds and sea-mice [25, 26].

The use of the term photonic crystal tends to be slightly ambiguous. Originally, it was coined to describe materials displaying a PBG. Nevertheless, it can also be used to describe any material showing periodic arrangement of dielectrics or metals, irrespective of whether they show a PBG. Such use of this term stems from solid state physics, in which a crystal stands for a material with a periodic lattice, exhibiting an electronic band gap in certain cases only. To increase clarity, the term photonic band gap material is then used to mean a photonic crystal having a photonic band gap. However, some dielectric structures may not even be periodic to result in peculiar photonic properties. Hence, the broader term microstructured materials is also in use [25].

2.5 Microstructured fibres

This section is split into three parts. The first one (Section 2.5.1) introduces the concept of a photonic crystal fibre, both solid-core and hollow-core. To start with, basic terms and naming convention based on fibre symmetry properties are presented. This is followed by a description of light propagation in a

mOF using the propagation diagram. Furthermore, three light guidance mechanisms occurring in SC and HC mOFs are explained: modified total internal reflection (Section 2.5.2) along with photonic bandgap and anti-resonant guidance (Section 2.5.3). Underlying physics and particular properties of fibres based on each mechanism are discussed. These include dispersion properties of mOF, fibre modality and the concept of endlessly single-mode fibres, and loss mechanisms.

2.5.1 Introduction

In a 3D photonic crystal with a total PBG for a range of wavelengths, no light from this range can propagate. Supposing a single point defect is introduced in the photonic crystal lattice, light generated in the defect will be trapped in its vicinity. If a linear (1D) defect is introduced (e.g., by drilling a hole in the 3D photonic crystal), light could propagate only along the defect, being prevented from entering the photonic crystal structure by the omnidirectional PBG. This resembles the way in which light is guided in an optical fibre by means of TIR. Hence, a photonic crystal fibre (PCF) is an optical fibre with the cladding having a photonic crystal structure. The core of a PCF can be seen as a linear defect in the photonic crystal cladding. The idea of PCFs originates from Philip Russel [11].

If light propagates primarily along one direction, as it is the case for a PCF, the photonic crystal structure of the cladding does not have to be three dimensional. For PBG guidance to occur, it suffices if the PBG is experienced by the radial (transverse) wavevector $k_{\perp}$ (see Figure 2-1 and Equation (2-1)). Hence, the periodicity in the photonic crystal cladding must be of the order of half wavelength of effective the transverse wavelength (λ_{eff}) calculated from $k_{\perp}$ (Equation (2-2)) and not from β or k_0. This, it turns, makes λ_{eff} considerably larger than the wavelength of light, thus the required photonic crystal periodicity can be decidedly bigger, which makes it a lot easier to fabricate [11].

Similarly to what was stated in Section 2.4, the exact periodicity of the cladding structure is not always required for fibre operation. In this case, the term photonic crystal, strictly speaking, cannot be used to describe the cladding and, thus, the fibre. Hence, the more general term microstructured optical fibre (mOF) has been introduced, which underlines the dimensions of the cladding structure rather than its periodicity. However, both terms are sometimes used interchangeably in the literature.

In PCFs and mOFs, the core does not have to display higher refractive index than the cladding for guidance to occur. Hence, both solid-core (SC) and hollow-core (HC) fibres can be manufactured, i.e., fibres having the core made of a solid material or an air (or vacuum) void, respectively. SC fibres were first reported in 1996 [179], while the HC ones, in 1999 [10], both consisting of arrays of air holes in silica.

Probably the simplest photonic crystal cladding results from “wrapping” a 1D Bragg mirror around a fibre core, leading to the concept of a Bragg fibre [180-182]. This example shows that a 1D photonic crystal (with RI modulation along fibre radius in cylindrical coordinates) is enough to ensure PBG guidance.

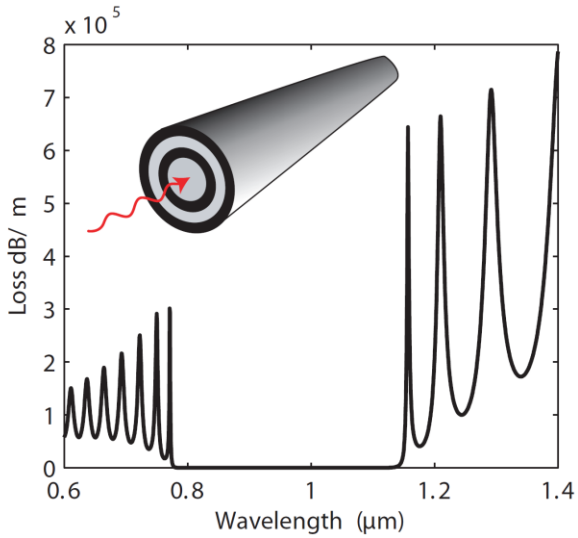

Figure 2-16. Example of the loss figure of a Bragg fibre against wavelength with the structure of a Bragg fibre being shown in the inset [26].

Although 1D photonic crystals can be used, the cladding of PCFs is normally made of a 2D photonic crystal. In this case, RI modulation appears in *x*-*y* plane, while the form of the structure is conserved along *z* axis (see Figure 2-1 for the directions). In a simple design of an SC PCF, such cladding consists of a 2D array of air holes running along the core made of a solid material (Figure 2-17(a)). Similarly, these are silica rods running along the fibre core in the case of a simple SC fibre (Figure 2-17(b)). Typically, SC and HC PCFs consist of the photonic crystal cladding made of a few hexagonal rings of holes (i.e., arranged on a triangular or hexagonal lattice). They are placed around the central core, which is formed by removing the central hole from the photonic crystal structure.

As opposed to Bragg fibres, RI contrast between air (or vacuum) and silica (or polymer) is enough for operation of fibres with a 2D photonic crystal cladding, which constitutes one of their advantages over Bragg fibres from the viewpoint of fabrication. Compared to conventional optical fibres, mOFs provide unprecedented freedom regarding the design of their structure and, hence, their characteristics, considerably broadening the range of their applications. Some examples of this will be given below, while manifold others have been presented in the literature [11, 25, 26].

Figure 2-17. Cross-sectional schematic of a typical (a) solid-core and (b) hollow-core PCF. White areas correspond to air (or lower RI) regions, while grey/black ones stand for solid (or higher RI) material. Both photonic crystal claddings are composed of five hexagonal rings of holes around the core [25].

Modes of microstructured fibres follow patterns of step-index modes only approximately. The step-index fibre naming convention (HE, EH, TM, TE) does not work for more complex mode shapes and, hence, designation of modes based on symmetries proposed by McIsaac is used instead [25, 183]. As the structure of most mOFs is also symmetric, this approach is very useful to classifying modes.

The notation C_n describes a structure having only n-fold rotation symmetry with no reflection symmetry. The angle $2\pi/n$ is the smallest angle connected with symmetry operation, where n is an integer (Figure 2-18). If a structure, along with rotation symmetry, also at least one reflection plane can be identified, if follows that the structure has exactly n planes of reflection symmetry. The angle between these planes is $\pi/2$, and they intersect exactly along the rotation symmetry axis. Such a symmetry group is referred to as C_{nv} (Figure 2-19). In the McIsaac's approach, fibre modes are divided into mode classes based on their azimuthal symmetry, each class containing infinite number of modes. A mOF of C_n symmetry has exactly n mode classes. The number of mode classes for a fibre of C_{nv} symmetry varies: it is $n + 1$ if n is odd, and $n + 2$ if n is even. The modes from each class are all either non-degenerate or two-fold degenerate. The notation $C_{\infty v}$ describes a special case for which $n \rightarrow \infty$ (Figure 2-19(c)).

Figure 2-18. Examples of structures having C_n symmetry (i.e., only rotational symmetry, no reflection symmetry). C_1 stands for no symmetry at all. Both structures are invariant through a rotation of $2\pi/n$ [25].

Figure 2-19. Examples of structures having C_{nv} symmetry. They are invariant through a rotation of $2\pi/n$ and have at least one reflection symmetry plane (dashed lines) [25].

The symmetry group C_n will be neglected in further considerations since the majority of mOFs belong to the group C_{nv}. In the latter, the first and second mode classes (p = 1, 2) contain non-degenerate modes. If n is even, there are two more groups of non-degenerate modes, which are added at the end of the mode class list (p = n+1, n+2). Modes from every class are characterised by different symmetry properties, which can serve to simplify calculations of the propagation constants and modal fields. For each symmetry class, it is enough to perform computations for a narrow range of angles with the vertex at the fibre centre (called a minimum sector) and apply appropriate boundary conditions at sector borders.

The two following types of boundaries are defined: short-circuit boundary condition, for which the tangential electric field equals 0 at the boundary, and open-circuit boundary condition, for which the tangential electric field at the boundary equals 0. For each symmetry group, a minimum sector lies between two planes of reflection symmetry. The minimum sectors for the point group C_{6v}, PCFs of

which are most-widely reported, are shown in Figure 2-20. This group possesses 8 mode classes. The minimum sector for the non-degenerate mode classes (p = 1, 2, 7, 8) equals $\pi/6$, whereas is it $\pi/2$ for the four two-fold degenerate classes p = 3, 4 and p = 5, 6. The non-degenerate modes can be labelled as C1, C2, C7, C8, according to their class number. The label for the degenerate modes from the classes 3 and 4 is C3/4, and from the classes 5 and 6 – C5/6. These labels are followed by a lowercase letter denoting the ordinary number of mode starting from *a* (e.g., C3/4-a, C1-b etc.). Modes are numbered in the order of decreasing value of the real part of the effective RI of each mode, similarly to the way it is done for conventional optical fibres. Basic modes and their labels in a C_{6v}-symmetry PCF corresponding to basic modes of conventional optical fibres are shown in Table 2-3.

Figure 2-20. The minimum sectors of a fibre having C_{6v} symmetry. Solid and dashed lines correspond to short- and open-circuit boundary condition, respectively [25].

Table 2-3. Basic modes of a hexagonal lattice PCF described based on symmetries and their counterparts in conventional optical fibres [25].

mOFs		Conventional fibres
Symmetry class	Mode label	Mode
3/4	C3/4-a	HE_{11}
2	C2-a	TE_{01}
5/6	C5/6-a	HE_{21}
1	C1-a	TM_{01}

Light propagation in a PCF with the cladding composed of a 2D array of holes can be described using a propagation diagram (Figure 2-21) [11]. It shows normalised frequency ($\omega\Lambda/c$, $k\Lambda$) versus normalised propagation constant (or normalised wavevector along fibre, $\beta\Lambda$) for a silica PCF, where Λ is spacing between the holes in the array. There are three regions of such a fibre: air, photonic crystal, and silica. Light propagation is prohibited in the black areas, either due to TIR or PBG. For a fixed optical frequency, the maximum value of $\beta\Lambda$ in every region is given by $k\Lambda n$, n being the RI in this region for the assumed frequency. The RI in the photonic crystal area (n_{PC}) lies between the RI of air (n_{air} = 1) and silica glass (n_{silica}). n_{PC} is frequency-dependent (dispersive), even assuming no material dispersion for air and glass in the analysis [11]. This dispersion is due to the photonic crystal structure itself and gives rise to peculiar properties of PCF, which will be discussed later. Light can propagate if $\beta < kn$ in the given region, while, for $\beta > kn$, it is evanescent. Transition from propagation to evanescence is marked on the diagram with the slanted lines, which correspond to $\beta = kn$ for every region ($n = n_{air}$, n_{PC}, n_{silica}). For $\beta < k$, light is free to propagate everywhere, and for $\beta < k \cdot n_{PC}$, it can propagate in photonic crystal and silica, being evanescent in air. When $\beta < k \cdot n_{silica}$, light can only propagate in silica, being evanescent elsewhere, while, for $\beta > k \cdot n_{silica}$, it is cut-off from propagation everywhere.

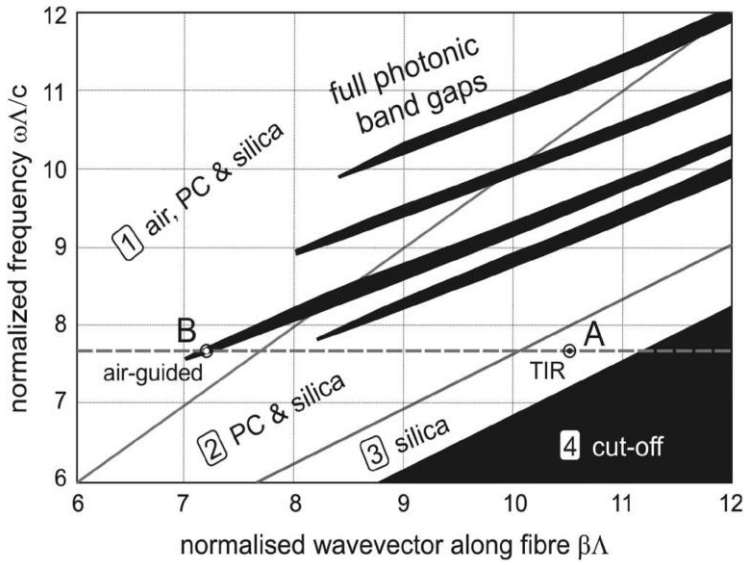

Figure 2-21. Propagation diagram for a silica PCF (45% air-filling fraction). The slanted lines separate the regions where light is free to propagate (1) everywhere, (2) in photonic crystal and silica, being cut-off in air, (3) only in silica, being evanescent elsewhere, (4) cut-off everywhere. The black areas denote full 2D photonic band gaps [11].

PBG guidance, which has been referred to so far, is not the only guidance mechanism in PCFs and mOFs. The following three distinct guidance mechanisms are usually distinguished and will be described below:

- modified TIR

- photonic bandgap
- anti-resonance.

Figure 2-22 shows examples of fibre structures relying on each guidance mechanism. Characteristics of light guidance in an mOF depends, among other things, on the relation between core and cladding RIs, which will also be discussed below.

Figure 2-22. Examples of structures of the innermost regions of microstructured fibres: a solid-core mOF of (a) low and (b) high air-filling fraction (predominantly modified-TIR guidance), (c) a hollow-core photonic bandgap fibre, and (d) an anti-resonant fibre based on the Kagome lattice [11].

2.5.2 Fibres with positive core-cladding RI difference ($n_{co} > n_{cl}$)

The group of fibres of positive core-cladding RI difference ($n_{co} > n_{cl}$) encompasses the most popular solid-core (SC) mOFs, whose core is made of silica or polymer, the cladding consisting of air (or vacuum) voids. Nevertheless, fibres making part of this class can also be fabricated using two types of glass or polymer having different RIs (e.g., doped or of different chemical formula). In the case of a positive core-cladding RI difference, PBG guidance can be obtained in some circumstances (high air-filling fraction). However, modified TIR (point A in Figure 2-17) is much more easily achievable and normally dominates in this group of fibres [11]. This is because modified TIR guidance can be seen as a special case of PBG guidance, in which a bandgap on which it relies always exists, irrespective of wavelength of the exact cladding structure [25]. Hence, this section will focus on modified TIR, while PBG guidance will be discussed in Section 2.5.3.

Modified-TIR guidance can be approximated by assuming the RI of the microstructured cladding being the average of the RIs of the cladding materials, e.g., of silica (or polymer) and air, the exact value depending on the air-filling fraction of the cladding. Such image resembles the familiar TIR mechanism of conventional fibres but can only serve as a first order approximation since it is unable to explain unique properties of mOFs compared to their conventional counterparts. Probably the most eminent of these distinct features of mOFs is, assuming an appropriate design, the ability to show endlessly single-mode (ESM) behaviour [184]. This means that, if light guidance occurs at all, the fibre is single-mode irrespective of the wavelength of light, contrary to conventional optical fibres (see Section 2.1.2 and Equation (2-3)).

Let us assume an SC PCF made of silica, whose cladding is composed of holes of diameter d, inter-hole spacing being equal to Λ. The photonic crystal cladding can be seen as being composed of "bars" forming a "cage" for propagating modes. Transverse effective wavelength of the fundamental mode in glass $\lambda_{eff} \approx 4\Lambda$ [11] (Equation (2-2)), which is clearly below the Rayleigh resolution limit of $\lambda_{eff}/2 \approx 2\Lambda$. Hence, the mode is "too large" and cannot "squeeze through" the passages between the wholes of the size $\Lambda - d$, being well confined to the core (Figure 2-23). HOMs have a smaller effective wavelength and, thus, can leak through the inter-hole channels if the relative hole size d/Λ is small enough. If d is getting larger compared to Λ, successive HOMs become trapped in the core.

Figure 2-23. Schematic representation of how modes are filtered in a SC PCF: (a) fundamental mode is trapped by the air holes and confined to the core, while (b) HOMs can leak through the cladding by means of the inter-hole channels [11].

The ESM behaviour can also be explained using the effective V parameter, which can be calculated for a wide range of frequencies following the analysis in [184] (Figure 2-24), assuming the core radius $\rho = \Lambda$. The number of guided modes can be estimated as $V_{PCF}^2/2$ [11] and, as can be seen from Figure 2-24, is almost independent of wavelength for high frequencies. Hence, ESM operation can be determined based on the geometry only. Despite different d/Λ threshold values for ESM behaviour being reported in the literature [11, 185, 186], the seemingly most complete analysis indicates the value of 0.405 [187]. For a PCF with a cladding of a hexagonal lattice, three basic regimes of fibre operation can be identified (Figure 2-25), where:

1) the fundamental mode is not confined
2) the fundamental mode is confined and HOMs are not
3) both the fundamental mode and some HOMs are confined.

Finally, as it has already been mentioned, photonic crystal cladding can be viewed as a dispersive medium [11], even when neglecting material dispersions of silica (or polymer) and air, of which the cladding is composed. RI of the photonic crystal cladding increases when the wavelength becomes shorter, approaching the RI of silica (or polymer). Hence, core-cladding RI difference lessens with

decreasing wavelength, which makes light penetrate ever deeper into the photonic crystal cladding (Figure 2-26). This, in turn, counteracts the usual tendency of a fibre to display ever more modes.

Figure 2-24. V parameter for SC PCF (hexagonal lattice) versus the ratio of hole pitch to vacuum wavelength plotted for different values of d/Λ [11].

Figure 2-25. Phase diagram (λ/Λ vs d/Λ) showing operational regimes of a SC PCF (hexagonal lattice): (grey area) the fundamental mode cut-off region, (dashed line) second mode cut-off threshold [25].

Figure 2-26. Schematic showing ever bigger penetration of light into a photonic crystal cladding as wavelength of light increases from left to right [26].

The unusual properties of the photonic crystal cladding allow much higher flexibility in manipulating fibre parameters. First, as it has been stated, ESM behaviour is dependent on geometrical parameters only (e.g., d/Λ for a cladding on a hexagonal lattice). Hence, SM fibres with cores of very large area can be fabricated (e.g., of diameter equal to 22 μm [12]), which are capable of transmitting much higher power than their conventional counterparts. Secondly, the described dispersive characteristics permit tuning fibre dispersion using a mOF of the same design but varying diameter [188]. Dispersion-flattened mOFs have also been reported [22, 189]. Moreover, the variety of possible fibres designs encompass fibres with multiple cores, which can be applied, e.g., to bend sensing [190]. Finally, appropriate design of the fibre microstructure can yield very high longitudinal birefringence, being orders of magnitude higher than stress-induced birefringence of conventional polarisation-maintaining fibres. Hence, their parameters can be markedly improved.

Another important difference between the characteristics of conventional and microstructured fibres is the loss mechanism. As it has been mentioned in Section 2.4, a photonic crystal would reflect strictly all light from its PBG only if the crystal was infinite in size. Hence, due to finite nature of a real-world photonic crystals, including claddings of PCFs, there is always some loss related to light leaking out through the microstructure. This is referred to as confinement or geometrical loss [25], which is an additional loss factor to those mentioned in Section 2.2.3. This process is equivalent to quantum mechanical tunnelling: evanescent field can tunnel through the holes of the cladding because they are relatively small. Similar phenomenon could be observed in conventional fibres of a sufficiently thin cladding [26]. Thus, all modes propagating in mOFs are leaky modes and not guided modes as in conventional fibres. However, if the microstructure is designed appropriately, confinement losses can be made negligible compared to other loss mechanisms.

Geometrical loss for standard hexagonal hole arrangement has been widely studied [25, 26, 191], considering, among other things, number of hexagonal rings (Figure 2-27(a)), wavelength (λ, Figure

2-27(b)), hole pitch (Λ, Figure 2-27(b), Figure 2-28), the ratio d/Λ (Figure 2-27, Figure 2-28), and differences between loss figures for a fundamental mode and HOMs (Figure 2-29). Figure 2-27(a) supports the claims made above regarding a photonic crystal cladding: the more rings of holes it is made of (i.e., the bigger the number of periods in the cladding), the lower the confinement loss. Moreover, the graph makes apparent that geometrical loss decreases for increasing hole diameter, which can be well understood intuitively: the wider the channels between the holes of the microstructure, the easier it is for light to escape through them. However, if ESM behaviour is desired, the ratio d/Λ cannot rise above ~0.4, as it was explained above. Hence, this threshold value is optimal from the point of view of the confinement loss of an ESM fibre, while the loss can be further decreased, e.g., by adding more rings of holes to the microstructure. Moreover, from Figure 2-27(b), it can be observed that the geometrical loss increases with wavelength (both for silica and polymer fibres). The loss is relatively small at the 650 and 850 nm regions, where microstructured POFs (mPOFs) are usually used. As can be seen from Figure 2-28, scaling the structure while keeping the ratio d/Λ constant also reduces the loss, which is favourable from the viewpoint of power delivery though a large core SC PCF mentioned above. Finally, Figure 2-29 shows the loss level as a function of hole pitch for the fundamental mode and higher order modes of an ESM PCF (d/Λ = 0.4 μm, λ = 1.55 μm). It follows that, despite HOMs being delocalised in ESM fibres, the loss difference between them and the fundamental mode can be relatively small at small values of Λ. These considerations, along with other studies reported in the literature, allow judicious design of fibre structure considering required characteristics. In the case of more exotic fibre designs, for which literature data is not available, one can always resort to computer simulations, which allow establishing exact parameters of virtually any fibre design. Among the most popular methods lie the finite element method (e.g., using the software COMSOL [95]) and the multipole method (e.g, using the programme CUDOS [192-194]), all available numerical approaches being discussed in the literature [25] [26].

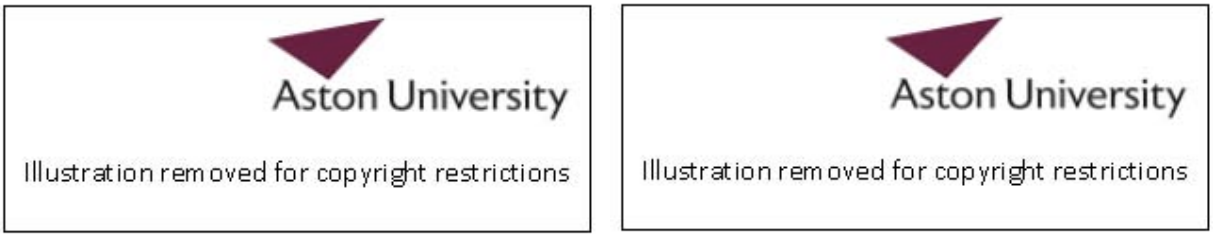

(a) (b)

Figure 2-27. (a) Confinement loss as a function of the ratio d/Λ for silica mOFs (hexagonal hole lattice) of varying number of rings around the core; hole pitch Λ = 2.3 μm and wavelength λ = 1.55 μm. (inset/see inset) (b) Confinement loss versus wavelength for silica mOFs of various hole diameter value; hole pitch Λ = 2.3 μm. [191].

Figure 2-28. Confinement loss as a function of pitch Λ for various values of the ratio d/Λ for silica mOFs of three hexagonal rings of holes; wavelength λ = 1.55 μm. Each curve corresponds to scaling the structure at a constant ratio d/Λ [25].

Figure 2-29. Confinement loss versus hole pitch Λ of a silica ESM mOF composed of three hexagonal rings of holes for the fundamental mode and two HOMs; wavelength λ = 1.55 μm, the ratio d/Λ = 0.4 μm [25].

2.5.3 Fibres with negative core-cladding RI difference ($n_{co} < n_{cl}$)

In the case of negative core-cladding RI difference ($n_{co} < n_{cl}$), e.g., for HC PCFs, modified TIR guidance is impossible. Instead, HCFs operate based on two other guidance mechanisms (point B in Figure 2-17):

- photonic bandgap (photonic bandgap fibres, PBGFs) [23, 24]
- anti-resonance, AR (anti-resonant fibres, ARFs) [23, 27, 195].

The former is the "classic" guidance mechanism found in all photonic crystals, which can be present both in SC and HC fibres. PBG results from zero density of states for light in a fibre cladding, while AR guidance relies on a combination of low (though not zero) density of states and inhibited coupling (wavenumber mismatch) of core and cladding modes. Both mechanisms are discussed below in some detail.

Photonic bandgap fibres

Probably the conceptually simplest case of a photonic bandgap fibre is Omnigude. Similarly to Bragg fibres, Omniguide fibres rely on the idea of a 1D Bragg mirror "wrapped around" the core, but with the core being made of an air void [196, 197]. For omnidirectional bandgap to be present, RI difference between the periodic dielectric layers around the core must be very high. This, in turn, results in lossy materials being used, which does not allow fibre to be used in telecommunications. However, the fibre found its use in other areas, e.g., in delivering CO_2 laser power.

However, PBGFs are usually based on a cladding made of a 2D air-suspended lattice of rods with an air defect constituting the core. This can be seen as an inverse of a solid-core mOFs with the cladding made of holes. In fibres, the PBG mechanism was initially modelled with numerical techniques originating from solid state physics, which were used to calculate frequency bands of a unit cell limited with periodic Bloch boundary conditions versus direction of wavevector [198-200]. Despite having brought much insight into fibre operation and having provided guidance for fibre optimisation, these techniques were based on the assumption of infinite and defect-free structure. This made them unable to model modes propagating inside a defect in a photonic crystal, i.e., a fibre core, nor to assess confinement losses due to final extent of a photonic crystal cladding [24]. Having recognised that, numerical techniques made specifically to study mOFs arose, either newly proposed or adapted from other fields, e.g., finite element [201], finite difference [202], multipole [192-194], or plane-wave expansion methods [203]. However, they were unable to help understanding the physical origins of PBG formation or effects of deviations from ideal periodicity and defect (i.e., core) termination on fibre properties [24]. Simpler methods proposed later relied on anti-resonant interactions within arrays of tightly spaced resonators in a fibre cladding [204, 205]. They allowed examining each cladding element separately and assessing its influence on the overall fibre characteristics, leading to further improvements of fibre designs.

Figure 2-30 shows in steps how PBG in a HC mPOF is created [24]. The violet horizontal lines at $w^2 = 0$ (i.e., $\beta = k_0$) denote the transition from air (below the line) to cladding (above the line). In Figure 2-30(a), a single silica rod surrounded by air (see the inset) results in the continuum of states in air and a familiar dispersion relation of distinct modes guided in the rod like in the case of a conventional optical fibre (see Section 2.1.2). The white regions correspond to the areas in the plane (v, β) where no modes can be sustained in either the cladding or the rod, meaning that the modes are in anti-resonance with them. Placing a few such silica rods close enough to each other changes the dispersion relation markedly (Figure 2-30(b)): multiple bandgaps below the air level are created. If the rods are brought slightly further from each other, the bands become shallower and wider (Figure 2-30(c)). Figure 2-30(d) shows unfavourable effect of introducing struts interconnecting, which are required in a realistic structure for mechanical stability. Higher order bandgaps are then deviated, owing to the dispersion relation of the fundamental space filling mode of the struts (marked with the red line). As a result, only the bandgap of the lowest-frequency remains below the air level and, hence, is capable of supporting air-guided modes. For this reason, HC PBGFs normally only display one bandgap as opposed to their SC counterparts.

Figure 2-30. Four steps explaining formation of a PBG [24]. The plots represent the function $w^2 = (\beta^2 - k_0^2)\rho^2$ vs the *v* parameter (see Equation (2-4)) for the structures showed in the insets, where the darker areas denote silica and the lighter ones – air. The violet horizontal lines mark the air level. See text for discussion.

The considerations presented above, relating to light guidance in a hollow (low RI) core, only provide the upper theoretical limit for the available PBG bandwidth produced by a periodic cladding. In order to guide light, the cladding periodicity must be broken by introducing the core. This can be a source of surface modes (similar to surface states in solid state physics at a semiconductor edge), which are parasitic from the viewpoint of loss and bandwidth [24].

The numerical approach applied to explain formation of a PBG can be used to gain deeper understanding of modes binding the bandgap and influencing loss (Figure 2-31). According to it, three types of cladding modes limit the PBG: one localised in the rods from the right (at longer wavelengths), in the struts from the left (at higher wavelengths), and in air from below (at lower values of effective

RI). Surface modes are created at the struts or rods in the core-cladding boundary (surface) and can be localised in the PBG, adversely influencing the loss and bandwidth. Strut modes of higher effective RI (originating from thicker or longer struts) can be introduced into the PBG from the shot-wavelength side. Similarly, rod modes of lower effective RI than the cladding average (originating from smaller or more tightly spaced rods) make rod surface modes appear at the long-wavelength side. In the hexagonal lattice, the lattice cells adjacent to the core are usually pentagonal, with the struts at the core-cladding interface being longer than others (see top insets in Figure 2-31), which is a source of strut surface modes in many actual fibre designs (see loss graph in Figure 2-31) [24, 206, 207]. In order to eliminate them, i.e., push them back to past the short wavelength edge of the PBG, thinner surface struts are required; their maximum thickness should be half (or slightly more) of cladding strut thickness [24, 206]. This has been shown experimentally to help remove surface modes from the PBG despite experimental complications regarding fibre manufacturing [208]. It has also been shown theoretically that even thicker struts would be acceptable if surface rods are spaced equally [207].

Figure 2-31. Bandgap map (effective RI $n_{eff} = \beta/k_0$ vs wavelength) showing a PBG (white area) for a fibre cladding based on the hexagonal lattice (displayed in the lower right corner; rod diameter = 600 nm, strut thickness = 120 nm). The vertical violet line marks the air level. Insets on the sides show strut, rod and air modes which limit the PBG from the left, right and below, respectively. Two top insets show the surface modes which can introduce additional loss and narrow the bandgap by anti-crossing with an air-guided mode (blue line) – see the lower plot. See text for details. After [23, 24].

Anti-resonant fibres

The mechanism of operation of anti-resonant fibres is different from this of PBGFs. Instead of being based on strictly zero density of states in the cladding, ARFs rely on low density of states (wavenumber mismatch between core and cladding) combined with inhibited coupling (low modal field overlap between core and cladding modes due to anti-resonant reflection) [23, 27]. AR guidance mechanism was historically first observed in fibres whose cladding was based on the Kagome lattice [209]. Despite looking similar to PBGF at first sight, closer examination revealed that the fibre does not support a PBG. Investigation into AR guidance mechanism led to negatively curvature fibres (NCFs) [27], which will be discussed below.

Anti-resonance guidance relies on the familiar phenomenon of constructive and destructive interference in thin films. It was also reported to be used for light confinement in planar slab waveguides [210]. In the latter arrangement, shown in Figure 2-32 (a), light propagates in air (RI = n_0) between two planes of glass (RI = n_1) of thickness t, propagation direction being parallel to the plates. Due to large difference between interplanar distance and wavelength of light ($W \gg \lambda$), transverse wavevector can be approximated as $k_t = k_0\sqrt{(n_1^2 - n_0^2)}$. Light hitting a single glass plate (Figure 2-32(b)) can pass through it directly, having phase Φ_0 after leaving. Alternatively, to go through the glass plate, light can be reflected back and forth inside the plate before leaving, which results in phase Φ_1. The phase difference $\Delta\Phi = \Phi_1 - \Phi_0$ equals $2tk_0\sqrt{(n_1^2 - n_0^2)}$. The resonance condition for transverse wavevector is met if phase difference is a multiple of 2π, i.e.:

$$t = \frac{m\lambda}{\sqrt{(n_1^2 - n_0^2)}}, \tag{2-40}$$

where m is a positive integer. Analogously, the antiresonance condition is fulfilled when $\Delta\Phi = (2m - 1)\,\pi$, hence:

$$t = \frac{(m - 0.5)\lambda}{\sqrt{(n_1^2 - n_0^2)}}. \tag{2-41}$$

Figure 2-32 (c) shows confinement loss for light propagating in the slab waveguide as a function of core width and glass thickness, assuming wavelength of light = 1.0 μm and RI of silica = 1.45 [27]. Three lowest-order transmission bands (minima of loss) are displayed, which are separated by high loss regions corresponding to glass thickness fulfilling the resonance condition at 0.48 μm, 0.97 μm and 1.43 μm (m = 1, 2, 3, respectively). It can be seen that the resonance conditions do not change with core width for a constant glass thickness. However, loss decreases with increasing core size.

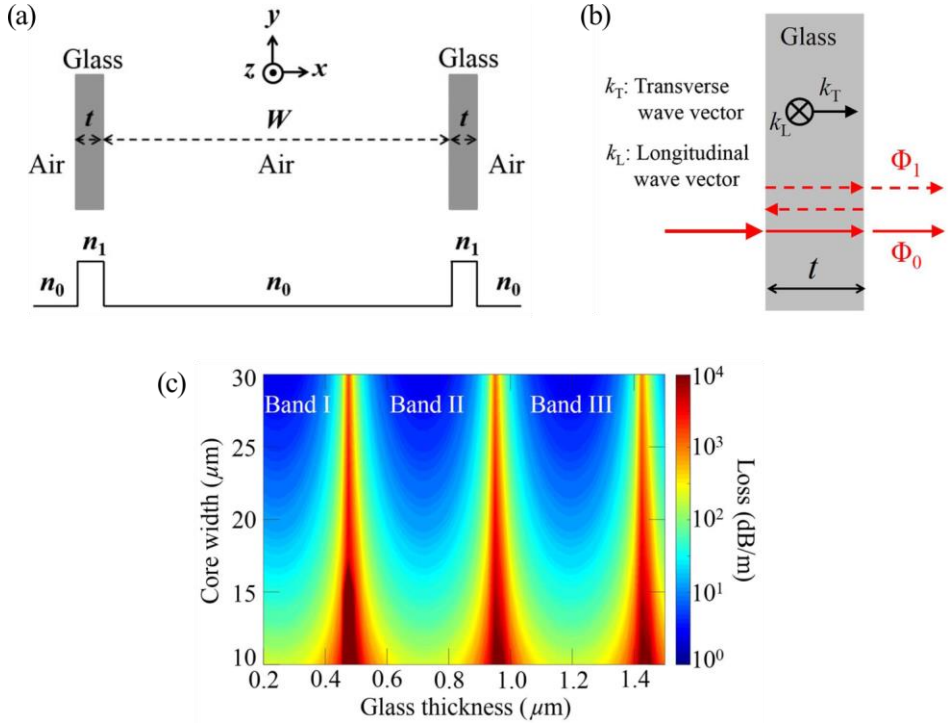

Figure 2-32. (a) Schematic of a planar slab waveguide composed of a single layer of air between two plates of silica glass. (b) Close view of a glass plate (see text for details). (c) Contour graph of loss of a single-layer slab waveguide as a function of core width and glass thickness [27].

The transmission bands at anti-resonances show clearly decreased leakage loss, but it is still high. In order to decrease it further, another glass plate of the same thickness *t* can be added at each side of the slab waveguide, resulting in a waveguide composed of three air layers (Figure 2-33(a)). Interplanar distance of the central (core) air layer, referred to as W_{core}, is equal to 30 μm like in the original single layer slab waveguide. Distance between the outer glass plates and these surrounding the core is referred to as $W_{cladding}$. Figure 2-33(b) displays the value of loss as a function of $W_{cladding}$. It can be observed that loss maxima are present if $W_{cladding}$ is equal to multiples of W_{core} (30 μm, 60 μm, 90 μm etc.), corresponding to resonance condition in the air-cladding layer ($2k_t W_{cladding} = 2m\pi$). Loss minima lie exactly between them, i.e., where the anti-resonance condition for the air cladding is fulfilled ($2k_t W_{cladding} = (2m+1)\pi$). Further, it can be noted that the outer glass plates in the three-layer waveguide can significantly decrease the loss. Comparing to the single-layer waveguide of the same core size (30 μm, see Figure 2-40(c)), the loss of the three-layer one decreases by about 4 orders of magnitude (from ~4 dB/m to ~6×10^{-4} dB/m).

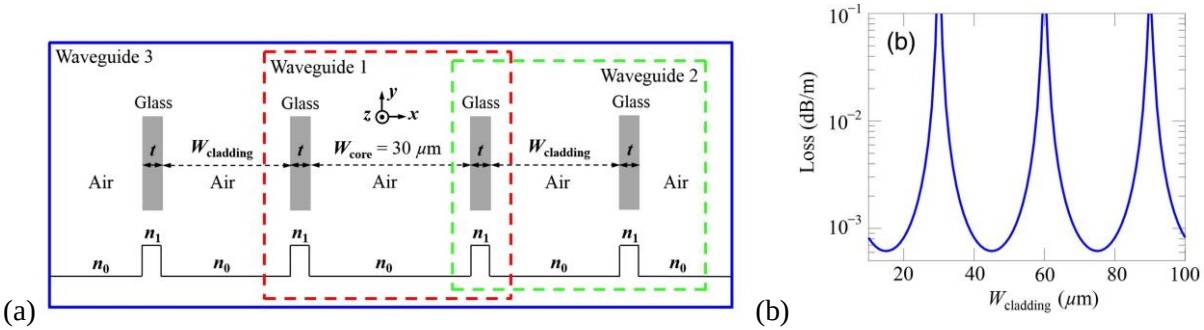

Figure 2-33. (a) Schematic of a planar slab waveguide composed of three layers of air between four plates of silica glass. (b) Loss of a three-layer slab waveguide as a function of cladding width [27].

Analogously to the planar slab waveguide, an annular core waveguide can be defined as a glass plate "wrapped around" a hollow core (Figure 2-34(a)). If glass thickness *t* is conserved, the resulting fibre shows the same resonance conditions as in the case of the slab waveguide (Figure 2-34(b)) [27].

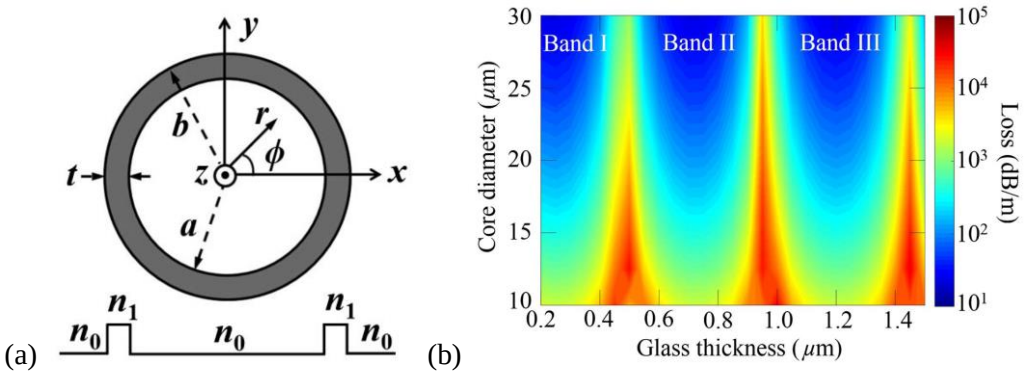

Figure 2-34. (a) Schematic of an annular waveguide composed of an air cladding surrounded by a tube of silica glass. (c) Contour graph of loss of an annular waveguide as a function of core width and glass thickness [27].

The structure of a typical negative curvature fibre composed of eight cladding tubes is shown in Figure 2-35(a), while Figure 2-35(b) displays confinement loss as a function of core diameter and tube thickness. For the same core diameters (e.g., 30 μm), geometrical loss of the NCF decreases by about 3 orders of magnitude compared to the annular fibre (see (Figure 2-34(b)). Compared to the latter, the loss graph of the NCF (Figure 2-35(b)) looks less regular, showing some fluctuations of the loss value. This is caused by the cladding tubes of the NCF touching and forming nodes, which are sourced of localised glass modes. They are also a source of leakage of light [211]. Introducing an air gap between adjacent tubes helps eliminating the nodes (anti-resonant nodeless fibre, ANF) decreasing confinement loss further (Figure 2-36) [27, 195]. An even larger improvement of light confinement can be achieved, e.g., by increasing the number of resonators arranged radially around the core by nesting them one inside another (nested anti-resonant nodeless fibre, NANF, Figure 2-36) [195]. In general, multiple parameters

of the resonators can be varied, including shape of a single resonator, number of resonators, number and shape of nested elements, with numerous results having been presented in the literature [212-221].

Moreover, research into the anti-resonant guidance mechanism helped to understand PBG guidance better. It has been found that PBG frequencies are largely influenced by the properties of individual rods and not their position in the lattice of the photonic crystal cladding [205, 222, 223]. Such behaviour explains why strict periodicities are often not required for PBG guidance to appear, which allows for some imperfections in fibre manufacturing process.

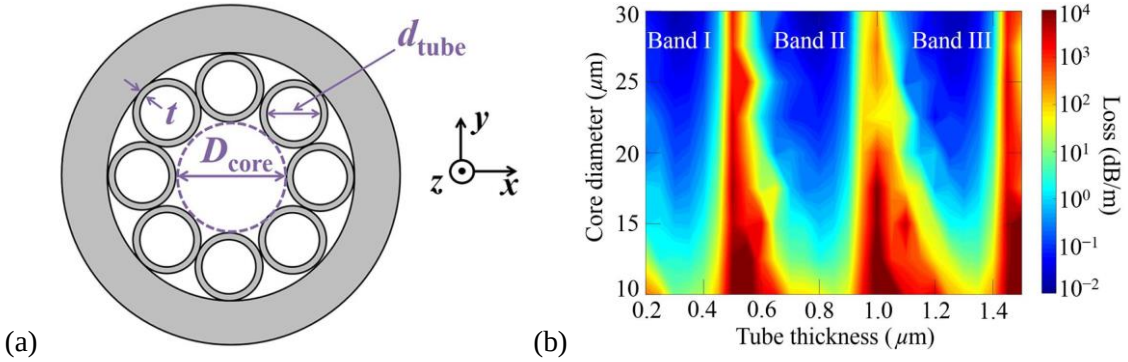

(a) (b)

Figure 2-35. (a) Structure of a typical tube lattice negative curvature ARF and (b) the corresponding contour graph showing loss as a function of core diameter and tube thickness [27].

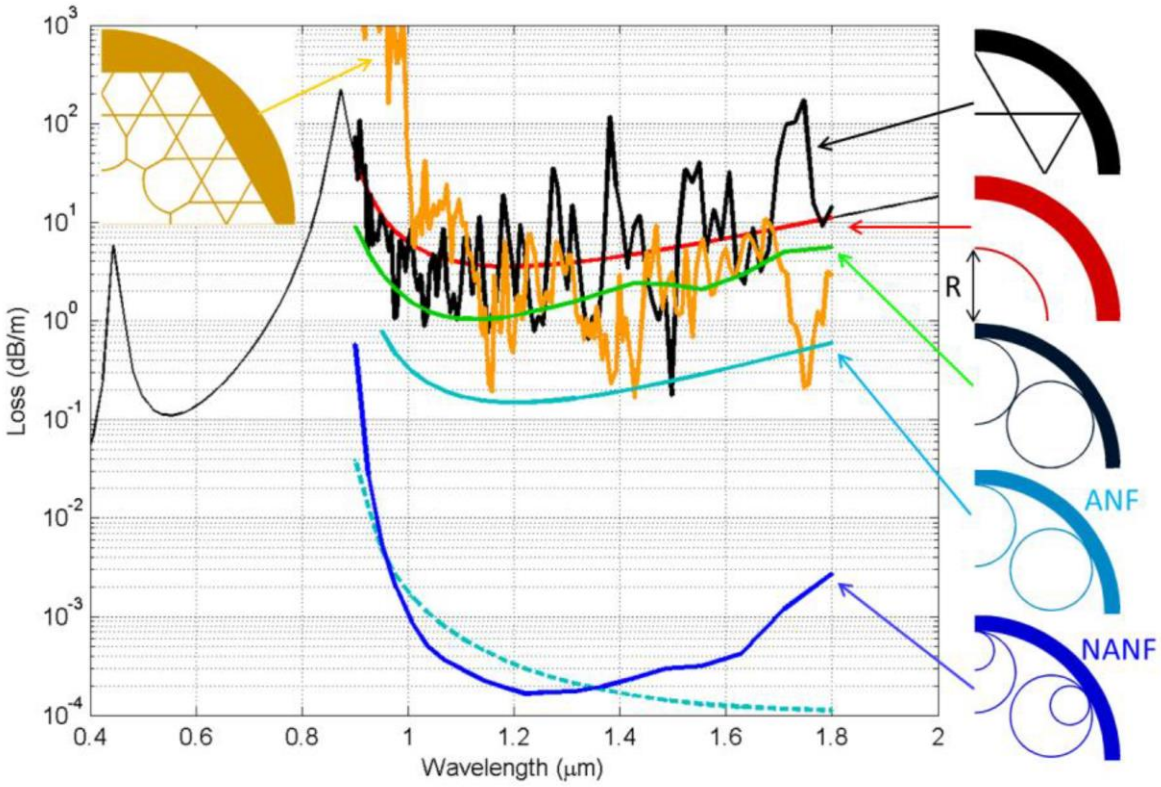

Figure 2-36. Comparison of confinement loss for various designs of ARFs: (yellow) Kagome fibre with negative curvature core, (black) hexagram fibre, (red) idealised Bragg fibre, (green) tube lattice ARF, (cyan) anit-resonant nodeless fibre (ANF), (blue) nested anti-resonant nodeless fibre (NANF). Core diameter and strut thickness are the same for all fibres and equal to 15 μm and 0.42 μm, respectively. The dashed line marks surface scattering loss (SSL) for both ANF and NANF [195].

Loss mechanism and modality

In total, five types of loss mechanisms in HCFs can be identified [23]:

- geometrical loss (leakage)
- surface scattering
- macro- and micro-bend loss
- material absorption (glass or polymer)
- intermodal effects.

Those that also exist in conventional fibres (i.e., excluding leakage and intermodal loss) are similar qualitatively but quantitatively they are rather different. Depending on a particular fibre (fibre type and parameters), one or two mechanisms are normally dominant. Confinement loss of both PBGFs and ARFs has been discussed above. Other loss mechanisms are introduced below.

In conventional fibres, scattering loss comes from Rayleigh scattering of fibre material. In HCFs, light is guided in air, whose Rayleigh scattering is negligible, but is it replaced by surface scattering at

air-glass interface. In general, it is hard to model precisely, and its scaling with fibre radius and wavelength of light depends on fibre type [23, 195, 224]. However, it can be a dominant loss mechanism in HCFs.

Moreover, loss in HCFs can originate from micro- and macro-bends. Their physical causes are the same as for conventional fibres. The former causes light to couple to more lossy modes, while the latter results in RI tilt and radiation tunnelling. The differences for this type of loss between conventional and HCFs lie in spectral dependence and scaling with wavelength [23].

Loss due to material absorption (glass or polymer) can be negligible compared to conventional fibres. Electromagnetic field overlap with the solid regions is very small in HCFs, amounting to ~10^{-3} in PBGFs and ~10^{-4}-10^{-5} in ARFs. Hence, material absorption loss is reduced by the same amount compared to conventional fibres since, in the latter, the entire field propagates in the solid parts. This leads to markedly broadens the spectral regions where glass absorption can be neglected. Moreover, NCFs transmitting even in the regions of extremely high material loss have been reported [211].

Finally, another source of loss in HCFs is in intermodal effects. Normally, multiple air-guided modes are free to propagate in their core. Loss of higher order modes is higher than this of the fundamental one. Due to various kinds of perturbations (e.g., twist, bent, scattering or defects) light can couple from less to more leaky modes.

Examples of simulated contributions of various loss factors to total loss compared with experimental measurements is presented in Figure 2-37 for a PBGF and an ARF (NANF). It can be observed that total loss of the former is mostly contributed to by micro-bend and surface scattering loss, while total loss of the latter – by micro-bend and confinement loss.

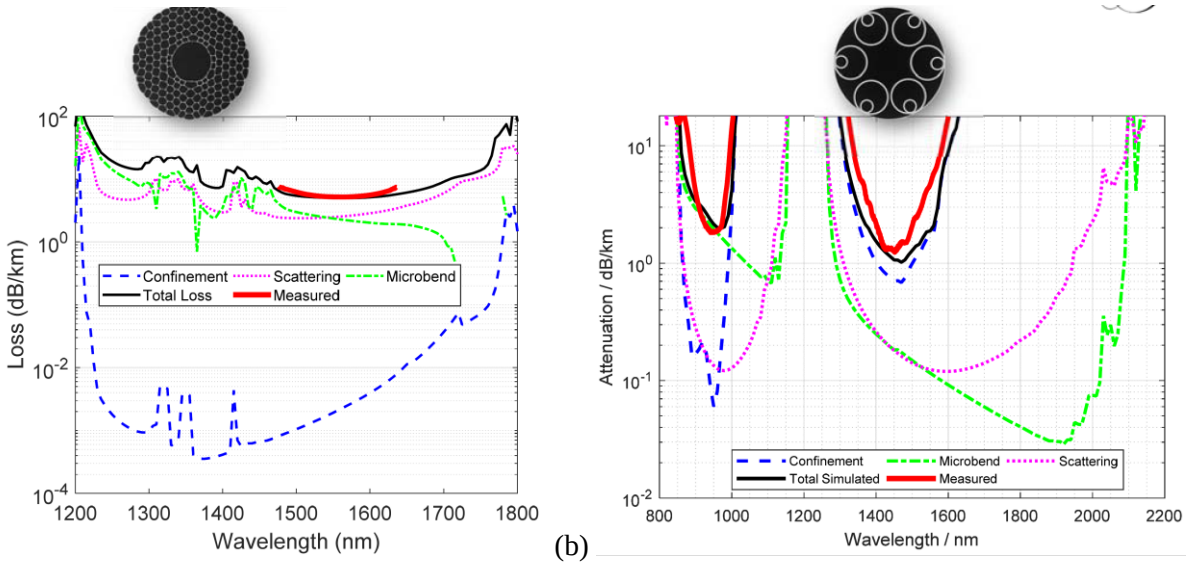

Figure 2-37. Simulation of mechanism contributing to total fibre loss compared with its measured values for (a) a PBGF [23] and (b) ARF (NANF) [28].

To sum up the guidance and loss mechanisms, a HC PBGF rely on multiple nodes arrange radially, all of which are in antiresonance. The advantages of this entail negligible leakage loss, which can be decreased to desired levels by increasing the number of rings of nodes. Moreover, the structure of HC PBGFs also ensures very low bend loss. However, for structural stability, structs interconnecting the nodes must be introduced. They are not in in anti-resonance anymore, which is at the origin of certain drawbacks of PBGFs. The struts narrow the bandwidth and eliminate higher order bandgaps. They are also responsible for high surface scattering loss, which normally is the dominating loss mechanism. Finally, PBGFs usually show low bend loss [23].

ARFs rely on membranes surrounding the core, all of which are in antiresonance. They ensure large bandwidth (spanning up to one octave), multiple low-loss transmission bands, and very low surface scattering loss. Surface waves in NCFs are of similar value to these in PBGFs, but light intensity at the core-cladding interface is lower. This makes surface scattering loss lower and quality of the interface less important. Nevertheless, due to a limited number of reflecting surfaces, the cladding size is smaller than in PBGFs, resulting in high leakage loss. However, it can still be lowered by further improvements to the cladding structure, which has been confirmed by recent advances (see below). Finally, NCFs usually show higher bend loss than PBGFs [23].

Regarding modality of HCFs, there are some differences between PBGFs and ARFs, although they both tend to be multimode [23]. This is because propagation loss for both types of fibres decreases with the increasing core size. Hence, core radius of HCFs tends to have the size of tens of micrometres, which is much bigger than wavelength of light and results in multiple modes being supported by the air core. At the cost of high loss, PBGFs can be made single-mode. The spectral region at which guidance occurs is determined in PBGFs by the cladding structure, so it must be to keep constant if guidance is to occur at the same wavelengths. Core size can increase stepwise by removing growing number of cladding cells, allowing only limited control over the core size. Full control over it is attainable in NCFs: their spectral operational range is designed by changing thickness of the membranes, while size of the core and of the cladding tubes can be tuned independently by arbitrary increments. Because the cladding tubes have smaller diameter than the core, effective RI of their fundamental mode is lower than this of the fundamental mode of the core. The latter has the highest effective RI of all core modes, i.e., higher than this of the fundamental cladding tube mode. Thus, the fundamental core mode finds no states in the tubes to couple to, in contrast to higher order core modes, for which there are cladding modes to couple to. Hence, by appropriately choosing the ratio of core diameter to cladding tube diameter, effective single mode operation can be achieved by inducing high loss for higher order core modes [225], which cannot be achieved in PBGFs.

Evolution of PBGF and ARFs

The concept of a PCF originates from Philip Russel, who was also among the authors of the first report on HC PBGF [10]. The PBGF reported back in 2004 still holds the lowest-loss record of 1.7 dB/km at 1565 nm [226]. It relied on a combination of a PBG cladding and a thick AR layer at the core-cladding interface. However, this resulted in strong surface modes, which limited 3dB bandwidth at the lowest-loss wavelength to <20 nm and deteriorated other fibre properties [227]. Further optimising fibre structure and thinning the core-cladding interface to eliminate surface modes resulted in 2012 in a fibre of 160 nm wide 3 dB bandwidth, being the widest ever reported [208, 227]. The fibre depends solely on PBG guidance and not AR, and its minimum loss figure was 3.5 dB/km at ~1500 nm.

AR guidance was first reported in a fibre based on Kagome lattice [209] in 2002, which yielded a huge bandwidth, with loss being below 3 dB/m from 350 to 1700 nm. It then evolved into the concept of negative curvature fibres in 2011 [228], resulting in loss figure of 180 dB/km at 1100-1400 nm. A milestone in the development of NCFs was the design of cladding made of non-touching (nodeless) tubes only [211], decreasing propagation loss further down to 50 dB/km at 3.4 μm. The lowest-loss fibre of this design was reported in 2017, with loss of 7.7 dB/km at 750 nm and ~60 dB/km at 1550 nm being close to the lowest theoretically predicted for this fibre design [229]. Further improvements resulted from modifications to the cladding design, which until then had been made of one ring of single circular tubes. Currently, the lowest-loss record of all types of HC fibres is held by a NANF (see Figure 2-36) reported in 2018, with the loss of 1.3 dB/km at 1450 nm (8 times loss of silica fibre) and 1.8 dB/km at 950 nm (2 times loss of silica fibre) [28].

Figure 2-38 allows tracing the evolution of loss figure of PBGFs and ARFs. It can be appreciated that ARFs have recently been very quick in decreasing the value of propagation loss, yet still leaving room for further progress.

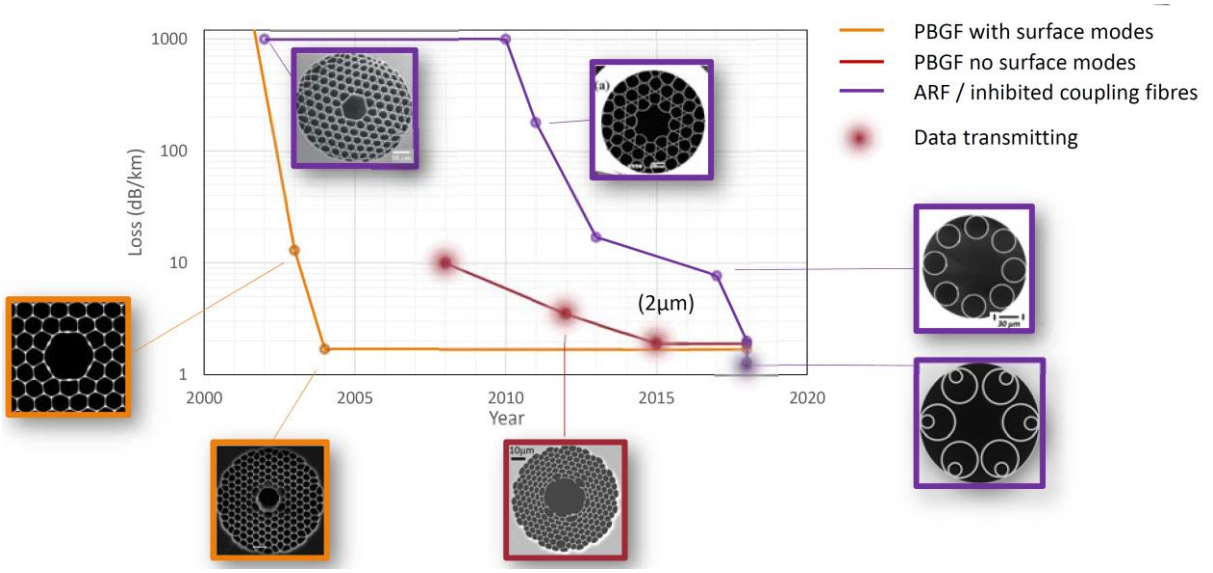

Figure 2-38. Evolution of overall fibre loss figure for PBGFs and ARFs in the recent years [23].

2.6 Fabrication of polymer optical fibres

This section reviews the technology of producing polymer optical fibres. The focus is put on fabrication of mPOFs according to the preform method. Various approached to the production of preforms themselves are also presented. The section concludes with reviewing applications of the FDM 3D printing technique to POF manufacturing.

2.6.1 The preform method

Various techniques have been proposed to manufacture conventional POFs. The continuous extrusion, batch extrusion, and preform methods have been reported to fabricate step-index conventional fibres [9, 230]. The latter method is the most versatile because it allows producing various types of POFs, e.g., conventional POFs of a more complicated RI profile (including graded-index), along with solid-core and hollow-core mPOFs. The steps involved in this method are discussed below.

The preform method starts from fabricating a large-scale structured preform, being essentially an enlarged version of the fibre to be produced. Various techniques are used for preform manufacturing, but the fibre drawing process is virtually independent of which one is applied, and largely the same procedure is followed for conventional and microstructured POFs [26]. When the preform is ready, it is drawn into fibre using a draw tower (Figure 2-39). The process begins with mounting the preform on a preform feeder and lowering into a furnace. Starting from the lower end, the preform is heated above its glass transition, to a temperature at which viscosity of the plastic decreases and the material can be easily deformed. Then, the lower end of the preform begins to drop out of the furnace due to gravitational force. The temperature of the material that has exited the furnace falls and, thus, material viscosity rises,

preventing from further shape change. Hence, material deformation (decrease of preform diameter) happens only in the furnace, in the so-called neck-down region. Fibre results from the material removed from the furnace being pulled down by a capstan at a constant speed. Diameter of the resulting fibre can be calculated from the mass conservation law according to the following equation [26]:

$$\frac{D^2}{d^2} = \frac{v_{draw}}{v_{feed}}, \tag{2-42}$$

where D and d are the preform and fibre diameters, respectively, and v_{draw}, v_{feed} – speeds of fibre drawing and preform feeding, respectively. Fibre diameter is monitored throughout the process by a diameter gauge, and drawing tension is controlled by a tension monitor. The drawing process ends with fibre being winded on a spool.

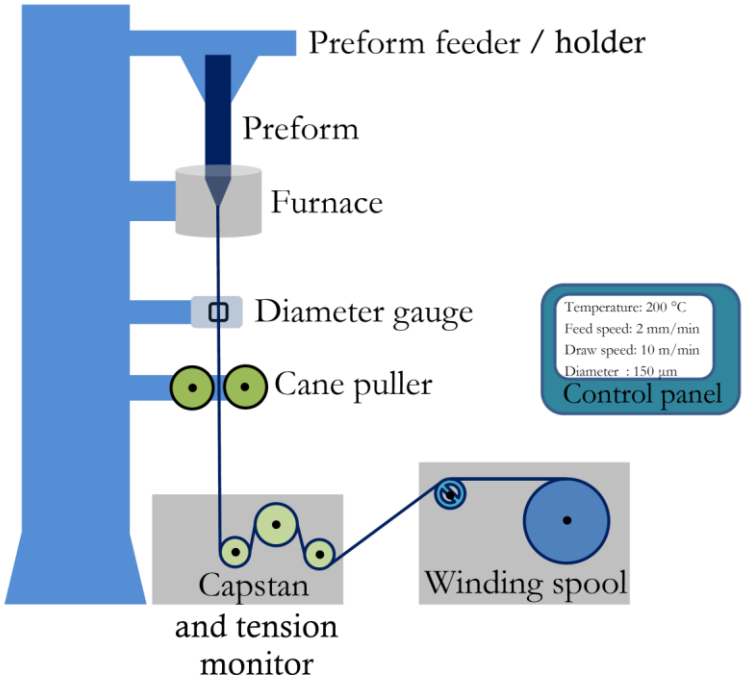

Figure 2-39. Schematic diagram of a POF draw tower. After [231] and [26].

Following the description presented above, preform is drawn directly to fibre. However, this involves huge diameter decrease on drawing (from single centimetres in preform to hundreds of micrometres in fibre, depending on desired parameters and equipment requirements). This, in turn, requires enormous speed difference between preform feeding and fibre drawing (compare Equation (2-42)). For better control of the drawing process, including minimising deviations to the design of the preform structure, an intermediate step between the preform and the fibre is often introduced. This relies on preform being drawn by a cane puller to form a cane with diameter between 2 and 6 mm. [26]. Subsequently, such a cane can be drawn into fibre directly. Alternatively, the cane can be sleeved with a close-fitting tube to form a secondary preform of about 12-mm diameter, from with the fibre is drawn.

2.6.2 Conventional preform fabrication techniques

Various processes have been reported to manufacture fibre preforms. Those for graded-index POFs are made by means of the gel polymerisation technique and diffusion technique [9], which are beyond the scope of this review. A broad range of techniques available for manufacturing mPOF preforms will be discussed below. These encompass:

- consecutive solvent evaporation,
- co-rolling,
- capillary stacking,
- drilling,
- extrusion,
- casting.

The consecutive solvent evaporation technique and co-rolling technique have been applied for the production of SC and HC Bragg preforms [232]. The former method consists of introducing dissolved polymer inside a rotating tube and subsequent solvent evaporation, leading to creation of a solid layer of a well-controlled thickness. A Bragg stack on the inner walls of the tube is created by alternating deposited polymers, and two pairs of materials have been reported: polystyrene/poly(methyl methacrylate) and polycarbonate/poly(vinylene difloride), resulting in preforms of up 15 layers. The co-rolling technique have been used to manufacture casted polymer bilayers of the same material pairs, which are then rolled onto a Teflon mandrel, yielding fibres made of up to 32 layers.

Capillary stacking is the technique of choice for manufacturing fibre preforms for SC and HC microstructured SOFs [10, 24, 179], but it was also successfully used to produce mPOFs [233]. This method relies on manually stacking multiple capillary tubes together inside an outer tube, allowing much freedom in constructing preform design. For example, the capillaries can be combined with solid rods, they can be made of different materials, and outer surfaces of the capillaries can be polished to form regular hexagons in cross-section, allowing very tight stacking.

Another method to fabricate preforms is drilling the holey structure into blocks of bulk material, produced by casting or extrusion. Both silica and polymer fibre preforms have been fabricated with this method [116, 122, 234-238]. However, drilling precise thin-walled structures into glass while avoiding cracks leading to glass fractures has been found cumbersome [234]. Hence, glass preforms are readily produced with other methods, mostly capillary stacking. In turn, drilling has been very popular in mPOF production – the first reported mPOF was fabricated this way [235]. This method allows fabricating designs which would be difficult or impossible to make with capillary stacking, for instance, graded-index mPOFs comprising aperiodic arrangement of differently sized holes [237].

Extrusion has been utilised to successfully fabricate non-silica glass and polymer fibre preforms [239-242]. In this method, a combination of high temperature and pressure is used to force bulk material

though a die of a specific pattern, which is reproduce in the extrudate. This allows fabricating preforms of shapes very difficult to fabricate by capillary stacking or drilling, e.g., suspended-core fibres [242].

Another process to produce fibre preforms is casting, which was used both for glass [243, 244] and polymer fibres [245]. It starts from assembling an array of rods of desired shape, size, and arrangement to form a mould in which casting is to occur. Then, an appropriate mixture of chemical species (i.e., monomer, initiator and chain-transfer agent) are introduced in the mould for polymerisation. The mixture normally needs degassing to avoid formation of bubbles. The polymerisation process leads to a solid preform, which is then removed from the mould. The latter can be enclosed, protecting the reaction mixture from contaminants, which can potentially yield preforms of very high purity. Moreover, interstitial holes – which can appear when capillary stacking is used – can be easily avoided by means of the casting method. Multiple variations of this technique are possible. For example, polymer pellets can be casted into all-solid preforms (i.e., non-structured), which can be further processed using the drilling technique [116, 122, 238].

2.6.3 Fused deposition modelling for POF fabrication

In recent years, the FDM process has been proposed as an alternative to the aforementioned conventional methods for POF preform fabrication. This was caused by the recognition of the particular qualities of FDM, which are absent in many other manufacturing techniques (see Section 1.1.1).

Several interesting publications regarding solid-core POFs arose. A step-index fibre was drawn from a preform made of two polymers, printed on a dual-head 3D printer [31]. The core of this fibre was made of styrene-butadiene copolymer and polystyrene (SBP) and the cladding, of modified polyethylene terephthalate glycol (PETG). In [32], cores of various shapes (made of polycarbonate, PC) and complementary claddings (made of acrylonitrile butadiene styrene, ABS) were printed separately and assembled together to form preforms, which were subsequently drawn. This demonstrated the ease with which 3D-printed shapes and, hence, fibre properties could be customised. Air-structured fibre drawn from a 3D-printed preform made of SBP was presented in [30]. Cladding structure of this fibre lied above the micrometric range. However, as fibre manufacturing followed the classical preform method, microstructured POFs should in principle be achievable this way provided the quality of 3D-printed preform is improved.

Hollow-core POF preforms fabricated by means of FDM have also been reported. The first one ever proposed was made of poly(methyl methacrylate) (PMMA) and drawn to the cane stage [246], which is a milestone of this thesis and is discussed in detail in Section 4.3. Later, the first HC POF drawn from 3D-printed preform made of acrylonitrile butadiene styrene (ABS) was presented [33]. This was followed by a publication on mid-IR HC mPOF drawn from 3D-printed preform made of PETG [34].

Finally, it is worth mentioning that FDM has also been used to fabricate POFs without the combination with the preform method. Coreless POFs drawn directly from 3D printer nozzle were

reported in [247], in which the preform stage in POF manufacturing was omitted. In addition, larger terahertz-range waveguides have been directly 3D-printed at the size required for use [248-251].

2.7 Fibre Bragg gratings

This section covers various topics relevant to both silica and polymer fibre Bragg gratings, with the focus on sensing applications. First, theoretical considerations on FBGs are presented, which encompasses the relation between RI modulation in fibre and FBG spectrum. The mechanisms of photosensitivity of POFs and SOFs are reviewed further. This is followed by a discussion of FBG fabrication techniques, highlighting their advantages and shortcomings. To finish with, grating sensitivity to measurands is considered, including strain, temperature, and humidity, along with the cross-sensitivity issues.

2.7.1 FBG theory

An illustration of a fibre Bragg grating (FBG) is a wavelength-selective mirror confined to fibre core. Speaking more precisely, it is a Bragg mirror (see Section 2.4), i.e., a 1D photonic crystal consisting in RI modulation along the fibre core. When the broadband light travelling in the core (λ_{broad} in Figure 2-40) reaches the FBG, a narrow range of wavelengths is reflected (λ_B), while the remaining part of the spectrum is transmitted ($\lambda_{broad} - \lambda_B$). The wavelength of light that is reflected matches the Bragg condition, i.e., the condition for constructive interference of the reflected light and destructive interference of the transmitted light. The Bragg condition can be derived from energy and momentum conservation [252]. The requirement of energy conservation is that the frequency of the incident wave is the same as of the reflected one ($\hbar\omega_f = \hbar\omega_i$). Momentum conservation, in turn, demands that the wavevector of the incident radiation ($\overrightarrow{k_i}$) plus the wavevector of the FBG ($\vec{K}$) is equal to the wavevector of the backscattered wave ($\overrightarrow{k_f}$):

$$\overrightarrow{k_i} + \vec{K} = \overrightarrow{k_f} \tag{2-43}$$

The FBG wavevector ($\vec{K}$) is normal to the grating planes and has a magnitude of $2\pi/\Lambda$, Λ being spacing between the grating layers (see Figure 2-40). The wavevector of the back-scattered light has the same magnitude as this of the incident light but opposite direction. The momentum conservation condition can then be written as [252]:

$$2\left(\frac{2\pi\, n_{eff}}{\lambda_B}\right) = \frac{2\pi}{\Lambda}. \tag{2-44}$$

Hence, the first order Bragg condition can be noted as follows:

$$\lambda_B = 2\,\Lambda\, n_{eff}, \tag{2-45}$$

where λ_B is the Bragg wavelength of the FBG, i.e., the free space centre wavelength of the back-scattered radiation, and n_{eff} is the effective RI of the fibre core at λ_B.

In addition, the FBG displays higher-order reflections at wavelength λ_m (where m = 2, 3, 4… and is the reflection order), which are fractions of the first-order Bragg wavelength (λ_B). The m-th-order Bragg reflection can be expressed as:

$$\lambda_m = \frac{\lambda_B}{m} = \frac{2\,\Lambda\,n_{eff}}{m}. \tag{2-46}$$

From the above equation can be seen that, if the initial grating period is increased m times ($\Lambda_{increased} = m\,\Lambda$), the m-th order Bragg reflection is observed at the initial, first-order Bragg wavelength ($\lambda_{increased} = m\,\lambda_m = m\,(\lambda_B/m) = \lambda_B$). In general, producing a fine spatial modulation pattern required for first-order Bragg reflection is not a straightforward task. Therefore, relying on higher-order reflections can be very practical as it can extend the range of techniques used for FBG fabrication to those that can only provide lower resolution (see Section 2.7.3).

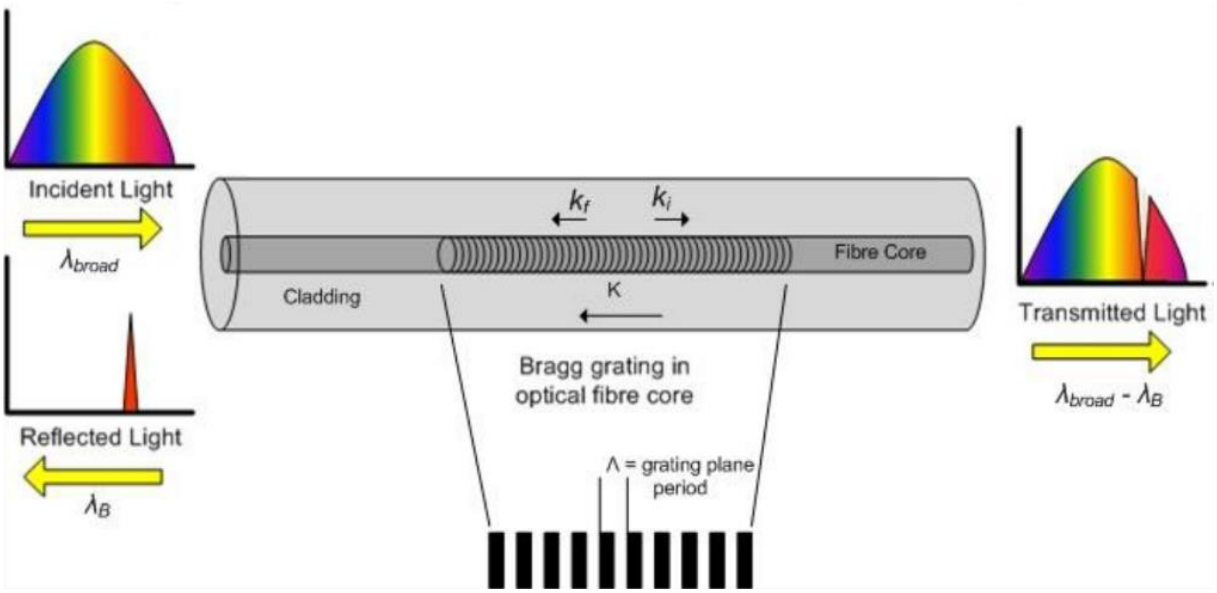

Figure 2-40. Schematic and principle of operation of a fibre Bragg grating. Note that the light spectra are simplified (see Figure 2-41). Adapted from [253].

The simplest example of an FBG is a uniform grating. It displays uniform RI modulation along the fibre core (see inset in Figure 2-41), which can be expressed as [252]:

$$n(z) = n_0 + \Delta n\,cos\left(\frac{2\pi z}{\Lambda}\right), \tag{2-47}$$

where Δn is the amplitude of the induced RI change (typically from 10^{-5} to 10^{-3}) and z – the distance along the fibre axis. The most widely used approach to determine the FBG spectrum is using the coupled-mode theory [254], which allows calculating how the forward mode of the light travelling in the fibre couples to the backward mode. This theory yields the following mathematical description of

the reflection spectrum of an FBG with a constant amplitude and constant period of RI modulation (Figure 2-41) [252]:

$$R(l,\lambda) = \frac{\kappa^2 sinh^2(sl)}{\Delta\beta^2 sinh^2(sl) + s^2 cosh^2(sl)}, \tag{2-48}$$

where $R(l, \lambda)$ in the reflectivity, being a function of the grating length l and the wavelength of light λ, κ is the coupling coefficient, $\beta = 2\pi n_0/\lambda$ and is the propagation constant, $\Delta\beta = \beta - \pi/\Lambda$ and is the detuning wavevector, and $s^2 = \kappa^2 - \Delta\beta^2$. For sinusoidal RI modulation, the coupling coefficient (κ) is expressed as:

$$\kappa = \frac{\pi \Delta n}{\lambda}\eta, \tag{2-49}$$

where η is the grating efficiency, which quantifies the overlap between the grating and the guided light. For FBGs written uniformly through the core, η can be approximated by the expression $1 - V^{-2}$, where V is the normalised frequency (see Equation (2-3)). The lobes on the sides of the main peak in Figure 2-41 come from the finite extent of the Bragg stack. The side lobes would disappear in the case of an infinitely long grating, and the sinc function describing the spectrum of a finite length FBG would transform into the delta function [252].

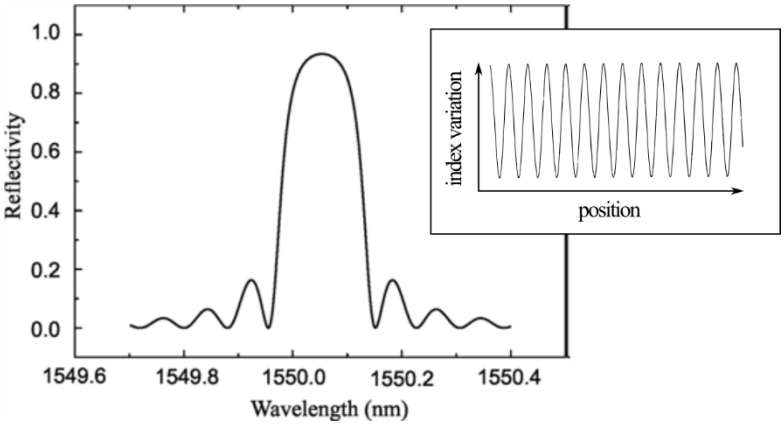

Figure 2-41. Spectral reflectivity of a uniform FBG. Inset shows RI modulation profile along the fibre axis. Adapted from [252].

If the Bragg condition is satisfied, the wavevector detuning ($\Delta\beta$) equals zero, and Equation (2-48) simplifies to [252]:

$$R(l,\lambda) = tanh^2(\kappa l) \tag{2-50}$$

From the above equation, it can be seen that the grating reflectivity increases with increasing grating length (l) or RI modulation strength (Δn; compare Equation (2-49)). The impact of the latter is presented in Figure 2-44.

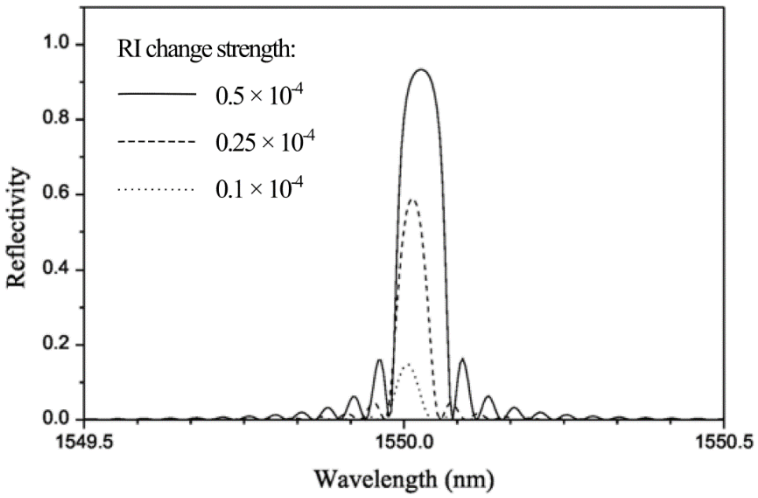

Figure 2-42. Spectral reflectivity of a 2-cm long FBG for different values of RI modulation strength. Adapted from [252].

Finally, the full width at half maximum (FWHM) bandwidth of an FBG can be approximated as [252]:

$$\Delta\lambda = \lambda_B S \sqrt{\left(\frac{\Delta n}{2n_0}\right)^2 + \left(\frac{1}{N}\right)^2}, \tag{2-51}$$

where N is the number of FBG layers; $S \approx 1$ for strong gratings (i.e., of near 100% reflectivity), and for weak FBGs, $S \approx 0.5$. As can be seen from the above equation, the stronger the RI modulation, the bigger the bandwidth. However, it falls with increasing number of grating layers (i.e., grating length). Figure 2-43 allows comparing the impact of the grating length on its bandwidth. The RI change (Δn) in the figure decreases with growing FBG length so that resulting gratings have the same strength (see Equation (2-50)). In such case, increasing grating length (1, 2, and 4 cm) results in decreasing grating bandwidth (0.15, 0.074, and 0.057 nm, respectively).

Equation (2-48) describes the reflection spectrum of an FBG with RI modulation of constant amplitude and period. In principle, more complex RI modulation functions are possible, resulting in more sophisticated shapes of grating spectra. Coupled mode theory can also provide their mathematical description, with multiple examples being available in the literature [254]. These include, chirped FBGs (Figure 2-44), in which the RI modulation profile has constant amplitude but varying frequency; in the simplest case, the frequency changes linearly (see the inset in Figure 2-44(b)). As a result, grating broadens with chirp strength at the cost of a decrease in grating reflectivity if RI change strength and FBG length are kept constant. Such broad gratings find their use, e.g., in compensating dispersion of optical communication systems as they allow achieving large dispersion of group delay [37, 38].

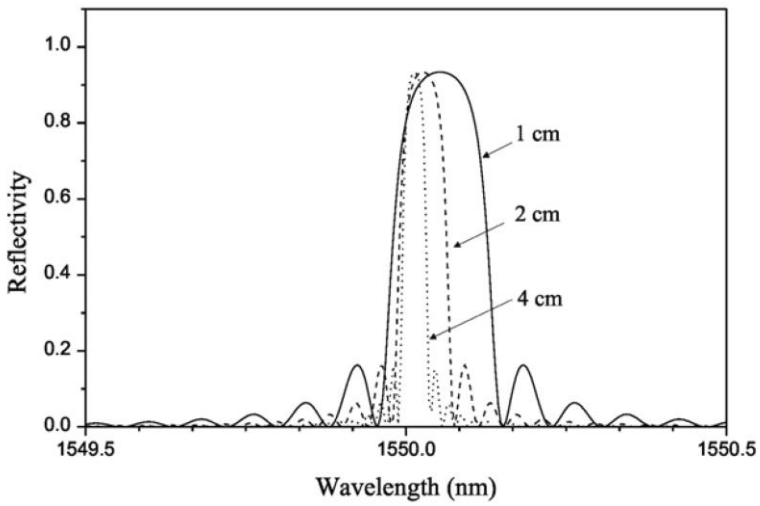

Figure 2-43. Spectral reflectivity of uniform FBGs, showing that increasing grating length results in decreasing grating bandwidth. The strength of RI change decreases with growing grating length so that all gratings have the same strength [252].

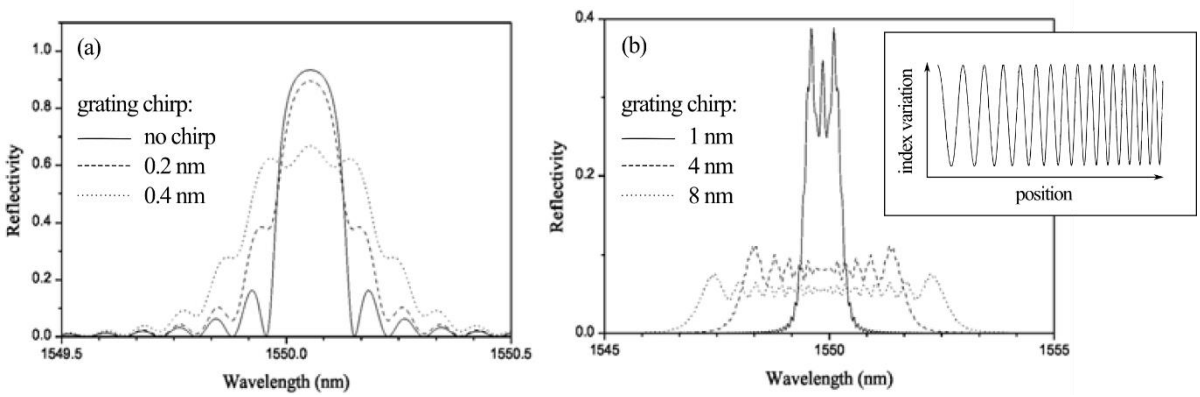

Figure 2-44. Spectral reflectivity of (a) weakly and (b) heavily chirped FBGs (note the difference in the reflectivity scales). The FBG length and RI change value for all the gratings are 10 mm and 1×10^{-4}, respectively. The chirp value is given over the whole FBG length. The inset in (b) shows RI modulation profile of a chirped grating. Adapted from [252].

Moreover, varying amplitude of RI modulation profile appropriately can give rise to apodised gratings (Figure 2-45). They are characterised by an extremely small amplitude of the side lobes, especially in the case of the constant average RI profile (compare Figure 2-41 and Figure 2-45, noting that the latter shows reflectivity and transmittivity on the logarithmic scale). This type of grating is particularly desirable in dense wavelength division multiplexing since suppressing side lobes minimises cross talk between the information channels [255].

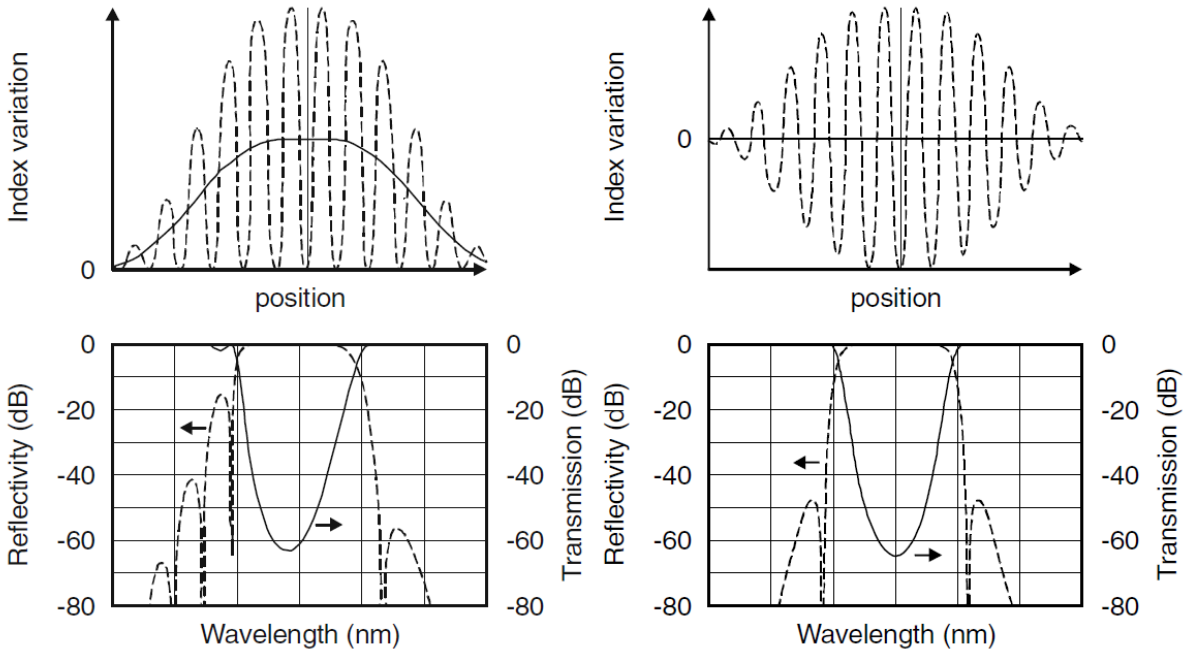

Figure 2-45. (top) RI modulation profile along with (bottom) corresponding reflection and transmission spectra for apodised FBGs: (left) varying and (right) constant average RI value. Note the logarithmic scale for reflectivity and transmittivity [252].

Yet another example of complex FBGs encompasses a phase-shifted grating, which is produced by introducing a phase shift to the uniform RI modulation profile (Figure 2-46). Reflectivity spectrum of such grating shows a distinct dip of a very steep edges and narrow bandwidth, allowing a more precise tracking of grating position than a uniform FBG.

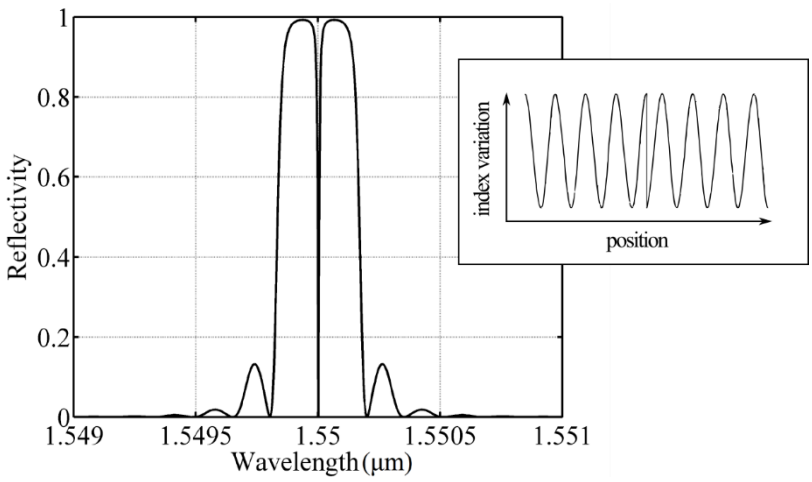

Figure 2-46. Spectral reflectivity of a phase-shifted FBG. The inset shows RI modulation profile along the fibre axis. Adapted from [256].

Finally, it must be mentioned that precise consideration of polymer FBGs (POFBGs) need to involve the loss factor, stemming from high attenuation of a polymer optical fibre itself. Fibre attenuation is

normally neglected when treating silica FBG (SOFBG) due to its negligible influence. A detailed analysis of POFBGs involving loss has been presented in [256].

2.7.2 Fibre photosensitivity

Photosensitivity in silica and SOFs

FBGs are most commonly inscribed by selective exposure of the fibre core to UV radiation, which induces a permanent change in RI. This phenomenon is referred to as fibre photosensitivity. Since the inscription of the first FBG, which was fabricated in a Ge-doped silica fibre (germanosilicate fibre) in 1978 [35], a few models have been proposed to explain the origins of the RI modulation in this type of fibre, including the colour centre [257], densification [258], stress relief [259] and dipole models [260]. They could be split into two categories: electronic models and structural models. The former relies on linking the photosensitivity with the presence of defects in glass, either being inherent to the glass structure or introduced during fibre manufacturing. The structural models, in turn, consist in connecting RI modulation with local structural changes to the material coming from the UV exposure. No single model managed to provide full explanation of experimentally observed RI changes. The densification model describes well the RI perturbation in non-hydrogenated germanosilicate fibres, whereas the colour centre model was found to account for a large proportion of RI modification in hydrogenated fibres [261]. Experimental results suggest that phenomena described by both classes of models (mainly the colour centre and densification models) occur simultaneously to yield photosensitivity of germanosilicate fibres at around 240 nm [262].

Photosensitivity was observed for UV illumination at different laser wavelengths, including 157, 193, 244, 325 and 351 nm [263-265], and in fibres of various types, containing other photosensitive dopants aside from germanium [266-269]. In some photosensitive fibres, germanium was completely absent, being substituted with other compounds (e.g., in aluminosilicate fibres, fluorozirconate fibres doped with cerium/erbium or fibres doped with rare-earth elements) [270-272]. Moreover, fibre photosensitivity can be further enhanced with hydrogen loading. This technique relies on exposing a fibre to high pressure hydrogen for 1-2 weeks at room temperature or at elevated temperatures for a shorter time (e.g., at 80 °C for 24 h) [273]. Hydrogen absorption to core of a germanosilicate fibre is also possible by means of the flame brushing method. It relies on a 20-min-long fibre exposure to a hydrogen/oxygen-fuelled flame at a temperature of up to 1700 °C [274].

Besides diverse types of dopants and fibre hydrogenation, various grating inscription regimes are possible, consisting primarily in various UV exposure times and intensities. All these techniques entail different physical mechanisms of photosensitivity. This have given rise to classification of FBGs into types; at least two approaches to such classifications have been reported in the literature [262, 273].

Photosensitivity in polymers and POFs

Since the first demonstration of photosensitivity of bulk PMMA in 1970 [67], continuous research effort has been directed to elucidate the underlying physical mechanism. A comprehensive study of bulk PMMA samples consisted in exposing them to laser radiation pulses of different wavelength and fluence and, subsequently, their investigation with XPS and FTIR spectroscopy [275, 276] (X-ray photoelectron spectroscopy and Fourier transform infrared spectroscopy, respectively). Irradiation at both 193 and 248 nm in general yielded RI increase until the material ablation threshold was reached. Multiple complex mechanisms were found to be involved in the process. At low irradiation (< 1000 laser pulses), UV-induced crosslinking between the ester side chains was identified. It was also probable that UV-curing of unreacted monomers was taking place simultaneously. Irradiation dose of 1000-2000 pulses led to partial breaking of the main molecular chain and, consequently, RI decrease. At irradiation doses > 2000, scission of ester side chain occurred, which was followed by pulling molecules closer together by the van der Waals forces, yielding an increase in density and, thus, RI. However, side chain scission was also destabilising the main molecular chain, resulting in its fragmentation and ablation at higher irradiation doses. The difference between irradiation with 193 and 248 nm wavelengths consisted in the fact that, in the latter case, RI change was more pronounced, and the material ablation threshold was lower. This was due to only partial side ester chain scission by 193-nm light compared to its complete cleavage when exposed to 248-nm radiation. The result of only partial side chain scission was lower degree of densification and, hence, lower magnitude of RI increase. Moreover, at 193 nm, a higher degree of side chain removal had to be induced before the main molecular backbone was destabilised enough to start fragmenting, which explains the higher ablation threshold at 193 nm. Finally, this research reported no RI change by the illumination at 308 nm.

The first POFBG in a SI PMMA fibre was inscribed in 1999 by laser irradiation at an even lower wavelength, 325 nm [68]. The photosensitivity mechanism of the used fibre was suspected to rely on photo-crosslinking and photo-polymerisation. The same paper reported an unsuccessful attempt to POFBG inscription by a 248 nm laser: only an ablation grating was formed on fibre surface with no FBG in fibre bulk, despite RI modification at that wavelength having been reported back in 1993 [277]. This inscription wavelength was then abandoned in favour of 325 nm until only lately. Moreover, POFs made of undoped PMMA were found to show higher photosensitivity when strained for inscription [278]. Straining, in turn, is known to enhance photo-degradation [279], which proved that this mechanism is also involved in POFBG growth.

In 2014, an inscription of a POFBG in only 30 s was reported at 248 nm using a nanosecond KrF laser [280]. The success in grating fabrication was due to keeping laser fluence low (below the ablation threshold for the material) and using the low repetition rate of 1 Hz. Later, a PMMA fibre doped with benzyl dimethyl ketal (BDK) was found to yield very strong gratings (98.4% reflectivity) upon illumination with a single 15-ns KrF laser pulse of an energy density of 974 mJ/cm^2 [281]. BDK is a

photo-initiator, which speculatively triggered the photo-polymerisation and photo-crosslinking processes. Moreover, POFBGs in the same fibre were demonstrated using a single pulse from a nanosecond Nd:YAG laser operating at 266 nm [282].

BDK was also reported to increase photosensitivity during continuous-wave inscription at 325 nm [283] and 355 nm [284], resulting in inscription time decrease to a few minutes from about 50 min for undoped PMMA. Other photosensitivity-increasing dopants to PMMA encompass fluorescein [285], trans-4-stilbenemethanol [127], and p-benzoquinone [286], the latter, though, having been only used in bulk samples and not in fibre.

It can be then concluded that the three mechanisms: photo-polymerisation, photo-crosslinking, and photo-degradation contribute to photosensitivity of POFs. The dominating one depends on chemical composition of material (content of unreacted monomers, molecular weight distribution, concentration of initiators, branching degree etc.) and on irradiation conditions (including illumination wavelength and fluence, pulse duration, and exposure time).

2.7.3 FBG fabrication techniques

A Bragg grating in the fibre core arises from refractive index modulation of a period comparable to the wavelength of light to be reflected from the grating (see Equation (2-45)). Thus, a very high precision in RI perturbation is required, and a number of techniques have been devised to ensure that. Among them count [252]:

- amplitude-splitting interferometry
- wavefront-splitting interferometry
- the phase-mask method
- point-by-point inscription
- direct writing
- inscription with a femtosecond laser.

Amplitude-splitting interferometry

The interferometric techniques form a family of manufacturing methods relying on exposing a fibre to the interference pattern of spacing required for inscription. A member of this family is an amplitude-splitting interferometer [36]. It involves splitting the inscription beam into two having equal optical power, which are then recombined to yield interference fringes (Figure 2-47). The fabrication set-up, besides the inscription laser, classically entails a cylindrical lens, a beam splitter and mirrors, but adding more elements in various arrangement is possible in principle.

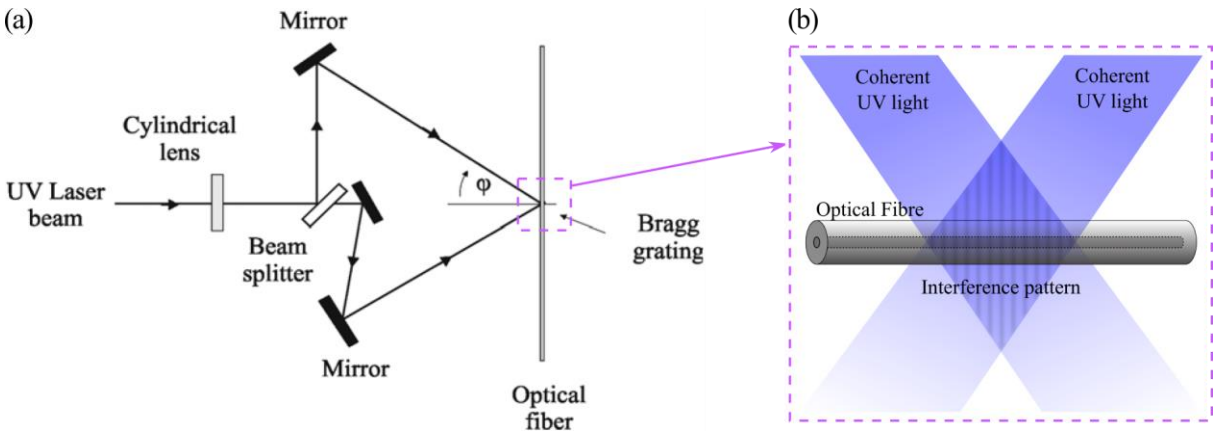

Figure 2-47. (a) Schematic showing operation of an amplitude-splitting interferometer [252] and (b) close view of the interferometric pattern over the fibre during inscription [256].

The period of the interference fringes (Λ) is a function of the half angle between the crossing UV beams (φ) and the irradiation wavelength (λ_i) [252]:

$$\Lambda = \frac{\lambda_i}{2\,sin\phi} \tag{2-52}$$

The period of the Bragg grating equals this of the interference pattern. Hence, the Bragg wavelength can be expressed through the Bragg condition (Equation (2-45)) as:

$$\lambda_B = \frac{n_{eff}\,\lambda_i}{sin\phi} \tag{2-53}$$

From the above equation can be seen that the Bragg wavelength can be tuned by changing λ_i or φ. While the former is confined to the photosensitive region of the fibre, there is no restriction to the latter. This can yield FBGs at any Bragg wavelength, which is one of the most notable advantages of the amplitude-splitting interferometry. Another relies on the possibility to introduce optical components into the arms of the interferometer to modify wavefronts of the intersecting beams. This can broaden the range of gratings that can be fabricated using this system to include, e.g., chirped FBGs. However, this fabrication method is not without its shortcomings. First, it shows large sensitivity to mechanical vibrations as submicron variation to the position of the optical components can result in interference pattern shifting over the fibre and, hence, spoiling the grating during inscription. Moreover, interference pattern can be affected by air currents, inducing local RI changes. Finally, inscription lasers used in this technique must show good spatial and temporal coherence and excellent stability of the output power and wavelength. It is also worth mentioning that the amplitude-splitting interferometry can be used to manufacture draw-tower gratings: a single laser shot is then delivered to a fibre after it leaves the draw tower and before it is coated.

Wavefront-splitting interferometry

Other interference FBG fabrication methods consist in splitting the wavefront rather than the amplitude. Two popular arrangements of wavefront-splitting interferometers encompass the prims interferometer [287, 288] and the Lloyd's mirror [289] (Figure 2-48(a) and (b)). The inscription beam is usually halved, and one half is reflected towards the other to create interference fringes (Figure 2-48(c)). A cylindrical lens is normally placed close to the fibre to focus the beam on the fibre core. Rotating the whole inscription assembly (the fibre and the mirror or prism) allows tuning the Bragg wavelength of the grating to be inscribed. This fabrication technique, compared to amplitude-splitting interferometry, relies on only one component, thanks to which susceptibility to mechanical vibrations is minimised. Moreover, the light beams are separated over a much smaller distance, hence the impact of RI modulation from air currents is reduced. However, wavefront splitting also displays certain limitations. First of all, the maximum grating length is limited to half the beam width. In addition, Bragg wavelength tuning involves rotating the inscription assembly, which can result in increasing the distance over which the two beams are separated, thus imposing higher requirements on the coherence length of the inscription beam. Finally, the wavefront passes over the prism or mirror edge, whose imperfections can distort the interference pattern.

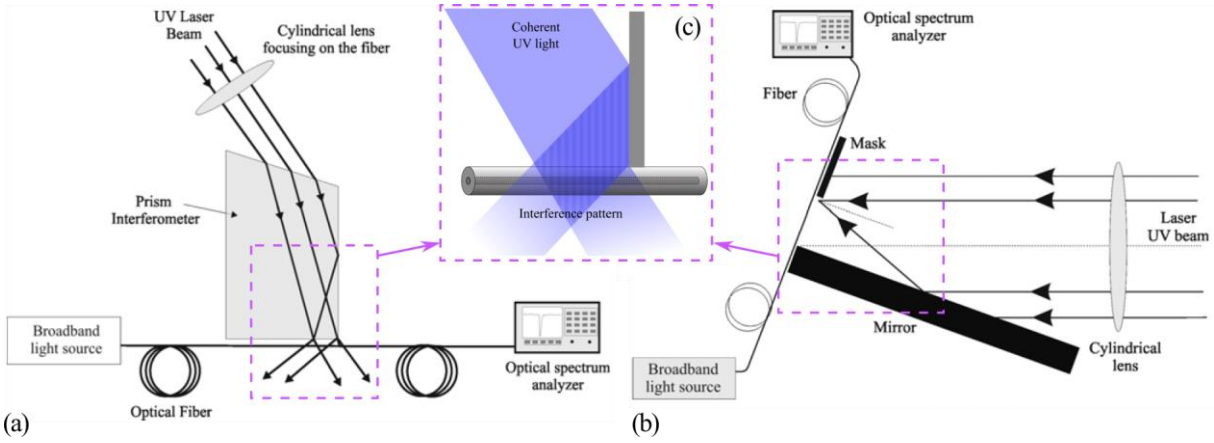

Figure 2-48. Wavefront-splitting interferometers: (a) the prism interferometer and (b) the Lloyd's mirror. (c) Close view of the interferometric pattern over the fibre during inscription. (a) and (b) adapted from [252], (c) adapted from [256].

The phase-mask technique

Another grating inscription method, the phase-mask technique [290], is one of the most effective. It involves the UV inscription beam being diffracted by passing through a phase mask (PM), yielding a few diffraction orders (Figure 2-49(a)). Their angles (φ_m), measured to the normal to the PM, can be calculated from:

$$m\,\lambda_i = \Lambda_{PM}(\sin\phi_m + \sin\phi_i) \tag{2-54}$$

where m is the diffraction order, λ_i – the inscription wavelength (nm), Λ_{PM} – the phase mask period (nm), and ϕ_i – the angle of the incidence beam to the normal to the PM. In the case of normal incidence (φ_i = 0), the phase mask period (Λ_{PM}) becomes:

$$\Lambda_{\mathrm{PM}} = \frac{\mathrm{m}\lambda_{\mathrm{i}}}{\sin\phi_{\mathrm{m}}} \tag{2-55}$$

Interference between plus and minus first diffraction order beams is responsible for creating the desired inscription pattern (Figure 2-49(b)). Thus, when using Equation (2-52) and assuming first order diffraction (m = 1), it can be seen that the PM period equals to double the period of the PM interference fringes responsible for FBG inscription: $\Lambda_{PM} = 2\Lambda$. Hence, considering the Bragg condition (Equation (2-45)), the Bragg wavelength of the resulting FBG can be expressed as:

$$\lambda_B = n_{eff}\,\Lambda_{PM} \tag{2-56}$$

The PM is designed so that most of the light is directed into the plus and minus first diffraction order (>70% of optical power), with the zero-order diffraction accounting usually for less than 5% of optical power. Minimisation of other diffraction orders is important so that they do not interfere with and deviate the assumed interference pattern.

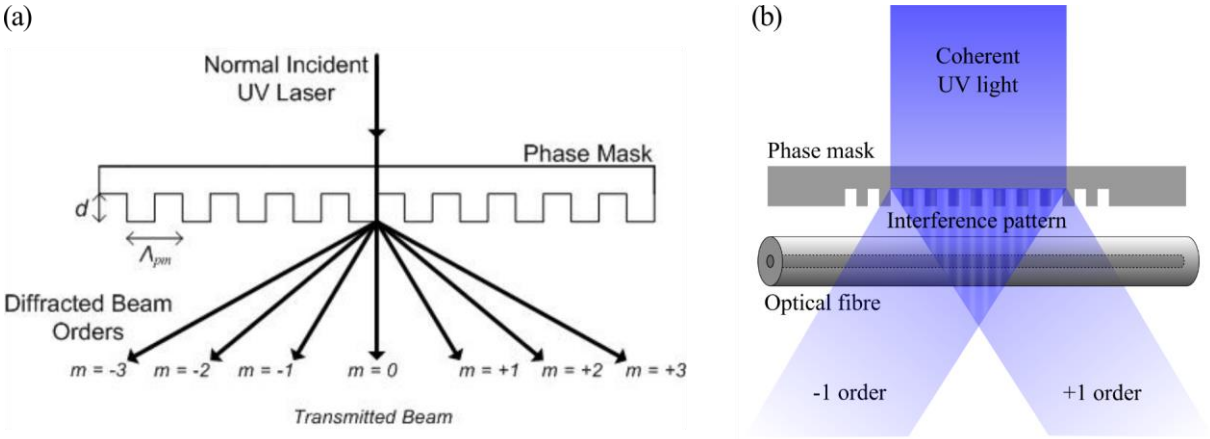

Figure 2-49. (a) Schematic of light diffraction by a phase mask yielding a few diffraction orders [253], and (b) schematic of the phase-mask inscription technique [256].

A PM can be produced holographically or by means of the electron-beam lithography [252]. The latter technique allows high flexibility in varying PM pattern and, hence, inscribing FBGs of complicated RI modulation functions. For inscription, the PM is placed directly on or in close proximity to the fibre (Figure 2-49(b)). Thanks to this, the inscription system becomes much less complex, allowing FBGs being reproduced robustly and in an inherently stable manner. Another advantage is minimised susceptibility to mechanical vibrations and capability of using inscription lasers of low temporal coherence, conversely to the interferometric techniques. However, spatial coherence of the

inscription beam is of importance and its high degree enables slight separation of the fibre from the PM to avoid scratching it. The most notable drawback of the phase-mask technique is a considerable cost of a PM. The fact that it can be customised to a high degree also means that each set of parameters (e.g., inscription wavelength, grating period, chirp) requires manufacturing a separate PM. This problem can be partly addressed by Bragg peak tuning techniques. They allow permanent Bragg wavelength shifts, especially large in the case of polymer gratings, which is discussed later in this section. Finally, it is worth mentioning that a PM can be used as a beam splitting element in the amplitude-splitting interferometry (Talbot interferometer) [273].

The point-by-point method

The point-by-point method [291] does not rely on interference, as opposed to the techniques presented so far. Instead, it consists in delivering single excimer laser pulses to the fibre, each pulse resulting in inscription of a single FBG plane. Before reaching the fibre, the pulses pass through a slit and then through a lens, which in effect projects the image of the slit onto the fibre. The latter is mounted on a high-precision translation stage, which is essential to this method. Its biggest advantage is extreme flexibility in varying parameters of the manufactured FBGs (e.g., length, pitch, RI change in each layer etc.). This enabled fabrication of complex devices like spatial mode converters [292] and polarisation mode converters (or rocking filters) [293], in which FBG period is varied from tens of micrometres to tens of millimetres. However, as consecutive grating layers are fabricated step-by-step, undesired changes to writing conditions (e.g., temperature change or air currents) can deviate the desired pattern. In addition, FBGs produced by the point-by-point method usually rely on 2^{nd} or 3^{rd} order reflection, as a grating period of about 530 nm required for first order Bragg reflection at 1550 nm is difficult to achieve in this technique.

The direct writing technique

Another FBG inscription technique, direct writing [252], can be seen as a combination of the point-by-point method and either of the two: amplitude-splitting interferometry or the phase-mask technique. In direct writing, two focused UV beams are overlapped, giving a circular spot size of a few micrometres. Linear interference pattern is created over the fibre core for inscription, after which the fibre is translated by one grating period and re-exposed. The grating is built up by repeated translation and exposure. Due to the step-wise nature of the fabrication process, this technique gives much freedom in altering various grating parameters, similarly to the point-by-point method. UV beam splitting can occur in an interferometric set-up [252, 273], in which case direct writing shares the requirements of the interferometric techniques for high laser and environmental stability. Alternatively, UV splitting can rely on a phase mask [294]. In this case, the fibre can be mounted on a piezoelectric transducer stage, which allows moving the fibre against the phase mask (Figure 2-50). The latter approach proved effective in producing apodised, chirped and phase-shifted gratings.

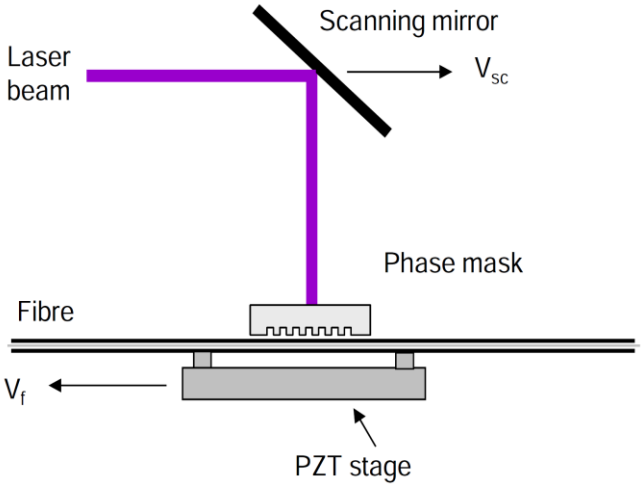

Figure 2-50. Schematic representation of direct writing inscription set-up relying on a phase mask [273].

Inscription by femtosecond later

Finally, is also possible to inscribe FBGs using a femtosecond laser [295, 296]. It is most often based on Titanium:Sapphire and operates at 800 nm (frequency tripling shifting it up to the UV range); the typical characteristics entail a pulse width of 100-150 fs, an energy per pulse of 0.02-10 μJ, and a repetition rate of 1 kHz [273]. Highly focused laser beam induces multi-photon absorption processes in the material, resulting in permanent RI change without the need for material sensitisation (hydrogenation or doping). In addition, the need for fibre stripping is eliminated. Two basic fabrication approaches are possible: the plane-by-plane and phase-mask methods. In the former, the fibre is places on a high-precision 2D-translation stage, and highly focused femtosecond pulses are directed one by one to the fibre core to form grating layers (Figure 2-51). The latter approach combines all the benefits of the phase-mask method with the possibility of quick inscription and wide variety of available materials without the need for pre-processing.

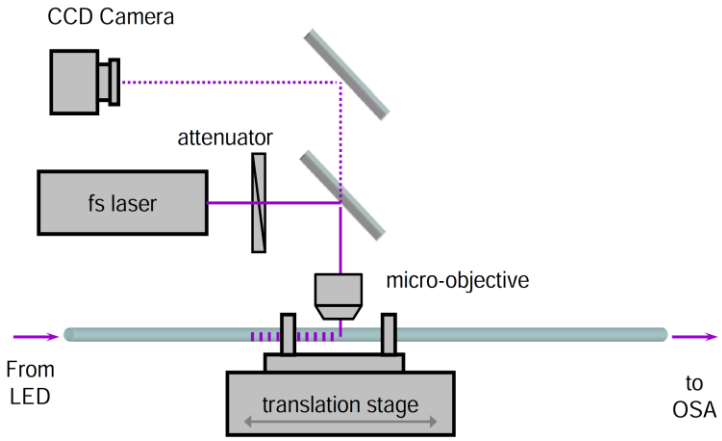

Figure 2-51. Schematic of plane-by-plane inscription by a femtosecond laser [273].

FBG pre- and post-processing techniques

Grating spectrum can also be shaped after inscription, including Bragg wavelength tuning. A variety of techniques serving this purpose have been reported, relying on fibre pre- or post-processing or post-processing the grating itself. The latter constitutes a separate research field and will be not expanded on as it is not applied in this research, the details being available in the literature [297].

One of the most useful fibre pre-processing approaches consists in straining it for inscription, which has been reported both for silica [298] and polymer fibres [278]. It relies on inscribing a grating in a strained fibre, with Bragg peak shifting to lower wavelengths when released after inscription. The amount of blueshift can be tuned by changing the extent of strain. The latter can be substantially bigger for POFs than for their silica counterparts due to much higher failure strain of polymer fibres (see Section 2.2.1).

Moreover, POFs can be annealed before inscription, which allows improving their behaviour, including stabilising their response to temperature and minimising their hysteresis [77, 134]. Annealing involves heating a POF above its β transition temperature (see Section 2.2.4), enabling relaxation of residual stress and molecular orientation introduced during fibre drawing (see Section 2.3). As a result, POF shrinks in length and grows in diameter [134]. In water-absorbing polymers (e.g., PMMA and PC, but not Zeonex), the stress relaxation process can be facilitated and accelerated by annealing POFs in high humidity conditions [134], for instance, in water. However, care must be taken not heat the fibre above the glass transition temperature of the plastic as this would allow shape deformation leading to loss of light guidance.

Furthermore, polymer fibres can be annealed after inscription of FBG. In this case, fibre shrinkage leads to a decrease in the Bragg wavelength; blueshifts of as high as 230 nm have been reported in the literature [77]. Finally, POFGBs can be tuned to longer wavelength by straining them when heated, with redshift of up to 12.5 nm having been presented [299].

2.7.4 Sensitivity to measurands

FBGs are capable of sensing strain [300-302], bend [303] and other types of mechanical deformation [304, 305], temperature [300, 301, 306], humidity [70, 77, 105], pressure [305, 307, 308], refractive index [309] and acceleration [310], among other physical quantities. The applications of POFBGs has been demonstrated in a number of fields, including medicine [75, 120, 311], biochemistry [309], aviation [79, 312], dosimetry [313], cultural heritage preservation [74] and integration with textiles [74]. This section discusses FBG sensitivity to three measurands that have been most widely described in the literature: temperature, strain and water (or humidity). This is because more complex sensors are usually constructed based on these basic physical quantities. Although FBGs demonstrate relatively high sensitivity, cross-sensitivity to different measurands remains challenging and, hence, is also considered in this section.

In principle, sensitivity of an FBG to a measurand *X* can be calculated by differentiation of the Bragg condition (Equation (2-45)), which takes the following form [254]:

$$\frac{d\lambda_B}{dX} = 2\frac{d}{dX}(\Lambda\, n_{eff}) = 2\left(n_{eff}\frac{d\Lambda}{dX} + \Lambda\frac{dn_{eff}}{dX}\right) = \lambda_B\left(\frac{1}{\Lambda}\frac{d\Lambda}{dX} + \frac{1}{n_{eff}}\frac{dn_{eff}}{dX}\right)$$
$$\therefore \Delta\lambda_B = \frac{d\lambda_B}{dX}\Delta X = \lambda_B\left(\frac{1}{\Lambda}\frac{d\Lambda}{dX} + \frac{1}{n_{eff}}\frac{dn_{eff}}{dX}\right)\Delta X. \quad (2\text{-}57)$$

It is worth mentioning that the terms $\frac{1}{\Lambda}\frac{d\Lambda}{dX}$ and $\frac{1}{n_{eff}}\frac{dn_{eff}}{dX}$ are normally independent on wavelength, so the sensitivity depends on the wavelength of light through λ_B. Hence, Bragg reflections at higher wavelengths usually display higher sensitivity.

Strain

In the case of sensing strain, Equation (2-57) becomes [262]:

$$\frac{d\lambda_B}{\epsilon} = \lambda_B(1 - P_e), \quad (2\text{-}58)$$

where ϵ is the strain $\left(\epsilon = \frac{dL}{L}\right)$ and P_e – the photo-elastic coefficient of the fibre. It is defined as:

$$P_e = \frac{n^2}{2}\left(p_{12} - \nu(p_{11} + p_{12})\right) \quad (2\text{-}59)$$

where p_{11} and p_{12} are the components of the strain-optic tensor (Pockels coefficients), and ν is the Poisson's ratio. Table 2-4 shows strain sensitivity values for FBGs inscribed in PMMA, PC, and silica, which were calculated using the experimental values of p_{11}, p_{12}, and ν reported in the literature. These strain sensitivities match well the experimental sensitivity values collated in Table 2-5 for silica and Table 2-6 for polymers. It can be observed that the sensitivity values are proportional to the light wavelength at which the sensor operates as it was mentioned before. It can also be noted that strain sensitivity of polymer gratings is only marginally higher than of their silica counterparts. However, the advantage of POFBGs lies in their considerably higher stress (or force) sensitivity, which stems from a decidedly smaller value of Young's modulus of polymer fibres when compared to SOFs (see Section 2.2.1). Moreover, due to much higher values of failure strain of POFs, they allow achieving markedly higher grating tunability. For example, reversible elastic behaviour for strains up to 13 mε and linear strain tunability of 48.4 mε have been observed for PMMA POFs. This resulted in a total tuning range of as high as 73 nm, which is about 10 times higher than in silica [314]. An example of strain tuning of a PMMA POF is shown in Figure 2-52.

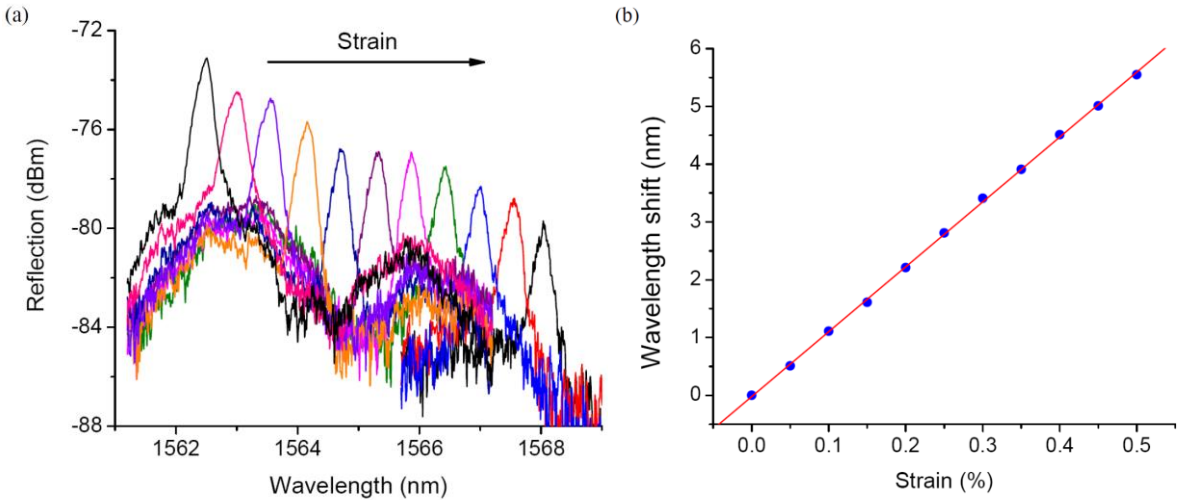

Figure 2-52. Strain tuning of a PMMA POFGB: (a) reflection spectra on FBG straining, (b) Bragg wavelength shift as a function of strain [315].

Table 2-4. Strain sensitivity values $\left(\frac{d\lambda_B}{\epsilon}\right)$ for FBGs in PMMA, PC and silica fibres calculated from experimental material parameters using Equations (2-58) and (2-59).

Parameter		PMMA	PC	Silica
p_{11}		0.300 [99]	0.252 [99]	0.126 [316]
p_{12}		0.297 [99]	0.321 [99]	0.274 [316]
ν		0.345 [317]	0.360 [317]	0.165 [102]
RI	*at 850 nm*	1.4859 [147]	1.576 [107]	1.4525 [318]
	at 1550 nm	1.4809 [147]	1.567 [107]	1.4440 [318]
P_e	*at 850 nm*	0.100	0.142	0.217
(Equation (2-59))	*at 1550 nm*	0.100	0.141	0.215
$\frac{d\lambda_B}{\epsilon}$ (pm/με)	*at 850 nm*	0.76	0.73	0.66
(Equation (2-58))	*at 1550 nm*	1.40	1.33	1.21

Table 2-5. Experimental values of strain and temperature sensitivity of SOFBGs (silica fibre with germanium-doped core) [58].

Wavelength (nm)	Strain sensitivity (pm/με)	Temperature sensitivity (pm/°C)
830	~0.64	~6.8
1300	~1	~10
1550	~1.2	~13

Table 2-6. Comparison of strain, temperature and humidity sensitivity of various POFBG sensors (both microstructured and SI)

Material, wavelengths	Strain sensitivity (pm/με)[a]	Temperature sensitivity (pm/°C)[a]	Humidity sensitivity (pm/%RH)
PMMA[b]			
at ~850 nm	0.54-0.77 [73, 319-321] up to 0.944[c] [73]	–	35.2-35.5±2.6[d] [77] 46 [122]
at >900 nm and <1500 nm	–	-4.3 at 60 %RH, ~950 nm [322] -7.6 at 60 %RH, ~1300 nm [322]	–
at ~1550 nm	1.13-1.46 [315, 319, 323, 324]	-8.3 at 60 %RH [322] -55±3 at 50 %RH [325]	35.2±0.4 at 25 °C [325]
Polycarbonate (PC)			
at ~850 nm	0.701 ± 0.003 [107]	-25.62±0.56 at 50 %RH, -25.86±0.63 at 90 %RH [105] -29.9±0.2 [107]	7.19±0.11 at 50 °C, 7.35±0.05 at 25 °C [105]
Topas 8007S-04			
at ~850 nm	0.64±0.04 [114]	-78±1 [114]	(0.26±0.12 at 25 °C)[e] [114]
at ~1550 nm	–	-36.5±0.3 at 55 %RH [326]	(-0.59±0.02 at 25 °C)[e] [114]
Topas 5013S-04			
at ~850 nm	0.76 at 50 °C, 0.80 at 100 °C [116]	~-14 [116] -17.4±0.1[f] at 50 %RH [117]	0.45±0.22[f] at 25 °C [117]
Cytop			
at <1500 nm	from 0.482±0.002 (at 517 nm) to 0.812±0.004 (at 883 nm) [327] 0.652 at 895 nm, 0.856 at 1043 nm, 0.1095 at 1249 nm [328]	–	–
at ~1550 nm	1.432 [328] 1.44 [329] 1.50-1.58±0.10 [330]	-17.62 at 23 %RH [329] -27.5±2.4 at 50 %RH [330]	10.3±1.8 at 36 °C [330] 14.7 at 30 °C [329]
Zeonex 480R			
at ~850 nm	0.77 [122]	-24.0±0.1 at 50 %RH [122]	0.75±0.42 at 50 °C [122]

[a] measurement in ambient conditions, unless mentioned otherwise
[b] due to very high sensitivity of PMMA POFBGs to humidity, only temperature sensitivity values in humidity-controlled conditions are reported
[c] with thermal and chemical treatment
[d] linear fit of non-linear response over 10-90 %RH and at 25, 50, and 75 °C
[e] limited precision due to accuracy of the climate chamber used
[f] Topas 5013S-04 core, Zeonex 480R cladding

Temperature

Temperature sensitivity of an FBG can be expressed, using Equation (2-57), as:

$$\frac{\Delta\lambda_B}{\Delta T} = \lambda_B\left(\frac{1}{\Lambda}\frac{d\Lambda}{dT} + \frac{1}{n_{eff}}\frac{dn_{eff}}{dT}\right), \tag{2-60}$$

where $\frac{1}{\Lambda}\frac{d\Lambda}{dT}$ is the linear coefficient of thermal expansion (LCTE, α; see Equation (2-8)), and $\frac{dn_{eff}}{dT}$ is the thermo-optic coefficient (TOC; see Equations (2-11) and (2-14)), while the term $\frac{1}{n_{eff}}\frac{dn_{eff}}{dT}$ is the normalised TOC (ξ). It must be noted that sometimes in the literature the latter expression is referred to as TOC and not normalised TOC, but this is not the case in this thesis. Noting LTCE and normalised TOC as α and ξ, respectively, Equation (2-60) can be rewritten as:

$$\frac{\Delta\lambda_B}{\Delta T} = \lambda_B(\alpha + \xi). \tag{2-61}$$

As it was explained in Section 2.2.4, different mechanisms dominate the value of TOC (and, hence, normalised TOC) in silica and polymers. In the latter, it is the contribution from thermal expansion (LCTE, α), while in the former – from thermal dependence of polarisability (ϕ). The values of theoretically calculated normalised TOC (Equation (2-14)) and temperature sensitivity resulting from them (Equation (2-61)) at different wavelengths of light are collated in Table 2-7. The experimental sensitivity values for silica and polymer FBGs are presented in
Table 2-5 and Table 2-6, respectively. It can be observed that, in the case of SOFBGs, both normalised TOC and LCTE are positive (with the former being of much higher magnitude), yielding positive temperature sensitivity. Its theoretical value is close to the experimental one, the latter being slightly larger. It can also be observed that neglecting the correction factor Λ_0 in Equation (2-14) yields theoretical values of temperature sensitivity that are closer to those observed experimentally.

The theoretical results for POFBG are much more ambiguous though. To discuss them, it is useful to rewrite Equations (2-60) and (2-61) so that they reflect anisotropy of CTE and TOC, which is very high in POFs:

$$\frac{\Delta\lambda_B}{\Delta T} = \lambda_B\left(\frac{1}{\Lambda_\parallel}\frac{d\Lambda_\parallel}{dT} + \frac{1}{n_\perp}\frac{dn_\perp}{dT}\right) = \lambda_B(\alpha_\parallel + \xi_\perp). \tag{2-62}$$

Since the light propagates along the fibre axis, it is the value of LCTE parallel to the fibre axis that is of importance in the above equation ($LCTE_\parallel$, $\alpha_{/\!/}$). Regarding the TOC, first, the light is almost exclusively polarised perpendicularly to the fibre axis. COMSOL simulations confirmed that electric field parallel to the fibre axis amounts only to 3.3% at maximum, the remainder being perpendicular to it. Secondly, it is expected that the TOC for all directions perpendicular to fibre axis is equal since the fibre does not display longitudinal birefringence. Hence, it can be safely assumed that the Bragg peak position depends on $TOC_\perp$ only, which is reflected in Equation (2-62).

Comparing the values of α and those of ξ calculated theoretically for polymers (Table 2-7), it can be noted that they are almost equal in magnitude but opposite in sign. Temperature sensitivities resulting from them (Equation (2-61)) can then be both positive and negative. When calculating temperature sensitivity from experimental values of both α and ξ, sensitivities of bigger magnitude are obtained, but for PMMA, they can also be either positive of negative. However, experimentally measured temperature sensitivity is clearly negative for all types of polymers and at all wavelengths (Table 2-6). It then follows from Equation (2-62) that a negative normalised $TOC_{\perp}$ dominates over a positive $LCTE_{\parallel}$. As it was discussed in Section 2.3.3, thermal expansivity of POFs along the drawing direction ($LCTE_{\parallel}$ in this case) is likely to be smaller than in bulk due to high molecular anisotropy of fibre. Nonetheless, it also results in a decrease in $TOC_{\perp}$, as discussed in Section 2.3.7. Negative temperature sensitivities of all POFBGs suggest that molecular anisotropy of POFs triggers smaller decrease in $LCTE_{\parallel}$ than in $TOC_{\perp}$. Exact calculations will be presented in Chapter 5 for the fibre whose manufacture is reported in this thesis.

It is also worth noting that, initially, there was some disagreement on the exact value of temperature sensitivity of PMMA in the literature. For example, the same authors reported two values of sensitivity at ~1550 nm as different as -360 pm/°C [331] and -149 pm/°C [332]. These discrepancies can be most probably explained by the fact that many reported measurements had been performed in ambient conditions before considerable influence of humidity on performance of PMMA POFBGs became evident [4, 333]. Under controlled humidity conditions, sensitivity values of PMMA POFBGs are reported to be smaller than the values cited above, oscillating at a range of minus tens of pm/°C. The effect of cross-sensitivity to humidity is most pronounced in PMMA (which is discussed below). For this reason, only temperature sensitivities measured at constant humidity are given in Table 2-6.

To account for cross-sensitivity of PMMA to water, Harbach [333] proposed changes to Equation (2-61). They consisted in assuming that, at constant relative humidity, LCTE (α) and TOC (ξ) are a function of temperature T and normalised water content w_n:

$$\alpha = \alpha_0 + \alpha_1 T + \alpha_2 w_n + \alpha_3 w_n T, \tag{2-63}$$

$$\xi = \xi_0 + \xi_1 T + \xi_2 w_n + \xi_3 w_n T, \tag{2-64}$$

where w_n is defined as

$$w_n = \frac{w}{w_{max}} = H^m. \tag{2-65}$$

In the above equation, w is the water content in polymer, w_{max} – maximal water content, H – relative humidity (%RH), and m – exponential factor resulting from data fitting ($m \approx 1.49$).

Table 2-7. Temperature sensitivities for FBGs made of PMMA, PC and silica calculated for 850 nm and 1550 nm using bulk experimental values of LCTE (α), RI, and TOC (ξ) as well as TOC values calculated theoretically.

Parameter		PMMA	PC	Silica
α ($\times 10^{-6}$ °C^{-1}) *experimental, bulk*		60-110 [71, 99, 141-143]	50-81 [71, 99, 141, 142, 144-146]	0.55 [139]
RI	*at 850 nm*	1.4859 [147]	1.576 [107]	1.4525 [318]
	at 1550 nm	1.4809 [147]	1.567 [107]	1.4440 [318]
ξ ($\times 10^{-6}$ °C^{-1}) *theoretical (Equation (2-14))*				
	at 850 nm	from -61 to -110	from -49 to -83	5.5 (6.6)[a]
	at 1550 nm	from -61 to -109	from -49 to -82	5.4 (6.5)[a]
$\frac{\Delta\lambda_B}{\Delta T}$ (pm/°C) *calculated from theoretical ξ (Equation (2-61))*				
	at 850 nm	from -1.2 to -0.27	from +0.52 to -2.1	5.1 (6.0)[a]
	at 1550 nm	from -1.4 to +1.0	from +2.2 to -1.8	9.2 (11)[a]
ξ ($\times 10^{-6}$ °C^{-1}) *experimental, bulk*				
	at 850 nm	from -71 to -95	from -57 to -109	~8.2
	at 1550 nm	from -71 to -95	from -57 to -110	~8.2
		[71, 99, 141, 144, 155, 334-338]	[71, 99, 141, 142, 144, 335-337, 339]	[254]
$\frac{\Delta\lambda_B}{\Delta T}$ (pm/°C) *calculated from experimental ξ (Equation (2-61))*				
	at 850 nm	from -9.1 to +13	from -6.0 to -24	7.4
	at 1550 nm	from -17 to +23	from -12 to -45	13.6

[a] values obtained using the data from [139] neglecting the correction factor Λ_0 in Equation (2-14)

Water

Affinity for water is a property distinguishing POFs from silica fibres. The latter are water-insensitive, although minimal response to a humidity change was reported for an SOFBG coming from its polymer coating [325]. Water absorption for all reported POFs is the highest for those made of PMMA. It amounts up to 2.1% [340, 341] for PMMA, compared to 0.3% for PC [342] and ~0.01% for Zeonex

[121] and Topas [113, 115]. POF swells when absorbing water, which results in an increase in the Bragg wavelength, which can be described using Equation (2-57) as:

$$\frac{\Delta\lambda_B}{\Delta H} = \lambda_B \left(\frac{1}{\Lambda}\frac{d\Lambda}{dH} + \frac{1}{n_{eff}}\frac{dn_{eff}}{dH} \right), \tag{2-66}$$

where H is the relative humidity (%RH), the term $\frac{1}{\Lambda}\frac{d\Lambda}{dH}$ is the swelling coefficient, and the term $\frac{1}{n_{eff}}\frac{dn_{eff}}{dH}$ – the normalised dependence of refractive index on humidity ($\%RH^{-1}$). Noting the last two terms as γ and η, respectively, the above equation can be simplified to:

$$\frac{\Delta\lambda_B}{\Delta H} = \lambda_B(\gamma + \eta) \tag{2-67}$$

Sensitivity of POFBGs to humidity can be considered linear for POFBGs made of PC, whereas gratings inscribed in fibres made of Zeonex or Topas are virtually humidity-insensitive (Table 2-6). However, in the case of PMMA, neither of the parameters γ or η is strictly constant. The latter is approximately linear but displays a decrease on increasing temperature. The parameter γ, in turns, shows linear behaviour for relative humidity from 40 to 100 %RH (Figure 2-53(a)), while it decreases < 40 %RH [4, 343, 344].

Another formalism for description of humidity sensitivity of POFBG at constant temperature was proposed by Harbach [333]. Namely, Bragg peak change of a grating was found to be linear with normalised water content w_n (Equation (2-65)). The grating used was made of PMMA and polystyrene copolymer, with the former being the dominating material. In this case, Bragg wavelength shift can be written as:

$$\Delta\lambda_B = \lambda_B(\gamma + \eta)\Delta w_n = \lambda_B(\gamma + \eta)(H_2^m - H_1^m), \tag{2-68}$$

where H_1, H_2 are the initial and final relative humidity values, respectively.

Figure 2-53(a) shows a representative linear humidity dependence of a PMMA POFBG above 40 %RH. Typical response time to water (Figure 2-53(b)) is a few tens of minutes, which may be too much for some applications. Water uptake into fibre core was shown to be facilitated by fibre etching. Decreased response time of 12 min has been achieved upon thinning a PMMA fibre from 190 to 135 µm in acetone [345]. Etching fibre diameter down to 25 µm in 1:1 mixture of acetone and methanol has resulted in a response time of less than 5 seconds in a POF made of PMMA [346].

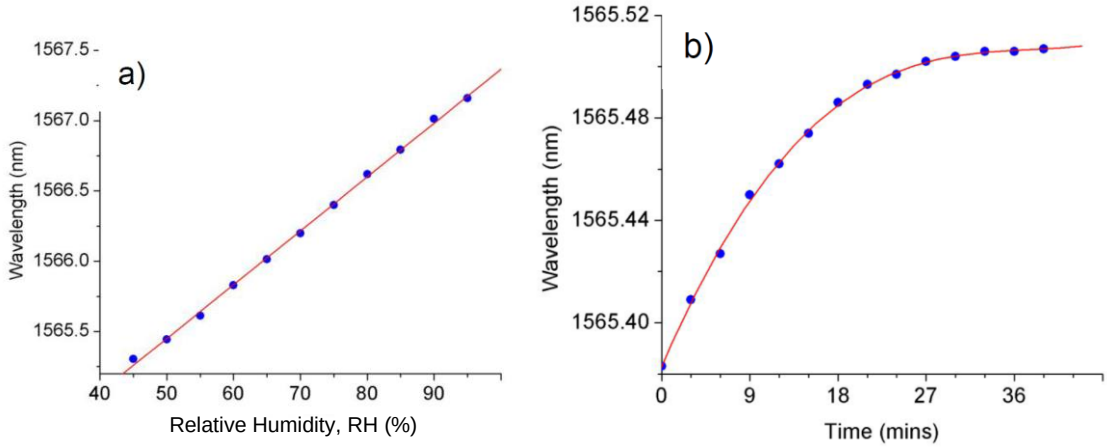

Figure 2-53. (a) Bragg wavelength vs. relative humidity at 22 °C, (b) time response for a saltatory humidity change [4].

Fibre annealing, discussed in Section 2.7.3 for Bragg peak tuning, was also reported to be beneficial in terms of stabilising humidity response of a PMMA mPOF [77]. Annealing the POFBG at a high humidity (90 %RH) and temperature (80 °C) rendered the humidity response free from hysteresis and the value of humidity sensitivity temperature-insensitive, totalling to ~35.2 pm/%RH.

Measurand cross-sensitivity

As it has already been mentioned, FBGs are in general cross-sensitive to various measurands, which may be seen as one of their most apparent drawbacks. Sensitivity to different measurands calculated according to Equation (2-57) is considered to be linearly additive [4, 333]. Hence, a combined effect of temperature and strain on the Bragg wavelength of an FBG can be described combining Equations (2-58) and (2-61):

$$\frac{\Delta\lambda_B}{\lambda_B} = (1 - P_e)\epsilon + (\alpha + \xi)\Delta T. \tag{2-69}$$

Similarly, if humidity sensitivity is significant, the term given by Equation (2-67) or (2-68) can be added accordingly. Non-linear response to any measurand can be accounted for by rendering parameters in any of the above equations non-linear, as it was done for PMMA POFBG (Equations (2-63) and (2-64)), in which case this was found to be particularly important.

The combination of Equations (2-61), (2-63), (2-64) and (2-68) can be used to explain the aforementioned high temperature sensitivity of POFBGs in ambient conditions on the example of a grating inscribed in a fibre made of PMMA and polystyrene copolymer, the former being the dominant material [333]. In fact, when relative humidity is not controlled, its value falls with increasing temperature. As a result, the POFBG actually measures combined effect of a temperature rise and a relative humidity decrease. Both effects result in a blueshift of the Bragg peak, which explains the high negative sensitivity of the grating. The Bragg peak response of the POFBG was accurately fitted in [333]

assuming that humidity variations with temperature follow the Goff-Gracht formula for saturation pressure of water vapour at different temperatures [347]. Grating sensitivity in this case was slightly non-linear, with the linear fit of the slope yielding -138 pm/°C. This was contrasted with temperature sensitivities in humidity-controlled environment: -10 pm/°C in dry conditions (RH ≈ 1.5 %RH) and -36 pm/°C in water (all values for the 1550 nm region).

2.8 Summary

This chapter introduced background required for the experimental work presented in the following part of the thesis. This information includes:

- conventional optical fibres (Section 2.1)
- material properties of optical fibres (Section 2.2)
- anisotropic properties of optical fibres (Section 2.3)
- photonic crystals (Section 2.4)
- microstructured fibres (Section 2.5)
- fabrication of polymer optical fibres (Section 2.6)
- fibre Bragg gratings (Section 2.7).

The information presented in Section 2.1 constitutes the background of all the other sections of this chapter and the other chapters in this thesis.

Sections 2.2 and 2.3 are referred to in Chapter 5, which presents the results of fibre drawing and discusses the characteristics of the resulting fibre.

Section 2.4 contains background information for Sections 2.5 and 2.7.

The content introduced in Section 2.5 allows appreciating the unique characteristics of the microstructured fibres. They are present in all the remaining chapters of this thesis. In Chapter 3, mPOF manufacture set-up is introduced and FBG inscription procedures are discussed. Chapter 4 features preform fabrication for microstructured optical fibres, and Chapter 5, the results of preform drawing. Finally, mPOF embedding is the core part of Chapter 6.

Section 2.6 allows comparing various POF fabrication techniques, underlining their particular capabilities and limitations. This allows them to be contrasted with fused deposition modelling to appreciate its unique qualities. Moreover, this section conveys the background information for Section 3.2.

Finally, Section 2.7 provides theoretical background of the FBGs, which is referred to in Chapter 5 and, most extensively, in Chapter 6.

Chapter 3 Experimental set-ups

This chapter presents the experimental set-ups and techniques used in this thesis. These entail FDM 3D printing, POF fabrication using a draw tower, and FBG inscription. The experimental set-ups for the strain tests and the temperature and humidity trails are described in the respective sections of Chapter 6 and not in this chapter. This is because they were upgraded during the research on fibre embedding, their evolution being driven by the experimental results. It was then found more logical to introduce these set-ups and describe their evolution together with the discussion of the strain, temperature and humidity results.

3.1 3D printing

All the 3D printouts presented in this thesis were fabricated using the UP! 3D printer (model 3DP-14-4A). It was an FDM printer designed to work with 1.75-mm-diameter filaments, and its maximal nozzle temperature was 300 °C. It featured a heated print bed, and its print volume was 140 × 140 × 135 mm (width × depth × height). The printer worked under the control of its proprietary slicer. This is a type of software that converts a 3D model to be printed into a set of G-code commands. They provide a step-by-step description how the printer parameters should be varied for the desired model to be 3D printed. The G-code commands include, e.g., direction and speed of movement of the nozzle and the printing bed, nozzle temperature, extrusion speed, speed of the cooling fan etc. Moreover, the FixUp3D extension was added to the slicer to extend its capabilities. Most of the 3D models were prepared by the author using SketchUp Make 2015-2017.

The UP! 3D printer was used to produce a wide variety of different designs. For example, various types of customised moulds for fibre embedding were fabricated, both large (Figure 3-1 and Figure 3-2) and small (Figure 3-3). The former structures printed of Nylon 12 were used in the research presented during the POF2016 conference [303].

3D printing was also combined with surface smoothing technique to provide better surface finish. After printing, the small embedding moulds (Figure 3-3) featured rather rough outer surfaces due to their small dimensions and limited resolution of the 3D printer. So that the smoothing technique could be applied, the moulds were printed from dissolvable plastics: ABS and HIPS (high impact polystyrene). The former was soluble in acetone, while the latter, in water. Droplets of solvents were deposited on the inner walls of each mould, yielding optically smooth surfaces after evaporation. The combination of HIPS and water was found more effective due to a longer solvent evaporation time and, hence, higher quality of the processed surfaces.

Furthermore, large (Figure 3-4) and small (Figure 3-5) specialised fibre holders were designed and printed to be used in photoacoustic experiments (ultrasound sensing). This research was published at the following conferences: SPIE Photonics Europe 2016 [75], SPIE BiOS Photon Plus Ultrasound: Imaging and Sensing 2016 [311], and SPIE Photonics Europe 2018 [120].The fibre holders were accompanied by the complementary lids, which were used to hold the POF firmly in place after being secured to the holders with screws. The holders also featured screw openings to facilitate mounting.

Other designs printed during the research described in this thesis entailed, e.g., fibre preforms and housing structures for fibre embedding. They are introduced in the chapters presenting each research topic (respectively, Chapter 5 and Chapter 6).

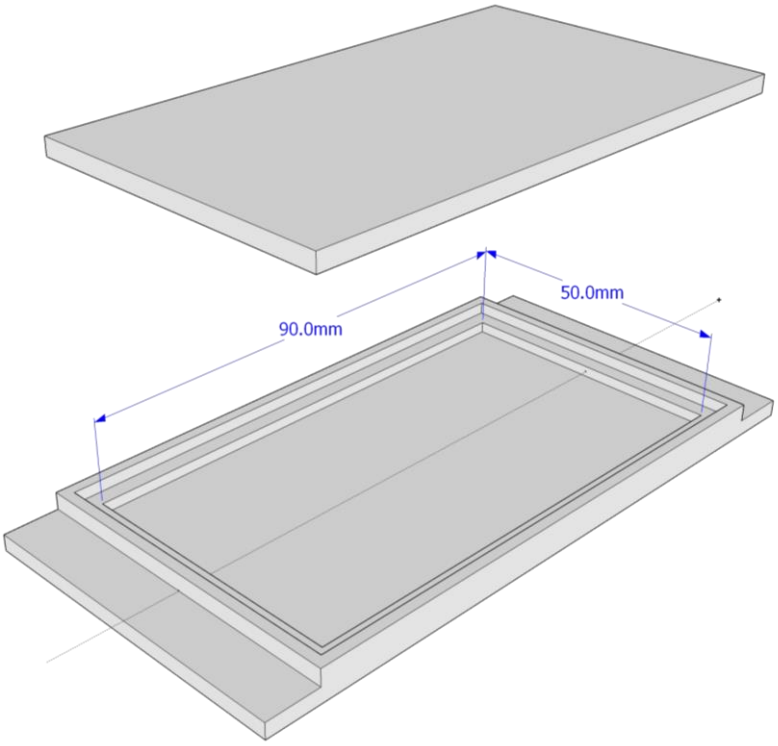

Figure 3-1. Example of a large rectangular mould used for fibre embedding (bottom) with a complementary lid (top). The dotted line marks the fibre position.

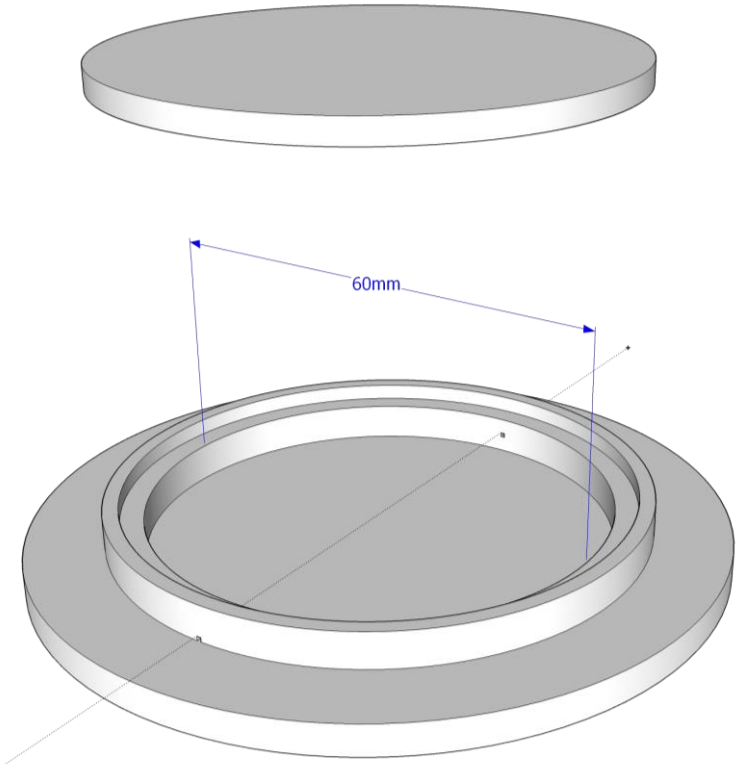

Figure 3-2. Example of a large circular mould used for fibre embedding (bottom) with a complementary lid (top). The dotted line marks the fibre position.

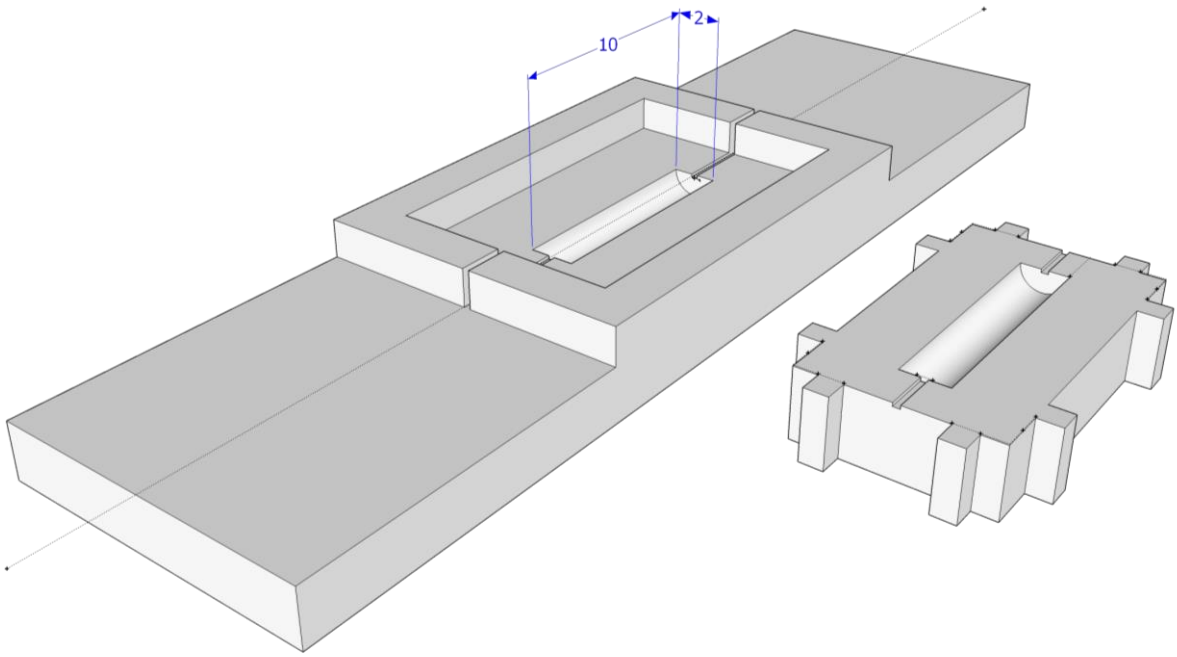

Figure 3-3. Example of a small mould used for fibre embedding (left) with a complementary lid (right). The dotted line marks the fibre position. The dimensions are in millimetres.

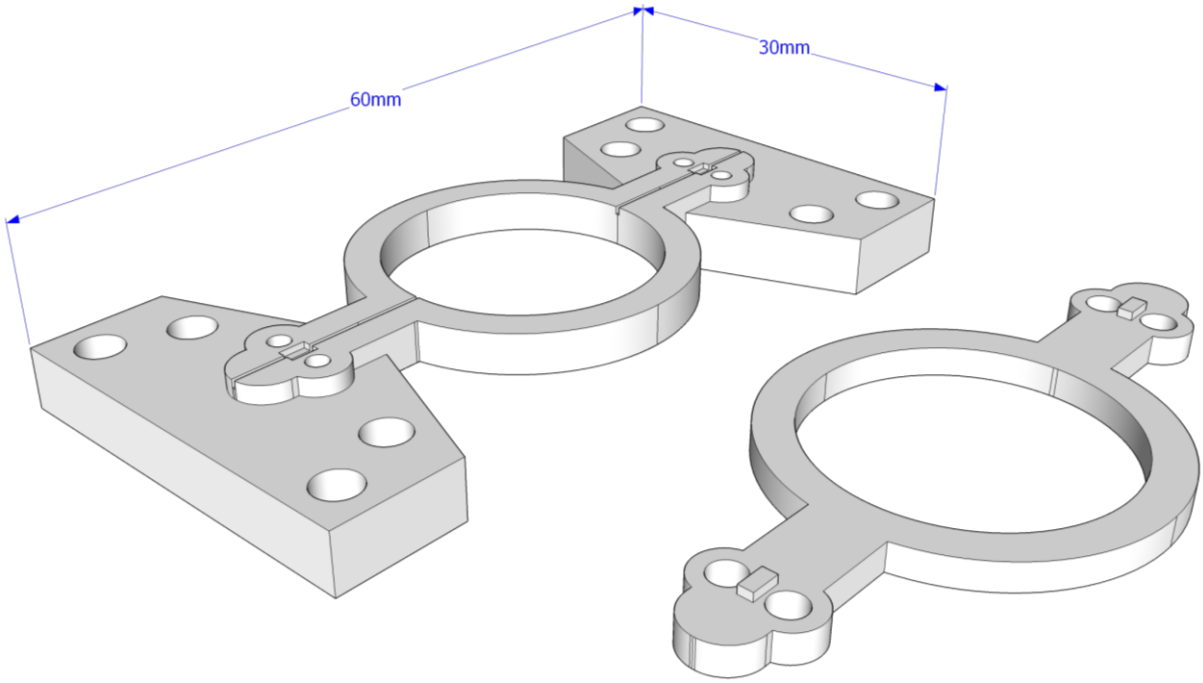

Figure 3-4. Example of a large fibre holder used in photoacoustic experiment (left) with a complementary lid (right). The screw openings were used for mounting the lid to the holder and the holder to its base.

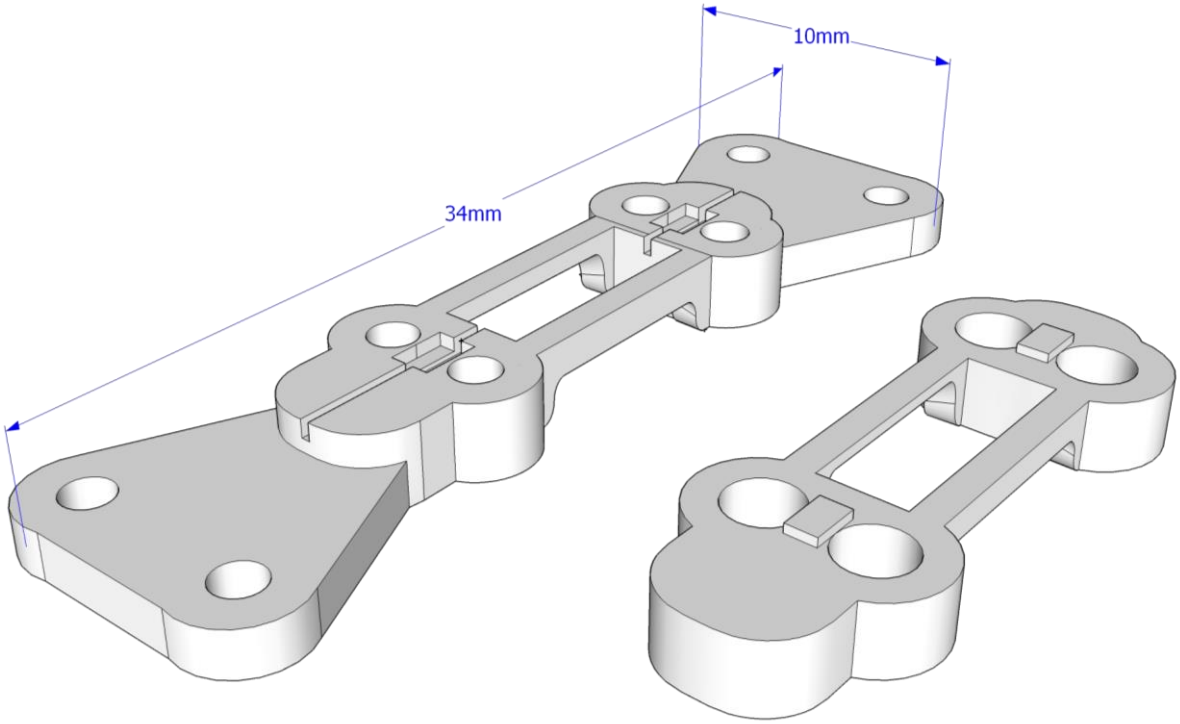

Figure 3-5. Example of a small fibre holder used in photoacoustic experiment (left) with a complementary lid (right). The screw openings were used for mounting the lid to the holder and the holder to its base.

3.2 POF fabrication

Microstructured polymer optical fibres presented in the course of this thesis were manufactured using the preform method (see Section 2.6). The preforms were fabricated by the author, which is detailed in Chapter 4. Some of them were subsequently machined, which allowed removing the relatively rough outer surface resulting from 3D printing. Machining was performed at a specialised mechanical workshop at Technical University of Denmark (DTU). Some preforms were also annealed in a conventional oven by Andrea Fasano (supervisor: Henrik K. Rasmussen) at Department of Mechanical Engineering, DTU. The purpose of this was twofold. First of all, it helped removing moisture from the preforms, which were made of water-absorbing materials (PMMA and PC). This was important as high water content in preforms during drawing is known to result in bubble formation within the fibre [231]. The bubbles act as centres of light scattering, greatly increasing fibre attenuation. In some cases, non-annealed preforms were found not to be drawable at all [231]. Second of all, the fibre preforms reported in this thesis were all fabricated by means of the FDM process, which produces objects containing multiple air voids in their bulk. Annealing was then used to help increasing transparency of the preforms by removing the air void, similarly to what was reported in the literature [30, 31]. Details of processes performed on each preform are described in their respective sections in Chapter 4.

In the next step, the preforms were drawn to canes by Getinet Woyessa (supervisor: Ole Bang) at Department of Photonics Engineering, DTU. The most successful cane, made of PC, was sleeved in a PC tube to form a secondary perform and, then, drawn to fibre, following the two-step drawing process (see Section 2.6). All of this was also performed by Getinet. The canes and fibre were fabricated using the POF draw tower at Department of Photonics Engineering, DTU (Figure 3-6), whose functioning follows the steps described in Section 2.6 (see also Figure 2-39). Summary of the fibre manufacturing process used in this thesis is shown in Figure 3-7.

The maximal preform diameter which could be fed to the draw tower furnace was 60 mm, so the preforms were designed to match this requirement after machining. The standard approach to fabricate preforms at DTU was drilling, which – relative to other preform manufacturing techniques described in Section 2.6 – normally results in preforms of high diameter. The possibility of feeding relatively big preforms was favourable from the viewpoint of the UP! 3D printer used to fabricate them. This was because fibre design could be reproduced more accurately than it would have been in small-diameter preforms. The bigger the preform, the higher the amount of detail that can be represented. Printing resolution of the UP! 3D printer could be found too low for small-diameter preforms, which could then limit its usability. Using the large-diameter DTU draw tower ensured that this was not the case.

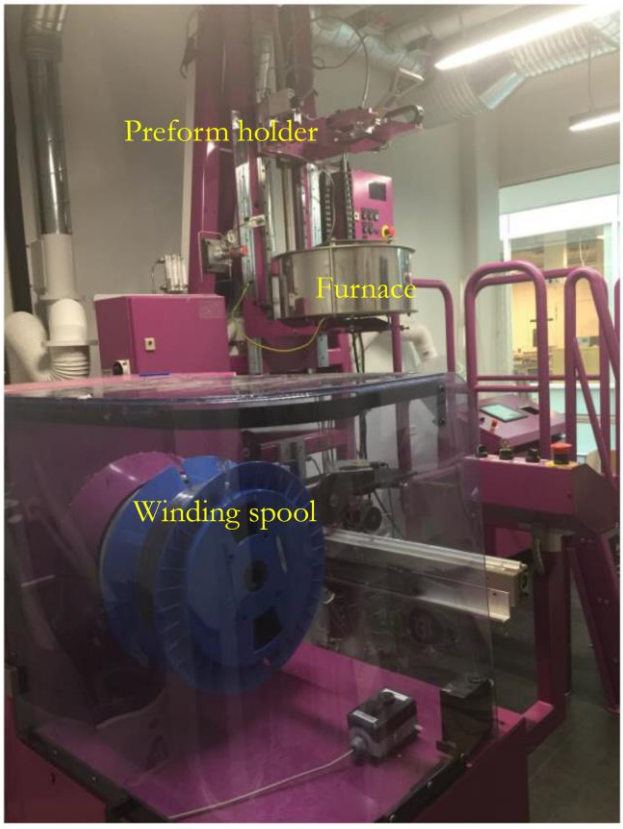

Figure 3-6. Photograph of the POF draw tower used to fabricate the canes and fibre presented in this thesis, Department of Photonics Engineering, Technical University of Denmark. Reproduced with permission from [231], ©Getinet Taffesse Woyessa and DTU Fotonik, 2017.

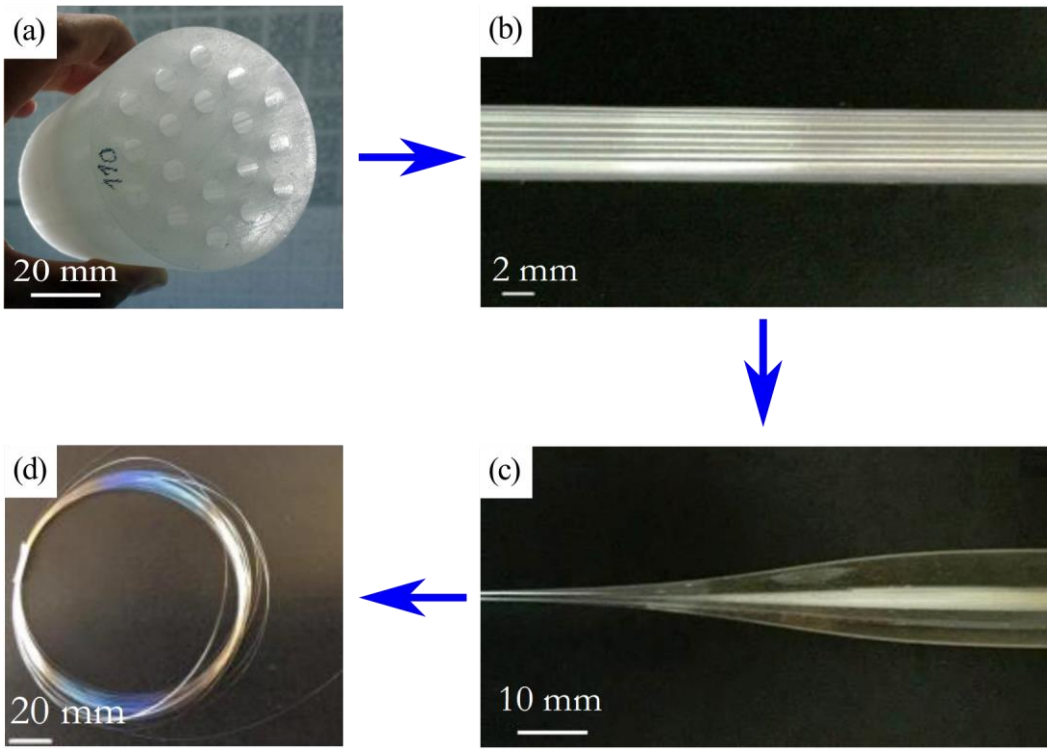

Figure 3-7. Photographs showing consecutive steps of the fibre manufacturing process followed in this thesis: (a) 3D-printed mPOF preform, (b) microstructured cane, (c) cane sleeved with a tube to form the secondary preform, (d) final fibre. Photographs (b), (c), and (d) adapted with permission from [231], ©Getinet Taffesse Woyessa and DTU Fotonik, 2017.

3.3 FBG fabrication

This section introduced FBG inscription set-ups, fabrication procedures, and fibres that were used in this thesis to fabricate both silica and polymer Brag gratings.

3.3.1 Introduction

In this thesis, FBGs were inscribed in two spectral ranges: around 850 nm and around 1550 nm. Much lower attenuation is displayed at 850 nm than around 1300 or 1550 nm by almost all POFs, including those utilised in this section to fabricate gratings in. Perfluorinated fibres like Cytop are a notable exception, see Section 2.2.3. The 1550-nm range, in turn, is the spectral range of choice for SOFBGs due to the lowest material attenuation at that wavelength. For this reason, it has long been established as the major telecommunication spectral range, which facilitates technology transfer by integration with existing fibre-optic systems. Hence, SOFBGs reported in this thesis had all been inscribed in the 1550-nm spectral region. In turns, almost all POFBGs used during this research had been fabricated at

~850 nm. The only exception were POFBGs in Cytop, inscribed by a femtosecond laser at Cyprus University of Technology.

A vast majority of the FBGs used in the course of this research was produced by the author using the phase-mask technique (see Section 2.7.3) and a HeCd laser. The same method combined with a KrF laser was applied by a group of collaborators to inscribe a Bragg grating (Section 5.3.3) in the polymer fibre whose manufacture is reported in this thesis (Chapter 5). Yet another POFBG (Section 5.3.2) was fabricated in this fibre by other collaborators employing the plane-by-plane femtosecond-laser inscription technique (see Section 2.7.3).

The choice of the phase-mask method, predominantly used in this thesis, was dictated by its relative simplicity compared to the other inscription methods (see Section 2.7.3) and accessibility of the appropriate equipment: the available phase masks (PMs) had been matched to the ranges of the broad band sources and the RIs of the fibres to be used as well as to the wavelength of the inscription laser. The latter was a 30-mW 325-nm continuous-wave HeCd laser (Kimmon IK3301R-G) producing a light beam of the Gaussian profile and 1.2-mm diameter before focusing for inscription, which is discussed later. Grating periods of the employed phase masks were 1034.2 and 1061.18 nm for FBGs at around 1550 nm, while for FBGs in the 850-nm range, these were 557.5 and 580 nm.

Two set-ups were used in this thesis to inscribe silica and polymer FBGs. In the first one, hereinafter referred to as horizontal (Figure 3-8(a)), the laser beam reflected from the mirror was hitting a fibre through a PM was oriented horizontally. The other set-up, hereinafter referred to as vertical, relied on laser beam vertically hitting a fibre through a PM, after being reflected from Mirror 4 (Figure 3-9). While, in principle, both systems could be used to inscribe silica and polymer fibre gratings, the latter were only inscribed in the vertical set-up. It allowed easier mounting of POFs, which are much more flexible than silica fibres and, hence, more difficult to handle in air, which would have been required in the horizontal system. The latter, in turn, was equipped with robust clamps especially well-suited for straining silica fibre. Moreover, a paper screen was placed so that the diffracted light beam could be observed on it after passing through the fibre (see Figure 3-8(a)), which facilitated adjustment of the set-up.

During inscription and usage, FBGs were normally interrogated in the reflection regime, i.e., observing the light reflected from grating. Light from a broadband source (BBS) was directed to an FBG through a 50:50 coupler (matched to the wavelength range of the light). The light reflected from the grating was passing again through the coupler and reaching an optical spectrum analyser (OSA), on which it was observed. The interrogation set-up in shown in Figure 3-8(b). In order to decrease loss, the coupler was sometimes substituted with a 1550-nm-range optical circulator, with a BBS being connected to port 1, FBG – port 2, and OSA – port 3. Two types of OSAs were used in this thesis (HP 86142A and HP 70951B), along with the following BBSs:

- Superlum SLD-371 centred at 830 nm (range: 795-865 nm)

- Thorlabs ASE-FL7002-C4 centred at 1560 nm (range: 1530-1610 nm).

FBG interrogation in reflection possesses several advantages over interrogation in transmission and is the usual approach in science and industry. In this work, of particular importance was that the reflection regime allowed observing very low intensity of reflected light, both during grating growth and usage. This allowed loosening requirements for grating strength and quality, which is significant in view of higher POF attenuation and less mature technology in general, including stability of fibre parameters and their connections. Moreover, observing FBGs in reflection facilitated automated tracking using specialised spectrometers or interrogators (see Chapter 6 for details). Their proprietary software allows benefiting from advanced peak tracking algorithms, which can be used also with low quality or multimode FBGs. Finally, the reflection regime used the same length of fibre for transmission of light to and from the grating. This enabled the FBG to be interrogated from one side only, which increased design flexibility and broadened the range of potential applications.

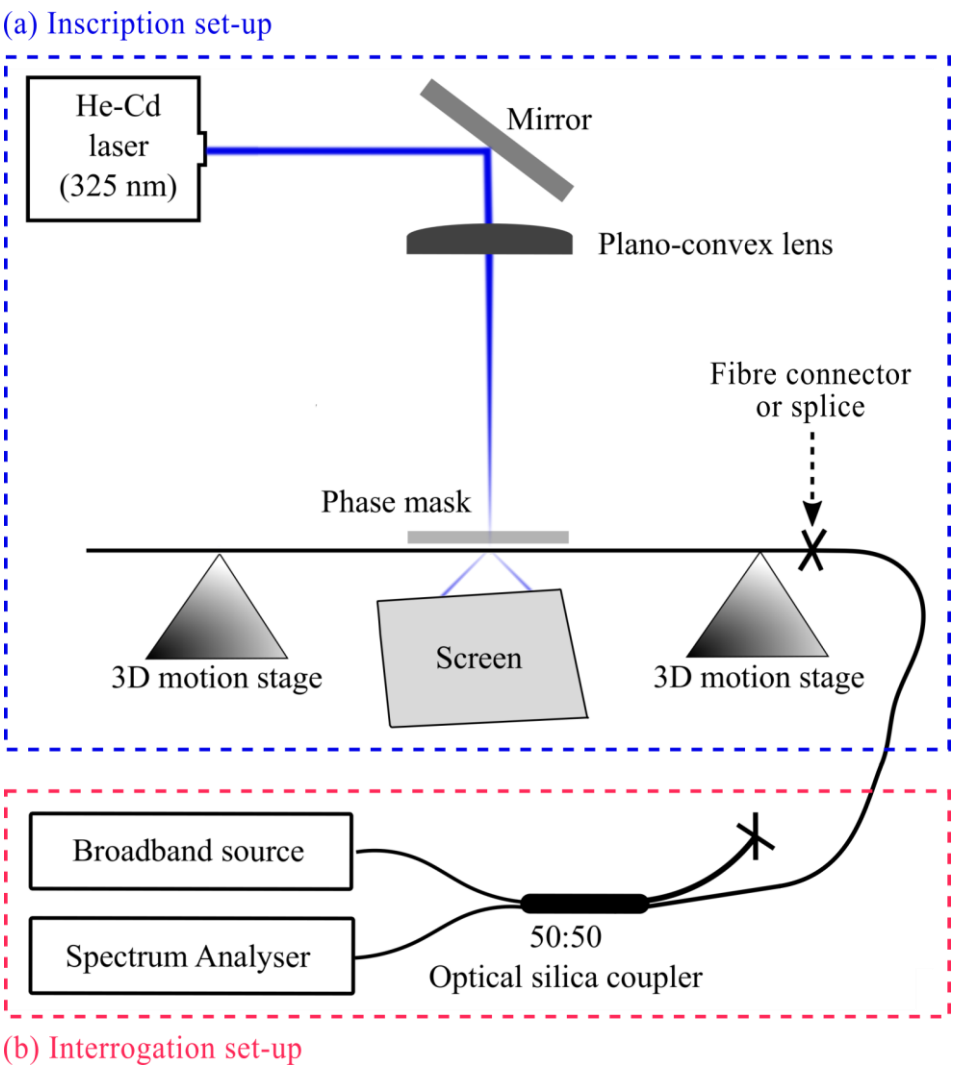

Figure 3-8. (a) Horizontal inscription set-up used in the thesis to fabricate SOFBGs. (b) Interrogation set-up employed during inscription, also with the vertical setup shown in Figure 3-9. Alternatively, the coupler was substituted with a 1550-nm-range optical circulator. Adapted from [256].

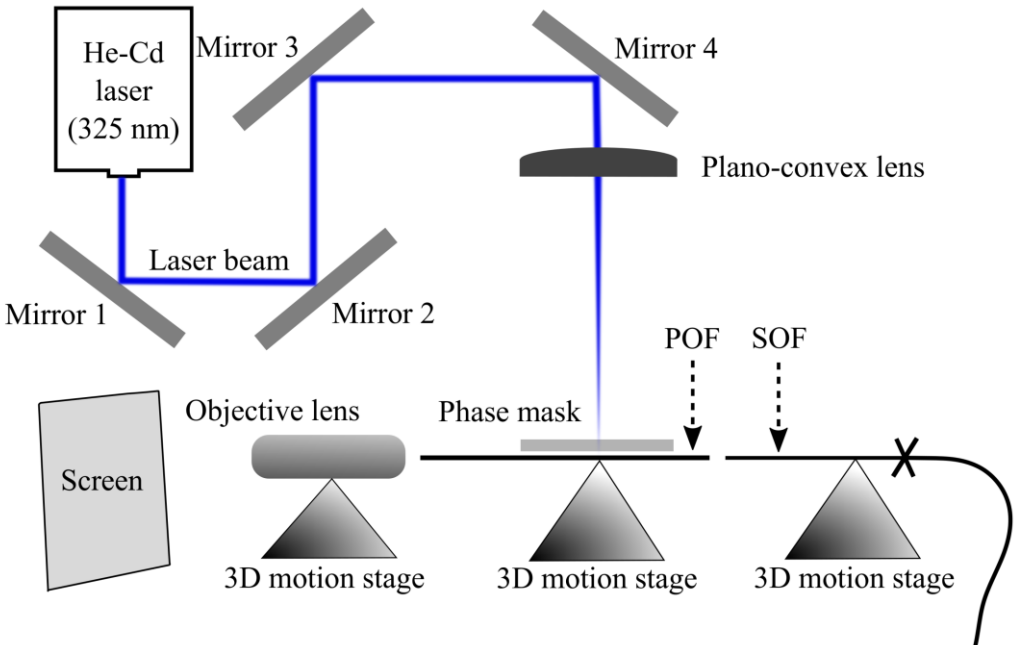

Figure 3-9. Vertical inscription set-up used in the thesis to fabricate both silica and polymer FBGs. Adapted from [256].

3.3.2 Inscription of silica FBGs

It should be noted that light at a wavelength of 325 nm is not ideal for inscription of SOFBGs as it is away from the range of maximal photosensitivity of silica (see Section 2.7.2). Grating inscription is still possible at this wavelength, but it requires more time. To accelerate inscription, photosensitive boron-doped fibres were employed (Fibercore PS980 and PS1250/1500), which are aimed to be applied without hydrogenation if the usual SOFBG inscription wavelength is employed. However, due to inscription at 325 nm, the hydrogen-loading step was not omitted.

SOFBG inscription procedure will be described based on the horizontal system, whereas the use of the vertical set-up will be introduced later when discussing fabrication of polymer FBGs. A hydrogenated silica fibre cannot be directly spliced to in order to monitor grating growth during inscription. Hence, it was either coupled to through a bare fibre adapter or spliced to after the fibre end was heated using a heat gun or flame and the hydrogen preventing splicing was released. In the next step, primary coating was selectively removed from the fibre over a length of a few centimetres, exposing the areas for FBG inscription. They should be ideally kept as small as possible since removing primary coating makes fibre fragile. Subsequently, the fibre was wiped with a tissue soaked in isopropyl alcohol (IPA) and mounted in fibre clamps. Following this, a PM was installed in a PM holder next to the fibre, after which it was ready for inscription. The laser shutter was opened, and laser light was focused onto the fibre through a plano-convex lens. Two lenses of different focal lengths were used: 10 cm and 2 cm, the latter giving smaller spot size in focus and, hence, higher power density. A lens was positioned so that it focused the light beam in the direction perpendicular to the fibre, while, in the

parallel direction, leaving the beam unaffected. This resulted in the beam profile becoming elliptical instead of circular, with the long axis (of the ellipsis) being adjusted so that it overlapped with the fibre core after appropriate adjustments. They were fed back by a pattern observed on the inspection screen, which the diffracted beam was hitting after passing through the PM and fibre. As a result, power density in the core increased, yielding quicker grating growth. The necessary adjustments often spoilt spectrum of the first FBG, which was then treated as a sacrificial. However, spectra of the next gratings were not affected as the adjustments were only performed once at the beginning of the inscription process. After the FBG had reached the desired characteristics, the laser shutter was closed, the fibre was unmounted and cut. The inscription process was then continued to fabricate further FBGs, starting from removing primary coating in the next piece of fibre as described above. Finally, ready gratings were annealed in a conventional oven at 80 °C for about 20 h to release all remaining hydrogen and allow being spliced to.

The basic inscription procedure described above could be modified to widen the range of fibre gratings to be fabricated. First, primary coating of the fibre could be left on instead of being removed, and FBGs were then inscribed through coating. This led to FBGs of increased mechanical robustness as the fragile glass surface was not exposed, which facilitated handling and future use. The primary coating did not distort grating spectrum, but it could possibly absorb some optical power. Hence, more care was taken with accurate adjustment of the set-up so that light was focused exactly in the core. The lens of 2-cm focal length was normally used, giving higher power density in focus.

Another possible variation to the basic grating fabrication procedure yields scanned gratings. The mirror in the horizontal system (Figure 3-8(a)) was mounted on a high-precision programmable translation stage, which allowed scanning the beam along the fibre during grating inscription. Length of scanned gratings was limited by length of the grooved area of the PM used, which was 10 mm for the 1034.2-nm PM and 20 mm for the 1061.18-nm one. Examples of spectra of a point and scanned SOFBGs inscribed through coating using the latter PM are shown in Figure 3-10. Their inscription times were 2 min 30 s and 19 min, respectively. For the scanned grating, scanning speed and length were 1 mm/s and 19 mm, respectively. This – considering a laser beam diameter of 1.2 mm – resulted in each part of the scanned grating (apart from the outermost ones) being illuminated over 1 min 20 s. Scanned FBGs display a clearly narrower reflection peak due to a larger number of grating layers (see Section 2.7.1), which could enhance peak tracking precision. FWHM of the point FBG was 0.27 mm, and of the scanned FBG, 0.10 mm (see inset in Figure 3-10), both measured on an OSA resolution of 0.06 nm, which is used throughout this section unless mentioned otherwise. The scanned grating is also visibly stronger than the point one, which is partly due to longer total inscription time. However, grating growth is not solely proportional to exposure time, so – even if the overall inscription times of both gratings were equal – comparison of their strengths would be complicated.

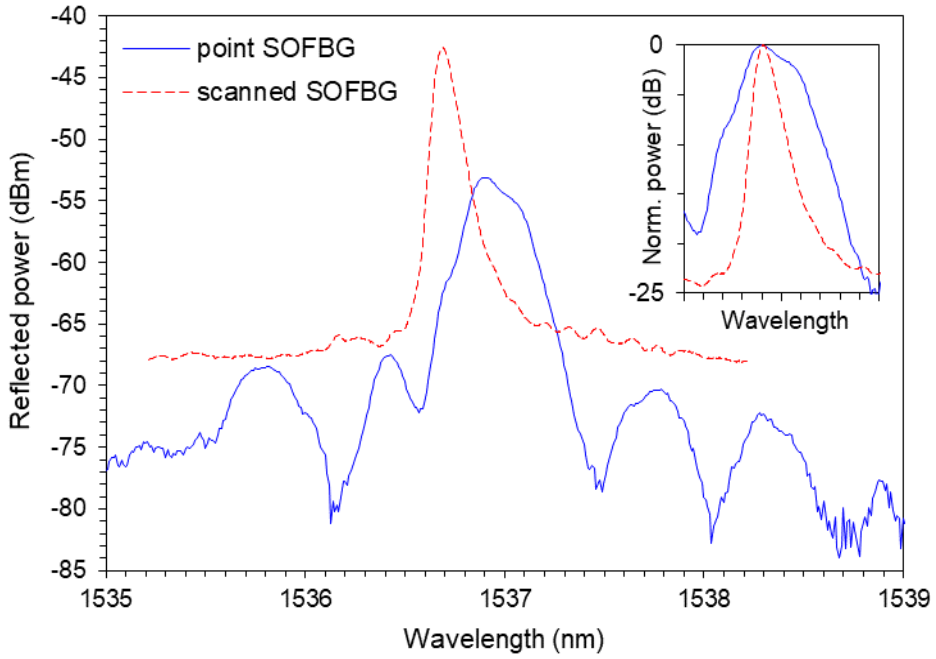

Figure 3-10. Examples of spectra of a point and scanned SOFBG. Inset shows both peaks normalised and shifted so that their maxima coincide, which allows comparing their bandwidths. (An OSA resolution of 0.06 nm is used throughout this section unless mentioned otherwise.)

Finally, fibre could be strained for inscription (see Section 2.7.3) after mounting in fibre clamps, which were secured with tape to prevent the fibre from slipping. This allowed wavelength multiplexing of FBGs inscribed through coating with the same PM at a distance of a few centimetres along the fibre. Thanks to straining for inscription, keeping fibre primary coating intact all along the fibre was possible, which was the requirement for use. Meeting it would have not been possible if FBGs had been inscribed in two separate pieces of fibre and spliced together. The spectrum of the second grating to be inscribed in the fibre was normally of visibly lower quality than of the first one, regardless of which one was inscribed with straining. Figure 3-11 shows steps of dual SOFBG inscription involving straining, taken at an OSA resolution of 0.06 nm/at the 0.06-nm OSA resolution. The spectrum of the lower-wavelength FBG looked imperfect, yet it was of good enough quality and strength to be useful. Spectral imperfections would normally be covered in practical applications: either by observing the reflection spectrum in linear scale, which is often done during FBG tracking (see Chapter 6) or by measuring the spectra at a lower resolution (e.g., often 0.5 nm).

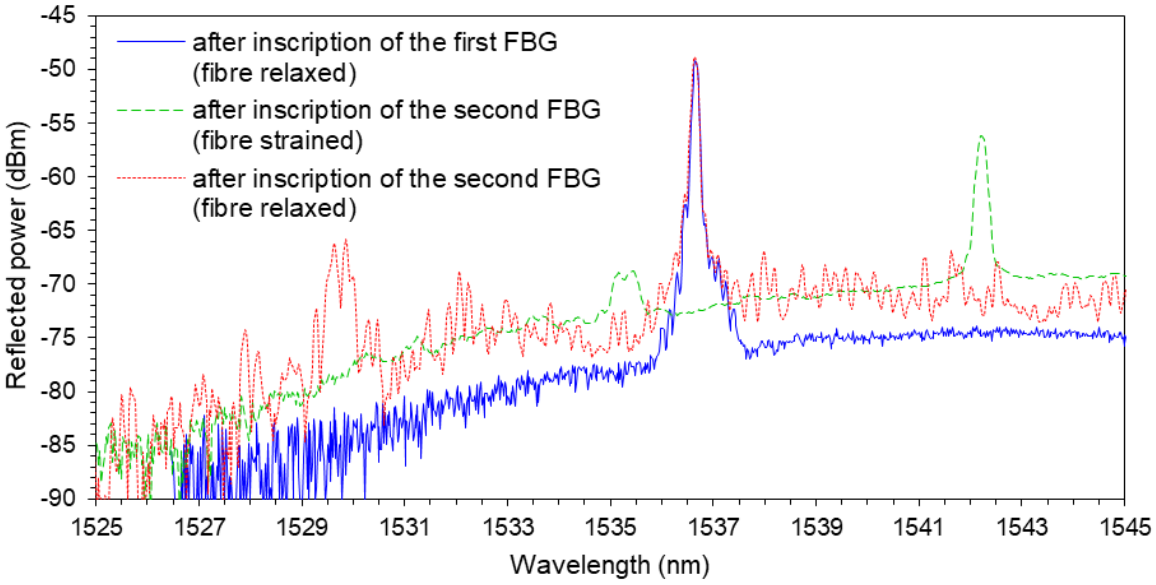

Figure 3-11. Spectra of consecutive inscription steps of a dual SOFBG involving straining. See text for details.

3.3.3 Inscription of polymer FBGs

In this thesis, polymer fibre Bragg gratings were successfully fabricated in the following fibres:

- PMMA mPOF doped with benzyl dimethyl ketal (BDK) [283]
- undoped Zeonex mPOF [122]
- undoped PC mPOF drawn from a 3D-printed preform reported in this thesis (see Chapter 5).

Polymer FBGs used in this research were only inscribed by means of the vertical system (Figure 3-9). Similarly to silica gratings, the POFBGs were monitored in the reflection regime during inscription (Figure 3-8(b)). The optical interrogation set-up was based on silica fibres and components, the only exception being the piece of POF in which the grating was to be inscribed. In order to monitor grating growth, silica fibre was used to butt-couple to the POF so it was important to ensure that its end surface was as smooth as possible. Hence, before mounting, ends of the POF were cleaved with a blade. Normally, the best results were achieved by cleaving fibre on a hot plate after the temperature of the blade and fibre stabilised at 70-90 °C, although cold cleaving was also possible. Cleaving quality could be assessed by observing the fibre end faces under an optical microscope, although it was often found quicker to proceed further and to re-cleave fibre ends again if it proved necessary later in the process. In the next step, the fibre was wiped with an IPA-soaked tissue, mounted on a V-grooved plate attached to a 3D motion stage, and secured with Kapton tape so that the fibre end was protruding from the plate by about 1 mm. The end face of the POF was then butt-coupled to with a silica fibre in an FC/APC connector, and some RI matching gel was put between them. To allow alignment, a red fibre-coupled laser (wavelength ~638 nm, optical power ~2.5-5.0 mW) was temporarily attached to the silica fibre

instead of the coupler (see Figure 3-8(b)). The light from the laser was propagating through the POF, exiting at the other end, and being projected on a paper screen via a microscope objective lens. The projection allowed assessing light coupling quality. The alignment relied on changing relative position of the SOF and POF using the 3D motion stages, leading to maximising light intensity in the core. If high enough coupling quality could not be achieved during the alignment, the fibre was unmounted from the stage, fibre ends were re-cleaved as described above, and the fibre was mounted and aligned again.

After ensuring satisfactory coupling to the core, the red laser was unmounted to return to the original configuration of the interrogation set-up. A PM was then placed on the POF resting in the V-grooved plate, on which pieces of a Kapton tape were distributed to prop the PM and secure it from scratches. When fibre mounting was finished, the shutter of the inscription laser was opened, and the laser beam was directed to the fibre through a set of mirrors and a plano-convex lens (see Figure 3-9). Normally, the lens of 10-cm focal length was used. However, some fibres were so photosensitive that the beam was only partly focused not to damage them, and, sometimes, the lens was not used at all. The latter pertains mainly to the PMMA mPOF doped with BDK. In order to assess alignment of the inscription set-up, paper screens were placed on the sides of the V-grooved plate (not shown in Figure 3-9 not to obscure the view; they were placed in front of and behind the PM in the plane perpendicular to the picture). Similarly to SOFBG fabrication, sometimes the inscription system needed aligning, which could spoil the reflection spectrum of the first POFBG to be inscribed, and it then might have to be sacrificed. However, this was not affecting further POFBGs as the appropriate set-up alignment was preserved. The grating growth was monitored on an OSA; when the required grating characteristics were achieved, the inscription was stopped, the POF unmounted, and the process could be restarted to fabricate another POFBG.

In the basic inscription procedure introduced above, the fibre and then the PM were placed on a V-grooved metallic plate. Positioning the PM was a difficult task due to the risk of breaking the glass or scratching it against metallic parts of the inscription system. Moreover, once positioned, the PM could not be slid on the plate without being lifted to protect it from scratches. This hindered PM alignment, which was required, e.g., to avoid inscription through scratched regions of the PM and to ensure that the modulation direction of PM grating is parallel to the fibre so that the resulting FBG was not tilted. To address these issues, a PM holder with a groove for fibre positioning was designed and 3D printed of acrylonitrile butadiene styrene (ABS; Figure 3-12). This yielded multiple advantages. First, the holder was printed of plastic, much softer than metal, which helped protecting the PM. Secondly, the holder allowed sliding the PM against the fibre, ensuring they were always oriented properly with respect to each other. Thirdly, the holder was designed so that there was little below the grated area of the PM that could rub against it and scratch it. The only object in contact with the grated PM area was the fibre, which – thanks to being suspended in air – did not pose much risk. Moreover, the holder was fitted with a paper screen below the PM (blue area in Figure 3-12), allowing to observe a diffraction pattern. This

facilitated monitoring of the inscription system, which was limited to the side screens only when the metalling plate was used. Finally, both the PM and fibre were appropriately levelled when in the holder, ensuring the PM did not wobble and was at the right angle to the inscription beam.

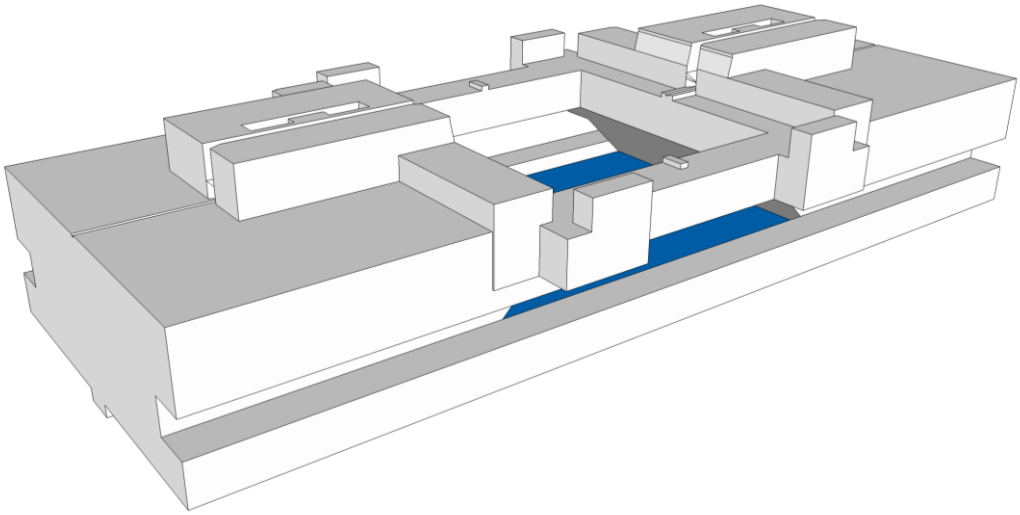

Figure 3-12. 3D-printed PM holder with a groove for fibre positioning used during POFBG inscription.

Evolution of a spectral pattern during FBG inscription through the 557.5-nm PM in the BDK-doped PMMA mPOF can be observed in Figure 3-13. Just after the inscription was started, a peak centred at 827.35 nm appeared (Figure 3-13(a)). During inscription, an ever-stronger peak to its right (centred at 827.75 nm) started appearing, and it grew bigger than the first peak by the end of inscription (Figure 3-13(b)). After closing the laser shutter, the left-hand side peak disappeared immediately (Figure 3-13(c)), proving that it was linked to ongoing laser illumination. Speculatively, the appearance of the left-hand side peak came from local heating of the fibre in the illumination spot. POFBGs normally show negative temperature sensitivity since their high negative TOC prevails over their positive CTE (see Section 2.7.4). Moreover, the blueshift could have been intensified because the fibre was slightly strained, which suppressed the effect of CTE and made the influence of negative TOC of the fibre even more pronounced [348]. Delicate fibre straining before securing it with Kapton tape for inscription was needed to avoid fibre curling. When the tape was removed and strain relaxed, the FBG peak moved to a shorter wavelength as expected (Figure 3-13(d)).

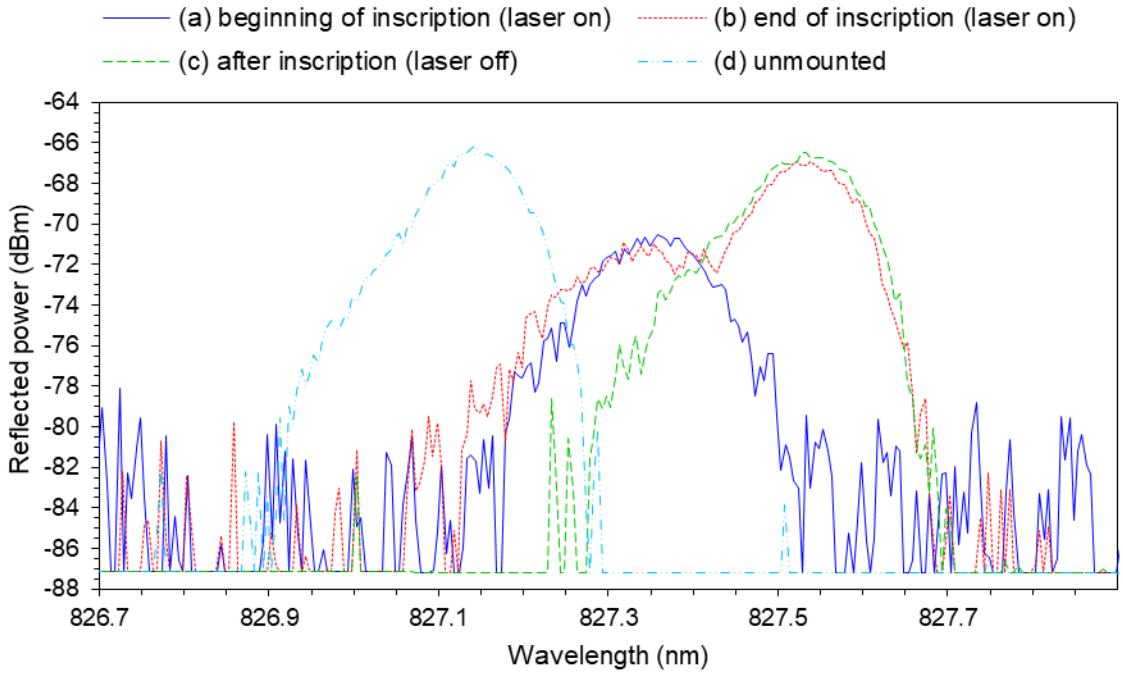

Figure 3-13. Evolution of a spectral pattern during FBG inscription in the BDK-doped PMMA mPOF. See text for details.

Similarly to silica FBGs, the basic POFBG inscription procedure described above could be modified to fabricate a wider range of various gratings. Figure 3-14 shows consecutive steps of POFBG wavelength tuning by straining fibre for inscription. To start with, a piece of POF was mounted in fibre clamps attached to 3D motion stages. The clamps were fitted with double-sided sticky pads, which held the POF firmly in place and protected it from crashing by excessive pressure that might arise from the clamps. The fibre was strained, and the grating was inscribed at ~828.1 nm with the 557.5-nm PM (Figure 3-14(a)). After the strain applied on the fibre was relieved (Figure 3-14(b)) and fibre unmounted from the clamps (Figure 3-14(c)), the Bragg peak blue-shifted by 5.9 nm to 822.2 nm. The fibre was then left to relax for 12 h, after which the reflection peak moved further to the left by some 0.2 nm (Figure 3-14(d)). The latter blueshift was probably coming from fibre hysteresis, which manifested itself due to a relatively high strain applied on the fibre during inscription. In the next example, the straining procedure was used to multiplex POFBGs written with the same phase mask in a single piece of the BDK-doped PMMA fibre (Figure 3-15). After inscribing the first grating in a relaxed fibre (Figure 3-15(a)), it was strained for inscription of the second FBG (Figure 3-15(b)). Afterwards, the external strain on the fibre was relieved, and the Bragg peak of the first FBG returned almost to its original position, stopping some 0.4 nm towards longer wavelength (Figure 3-15(c)). The difference can be ascribed to fibre hysteresis discussed above (compare Figure 3-14(c) and (d)). Note that the hysteretic behaviour was not observed during a similar procedure of straining silica fibres for dual FBG inscription (compare Figure 3-11).

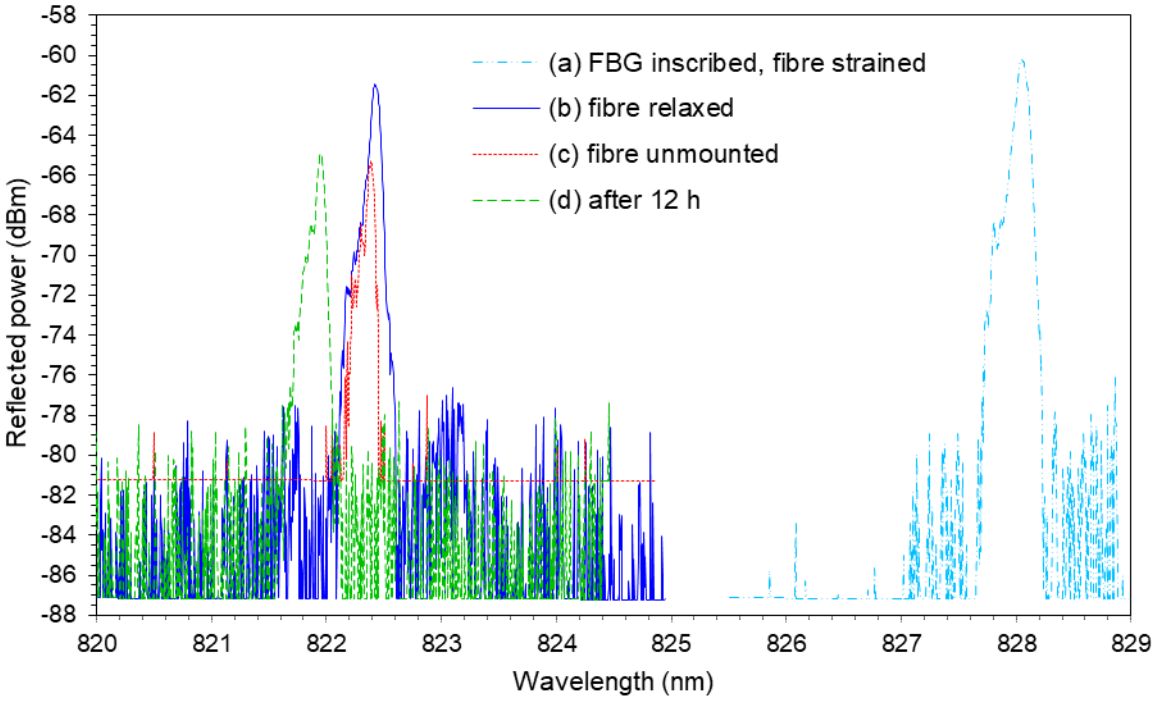

Figure 3-14. Steps of FBG inscription in the BDK-doped PMMA mPOF involving straining. See text for details.

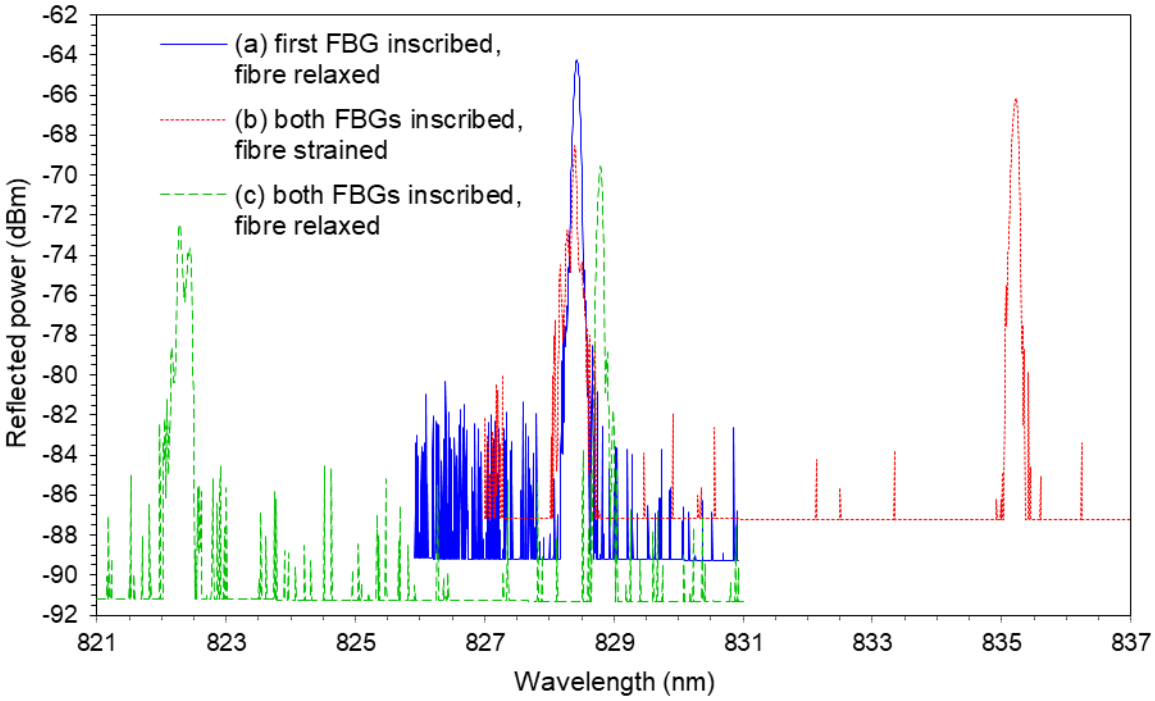

Figure 3-15. Steps of dual FBG inscription in the BDK-doped PMMA mPOF involving straining. See text for details.

Other variation to the basic inscription procedure consists in fabricating scanned gratings, similarly to what was described for SOFBGs in Section 3.3.2. In the vertical inscription set-up, the mirror mounted

on the programmable translation stage used for scanning was Mirror 1 (see Figure 3-9). In addition, some fibre was annealed before inscription to improve its stability in various respects (see Section 2.7.3).

Furthermore, post-inscription annealing could be applied to tune a POFBG to a lower wavelength. Figure 3-16 shows water annealing of a POFBG inscribed with the 580-nm PM in the BDK-doped PMMA mPOF (inset in Figure 3-16). Peak position was observed on a relatively low OSA resolution and sensitivity (1 nm and -78 dBm, respectively) to ensure high sweeping speed, which allowed easier monitoring of peak position shifting. A too high shifting speed would suggest a too high water temperature, which might damage the fibre. The Bragg peak started moving left at a water temperature of ~50 °C (Figure 3-16(b)). The maximal acceptable water temperature was found to be ~58 °C so it was kept at ~55 °C throughout the process, which took ~45 min. By the end of annealing (Figure 3-16(c)), the Bragg peak moved to from 862.2 to 848.5 nm. After the POF was removed from water and its temperature decreased to room temperature, the peak redshifted by 0.5 nm to 849.0 nm (Figure 3-16(d)), which was expected of a POFBG due to its negative temperature sensitivity (see Section 2.7.4). Finally, a blueshift of the peak by 1.9 nm to 847.1 nm was observed after the fibre dried (Figure 3-16(e)), stemming from positive humidity sensitivity of a polymer grating (see Section 2.7.4). Successful fibre annealing was also performed for POFBGs inscribed in the same fibre at a different wavelength (peak shift from 829.0 to 816.7 nm, Figure 3-17) and in the Zeonex fibre (peak shift from 844.4 to 812.4 nm).

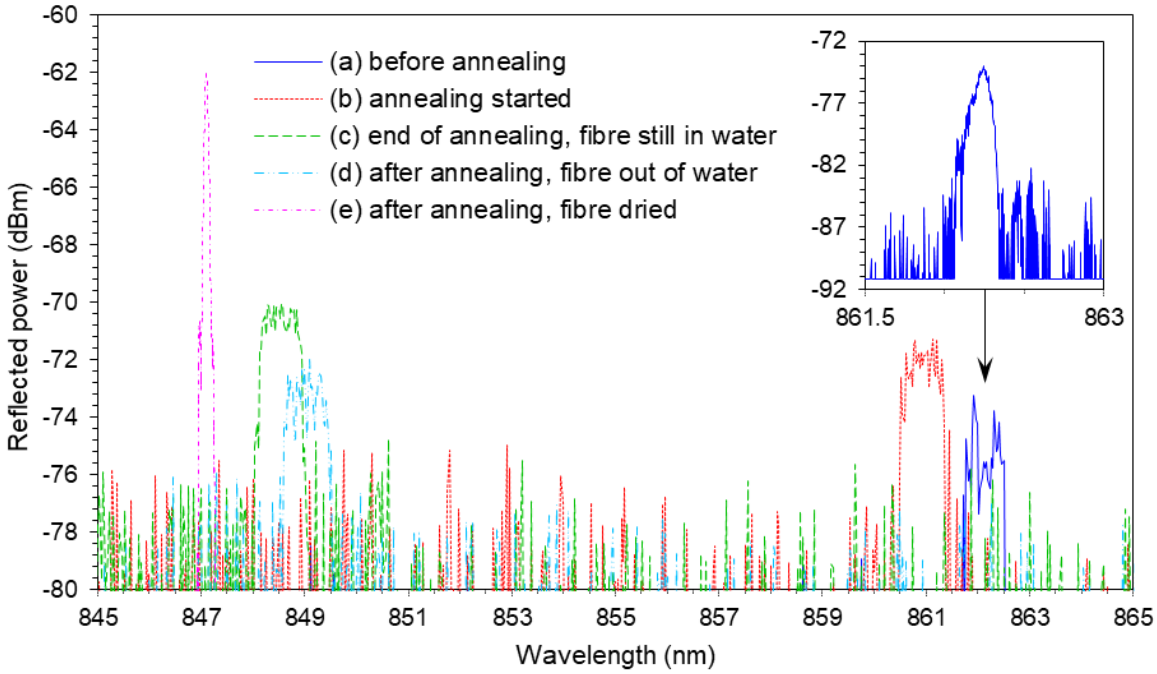

Figure 3-16. Consecutive steps of annealing a POFBG inscribed in the BDK-doped PMMA mPOF. See text for details. OSA sensitivity -78 dBm, resolution: (a)-(d) 1 nm, (e) 0.06 nm. Inset shows spectrum (a) at an OSA resolution of 0.06 nm and a sensitivity of -85 dBm.

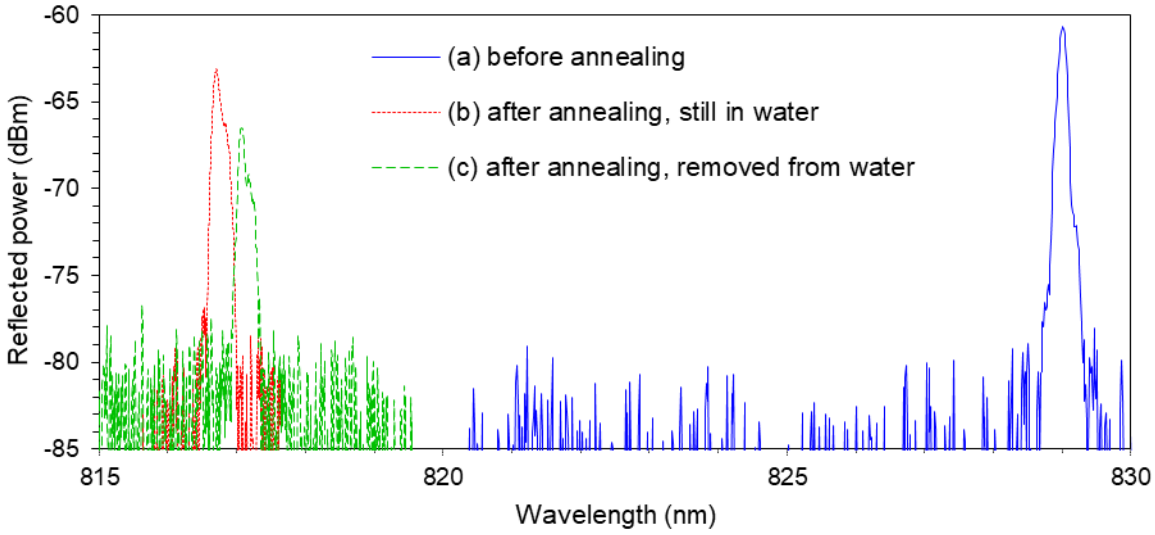

Figure 3-17. Consecutive steps of annealing a POFBG inscribed in the BDK-doped PMMA mPOF at an OSA resolution of 0.06 nm.

3.4 Summary

This chapter introduced three experimental techniques and the related set-ups used in the following part of this thesis. They include FDM 3D printing, POF manufacturing using a draw tower, and FBG inscription.

Fused deposition modelling (Section 3.1) was used to fabricate POF preforms, which is described in Chapter 4. This method was also applied extensively during the research on fibre embedding, which is reported in Chapter 6.

The 3D printed solid-core PC preform, which was the most successful, was subsequently drawn to fibre following the method described in Section 3.2. The results of this research are presented in Chapter 5.

The FBG production techniques, described in Section 3.3, were applied to inscribe gratings in the PC fibre drawn from the 3D-printed preform, which is presented in Chapter 5. Furthermore, these grating manufacture approaches were used to fabricate FBGs to be embedded, which is described in Chapter 6.

Finally, it should be reminded that the experimental set-ups for the strain tests and the temperature and humidity trails are described in the respective sections of Chapter 6 and not in Chapter 3. This is because they were upgraded during the research on fibre embedding, their evolution being driven by the experimental results. It was then found more logical to introduce these set-ups and describe their evolution together with the discussion of the strain, temperature and humidity results.

Chapter 4 Fabrication of polymer optical fibre preforms

This chapter presents achievements in applying the FDM 3D-printing technique to advancing the technology of solid-core and hollow-core mPOF preform fabrication. The introduction presents the issues related to the use of FDM to POF manufacturing which are tackled in this chapter. Moreover, materials used in this chapter for fibre manufacturing are presented. The next section tackles the question of transparency optimisation of 3D printout, which is the key enabling factor for drawing fibre of good quality. The four following sections provide description of hollow-core and solid-core designs, based on which POF preforms were manufactured from PMMA and PC. Various aspects of the preform manufacturing process are discussed, and the chapter concludes with proposals of how to improve it further.

4.1 Introduction

The potential benefits of using FDM for fabricating POFs were introduced in Chapter 1 and Chapter 2. However, for POFs to be fabricated, the following aspects of their manufacturing process must be optimised or proved to meet the requirement for fibre drawing. First, printing parameters must be optimised, with a focus on transparency optimisation.

Despite all the advantages of the FDM technique previously discussed, it is intrinsically not well-suited for manufacturing transparent printouts, compared to, e.g., stereolithography. The latter method relies on 3D printing with UV-curable resins, resulting in non-thermoplastic printouts, which cannot be used for fibre drawing. In FDM, a printout layer is created by melting together threads of plastic filament, normally leaving air voids between them, which leads to creating sources of light scattering. Consequently, transparency optimisation of FDM-printed structures relied on assuring that adjacent threads melt together as much as possible, leaving no or minimum air voids in the printout. Secondly, light scattering of POF preforms can be further minimised by preform annealing. However, the printed preform must show stable behaviour in order to withstand prolonged exposure to high temperature, displaying no material yellowing and no deviation of printout geometry. Finally, the prepared preform must be drawable, showing no abrupt changes in the response to temperature gradient and, hence, little modification of geometry during drawing. The latter is all the more important because preforms are to be drawn into fibres without the assistance of pressure due to technical limitations of the draw tower used.

Two materials were used throughout this chapter: PMMA and PC. This is because, first, they were commercially available in the form of spooled filament of clear material (i.e. non-coloured and without intentional additives) [349]. They were transparent to eye and, thus, seemed promising candidates for printing POF preforms. Secondly, each material has certain advantages. PMMA is the most-widely-used and best-studied material for POF drawing, so it has a range of literature results to compare to. PC, in turn, was chosen due to its highest glass transition temperature (145 °C) and highest operational temperature (125 °C) compared to all POF materials reported so far [105, 107] (see Table 2-1). Thirdly, both PMMA and PC had been previously used to successfully fabricate POFs using the drill-and-draw technique, starting from casting PC plastic granulates in-house [105, 107, 238] or from casted or extruded PMMA rods available commercially [350, 351].

It must also be mentioned that quantitative information on material properties of commercially available 3D printing materials are usually very scarce. This was also the case for both utilised filaments. In particular, the molecular weight of material is normally unknown, whose optimal value for drawing is around 60,000 g/mol [26]. Moreover, commercially available 3D printing filaments are not optimised for optical use, and even materials labelled transparent do not necessarily have high enough transparency to be used in optical fibres. Hence, their suitability often cannot be predicted and must be tested experimentally.

All the printouts presented in this chapter were printed in-house at Aston University. The machine was the UP! 3D printer, and it was working with the dedicated UP! slicer (software which transforms a 3D model into a series of printer commands) with the FixUp3D extension.

The core part of Sections 4.2 and 4.5 has been submitted to the journal Optics Express, while a more detailed description is presented in this thesis. Section 4.3 was published as a conference paper and poster at POF 2016 Conference [246].

4.2 Optimisation of transparency of 3D printouts

All printouts described in this section were printed from PMMA and PC filaments supplied by Dr 3D Filament [349], dried for ~1 day at 85 °C for drawing. This was found particularly important for PMMA, as it can absorb much more water than PC (up to 2.1% [340, 341] vs 0.3% [342], respectively). If the PMMA was not dried, water contained in it was observed to boil at nozzle outlet during printing at high temperatures and low speeds, and dried materials were discovered to yield the highest printout transparency as discussed below.

Transparency optimisation experiments were performed on 4 mm thick slices of the actual hollow-core preform to be 3D printed (see Figure 4-2 for preform design). The key printing parameters were varied, including nozzle temperature, printing speed (speed of movement of printing nozzle), filament feed rate and nozzle temperature. The values for layer thickness, nozzle diameter and printing bed temperature were kept constant. After printing, the samples were polished from top, bottom and side, and the transparency was evaluated visually. The number of slices printed from PMMA and PC during transparency optimisation was 34 and 36, respectively, while the total number of all samples used for transparency evaluation was 114 and 57, respectively.

All the considered parameters are machine- and filament-dependent, so the optimised values should be treated as an indication only. Moreover, the slicer and control software of the UP! printer uses a non-standard parameter set for infill, which is not easily comparable with those of other slicers. For these reasons, qualitative discussion of optimisation process is presented below, and quantitative data are provided where possible. The summary of the optimisation results of the 3D printing parameters from the viewpoint of printout transparency have been collated in Table 4-1.

Nozzle temperature

Nozzle temperature values from 250 °C to 300 °C with 10 °C step were tested to find that the optimal temperature values from the viewpoint of transparency were 280-290 °C for PMMA. For the temperatures below 280 °C, filament threads seemed not to melt together well, whereas for 300 °C viscosity was probably too low. The nozzle temperature used for fabricating PMMA preforms was decided consequently to be 290 °C. PC filament has a higher glass transition and softening temperature than PMMA and hence should be printed at higher nozzle temperature. Its highest settable value for the 3D printer was 300 °C, which was used for printing PC preforms.

Filament feed rate

When varying the filament feed rate, an optimum speed was identified, while both too high and too low values were found to decrease transparency. Too low values resulted in volume of printout not being fully filled in. Too high feed rates made excessive material aggregate on printout walls, which, in turn, lowered the printing accuracy and hindered operation of the printer. Moreover, air voids at thread junctions were found bigger in this case (see also Section 4.5.2).

Table 4-1. Summary of the optimisation results of the 3D printing parameters from the viewpoint of printout transparency.

Printing parameter	Comment
Printing speed	as small as possible (5 μm used); the lower the printing speed, the longer the overall fabrication time
Nozzle temperature	optimal – both too high and too low infill rates deteriorate transparency; 280-290 °C for PMMA, 300 °C at minimum for PC
Infill rate	optimal – both too high and too low infill rates deteriorate transparency
Nozzle diameter	as small as possible and matched with the layer thickness (300 μm used); nozzles of a diameter <300 μm are prone to clogging
Layer thickness	as small as possible and matched with the nozzle diameter (150 μm used); the lower the layer thickness, the longer the overall fabrication time
Bed heating	maximum to avoid or minimise sample warping (105 °C used); ideally, a heated printing chamber should be used

Printing speed

The printing speed, which is the speed at which the nozzle moves, was decreased steadily from 40 mm/s down. The general rule was found to be that the lower the speed, the better the transparency. Practical constraints are the only limiting factor keeping the speed high, as lowering the printing speed increases overall manufacturing time. Transparency improvement at low printing speed seems to be linked to heat transfer from nozzle to sample. Lowering printing speed allows a given region of printout to absorb more heat from nozzle as it approaches before the material is deposited. Such a mechanism would also explain the difference in transparency between the samples printed on heated (105 °C) and non-heated printing bed (compare Figure 4-1 (c) and (d)).

Nozzle diameter

The nozzle diameter influences the resolution in *x*-*y* plane (directions marked in Figure 4-8(a)) – the smaller the nozzle diameter, the better the resolution and reproduction of planar details. However, the smaller the nozzle diameter, the more time it takes to build the entire volume of printout at the same printing speed. Nozzles of small diameter (from around 300 µm down) are also prone to clogging, which hinders the fabrication process.

Layer thickness

The layer thickness determines the resolution in *z* direction. The smaller it is, the smoother the vertical walls are (see Fig. 3(c)). However, as with the nozzle diameter, the smaller the layer thickness, the longer it takes to produce the whole printout. The layer thickness must also be matched with the nozzle diameter, ideally being around 50% of the nozzle size. As a consequence of these considerations, the layer thickness was set to 150 µm, and diameter of the nozzle used was 300 µm.

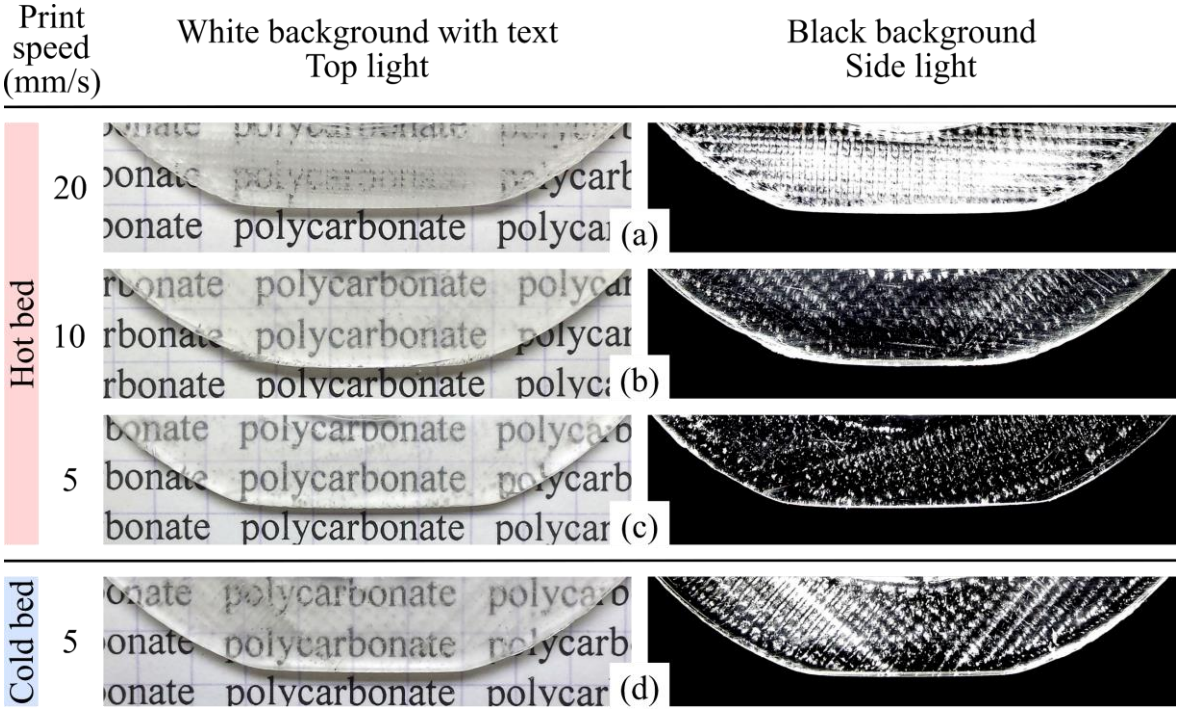

Figure 4-1. Comparison of transparency of polished circular test printouts for different print speeds and printing bed temperatures (hot bed – 105 °C, cold bed – room temperature). (Left) Photographs of the samples with front lighting and resting on white squared paper (5 mm pitch), accentuating the variable transparency of the samples. (Right) Photographs of the same samples on a black background illuminated from the side (the bottom edge of the pictures). This lighting accentuates the density and localisation of air voids in the samples.

Printing bed temperature

The printing bed temperature could also be set and was kept at around 105 °C (the highest settable value for the machine). As it has already been mentioned, the higher the temperature of the adjacent threads, the better they melt together. However, the favourable influence of the printing bed temperature was only visible until around 2 cm up from the printing bed, while, at higher distances, the heat coming from the printing bed was being dissipated. Probably a heated printing chamber would be of benefit to the preform printing process. This would mean the entire printout would be kept at a high temperature, allowing it to heat up more as nozzle approaches compared to the case when a heated chamber is not used. Hence, transparency could possibly be even higher, or, alternatively, the same transparency would be achieved at a higher printing speed. It is speculated that heated chamber temperature should ideally be as high as possible but just below glass transition temperature of the material used, so that it does not flow after being deposited. Moreover, a heated printing chamber should also help to decrease printout warping and detaching from printing bed, as well as to lower internal stress of printout.

4.3 Fabrication of hollow-core PMMA preform and drawing to cane

In this section, fabrication of the first 3D-printed PMMA preform for polymer optical fibre drawing is described. This research has been originally published during POF 2016 Conference (a as conference paper and poster) [246]. It was printed of commercial PMMA filament by means of the fused deposition modelling technique. The preform was drawn to cane, proving good enough quality of drawing process and the PMMA molecular weight to be appropriate for drawing. This ascertains that the manufacturing process provides preforms suitable for hollow-core fibre drawing.

4.3.1 Collaboration statement

The work described in this section was done in collaboration with the following partners:

- Andrea Fasano (supervisor: Henrik K. Rasmussen) from Department of Mechanical Engineering, Technical University of Denmark (DTU)
- Getinet Woyessa (supervisor: Ole Bang) from Department of Photonics Engineering, DTU

The idea of the described research originates from the author and Andrea Fasano. Andrea provided the initial preform design according to directions from the author to fit best to the requirements of the 3D printer used. Andrea Fasano performed the post-print processing and Getinet Woyessa drew the fabricated preform to cane. Andrea Fasano provided the description of the preform design and of the procedure and results of preform annealing, post-processing and drawing to cane. Images of the cane and its measurement data were also provided by Andrea Fasano. The author and Andrea Fasano jointly discussed the results, based on which the author produced the text presented in the thesis.

4.3.2 Design

The advantage of any hollow-core design lies in greatly reducing importance of material absorption (although not reducing it completely – see Section 2.5.3), as guidance in NCFs has been demonstrated even in the regions of extremely high material absorption [211]. Of the two currently most popular HCF types, PBGF and NCF, the latter was chosen. This was motivated by a smaller number of details in the design and, presumably, lower printing accuracy being sufficient. Moreover, numerical simulations suggest there is still much room for leakage loss decrease by further changes to fibre design, which was confirmed by the recent advances (see Section 2.5.3 for details).

The chosen design was adapted from [352], which seemed the simplest of many NFC designs from the viewpoint of the 3D printing approach and equipment used. The design was originally used for drawing silica fibre and consisted of 8 capillaries fitted into an outer tube of a larger diameter and thickness. The capillary stacking method was used to fabricate the original preform – single capillaries were fused together by means of an oxygen-hydrogen burner. The cladding capillaries were pressurised for drawing in order to avoid deviations to their shape.

The adapted design used in this chapter (prepared in SolidWorks 2015) keeps the proportions and shape of the original one, with the dimensions being adjusted to accommodate to the furnace of the draw tower used (Figure 4-2). The preform height was 102.5 mm, and the resulting diameter of air core, 20.4 mm.

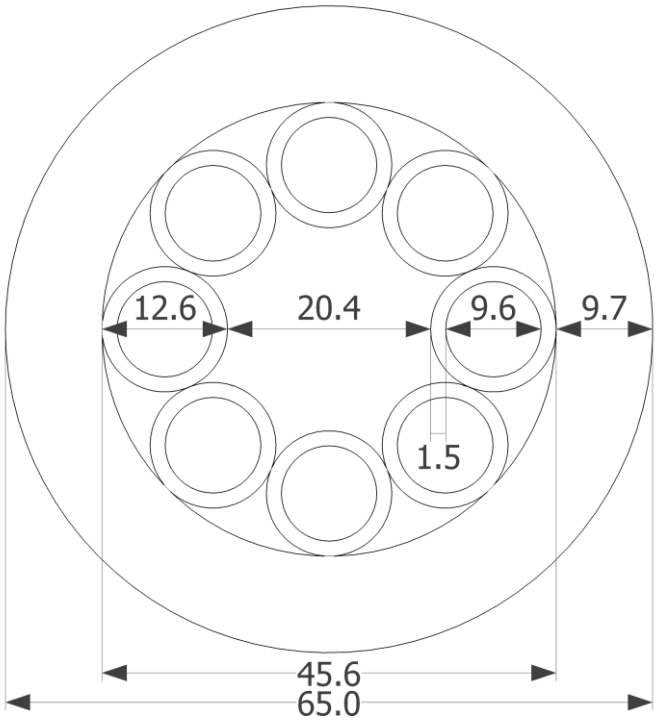

Figure 4-2. Cross-section view of the preform to 3D print. All dimensions in mm.

4.3.3 3D printing and post-print processing

The 3D printer settings optimised for PMMA, arising from Section 4.2, were used to fabricate the preform: printing speed = 5 mm/s, nozzle temperature = 290 °C, printing bed temperature = 105 °C (the highest settable value). The preform was printed in 9 days, 16 h and 43 min (~233 h), consuming ~227 g of the material (Figure 4-3(a)). The printing time was much longer than that reported in the literature for other 3D-printed POF preforms, which was 6 h for an SC air-structured one [30] and 21.5 h for an SC SI one [31]. Such a long printing time stemmed from the optimised printing settings described in Section 4.2 and was aiming to provide the highest practically achievable transparency of preform.

The preform manufacture time of over 9 days was very long compared to time which could be achieved by the drill and draw method, which is the most popular approach to manufacture mPOFs. If drilling is performed in commercial plastic rods of optical quality, it only takes single hours to CNC-machine the preform. However, such rods are not available for many interesting materials. The preform manufacture time is markedly longer if the bulk material in which the structure is to be drilled must be casted first. The two PC mPOFs reported in the literature [105, 107] were fabricated starting from the in-house made casts by the drill-and-draw method. The times required to fabricate the casts were not reported though.

As it was discussed in the previous section, the long time required to 3D print the preform came from a slow nozzle speed of 5 mm/s yielding higher printout transparency. This, in turns, stemmed supposedly from the need for heat transfer from the nozzle to the printout before the nozzle deposited the molten material. It is then speculated that the use of a heated printing chamber, keeping the sample just below its glass transition point, would allow using much higher printing speeds and, hence, accelerate the now long preform fabrication process.

The preform was dried for two days at 85 °C, after which it was machined in order to reduce surface roughness resulting from 3D printing. The final diameter of the outer tube and length of the preform were 60.0 mm and 100.0 mm, respectively, giving an aspect ratio of 0.6. The preform was then dried at 80 °C for six days before drawing (Figure 4-3(b)).

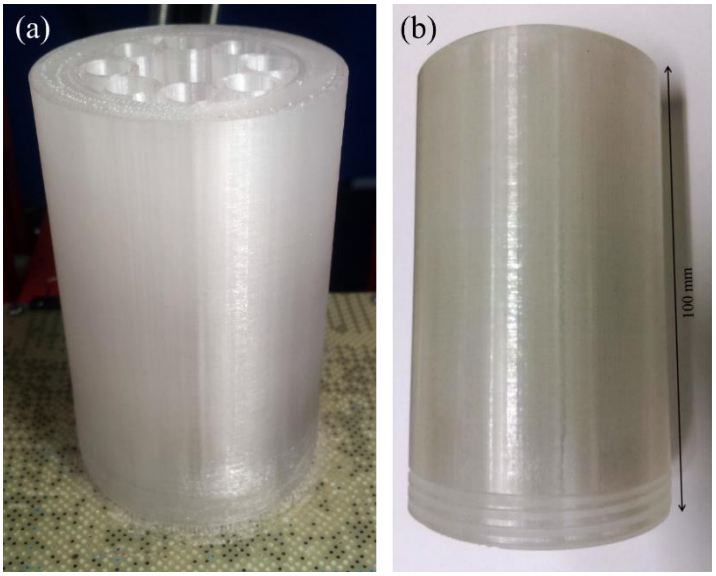

Figure 4-3. Hollow-core PMMA mPOF preform (a) after printing, (b) after machining and annealing.

4.3.4 Drawing to cane

Preform drawing was started at a relatively low temperature – around 50 °C below the usual temperature for commercial PMMA rods, which is around 190 °C. It was increased gradually to find the minimum temperature suitable for drawing. As it was mentioned, molecular weight of the PMMA was unknown, making it difficult to estimate the correct drawing temperature. Furthermore, the cladding structure of the NCF preform was much more delicate than a solid-core one, so care was taken not to damage it. This was all the more necessary since pressurisation of capillaries was not available. The adequate drawing temperature was found to be 180 °C, which is 10 °C below the usual one. Drawing was also conducted at a relatively high tension, which was reported to decrease surface roughness and, so, help reduce fibre attenuation [353]. Several canes were obtained from the NCF mPOF preform are shown in Figure 4-4.

The cross-section of one of the HC PMMA mPOF canes is displayed in Figure 4-5. From the figure two phenomena can be identified. First of all, some capillaries moved away from each other, leading to formation of gaps in the structure of the fibre cladding. This could have been caused by having a too big temperature gradient within the preform, as even a small inhomogeneity in heat distribution during drawing can strongly affect the fluid mechanical response the structure and break its initial symmetry. Moreover, the individual capillaries were not joint together well, which resulted from the 3D printer nozzle drawing each circle individually when printing capillaries. In addition, the capillaries became elliptical in cross-section (see Table 4-2 for the list of geometrical parameters). As a result, the air core diameter relative to the outer diameter was larger than at the cane stage than at the preform stage (2.2 mm/4.7 mm=47% instead of 20.4 mm/60.0 mm=34%). The thickness of capillary walls was also

higher in the cane than in the preform. All this is believed to stem first from non-optimal drawing conditions, which would need experimenting with, and, secondly, from the lack of overpressure in the capillaries, which could have helped keeping their initial shape from deforming. The distorted shape of the canes could also be a consequence of thermal instability of the used PMMA filament. This is discussed in Section 4.6 describing a SC PMMA preform, because the influence of the presumed thermal instability was much more pronounced there.

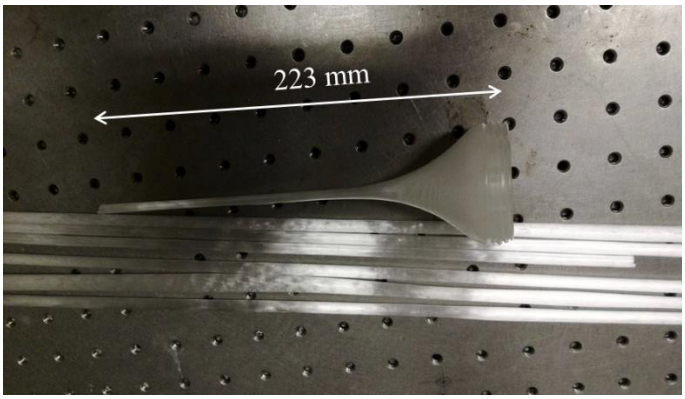

Figure 4-4. Hollow-core PMMA mPOF canes obtained from 3D printed preform drawing.

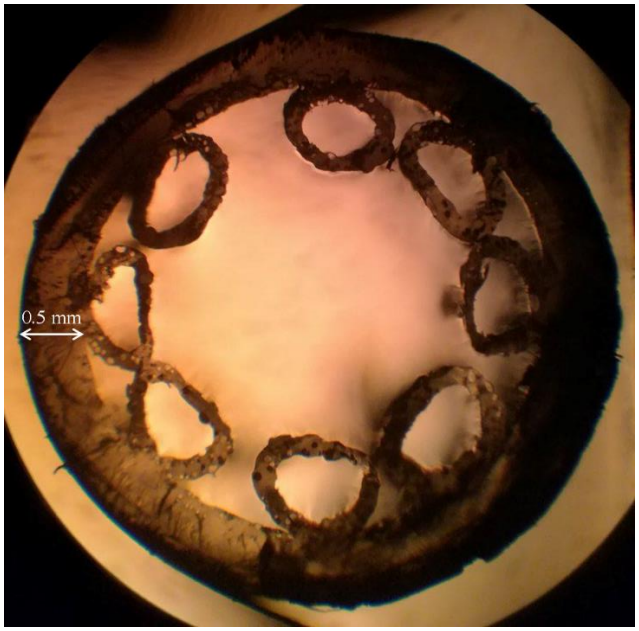

Figure 4-5. Cross-section of a HC PMMA mPOF cane.

Table 4-2. Average geometrical parameters for a HC PMMA mPOF cane.

Wall thickness of the capillaries	0.16 mm
Wall thickness of the outer tube	0.5 mm
Diameter of the air core	2.2 mm
Major diameter of elliptical holes	0.6 mm
Minor diameter of elliptical holes	0.4 mm
External diameter of the cane	4.7 mm

4.3.5 Summary

To the best of the author's knowledge, this section presented the first 3D-printed hollow-core preform made of PMMA for POF drawing. It is expected that, building on these results, further optimisation of the drawing process should be possible, leading to favourable mechanical and optical preform properties. The preform was proven to be drawable, which implies that the optimised procedure should be suitable for producing hollow-core POF. However, improvement of design and drawing conditions are still required.

4.4 Improved hollow-core design for PC and PMMA preforms

This section describes an upgraded hollow-core preform design and preforms fabricated based on these designs.

The need for an upgrade to the design presented in Section 4.3 arose from the results of drawing the preform to cane presented there (Figure 4-5). If the fibre fabrication process described there had been continued, it would have been expected that the main problem for effective light guidance would have been separation and deformation of capillaries surrounding the hollow core, as these could grow even bigger while drawing cane to fibre. In the design from Section 4.3 (hereinafter referred to as "old"), circles forming capillaries and outer tube were just touching each other and not crossing. Hence, nozzle of the 3D printer was drawing circumference of each capillary as an individual circle. This resulted in weak connection between adjacent capillaries and between capillary and outer tube.

To tackle these issues, an upgraded design was proposed, in which the circles corresponding to outer diameter of cladding capillaries crossed with each other and with the outer tube (Figure 4-6). This ensured firm connection between adjacent capillaries (red dotted circles) and between capillaries and outer tube (green dot-dashed circles), aiming at ensuring that the capillaries did not separate during drawing.

However, a few caveats to the new design must be added. To minimise confinement loss, nodes between cladding capillaries must be avoided as they have been found to support modes which facilitate

outcoupling light from the core [211]. The changes to the design were proposed assuming that the preform were to be drawn without pressure assistance. It was envisaged that increased mode density in the capillary nodes would have less of detrimental effect than deforming the cladding structure to the point where capillaries detach from each other. However, the optimal cladding structure should display a gap between cladding capillaries for light optimal confinement [27]. Consequently, to further optimise fibre design, the drawing set-up should ideally be extended to allow pressure-assisted drawing. Moreover, optimised material properties would be desired. For example, a tailor-made PMMA filament could be used, whose exact composition and properties would be known. Alternatively, the preform can be printed of the commercial PC filament, because it showed much lower thermal instability, leading to successfully manufacturing a solid-core fibre (Section 4.5). Possibly, a preform made of an optimised material can be drawn even without the use of pressure as it was reportedly done for silica NCF [211].

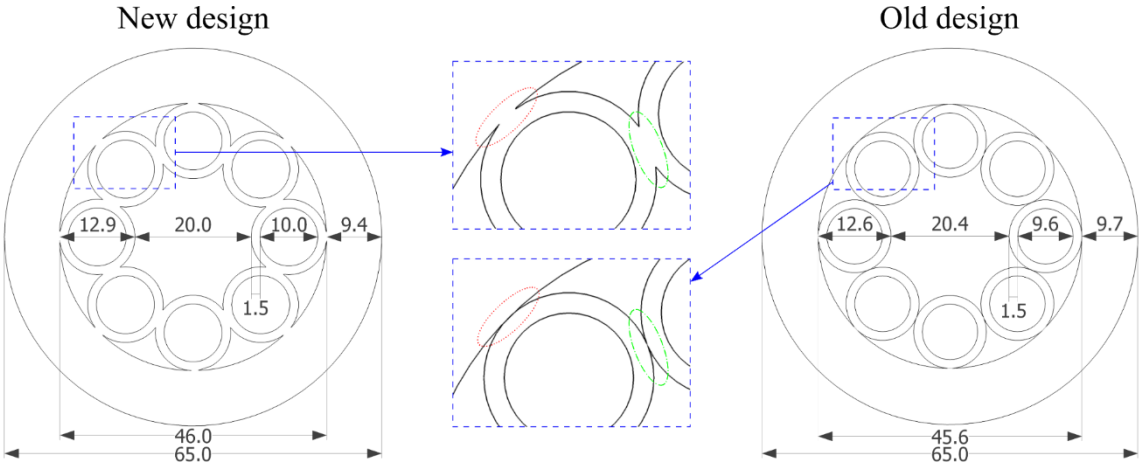

Figure 4-6. Cross-section view of the new and old designs of hollow-core preforms. Differences between the designs are circled around in the magnified view.

The new design was used to 3D print hollow-core preforms of PC and PMMA, using the printing parameters from Section 4.2. The PC preform was produced in ~9 days, 16 hours and 30 min (232.5 h), consuming ~217 g of the material. For the PMMA preform, these were 9 days and 16 h (232 h) and 227 g, respectively.

The changes in the design resulted in expected changes in the manufacturing process. As can be seen from photographs, the printed preforms indeed displayed a stronger link between adjacent capillaries and between capillaries and outer tube. This structural change was reproduced equally in the PC and PMMA preform printouts, hence only a photograph of the former is shown (Figure 4-7(a)).

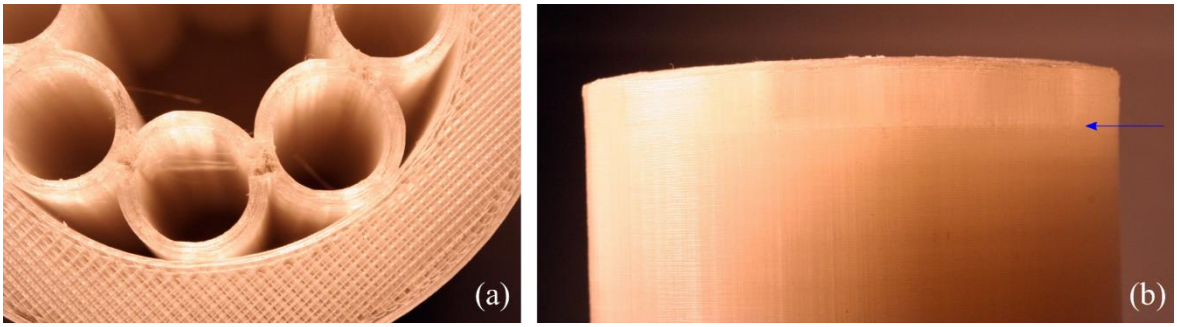

Figure 4-7. Photographs of the HC PC preform printed according to the new design. (a) Top view, accentuating sound connection between adjacent capillaries. (b) Side view of the bottom end of the preform, showing warp of the bottom surface and a crack in the side wall (marked with an arrow). Note higher transparency of the preform towards the bottom surface (visible from the marked crack up, see also Section 4.2).

Compared to the HC PC preform, the HC PMMA one displayed fewer problems related to temperature differences within the printout. First of all, it was much easier to assure high enough adhesion between the printout and the printing bed and hence avoid warping, as opposed to the HC PC preform (Figure 4-7(b)). Similar issues were observed in the SC PC preform (compare Figure 4-9 and Section 4.5 for more details). This was presumably due to higher glass transition temperature of PC (145 °C [107]) in comparison with PMMA (106 °C [106]) and the need resulting from this for higher temperature of the heated bed, which was unachievable due to hardware limitations. Moreover, no cracks were identified on the side walls of the PMMA preform, while they were found in both HC (Figure 4-7(b)) and SC PC (Figure 4-9) ones. This might have resulted from using an adequate nozzle temperature for the PMMA preform (290 °C) and a too low, for the PC ones. The latter was limited to 300 °C by the equipment constraints. As a result, the layers of the PC preforms might have not melt together well enough during the layer deposition. Another reason for crack formation in the PC preforms might possibly have been that heated bed temperature was too low as discussed above, resulting from the difference in glass transition temperature between PC and PMMA. This might be partly addressed by the use of heated printing chamber (see Section 4.2). However, the issues regarding the PC preforms do not cause any problems from the viewpoint of fibre manufacturing, because the side walls are normally machined down before drawing preform to cane (as described in Section 4.3.3 for the HC PMMA preform and in Section 4.5.2 for the SC PC one). Furthermore, the bottom part of preform, where the warping is most pronounced, is sacrificed during drawing to the cane.

Both HC preforms manufactured according to the new design look promising and are still waiting to be drawn. In view of the issues with annealing 3D-printed PMMA preform described in the next section, the HC PMMA preform can probably only be drawn without prior annealing, i.e. the way described in Section 4.3. On the contrary, the SC PC preform had been successfully annealed before drawing

(Section 4.5). This suggests that annealing of the HC PC preform would be advisable, as it should reduce the internal stress and increase transparency by removing air bubbles trapped in the material.

4.5 Fabrication and characterisation of solid-core PC mPOF preform to be drawn to fibre

The section describes the solid-core preform design and explains the rationale behind it. Based on optimisation of transparency of 3D printouts presented in Section 4.2, a PC SC mPOF preform is 3D printed, characterised, and post-processed. The preform was of good enough quality to draw it into a fibre, which is presented in Chapter 5.

4.5.1 Collaboration statement

The work described in this section was done in collaboration with the following partners:

- Andrea Fasano (supervisor: Henrik K. Rasmussen) from Department of Mechanical Engineering, Technical University of Denmark (DTU)
- Getinet Woyessa (supervisor: Ole Bang) from Department of Photonics Engineering, DTU

The idea originates from the author and Andrea Fasano. Andrea Fasano provided the initial preform design and changed it according to directions from the author to fit best to the requirements of the 3D printer used. Andrea Fasano and Getinet Woyessa annealed and machined the preform.

The preform was manufacture by the author. The descriptions of the experiments were prepared by the author based on text and data provided by the collaborators involved in each experiment. All other text, along with photos, descriptions, and discussions were produced solely by the author.

4.5.2 Fabrication of the preform

The rationale behind the initial preform design was to make it as easy as possible to be reliably reproduced by the printer. Consequently, a simple two-ring structure in a hexagonal arrangement was printed (top view shown in Figure 4-8(a)), which has previously been shown to guide light [26]. The hole diameter (d) was set to 6 mm and the hole pitch (Λ, distance between centres of adjacent holes) to 12 mm. The preform diameter and height were 65 mm and 105 mm, respectively. Before drawing, the preforms were machined down to 60 mm and 100 mm, respectively.

The preform (Figure 4-8) was printed on heated bed (~105 °C) at the speed of 5 mm/s and the nozzle temperature of 300 °C (other settings were the same as in Section 4.2), taking ~323 hours in total and using ~292 g of material. The printout warped a little during printing (the sides of the raft detached from the printing bed), resulting in a slightly rounded bottom surface. This somewhat decreased the volume of the printout, resulting in some material not fitting in the printout and aggregating on the sidewalls (see Figure 4-9(a), (c)). Warping is a common problem in FDM systems and originates from the

temperature difference between nozzle and printout. That issue is partly addressed by the heated printing bed, but it cannot be eliminated completely this way, especially that glass transition temperature and, hence, required nozzle temperature for the PC are the highest of all polymers used for POF manufacturing (see Table 2-1). In the case of this preform, warping was not an issue because it did not distort the designed geometry above the bottom surface. The quality of the top and bottom sections is not overly important since they are sacrificed during fibre drawing stage.

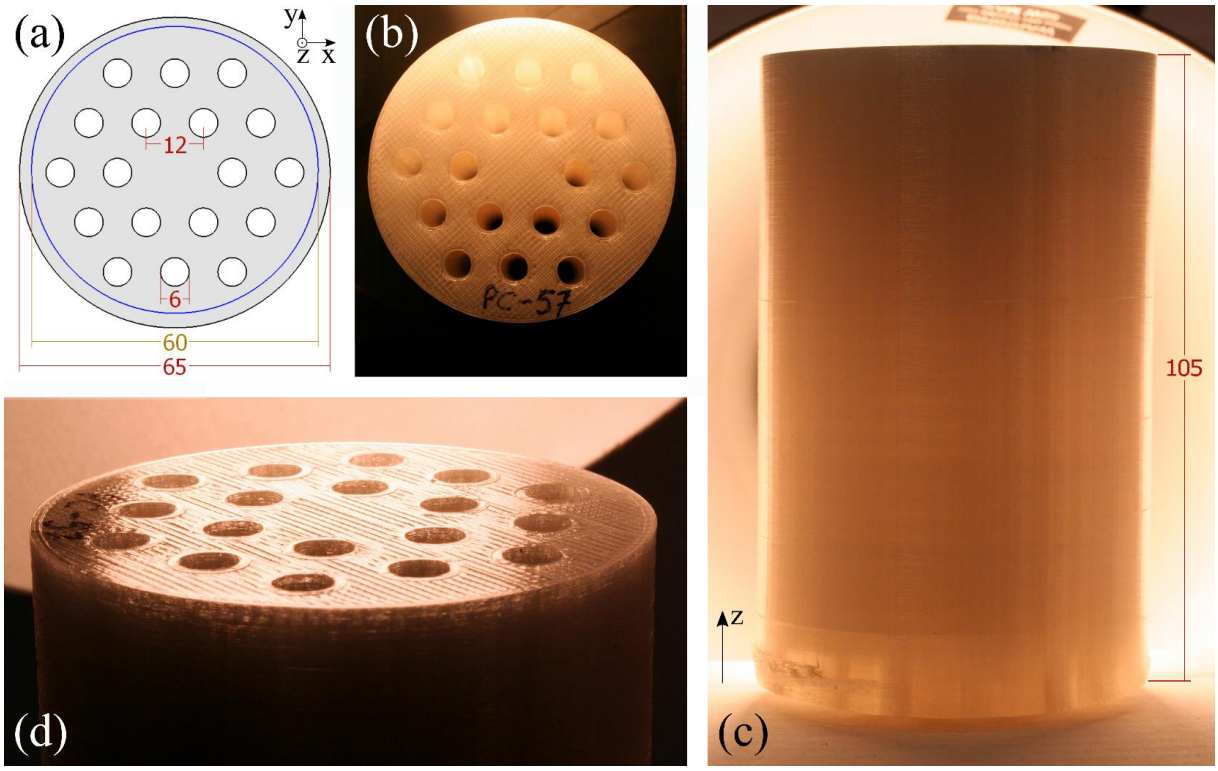

Figure 4-8. (a) Top view of the preform design. The blue ring shows the machined down diameter. (b) Top view of the printed preform (illuminated from the top edge). (c) Side view of the printed preform (illuminated from behind). (d) View of the top surface of the printed preform. All dimensions in mm.

A close inspection of the printout revealed some cracks on the sidewalls between adjacent layers (see Figure 4-9). These are probably caused by high inner strain in the printout introduced during printing, which in FDM-produced printouts is known to be high [354]. The depth of the cracks is estimated from the pictures to be 5 mm at maximum. The cracks are not expected to cause any major issues, especially because the sidewalls of the preform are machined down by 2.5 mm before drawing. The use of heated printing chamber could help addressing the problem of both warping and cracks.

It can be seen that better transparency was observed towards the bottom of the printout (Figure 4-8(c) and Figure 4-9). This phenomenon is believed to be due to the effect of heating from the printing bed. Since the distance between nozzle and printing bed increases during printing, the influence of the heat

from the printing bed decreases progressively. The transparency of the middle section of the preform, from which the fibre is drawn, is therefore closer to that of the cold bed test printout (see Figure 4-1(d)).

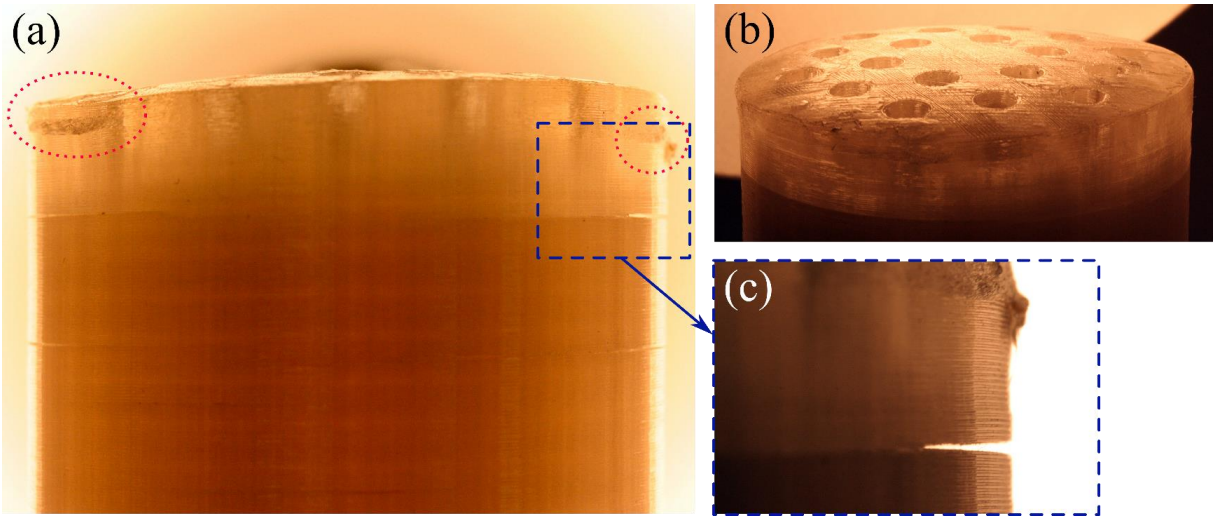

Figure 4-9. (a) Side view of the bottom end of the printed preform (backlit). The red dotted rings indicate material aggregated on the sidewalls during printing. The blue square shows an example of crack in the sidewall. (b) View of the curved bottom surface of the preform (compared to the flat top surface shown in Figure 4-8(d)). (c) Magnified view of a crack in the sidewall and aggregated printing material. Also note higher transparency of the preform towards the bottom surface in (a) and (b).

4.5.3 Preform post-processing

The finished preform was annealed in a conventional oven at 130 °C for 4 weeks to remove air bubbles trapped in it and, hence, increase transparency [30, 31]. It was then machined in order to remove the rough outer surface and make its dimensions suitable for cane drawing using the polymer draw tower described in Section 3.2. The resulting length and outer diameter were 100 mm and 60 mm, respectively. The preform was then further annealed prior to drawing for 4 more weeks under the same conditions. The resulting preform was found to be of high quality, allowing it to be successfully drawn to fibre, which is described in detail in Chapter 5.

4.6 Fabrication of solid-core PMMA preform

Following the successful fabrication of microstructured PC fibre from the 3D-printed solid-core PC preform (see Section 4.5), an attempt was made to draw fibre from PMMA based on the same design. The results are described in this section. Commercial PMMA filament (like in Section 4.2) was used to fabricate the PMMA preform, and 3D printer settings optimised for PMMA (Section 4.2) were adopted. The resulting preform was printed in 13 days, 9 h and 46 min (~322 h), consuming ~306 g of the material (see Figure 4-10 and Figure 4-11).

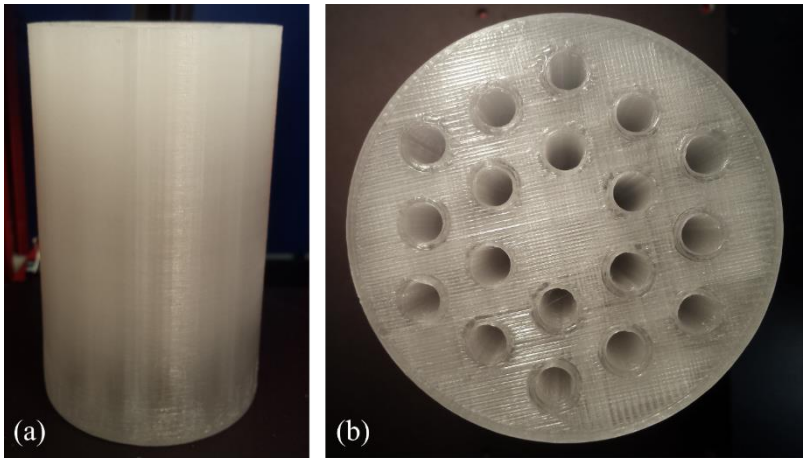

Figure 4-10. (a) Side view of the fabricated solid-core PMMA preform (positioned as printed). Note higher transparency towards the bottom. See also Figure 4-11. (b) Top view of the SC PMMA preform.

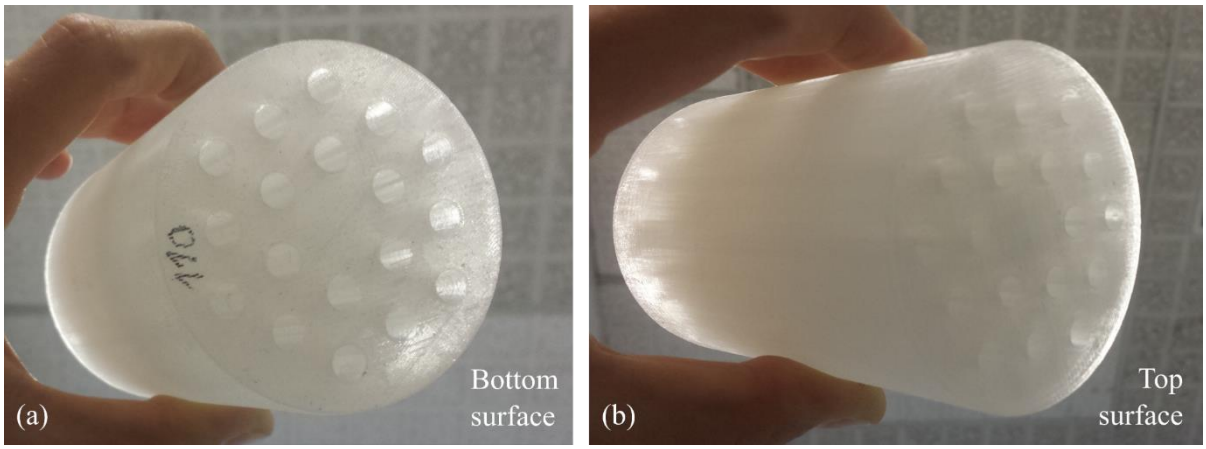

Figure 4-11. Comparison of transparency of top and bottom regions: (a) bottom surface facing viewer, (b) top surface facing viewer. Note higher transparency towards the bottom surface as discussed in Section 4.2.

Compared to the SC PC preform (Section 4.5), the SC PMMA preform showed fewer problems resulting from the temperature difference within the printout (cracks, warping, issues with adhesion to the printing bed). The discussion of differences between PC and PMMA HC preform, presented in Section 4.4, pertains equally to SC preforms (this section and Section 4.5).

In the next step, the preform was annealed in order to remove air bubbles trapped in it during 3D printing. This had been previously found to bring visible increase in transparency of the PC preform (Section 4.5.3). The annealing process was performed at DTU by Andrea Fasano (Department of Mechanical Engineering, supervisor: Henrik K. Rasmussen). This was the first attempt to anneal a 3D-printed PMMA preform. The PMMA preform described earlier was hollow-core (Section 4.2), in which case material transparency was not as important, and hence it had not been annealed to avoid complicating the manufacturing process. The standard approach at DTU to anneal preforms prior to

drawing is to gradually increase temperature up to a point that is near the glass transition temperature for the specific material. During annealing, the SC PMMA preform started deforming abruptly after reaching a certain temperature, despite it only rising very slowly. This had not been observed previously for any preform made at DTU by drilling cast or extruded materials and, thus, had not been expected. The shape of the preform was deformed to the point that it was unsuitable for drawing.

It is speculated that such behaviour might be due to the commercial 3D-printing PMMA filament containing some proportion of unreacted monomers, which rendered the printout thermally unstable at elevated temperature. If this was the case, unreacted monomers in the filament would be considered a flaw in the filament fabrication process. However, it should be noted that the 3D-printer filament fabrication is not specifically optimised for preform annealing conditions (temperature, pressure, and processing time). Moreover, exact composition of commercially available 3D printing filaments is normally not disclosed. Possibly, using a tailor-made filament of precisely known composition and containing no unreacted monomers would help tackle thermal instability of the PMMA preform. Another advantage of that approach would be the possibility to optimise transparency of the filament material at the same time to make it suitable for optical use. No FDM filaments optimised for optical applications were available commercially at the time of this research. It should be noted that thermal instability of the PMMA material used might have also been at the origin of the geometrical distortion of the HC PMMA preform after drawing to cane that was described in Section 4.3.

Despite presumed thermal instability, the SC PMMA preform could have in principle been reprinted and attempted to be drawn without annealing. However, as it was stated in Section 4.5, annealing the PC preform improved its optical transparency much. Yet, attenuation of the fibre drawn from it was high (Chapter 5). Thus, it was suspected that, even if a fibre could be successfully drawn from a non-annealed 3D-printed HC preform, its very high attenuation value would prevent any practical application.

4.7 Conclusions

In this chapter, five preforms were presented: three hollow-core ones (one made of PC, the two other of PMMA) and two solid-core ones (one made of PC, the other of PMMA). Two designs for hollow-core preforms were shown, where the new one was fed back with the drawing result of the preform based on the old one. The hollow-core PMMA preform was successfully drawn to cane, which was the first reported HC cane for POF drawing.

Several issues regarding 3D printing preforms for POF drawing were reported, many of which were addressed during this research, while some solutions were suggested for the other. First, producing printouts of high transparency by means of the FDM technique was found to be challenging. Low transparency was due to air bubbles trapped within printout, which was seen as an inherent problem of this technique. The transparency optimisation process led to adjusting 3D printing parameters to yield:

an appropriate feed rate and thread line spacing to exactly feed in required amount of material, a relatively high but appropriate nozzle temperature (depending on polymer used), and a low printing speed (the lower, the better). The PC preform transparency was also increased by post-print annealing. Secondly, difficulties in printing PMMA at high nozzle temperature and low printing speed were reported, which were ascribed to relatively high water absorption of PMMA compared to other polymers. This was overcome by drying the PMMA filament at 85 °C prior to printing, as high temperature and low speed are required for transparency optimisation and, hence, could not be compromised. Thirdly, PC preform warping and cracks on its surface were described. They are believed to be caused by internal stress of printout due to high temperature difference between the printout and the nozzle. Whilst in general not posing a problem for fibre drawing, these difficulties may be decreased by the use of a heated printing chamber. This should also be of benefit to overall transparency of printout or should allow the printing time to be decreased, or both. Finally, preforms made of PMMA were found to be damaged during annealing, which was, speculatively, coming from the presence of unreacted monomers in the commercial filament used. Tailor-made printing filament of precisely known chemical composition might help addressing the problem. Potentially, this could also improve transparency of PC preforms if high purity filament made from optical-quality material is used.

The research presented in this chapter proved that the FDM technique is capable of 3D-printing POF preforms that are drawable: a hollow-core PMMA preform was drawn to cane (Section 4.3), and Chapter 5 reports a fibre drawn from the solid-core PC preform. While still some issues persist, these prove the feasibility of the FDM technique to produce preforms for POF drawing, which can enable producing preforms of shapes that would be very difficult to fabricate by other means.

Chapter 5 Fabrication and characterisation of solid-core PC mPOF with FBG inscription

The work described in this chapter follows on from Section 4.5, which described 3D printing, characterisation, and annealing of the solid-core PC mPOF preform. This chapter introduces a fibre drawn from this preform. First, fibre drawing is presented. The resulting POF is characterised, which includes cleaving and light coupling to core, modelling of light propagation, cut-back attenuation measurements and dynamic thermomechanical analysis, including calculation of thermal expansion coefficient. Finally, FBGs inscribed with different lasers and techniques are shown and characterised, and the thermo-optic coefficient of the fibre is calculated. Three lasers were used for the inscription: 325 nm continuous wave, 517 nm pulsed femtosecond and 248 nm nanosecond.

A number of novelties are reported in this chapter. First, the SC PC fibre was the first microstructured SC fibre drawn from 3D-printed preform and the first such fibre to be single-mode (at both 870 nm and 1550 nm). Secondly, the SC PC fibre displayed the lowest attenuation of all the POFs drawn from 3D-printed preforms over the entire measured spectrum (550-2200 nm). Thirdly, the FBG inscribed in POF drawn from 3D-printed preform was the first to be reported.

The core part of this chapter has been published in IEEE Sensors Journal [355], while a more detailed description is presented in this thesis.

5.1 Collaboration Statement

The work described in this section was done in collaboration with the following partners:

- Getinet Woyessa (supervisor: Ole Bang) from Department of Photonics Engineering, Technical University of Denmark (DTU)
- Rui Min (supervisor: Beatriz Ortega and Carlos A. F. Marques) from ITEAM Research Institute, Universitat Politècnica de València, Valencia, Spain
- Arnaldo Leal-Junior (supervisors: Anselmo Frizera-Neto, Carlos A. F. Marques, and Maria José Pontes) from Telecommunications Laboratory (LABTEL), Electrical Engineering Department, Federal University of Espírito Santo, Brazil
- Antreas Theodosiou (supervisor: Kyriacos Kalli) from Photonics and Optical Sensors Research Laboratory, Cyprus University of Technology
- Carlos A. F. Marques from Instituto de Telecomunicações, University of Aveiro, Portugal

Getinet Woyessa drew the preform to cane and fibre Rui Min and Carlos Marques performed cut-back attenuation measurements of the resulting fibre, which were recalculated into attenuation by the author. Both corresponding plots were prepared by the author. Analysis of the results was performed by the author. Dynamic mechanical analysis of the fibre was conducted by Arnaldo Leal-Junior with extensive consultation with the author. The figures were prepared jointly by Arnaldo Leal-Junior and the author. Following calculation and discussion of CTE were performed by the author. Rui Min and Carlos Marques recorded spectra and performed thermal analysis of the FBG fabricated by the author (FBG1). The author did calculations for and prepared the corresponding plots. Calculation and discussion of thermo-optic coefficient were conducted by the author. The FBG inscribed by femtosecond laser (FBG2) was manufactured and characterised by Antreas Theodosiou, who also provided the respective figures. Rui Min and Carlos Marques fabricated the FBG inscribed by a krypton-fluoride laser (FBG3) and measured the spectrum, based on which the author did calculations for and prepared the corresponding plot.

The descriptions of the experiments were prepared by the author based on text and data provided by the collaborators involved in each experiment. All other text, figures, descriptions, simulations, calculations, and discussions were produced solely by the author, who also manufactured all other samples and performed all other experiments.

5.2 Fibre drawing and characterisation

5.2.1 Fibre drawing

The SC PC preform fabricated in Section 4.5 was used to manufacture the fibre. The fibre was produced using the two-step heat and draw method [26], where, first, the preform was drawn into intermediate canes at a temperature of 180 °C. The canes were 6 mm in diameter and 50 cm in length. Each cane was subsequently inserted in a PC sleeving tube. The resulting composite canes were annealed for 10 days at 130 °C to ensure that all bubbles trapped in the sleeving tube and cane were removed. Then, one of the composite canes was drawn to fibre at a temperature of 185 °C. In the remaining part of the text, the resulting fibre is referred to as 3D PC mPOF. According to Equation (2-17), the draw ratio of the initial preform (i.e., not the sleeving tubes) was calculated to be ~5.17×10^6.

5.2.2 Fibre cleaving and light coupling to core

Figure 5-1(a) shows a microscopic image of a cleaved facet of the 3D PC mPOF (blade temperature ≈ 75 °C). The darker inner region corresponds to the preform, and the lighter outer one , to the sleeving tube. The air voids at the interface of the two regions come from the sleeving process. They are often present in POFs manufactured using the two-step drawing method and do not hinder fibre operation. In the magnified image (Figure 5-1(b)), the core is clearly visible. Its diameter was measured to be ~8 μm.

The literature reports the optimal cleaving temperature for a PC mPOF fibre to be 80°C [105, 107]. In this instance a temperature of 75°C yielded the best cleave quality for the temperature values that were tested, where both the fibre and the blade were heated. However, this temperature was possibly still a little too high for this fibre as can be inferred from the slight ellipticity of the microstructure holes [356]. In this research, fibre cleaving was performed manually using a blade and a hot plate, which only gave limited control over the process. Further optimization of cleaving temperature was not undertaken as the cleave quality was found enough for light coupling. Such optimization often involves specialized cleaving apparatus and is a separate research question [356-358] beyond the scope of this work.

Red light from a fibre-coupled semiconductor laser (wavelength ~638 nm, optical power ~2.5-5.0 mW) was butt-coupled into the fibre (fibre length = 38.1 mm) and projected onto a screen (experimental set-up in Figure 5-2) to observe the clear core guidance, shown in Figure 5-1(c). Core guidance was visible by eye over fibre lengths of ~10 cm. For this wavelength of light, only cladding guidance from the outer tube was observed at longer fibre lengths (see Figure 5-1(d)).

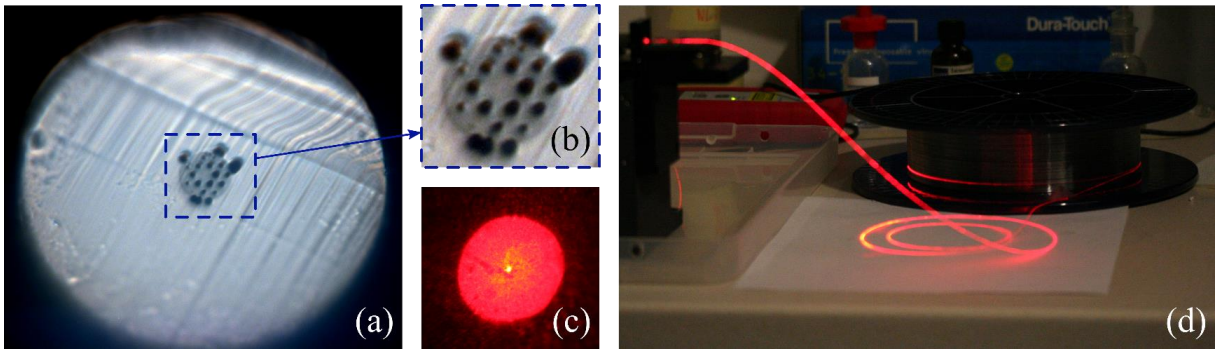

Figure 5-1. (a) View of a cleaved fibre facet (blade temperature = 75 °C; fibre outer diameter = 170 µm, fibre core diameter = 8 µm). (b) Magnified view of the fibre core. (c) Image of a fibre end projected on screen (fibre length of 38.1 mm) with clear core guidance. See Figure 5-2 for the experimental set-up. (d) Photograph of butt-coupling to the fibre on spool.

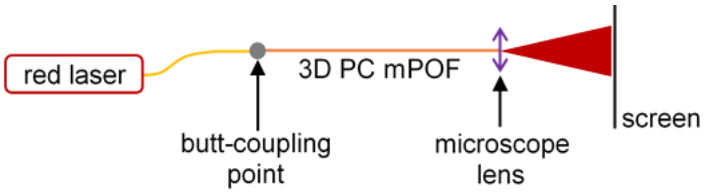

Figure 5-2. Schematic showing the experimental set-up used for checking core guidance (fibre length = 38.1 mm). The image observed on the screen is shown in Figure 5-1(c).

5.2.3 Simulation of the confinement loss and modality of the fibre

For a microstructured fibre to display endlessly single-mode behaviour, the d/Λ ratio should be less than 0.406 [187]. Here the chosen dimensions of hole diameter and pitch of the preform would result in $d/\Lambda = 0.5$. After drawing, the geometry of the fibre changed and the diameters of the holes in the inner ring (d_{inner}) were visibly bigger than those in the outer ring (d_{outer}), the measured geometry being: $d_{inner} = 2.7$ µm, $d_{outer} = 1.45$ µm, $\Lambda = 5.4$ µm (see Figure 5-1(b)).

For non-endlessly mPOF, there is no strict criterium to differentiate single-mode and multi-mode behaviour. As opposed to step-index fibres, all modes in microstructured optical fibres have some non-zero confinement loss due to finite number of microstructure rings. However, a large enough number of rings (often 8) ensures that the confinement loss is negligible compared to other loss mechanisms [25, 26]. Hence, fibre modality is often designated based on acceptable value of loss for a particular application, and in the case of high loss for second mode, fibre can be considered "essentially" single-mode. A useful approximation of the cut-off wavelength based on fibre geometrical parameters was presented in [187]. There, the cut-off wavelength was defined as the transition between delocalised single-mode (the second mode not being localised in core) and localised multi-mode behaviour (second and possibly higher order modes localised in core). However, this cut-off wavelength was defined for an ideal silica fibre made of 8 rings of even holes.

In order to assess the confinement loss and modality of the fibre, COMSOL (v. 4.3) [95] and CUDOS (v. 2) [192-194] software packages were used to run simulations on the described geometry. They gave very similar results regarding real part of effective refractive index (Re(n_{eff})) and modal patterns, while the imaginary part of n_{eff} (Im(n_{eff})) was more easily resolved by CUDOS. Simulations were performed for the two wavelengths (870 nm and 1550 nm, see Figure 5-3 and Table 5-1) at which FBGs were inscribed (Section 5.3). Material refractive indexes used were 1.577 and 1.567, respectively [107]. Simulations at 1550 nm resulted in virtually the same plots as at 870 nm (Figure 5-3).

As it was mentioned in Section 2.5.1, the McIsaac's convention to designation of modes based on symmetry is more appropriate for mOFs than the naming traditionally used for conventional optical fibres (HE, EH, TM, TE). Hence, the McIsaac's approach is also used in simulations of 3D PC mPOF. Its symmetry group is C_{6v}, which gives 8 classes of modes: 4 non-degenerate ones (1, 2, 7, 8) and two pairs of two-fold degenerate classes (3 and 4, 5 and 6).

From simulation, the confinement loss of the second mode was found to be much larger than the fundamental mode at both 870 nm and 1550 nm (220 times and 122 times, respectively). The second least lossy mode at both wavelengths (equivalents of E^{x}_{23} and E^{y}_{23} modes of step-index waveguide of rectangular symmetry) showed losses 41 times higher (870 nm) and 48 times higher (1550 nm) than the fundamental. These values imply that the confinement loss would prevent higher order modes from propagating over more than a few cm, while guiding the fundamental mode over hundreds of cm. Hence, 3D PC mPOF can be considered single-moded at both 870 nm and 1550 nm. Effective single-mode behaviour can also be inferred from modal field patterns (Figure 5-3) that show that the second mode is not fully localised. This is especially visible in electric field magnitude plot and is supported by the relatively high loss value.

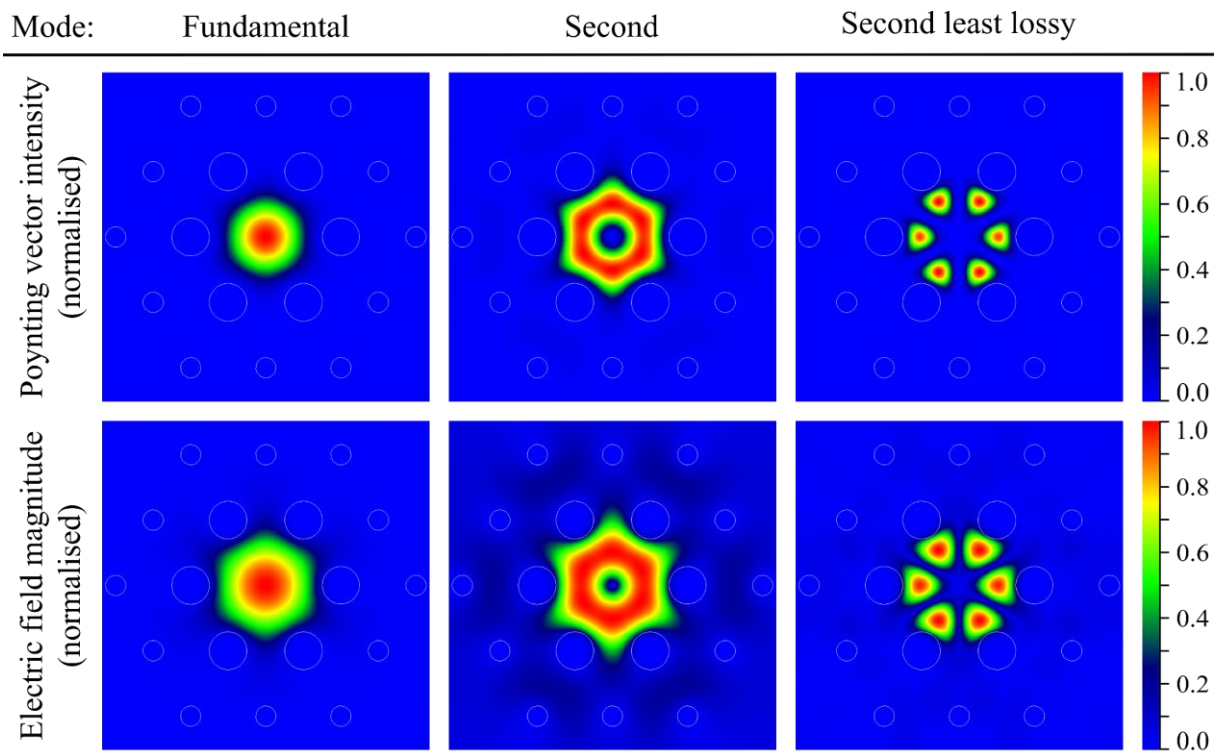

Figure 5-3. Poynting vector intensity and electric field magnitude for the fundamental, second and second least lossy modes simulated for 3D PC mPOF at 870 nm in CUDOS.

Table 5-1. Results of CUDOS simulations for fundamental, second and second least lossy modes for 870 nm and 1550 nm

Mode	Fundamental	Second	Second least lossy
Mode class	3/4 (degenerate)	2 (non-degenerate)	5/6 (degenerate)
Step-index waveguide equivalent	HE_{11} (circular symmetry)	TE_{01} (circular symmetry)	$E^{x/y}_{23}$ (rectangular symmetry)
	Wavelength = 870 nm		
Re(n_{eff})	1.57535279891	1.57296137794	1.56379542212
Im(n_{eff})	$1.75892967786 \times 10^{-7}$	$3.86335837268 \times 10^{-5}$	$7.15216328426 \times 10^{-6}$
Confinement loss (dB/cm)	0.11033757	24.23482671	4.48654826
	Wavelength = 1550 nm		
Re(n_{eff})	1.56194339477	1.55462887006	1.52603245572
Im(n_{eff})	$1.23636037073 \times 10^{-6}$	$1.50868839412 \times 10^{-4}$	$5.90364581028 \times 10^{-5}$
Confinement loss (dB/cm)	0.4353189302	53.1204843936	20.7865670839

To investigate fibre modality further, fibre parameters were compared with [187] to check whether the fibre is in delocalised single-mode or localised multi-mode operation region. For comparison, the hole diameter was averaged over both inner and outer ring of the actual geometry to give the following: d = 2.4 μm, Λ = 5.4 μm, $d/\Lambda = 0.\dot{4}$. These results compared to [187] also suggest the fibre is in delocalised single-mode operation at 870 nm and 1550 nm.

5.2.4 Fibre attenuation measurements

The fibre attenuation was measured using the cut-back method [359], in which the attenuation is characterised using the transmission spectra for different lengths of the same piece of fibre (starting with the longest chosen fibre length and shortening it each time after measuring the transmission spectrum).

Light from a supercontinuum source (Fianium White laser WL-SC-400) was launched via a silica fibre into one end of the 3D PC mPOF under test. The two fibres were fixed together using a ceramic ferrule. The other end of the 3D PC mPOF was placed in a second ceramic ferrule and connected directly to an optical spectrum analyser (OSA). Two OSAs were used: a Yokogawa AQ6373B for the wavelength range 400-1200 nm and a Yokogawa AQ6370 for the 1200-2400 nm range. Transmission spectra were recorded for 7 fibre lengths, starting at 86 cm and finishing at 26 cm, giving 10 cm length decrements between measurements. In order to minimise the end face influence and maximise transmission, the fibre was cleaved and tested a few times at each fibre length. This resulted in recording multiple spectra for every fibre length, and the ones yielding maximal transmission are shown in Figure 5-4. The change of each fibre length due to making a few cleaves was negligibly small (1-2 mm) and, hence, its influence could be neglected.

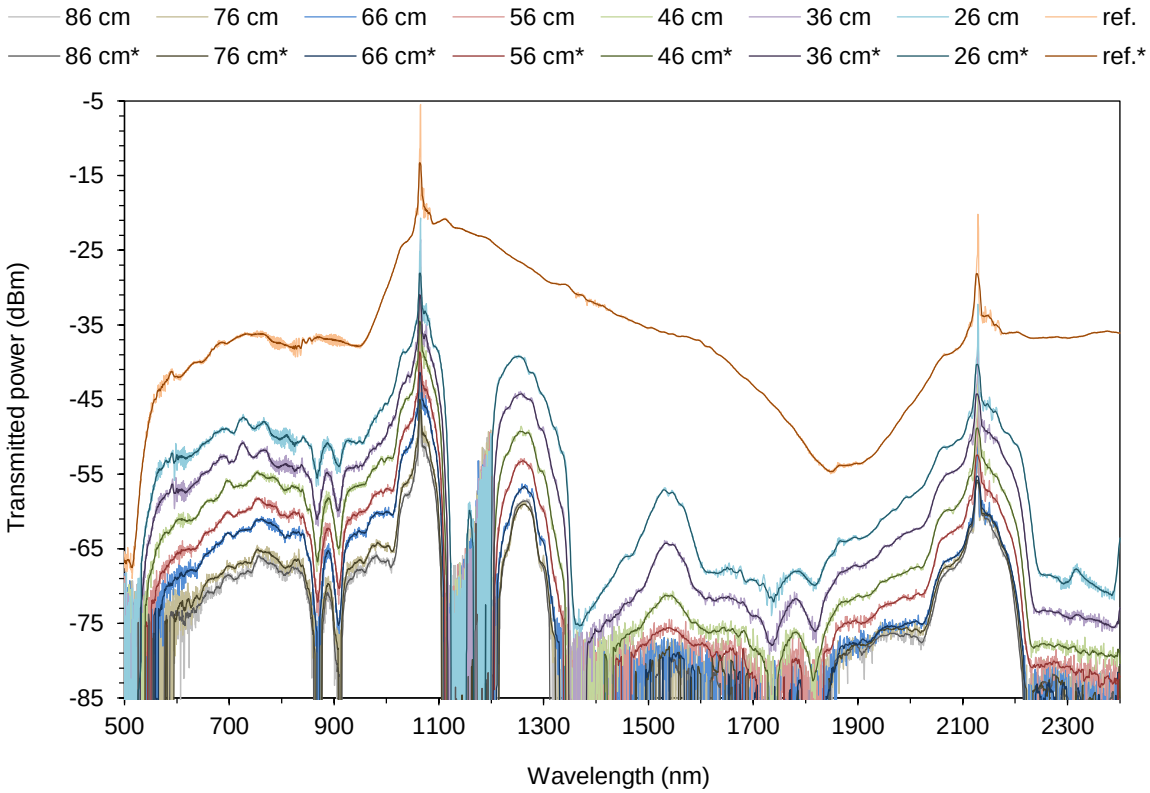

Figure 5-4. Transmission spectra for different lengths of the same piece of 3D PC mPOF used for cut-back attenuation calculations. Reference spectrum (marked "ref.") comes from the supercontinuum light source attached directly to OSA. In order to reduce noise, moving averages (darker lines, data series marked with *) have been plotted over original spectra (lighter lines). In this chapter, moving averages for each spectral point have been calculated using 5 neighbours to its left and right, resulting in 11 spectral points being averaged over.

Due to the low transmission power for the longer fibre lengths only the data from the three shortest fibre lengths (26, 36, and 46 cm) was used for calculating the attenuation. For each spectral point, the attenuation plot (Figure 5-5) shows the slope resulting from the linear regression (least squares method) of the 26, 36, and 46 cm data series. In some spectral regions (1110-1205 nm, 1340-1435 nm, 1729-1747 nm), the calculated attenuation curve was very noisy due to bands of high material absorption, and hence the results in those regions are not credible. The data in the spectral region below 550 nm was discarded due to low light source intensity. The shape of the attenuation spectrum seems to align well with this measured for the PC fibre draw from a drilled preform [107], except for wavelengths below 750 nm, which is the range that would be more susceptible to scattering losses at the air-polymer interface in the hole region.

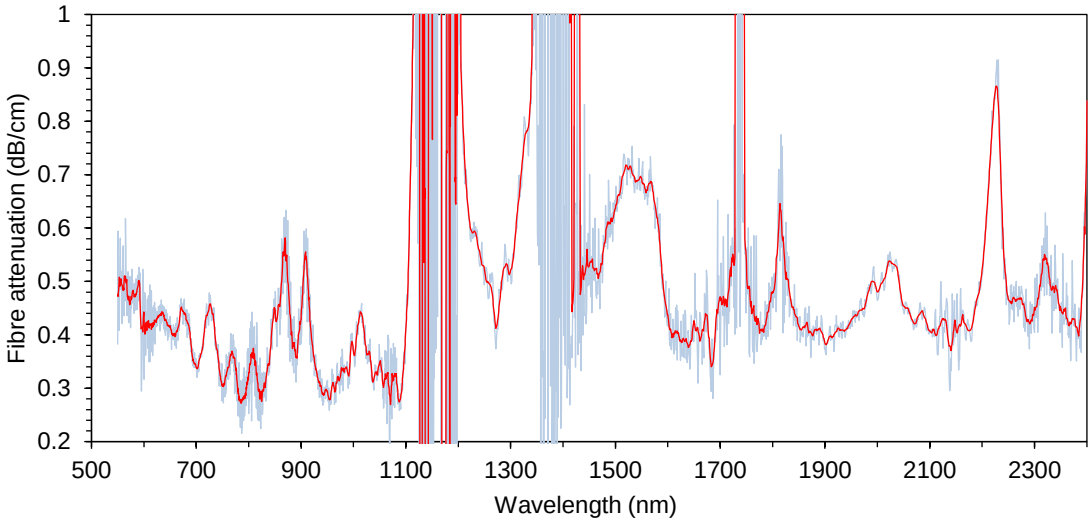

Figure 5-5. Attenuation plot of the 3D PC mPOF calculated based on the transmission spectra for the three shortest fibre lengths in Figure 5-4 (26, 36, and 46 cm). Moving average (red) of the attenuation has been plotted over the original spectrum (blue) to reduce noise.

It must be acknowledged that, due to the high fibre attenuation, the fibre lengths used for attenuation calculations had to be rather short. As the cladding transmission of red light (~638 nm wavelength) was visible to eye over tens of cm (see Figure 5-1(d)), it is likely that Figure 5-4 is the transmission through the combined cladding and core. Hence, it is uncertain how accurate the attenuation plot is for the 3D-printed core.

The lowest attenuation of ~0.27 dB/cm for 3D PC mPOF is found in a few spectral regions (780-785 nm, 820-825 nm, 953-956 nm, 1070-1090 nm). Attenuation calculated in Figure 5-5 is the lowest reported in the literature so far for solid-core POFs (including step-index ones) drawn from the 3D-printed preform at any wavelength (see Table 5-2). However, Table 5-2 also shows that losses for fibres drawn from mechanically casted and drilled PC preforms are up to 8 times lower, which leaves room for optimisation.

There are a number of potential reasons for the high fibre attenuation. It might be due to lower transparency of the 3D printed preform compared to the sleeving tube (note darker region corresponding to the preform in Figure 5-1(a), (b)). Also, the transparency of the 3D printing PC filament used was not optimised for optical purposes, and the preform was manufactured in open laboratory conditions, allowing airborne impurities to be incorporated into the printout. Another factor potentially lowering the core guidance might be related to the microstructure design. Normally, three rings of microstructure are considered as the minimum requirement for assuring good confinement of core modes so that they are not outcoupled to cladding. However, in this research, a two-ring microstructure was used in order not to compromise 3D printing resolution. Furthermore, the holes of the outer ring of the microstructure were much smaller than those of the inner ring; and at some points, they were not present at all (see

Figure 5-1(b)). This was shown in the simulations to deteriorate confinement of guided modes. Finally, the facet cleaving quality, which leaves much room for optimization, might be limiting the maximal core guidance length. All the listed reasons can be addressed during further research to improve the core guiding conditions.

Compared to simulations in Section 5.2.3, it can be noted that confinement loss (~0.11 dB/cm) accounts for ~22% of total loss at 870 nm (~0.50 dB/cm). This ratio changes at 1550 nm, where confinement loss contributes as much as ~63% (~0.44 dB/cm) of the total loss (~0.69 dB/cm) although for the measurement the noise level at 1550 nm is relatively high.

Table 5-2. Comparison of attenuation (dB/cm) of solid-core POFs from 3D-printed and drilled preforms[a]

	3D-printed preforms				Drilled preforms	
Wavelength (nm)	SI-POF [32] (PC+ABS)	Air-structured POF [30] (SBP)	SI-POF [31] (SBP+PETG)	3D PC mPOF (this chapter, PC)[b]	mPOF [107] (PC)	Optimised mPOF [105] (PC)
543			0.64	0.53		
632-633	0.7-1.8[c]	~1.5		0.44	0.16	0.055
819				0.29		0.041
833.5				0.32	0.089	
1047-1052			0.44	~0.34[d]		
1064		~0.75		0.33		
1520-1560			0.94	~0.68[d]		
1550		~1.51		0.69		

[a]Fibre materials are given in brackets after fibre name; for step-index (SI) fibres, both core and cladding materials, respectively, are given.

[b]For full attenuation spectrum, see Figure 5-5.

[c]Attenuation depending on 3D-printed core shape: square core – 1.2 dB/cm; triangular core – 1.3 dB/cm; rectangular core – 1.8 dB/cm. Attenuation of 0.7 dB/cm measured for circular core of solid material (not 3D-printed). [d]Average values for the wavelength range.

5.2.5 Dynamic mechanical analysis of the fibre

Dynamic mechanical analysis (DMA) was used to evaluate the mechanical characteristic of the fibre. DMA is a well-established method for polymer characterisation used in different fields including industrial [360], automotive [361], aircraft [362] and biological applications [363]. In this technique, a sample is fixed at one end, and an oscillatory tensile load is applied on the other. This results in performing sequential strain cycles with controlled frequency and displacement. Moreover, the method can also involve temperature variation. This then allows evaluating dependency of Young's modulus of sample on all the mentioned parameters (strain, temperature and strain cycle frequency). Such analysis has previously been used to characterise POFs of various structures and made of different materials, including PMMA microstructured polymer optical fibres (mPOFs) [104], PMMA step-index fibres [364], mPOFs of different materials (Topas 5013S-04, Zeonex 480R, polycarbonate) [112], and CYTOP graded-index fibres [365].

Dynamic mechanical analysis (DMA) was performed on the 3D PC mPOF to evaluate the Young's modulus with respect to temperature and strain cycle frequency (following standard ASTM D4065), and thermal expansion coefficient of the fibre (standard ASTM E831-14). The equipment used for the stress-strain cycles in the strain limit up to 11% was a DMA 8000 (Perkin Elmer, USA).

The first test performed was the implementation of a series of stress-strain cycles, which allowed the Young's modulus of the 3D PC mPOF at room temperature to be estimated as 2.47±0.10 GPa (determination coefficient $R^2 = 0.9979$) – see Figure 5-6. The confidence interval (CI) for measurement errors throughout this section is 95%, unless otherwise noted. The Young's modulus was estimated through the slope of the linear region of the stress-strain curve (in the range 0.05-0.3%). From Figure 5-6, it is also possible to estimate yield stress, which is stress at which stress-strain curve shows non-linear behaviour. Such non-linear behaviour was noted for the stress higher than about 60 MPa. Yield stress is within the range for the PC material (59-70 MPa [110]), while Young's modulus slightly exceeds its upper range value (2-2.44 GPa [110]). Moreover, the Young's modulus obtained for the 3D PC mPOF is close to the one estimated for the drilled preform 3-ring PC mPOF in [111] (2.70±0.01 GPa), [112] (2.89±0.30 GPa), and [107] (3.03±0.10 GPa).

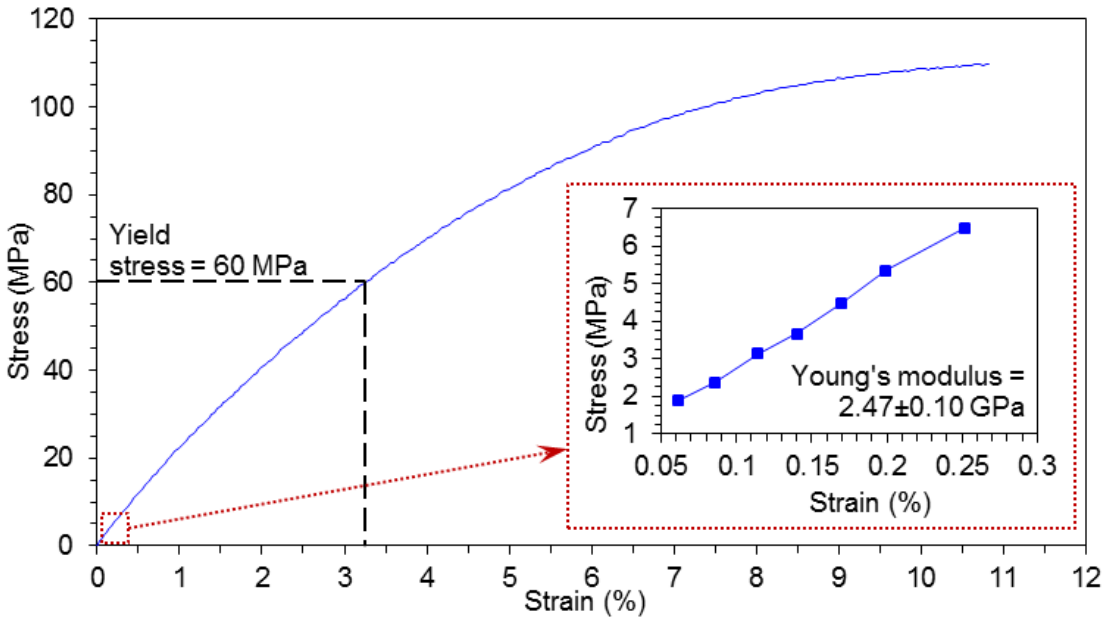

Figure 5-6. Stress-strain cycles and Young's modulus of the 3D PC mPOF.

In the Young's modulus characterisation with respect to temperature, the strain cycle frequency used was 1 Hz, while temperature was varied from 25 °C to 140 °C. The strain range was 0-0.2%. The 3D PC mPOF exhibits a linear decrease of its Young's modulus with respect to a temperature increase with a slope of −4.775±0.094 MPa/°C (R^2 = 0.9968; see Figure 5-7(a)). The maximum Young's modulus variation is similar to that obtained in [112] for a drilled PC mPOF (about 0.5 GPa). However, for the 3D PC mPOF, the Young's modulus decrease shows higher linearity than in [112].

Figure 5-7(b) shows the Young's modulus variation with respect to strain cycle frequency. The temperature was about 27 °C, the frequency range was 0.01-10 Hz, and the strain range was 0-0.5%. The fibre exhibits an increase of Young's modulus with frequency until 5 Hz, after which sharp decrease of Young's modulus is noted. Such behaviour was also observed for PMMA, Topas 5013, Zeonex 480R, and PC mPOFs in [112]. However, in the case of the 3D PC mPOF, the Young's modulus variation with respect to frequency is higher, and the slope of 302±14 MPa/$\log_{10}$(Hz) (R^2 = 0.9959) was obtained in the range 0.01-5 Hz. This seems to contradict the results reported in [111], showing no Young's modulus dependence on frequency, which might be due to different measurement equipment.

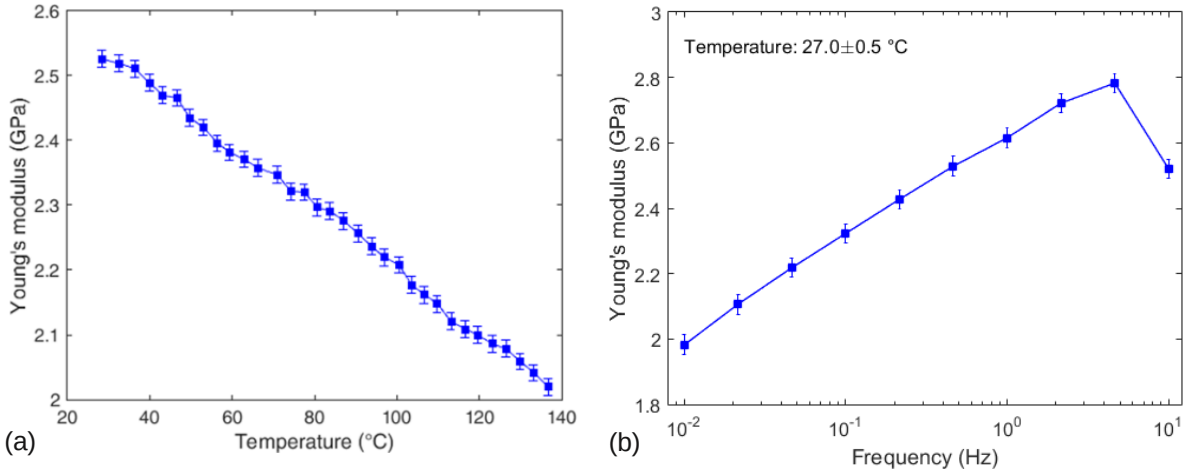

Figure 5-7. Young's modulus variation for the 3D PC mPOF as a function of temperature (a) and strain cycle frequency (b). Error bars show mean deviation.

Finally, the linear thermal expansion coefficient (linear CTE, LCTE) of the 3D PC mPOF was evaluated using TMA mode of the DMA 8000 device. A small constant tensile load (F = 0.01 N) was applied on the fibre, and fibre strain was observed while changing temperature (see Figure 5-8). Total variation of fibre strain (ε_{total}) with temperature was ascribed to two factors, thermal expansion (ε_{TE}) and different response to stress caused by tensile load (ε_{σ}), coming from dependence of Young's modulus on temperature (measured earlier) [366]:

$$\varepsilon_{\mathrm{total}}(\Delta T) = \varepsilon_{\mathrm{TE}}(\Delta T) + \varepsilon_{\sigma}(\Delta T). \tag{5-1}$$

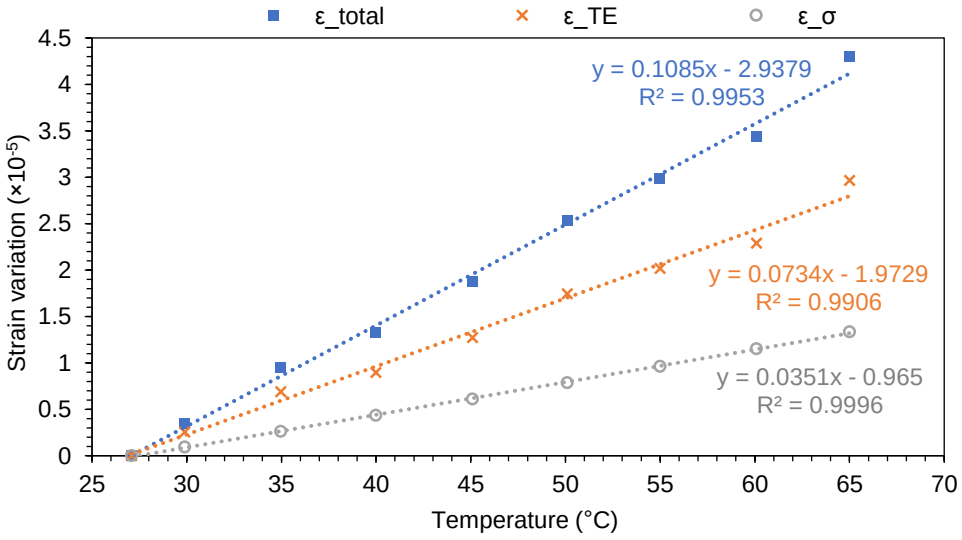

Figure 5-8. Strain variation of the 3D PC mPOF (ε_{total}) as a function of temperature. It was split into strain due to thermal expansion (ε_{TE}) and different response to stress caused by tensile load of 0.01 N, coming from dependence of Young's modulus on temperature (ε_{σ}). See Equations (5-1)-(5-3) for details.

In the TMA method, ε_σ can often be neglected because it normally is much smaller than ε_{TE} due to very small value of force from tensile load. However, in case of this fibre, ε_{total} was found to be so small that neglecting ε_σ would deviate the value of LCTE. ε_σ and ε_{TE} can be written as:

$$\varepsilon_{TE}(\Delta T) = \alpha_{\parallel} \cdot \Delta T \tag{5-2}$$

$$\varepsilon_{\sigma}(\Delta T) = \frac{\sigma}{E(\Delta T)} - \frac{\sigma}{E_0} = \frac{\sigma}{\frac{dE}{dT} \cdot \Delta T + E_0} - \frac{\sigma}{E_0} \tag{5-3}$$

where: $\alpha_{\parallel}$ (°C^{-1}) is the linear CTE along the fibre axis, ΔT (°C) is the temperature change above the initial temperature of the experiment (T_0 = 27.10±0.01 °C), $\sigma = F/A$ (Pa) and is the stress on the fibre coming from tensile load F = 0.01±0.002 N acting on fibre area A (m^2), $E(\Delta T) = dE/dT \cdot \Delta T + E_0$ (Pa) and is the Young's modulus of the fibre, dE/dT (Pa/°C) is the dependence of Young's modulus on temperature, and E_0 (Pa) is the Young's modulus at T_0. In Equation (5-3), subtraction of the second term (σ/E_0) is required to make ε_σ start from zero at T_0.

By measuring the cross-sectional area of the fibre from the microscope image (A = 22,500±500 μm^2), σ was estimated to be 4.45±0.98×10^5 Pa. This stress caused the fibre to be prestrained by 175±39 με at the beginning of the experiment (at T_0), which is the value of the second term (σ/E_0) in Equation (5-3). Changes to ε_σ coming from decrease of cross-sectional area of the fibre upon straining were found to be very small and hence were ignored. Based on the experiment described earlier (see Figure 5-7), dE/dT and E_0 were calculated to be -4.775±0.094 MPa/°C and 2.5479±0.0084 GPa, respectively. Inserting these values to Equations (5-1)-(5-3) allowed to plot ε_σ and ε_{TE} along with the experimental values of ε_{total} in Figure 5-8. The value of LCTE along the fibre axis ($\alpha_{\parallel}$) coming from linear regression was 7.34±0.53×10^{-7} °C^{-1} (CI = 95%).

This LCTE is about two orders of magnitude smaller than those usually encountered in the literature for PC material, which are in the range of 5.0-8.1×10^{-5} °C^{-1} (in bulk as well as in the form of thin films and pellets) [71, 99, 141, 142, 144-146]. For this reason, special care was taken to ascertain the obtained value is accurate. The calculated LCTE value was cross-validated by manual calculations to check the experimental error yielded by the total differential method and gave the result of 7.3±1.5×10^{-7} °C^{-1}. The larger experimental error obtained does not change the two orders of magnitude difference between the calculated value and the literature ones. The discrepancy between the experimental value of LCTE of the fibre and the literature values for bulk PC can be ascribed to the expected high anisotropy of the fibre, as explained in Section 2.3. This will be further discussed during the analysis of the thermo-optic coefficient of the 3D PC mPOF in the next section.

5.3 Fibre Bragg grating inscription and testing

5.3.1 Inscription using a continuous-wave helium-cadmium laser

A fibre Bragg grating (FBG1) was inscribed in the manufactured PC fibre by a phase-mask technique [69] using a Kimmon 325 nm CW HeCd laser (model IK3301 R-G). The laser beam (power ~23 mW and ~1.2 mm diameter) was focused on the fibre through a cylindrical lens of 11 cm focal length. An Ibsen Photonics custom-made phase mask of 557.50 nm pitch was placed directly on the fibre. The inscription time was 13 min. FBG1 was inscribed 10-15 mm away from the butt-coupling fibre end in order to minimise losses of optical power due to fibre attenuation. After the inscription, FBG1 was interrogated through a 3dB coupler (see Figure 5-9) using a supercontinuum light source Fianium White laser WL-SC-400 and a Yokogawa AQ6373B optical spectrum analyser. The reflection spectrum recorded by OSA is shown in Figure 5-10. The calculated effective refractive index of the fibre core at the Bragg wavelength ~871.8 nm is 1.5638.

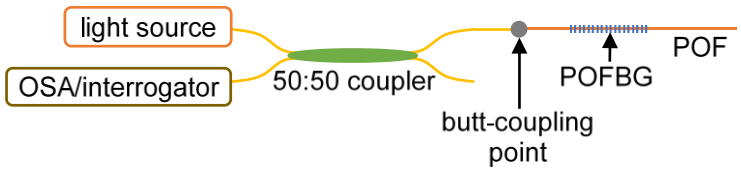

Figure 5-9. Schematic showing the FBG interrogation set-up used in this chapter.

The response of FBG1 to temperature was tested. In order to facilitate grating interrogation, a silica pigtail was glued to the mPOF with FBG1. Some UV-curable glue (Norland Optical Adhesive 78) was placed in the junction point between silica and polymer fibres. They were positioned with respect to each other so that reflection spectrum was single-mode, and then the UV glue was cured. However, after curing the glue, the reflection spectrum of FBG1 displayed two peaks rather than one due to change in light coupling conditions. As it was explained in Section 5.2.3, ~1-1.5 cm distance between gluing point and the POFBG allowed higher order modes to propagate. A longer distance between fibre end and the FBG would increase the loss for higher order modes greatly and render them invisible.

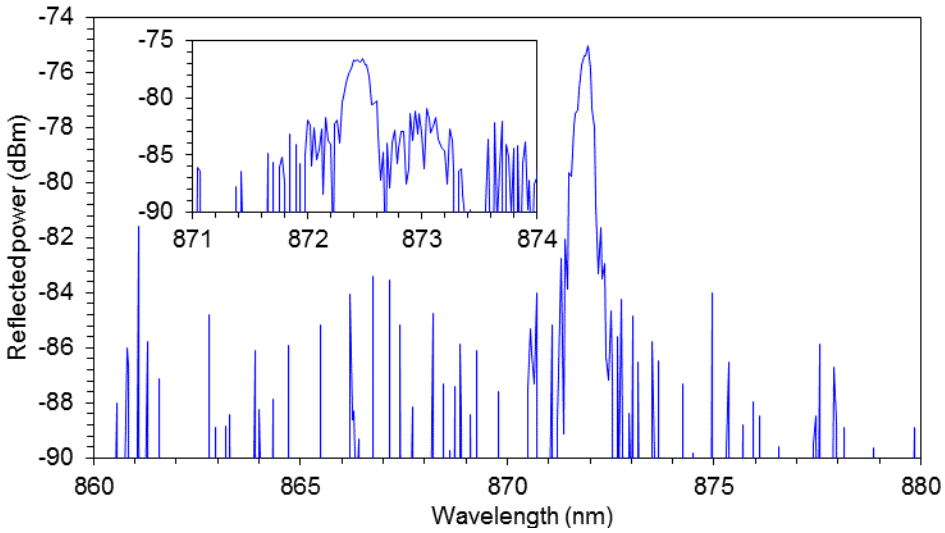

Figure 5-10. Reflection spectrum of an FBG (FBG1) inscribed in the 3D PC mPOF using HeCd 325 nm laser. Depending on light coupling conditions, reflection spectrum can display one (main plot) or more peaks (inset).

FBG1 was subsequently placed in a small V-groove on a Peltier plate and covered with some silicone grease to increase thermal conduction. The temperature was increased using a temperature electronic controller (TEC) from 27ºC to 42ºC in steps of 5ºC in room environment. The recorded spectra are shown in Figure 5-11, along with their moving averages serving to increase legibility of the plot. The temperature sensitivity was calculated from the moving averages by taking the central wavelength of -3dB bandwidth of either peak at different temperatures (see inset in Figure 5-11). The calculated temperature sensitivity was around -21.3±1.9 pm/ºC (-21.2±1.9 pm/ºC for the left peak and -21.4±1.0 pm/ºC for the right one). This value was similar to the ones achieved in previous studies on PC mPOFs: -25.8 pm/ºC in a humidity-controlled environment [105] and -29.9 pm/ºC in a room environment [107]. Lack of humidity control does not seem to have major impact on achieved temperature sensitivity values, as the humidity sensitivity of PC mPOF is only 7.25 pm/%RH (as opposed to 27.4-35.5 pm/%RH for POFs made of PMMA [4, 367]).

Knowing the temperature sensitivity of FBG1 ($\Delta\lambda_B/\Delta T$), the effective RI (n_{eff}) of the fibre core at ~871.8 nm (λ_B) and the LCTE of the fibre along fibre axis ($\alpha_{//}$) allowed the thermo-optic coefficient perpendicular to fibre axis (TOC$_\perp$, $dn_\perp/dT$) to be calculated. The fibre does not display longitudinal birefringence, so the TOC for all directions perpendicular to fibre axis is equal. COMSOL simulations showed that only up to ~3.3% of electric field is parallel to fibre axis, the remainder being perpendicular to it. Hence, it can be safely assumed that the Bragg peak position depends on TOC$_\perp$ only. According to the equation describing Bragg wavelength change on temperature [334]:

$$\frac{\Delta\lambda_B}{\lambda_B} = \left(\frac{1}{n_{eff}}\frac{dn_\perp}{dT} + \alpha_\parallel\right)\Delta T \qquad (5\text{-}4)$$

thermo-optic coefficient can be expressed as:

$$\frac{dn_{\perp}}{dT} = n_{eff}\left(\frac{1}{\lambda_B}\frac{\Delta\lambda_B}{\Delta T} - \alpha_{\parallel}\right) \tag{5-5}$$

Using the above equation, $TOC_{\perp}$ was calculated to be -39.4±3.7×10^{-6} °C^{-1}. The experimental error was estimated with the total differential method. It should be noted that the obtained $TOC_{\perp}$ value is less than those found in the literature for PC in bulk and in the thin film form (TOC_{av}: -90 to -172×10^{-6} °C^{-1}, most sources giving the value of about -107×10^{-6} °C^{-1}) [71, 99, 141, 142, 144, 335-337, 339]. As with the LCTE, this lower value of $TOC_{\perp}$ can suggest that TOC is anisotropic, which would be justified in view of high anisotropy of molecular arrangement. Very high TOC anisotropy has been reported for PC in the form of a 2.6 mm thick film, for which TOC for TE polarisation equals -3.6×10^{-4} °C^{-1}, while this for TM polarisation, -1.4×10^{-4} °C^{-1} [338].

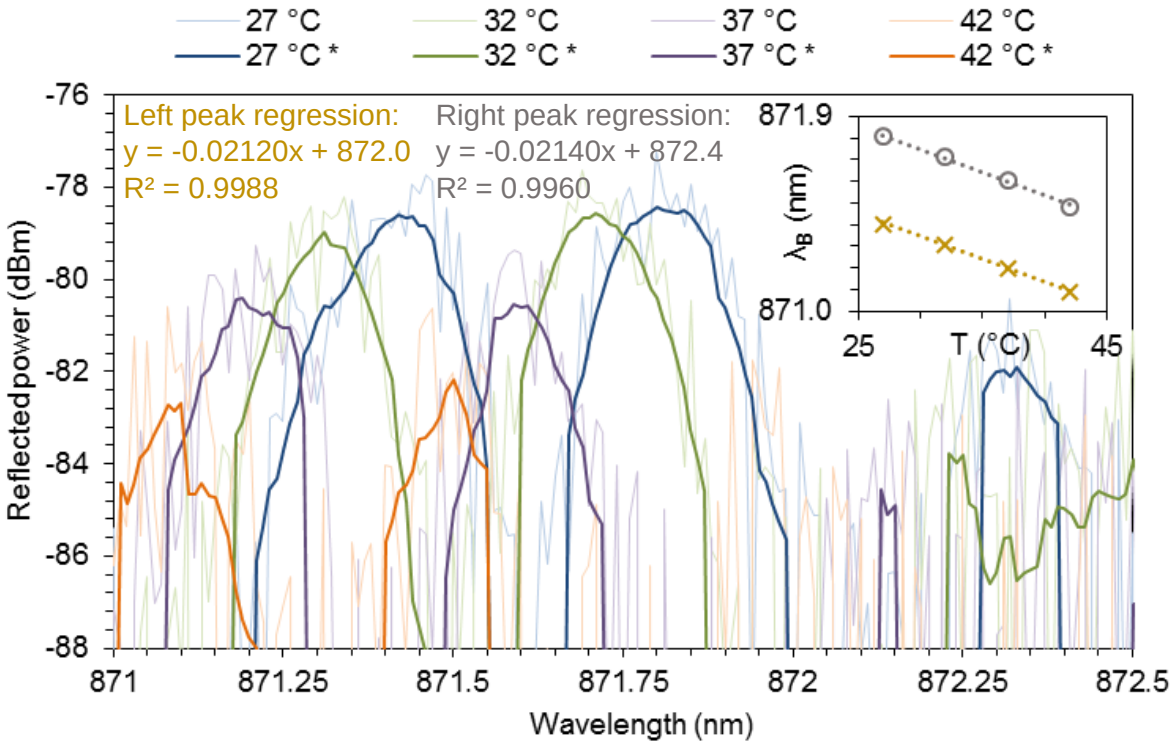

Figure 5-11. Spectra of FBG1 recorded at different temperatures. Note two peaks in each spectrum corresponding to two different modes. Temperature sensitivity calculations performed on both peaks gave almost identical results (inset). In order to reduce noise, moving averages (darker lines, data series marked with *) have been plotted over original spectra (lighter lines).

The very low value of $TOC_{\perp}$ compared to TOC_{av} implies that $TOC_{\parallel}$ should be very high. The precise formula is given by the temperature derivative of Equation (2-30):

$$\frac{dn_{\parallel}}{dT} = \frac{1}{n_{\parallel}}\left(3n_{av}\frac{dn_{av}}{dT} - 2n_{\perp}\frac{dn_{\perp}}{dT}\right) \quad (5\text{-}6)$$

However, to calculate $TOC_{\parallel}$ according to this formula, values of $n_{/\!/}$ and $n_{\perp}$ need to be known. Ideally, they would have to be measured experimentally. However, as polymer molecules in the fibre are expected to be very highly oriented (the orientation function $f_{or} \approx 1$), $n_{/\!/}$ and $n_{\perp}$ can be assumed to be close to their corresponding intrinsic values: $n_{\parallel} \approx n_{\parallel}^{0}$, $n_{\perp} \approx n_{\perp}^{0}$ (see Equations (2-18), (2-24), and (2-26)).

A simpler but slightly less accurate equation can be used instead, which allows avoiding the use of the assumed values of $n_{/\!/}$ and $n_{\perp}$:

$$\frac{dn_{av}}{dT} = \frac{\frac{dn_{\parallel}}{dT} + 2\frac{dn_{\perp}}{dT}}{3}, \quad (5\text{-}7)$$

hence:

$$\frac{dn_{\parallel}}{dT} = 3\frac{dn_{av}}{dT} - 2\frac{dn_{\perp}}{dT}. \quad (5\text{-}8)$$

The results of calculations by means of both equations, using the calculated value of $TOC_{\perp}$ and the extreme literature values for TOC_{av} and Δn^{0}, are collated in Table 5-3. The values of intrinsic birefringence of PC (Δn^{0}) reported in the literature range from 0.11 to 0.236 [368], and n_{av} = 1.577 at 850 nm [107]. Values of $n_{/\!/}$ and $n_{\perp}$ were calculated according to Equation (2-30). The calculated value of $TOC_{\parallel}$ ranges from -178 to -437 $\times 10^{-6}$ °C^{-1}.

Table 5-3. Values of $TOC_{\parallel}$ calculated from averages (Equations (5-6) and (5-7)) using the literature values of TOC_{av}, and Δn^{0}, and the measured value of $TOC_{\perp}$.

Equation	TOC_{av} ($\times 10^{-6}$ °C^{-1}) (extreme values)	Δn^{0} (extreme values)	$TOC_{\parallel}$ ($\times 10^{-6}$ °C^{-1})
(5-6)[a]	-90	0.11	-185
		0.236	-178 (min)
	-172	0.11	-420
		0.236	-402
(5-7)	-90		-191
	-172		-437 (max)

[a] Average RI value used in the calculations: n_{av} = 1.576 at 850 nm [107]

These values of $TOC_{\parallel}$ were attempted to be cross-validated with those predicted theoretically using the Vuks equations and the orientation function. For this purpose, the value of $TOC_{\parallel}$ resulting from Equation (2-33), which describes the dependence of birefringence on temperature, was calculated. Due to the very high draw ratio of 3D PC mPOF, it can be assumed that the angle θ between the draw direction and the intrinsic unit of PC ≈ 0°, so the orientation function $f_{or} \approx 1$. However, θ values from the range 0-30° were used in calculations to check the error that is brought to the results by the uncertainty of θ. The value of θ was found not to have much impact on the results of $\frac{d(\Delta n)}{dT}$, as the terms f_{or} and $\frac{df_{or}}{dT}$ partly cancel each other out: the former decreases while the latter increases when θ rises. Changes in θ can thus be neglected/ignored. On the other hand, the term $\frac{d(\Delta n^0)}{dT}$, calculated according to Equation (2-38), increases when Δn^0 increases: the bigger the Δn^0, the bigger the $\frac{d(\Delta n)}{dT}$. The latter term can also be expressed through Equation (2-23) as:

$$\frac{\mathrm{d}(\Delta \mathrm{n})}{\mathrm{dT}} = \frac{\mathrm{dn}_{\parallel}}{\mathrm{dT}} - \frac{\mathrm{dn}_{\perp}}{\mathrm{dT}}, \tag{5-9}$$

thus:

$$\frac{\mathrm{dn}_{\parallel}}{\mathrm{dT}} = \frac{\mathrm{dn}_{\perp}}{\mathrm{dT}} + \frac{\mathrm{d}(\Delta \mathrm{n})}{\mathrm{dT}}. \tag{5-10}$$

The latter equation was used to calculate values of $TOC_{\parallel}$ predicted theoretically, which were collated in Table 5-4. As can be seen from it, the theoretical $TOC_{\parallel}$ values are much lower than those calculated from the averages (Table 5-3), even considering different values of VCTE, TOC_{av} and intrinsic birefringence reported in the literature. The highest magnitude of the theoretically predicted $TOC_{\parallel}$ is -98×10^{-6} °C^{-1}, while the lowest magnitude of $TOC_{\parallel}$ calculated from the averages is -178×10^{-6} °C^{-1}. It is probable that, due to a very high degree of molecular orientation and, possibly, some unrelaxed residual stress, fibre behaviour is different than what would be expected from the theory. It might be that, for such highly oriented polymer material, some material parameters can exceed those reported in the literature, and hence, they should rather be measure than assumed. These could entail VCTE (or $LCTE_{\perp}$), mean RI (n_{av}), transverse birefringence (Δn), angle of molecular orientation (θ), average TOC (or $TOC_{\parallel}$), and thermal dependence of birefringence $\left(\frac{d(\Delta n_{av})}{dT}\right)$. Thus, further studies are required to fully understand fibre behaviour.

Table 5-4. Values of $TOC_{\parallel}$ calculated from Equation (5-10) using the literature values of VCTE, TOC_{av}, and Δn^0, and the measured value of $TOC_{\perp}$.

VCTE ($\times 10^{-6}$ °C^{-1}) (extreme values)	TOC_{av} ($\times 10^{-6}$ °C^{-1}) (extreme values)	Δn^0 (extreme values)	$TOC_{\parallel}$ ($\times 10^{-6}$ °C^{-1})
150	-90	0.11	-54 (min)
		0.236	-71
	-172	0.11	-66
		0.236	-97
243	-90	0.11	-55
		0.236	-72
	-172	0.11	-67
		0.236	-98 (max)

5.3.2 Inscription using a femtosecond laser

Another FBG (FBG2) was inscribed in the manufactured fibre by means of a femtosecond laser system (High Q Laser FemtoREGEN) operating at 517 nm with 220 fs pulse duration. The fibre sample was fixed to a glass slide to minimise unwanted strain and bending and was subsequently mounted onto a 2D air-bearing translation system (Aerotech) for accurate motion control during inscription. The laser beam was focused on the fibre core by a long working distance objective (×50, Mitutoyo) using another translation stage. The laser pulse energy and repetition rate were set to ~50 nJ/pulse and 1 kHz, respectively.

Using the plane-by-plane inscription method [97, 369, 370], 1000 planes were inscribed in the fibre core with a period of ~1.97 μm, giving a total grating length of 2 mm (see Figure 5-12(a)).

The fibre was cleaved with a cold blade and butt-coupled to using silica fibre and refractive index matching gel. It was subsequently illuminated through a 3dB coupler (see Figure 5-9) using a broadband light source (ASE730, Thorlabs, range 1530-1610 nm). The reflection spectrum of the grating was measured using a commercial FBG interrogator (IBSEN IMON 512 HS), see Figure 5-12(b). The effective refractive index of fibre core at ~1562 nm (4^{th} order FBG reflection) according to the resultant reflection spectrum was estimated to be ~1.586.

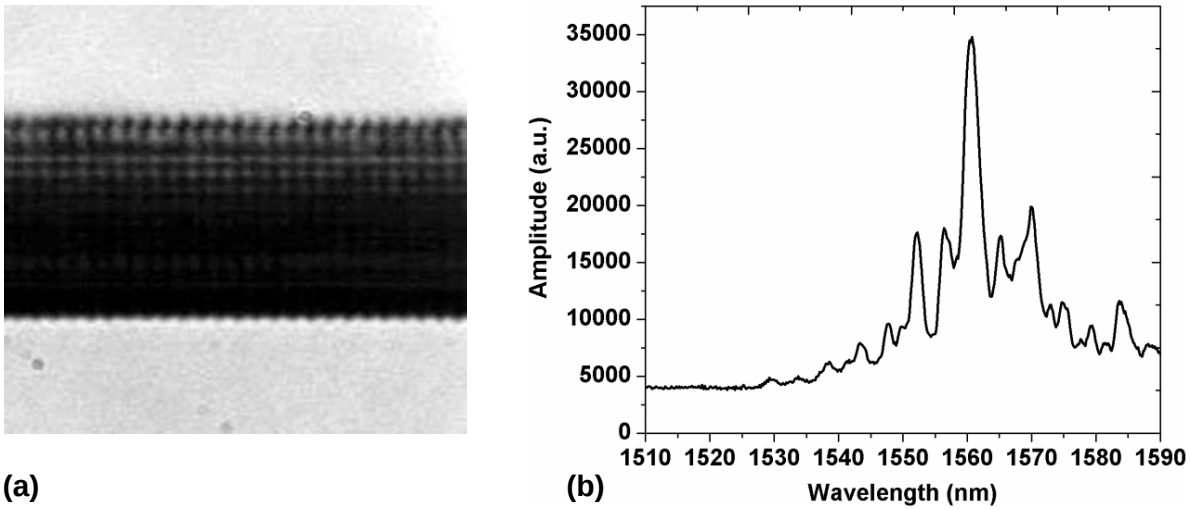

Figure 5-12. (a) Microscopic image (side view) of the FBG inscribed in 3D PC mPOF by femtosecond laser (FBG2). (b) Reflection spectrum (4th order) of FBG2.

The operation of FBG2 was tested qualitatively to confirm the behaviour expected of an FBG. The test set-ups allowing quantitative characterisation of the grating response were unavailable at the time of this experiment. Figure 5-13(a) shows the response of the grating to random vibrations of the optical table after hitting it three times. The response of the grating to three breath cycles is shown in Figure 5-13(b). Here, the Bragg peak wavelength decreases with the increased temperature from each exhalation, yielding negative temperature sensitivity (in line with the results achieved in Section 5.3.1).

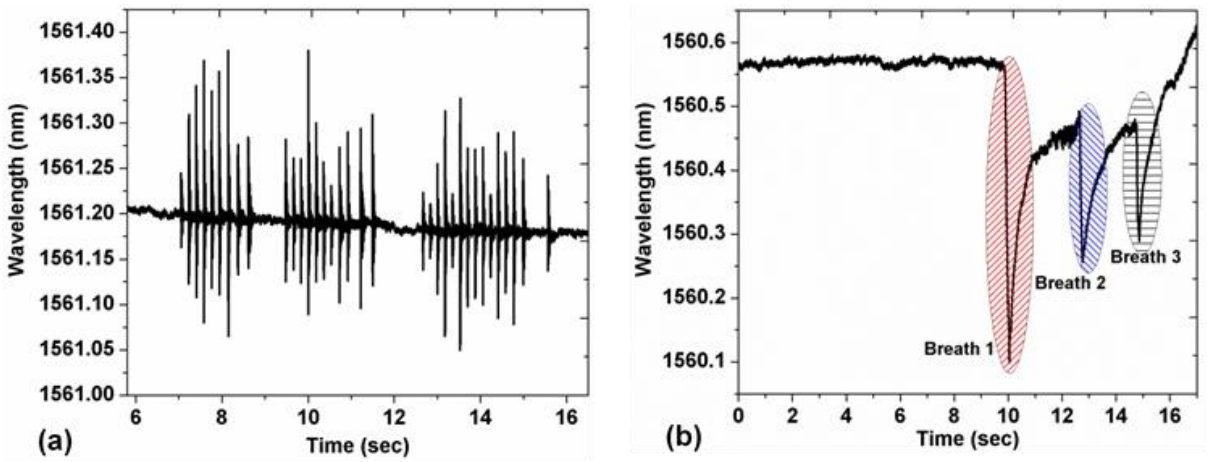

Figure 5-13. (a) Time response of FBG2 to vibration induced by hitting the optical table. (b) Time response of the FBG to three breathing shots, resulting in pulses of warmer and more humid air. As shown earlier, the POFBG shows negative temperature sensitivity. The Bragg wavelength increase after t = 16 s in (b) might be due to positive humidity sensitivity of the fibre [105].

5.3.3 Inscription using a krypton-fluoride laser

A Coherent Bragg Star Industrial-LN krypton-fluoride (KrF) excimer laser system operating at 248 nm wavelength was employed to inscribe the third FBG introduced in this chapter (FBG3). The pulse duration and pulse repetition rate were 15 ns and 1 Hz, respectively. The laser beam profile was measured as a rectangular Tophat function of 6.0×1.5 mm^2 size and 2×1 $mrad^2$ divergence. It was focused onto the fibre core utilizing a plano-convex cylindrical lens (Newport CSX200AR.10) with the focal length of 20 cm. The effective spot size of the beam on the fibre surface was 20.0 mm in width and 32.4 μm in height. A slit perpendicular to the fibre direction is used to reduce the width of the beam, which defines the physical length of the grating structure (in this case 5 mm long). A 10 mm long phase mask customised for 248 nm inscription wavelength with pitch of 567.8 nm was used for Bragg grating inscription at the 850 nm spectral region. A supercontinuum source (Fianium White laser WL-SC-400) and an optical spectrum analyser (Yokogawa AQ6373B) were used to measure power reflected from the grating through a 3dB coupler (see Figure 5-9).

Due to high fibre attenuation at this wavelength short fibre sections of around 4 cm were used. They were butt-coupled to an APC silica pigtail and a small amount of index gel was inserted to reduce Fresnel reflections. It took 5 min to inscribe a grating (300 pulses at 1 Hz pulse repetition rate, 0.6 mJ energy per pulse). The resulting FBG was 5 mm long and its Bragg wavelength was 887.25 nm (see Figure 5-14). From the Bragg peak the effective refractive index at that wavelength was calculated to be 1.5626, which is very close to this calculated in Section 5.3.1 (1.5638 at ~871.8 nm) and in [107]. The test set-ups allowing characterisation of the grating response were unavailable at the time of this experiment, so quantitative tests of the FBG operation could not be performed.

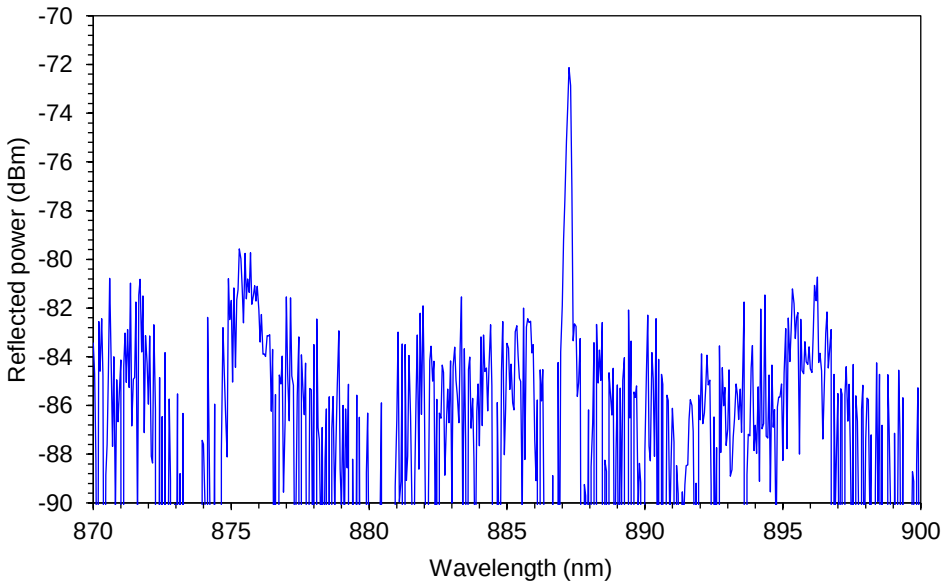

Figure 5-14. Reflection spectrum of a 248nm KrF laser-inscribed FBG in the 3D PC mPOF.

5.4 Conclusions

This chapter reports the first single-mode microstructured solid-core fibre drawn from a 3D-printed preform (introduced in Section 4.5) and the first such fibre to be single-mode (at both 870 nm and 1550 nm). The SC PC fibre displayed the lowest attenuation of all the POFs drawn from 3D-printed preforms over the entire measured spectrum (550-2200 nm). The quality of the fibre was sufficient to demonstrate the first inscription of fibre Bragg gratings within a fibre of this type. Whilst the preform fabrication process is not optimal in terms of the optical transparency of the fibre produced at this stage, it guides light over a sufficient distance to show the successful inscription of fibre Bragg gratings using three different laser systems: a 325 nm CW laser, a 517 nm pulsed femtosecond laser and a 248 nm pulsed nanosecond laser. The success of these different inscription approaches proved good photosensitivity of the fibre, similar to this of POFs manufactured with the conventional methods. Mechanical testing of the fibre showed that the 3D printing approach did not introduce any unexpected or undesirable characteristics. The fibre attenuation was the lowest reported so far for a POF drawn from a 3D-printed preform. The measured linear coefficient of thermal expansion was found to be two orders of magnitude smaller than for isotropic bulk material. Thermo-optic coefficient of the fibre was calculated to be only ~37% of this for isotropic bulk PC. Both of these are ascribed to high anisotropy of molecular arrangement in the 3D PC mPOF, but further studies are necessary to fully understand fibre behaviour.

The presented research confirmed suitability of the FDM technique to be used in manufacturing of POFs that could be of practical use. Such approach can bring rise to POFs drawn from preforms of shapes that would be very difficult to fabricate by other means.

Chapter 6 FBG embedding and packaging

This chapter presents the work on embedding and packaging both silica and polymer FBGs performed by the author. It has been split into two parts. The first one (Section 6.1) presents the embedding results using the early design of the housing structure and testing set-ups. First, description of the design of the sensing patches and the embedding procedure are introduced. After fabrication, responses of the packaged sensors to strain and temperature are measured and discussed, including sensitivity and hysteresis. The second section (Section 6.2) presents the upgraded design of the housing structure and testing set-up based on the results and issues reported in the previous section. The rationale of the upgrades is extensively described. According to them, SOFBGs are embedded and their strain response is thoroughly tested and discussed, including experimental artefacts, strain sensitivity, stability of Bragg wavelength in time and hysteresis. Finally, the response of two of the samples to temperature and humidity is presented. After describing the testing set-up and procedures, the test results are thoroughly discussed from the viewpoint of the sensing applications. This includes the phenomena observed in the tested samples: the fibre slippage and the evolution of the reflection spectra. Furthermore, the values of temperature and strain humidity are calculated and discussed.

6.1 Early housing structure and testing procedures

The work described in this section was presented during the conference SPIE Photonics Europe 2016 [301] in Brussels, Belgium, and Sixth European Workshop on Optical Fibre Sensors (EWOFS 2016) [300] in Limerick, Ireland.

6.1.1 Introduction

During inscription and usage, FBGs were interrogated in the reflection regime, i.e., observing the light reflected from grating (see Figure 6-1). Light from a broadband source (BBS) was directed to an FBG through a 50:50 coupler (matched to the light wavelength range). The light reflected from the grating was passing again through the coupler and reaching an optical spectrum analyser (OSA) on which it was observed. In order to decrease loss, the coupler was sometimes substituted with a 1550-nm-range optical circulator, with a BBS being connected to port 1, FBG – port 2, and OSA – port 3. An alternative interrogation approach at the 1550 range consisted of using an integrated interrogator to which the fibre was connected directly instead of the whole interrogation setup (BBS, OSA, and coupler). The advantage of using the interrogator was the capability of high-speed readout and the proprietary software using various peak tracking algorithms. The following devices were used:

- BBSs:
  - Superlum SLD-371 centred at 830 nm (range: 795-865 nm)
  - Thorlabs ASE-FL7002-C4 centred at 1560 nm (range: 1530-1610 nm)
- OSAs:
  - HP 86142A
  - HP 70951B
- interrogator: HBM DI110 (range: 1510-1590 nm, frequency up to 1 kHz)

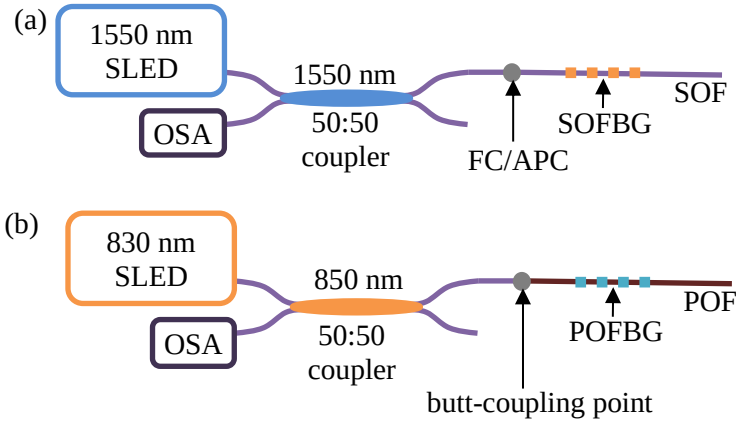

Figure 6-1. Experimental set-up for interrogation of (a) SOFBGs and (b) POFBGs.

6.1.2 FBG inscription

Both the SOFBGs and POFBGs were inscribed in-house by the phase-mask method (see Section 2.7.3) using a Kimmon 325-nm HeCd laser (model IK3301 R-G, optical power of 35 mW).

SOFBGs

Two gratings spaced by 50 mm (centre to centre) were inscribed through-coating on one piece of hydrogen-loaded Fibercore PS 1250/1500 fibre using an Ibsen Photonics custom-made phase mask

(1061.18 nm pitch). The scanning length, speed, and time of both gratings were 9 mm, 7.4 μm/s, and 12 min, respectively. The resulting gratings had the following Bragg peak wavelengths and reflection strengths: SOFBG1 – 1536.7 nm and -47.8 dBm; SOFBG2 – 1530.4 nm and -50.0 dBm, respectively. SOFBG2 was strained before inscription, in order to give a Bragg wavelength difference between the two gratings (see Section 3.3.2).

POFBGs

Two POFBGs were inscribed using an Ibsen Photonics custom-made phase mask (557.50 nm pitch) on a highly-photosensitive 125-μm microstructured POF made of poly(methyl methacrylate) (PMMA) doped with BDK. This was a different type of fibre than the 3D PC mPOF, whose manufacture was presented in Chapter 5. Its fabrication and characterisation is thoroughly discussed in [283]. The scanning length, speed, and time of the grating embedded in polylactic acid, PLA (PLA-POFBG), and acrylonitrile butadiene styrene, ABS (ABS-POFBG), were both 5.2 mm, 2.2 μm/s, and 30 min, respectively. The resulting gratings had the following Bragg peak wavelengths and reflections strengths: PLA-POFBG – 828.3 nm and -68.4 dBm; ABS-POFBG – and 828.4 nm and -68.2 dBm, respectively.

6.1.3 FBG embedding

All sensing patches housing the FBGs were fabricated with the UP! printer (model 3DP-14-4A). The embedding procedure was similar for both SOFBGs and POFBGs; the differences are given in the respective subsections. The 3D printing process was paused midway, at the height at which the full depth of the embedding channel was reproduced and just before deposition of the layer that was about to cover it. If a glue was used, it was then placed at the bottom of the channel, before the fibre was inserted. Whether the glue was used or not, glue type, and deposition procedure were varied depending on the sample. Finally, the printing process was resumed to complete the housing structure. 3D designs of the sensing patches with the grating embedding points marked on them are shown in Figure 6-2.

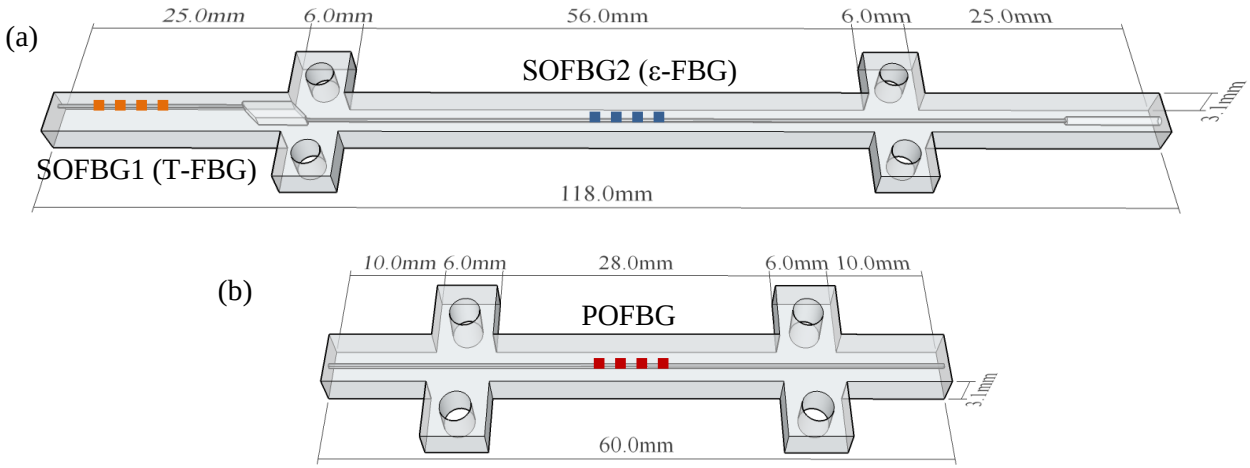

Figure 6-2. 3D view of the housing structures for (a) SOFBGs and (b) PLA-POFBG (the design for ABS-POFBG is almost the same as b, see text for details). Dotted lines mark the positions in which the gratings are embedded.

SOFBGs

The housing structure prepared for the silica gratings was intended to demonstrate the possibility of embedding multiple gratings in one sensing patch, each one of which can be set to sense a different physical quantity. In this particular case, two gratings embedded in one patch were meant to provide temperature-insensitive strain reading. Strain was applied between the two mounting supports perpendicular to the channel: one of them was fixed, while the other one was clamped to a translation stage. SOFBG1 (or the temperature-sensing grating, T-FBG) was placed outside the straining region, hence was expected not to sense any strain. SOFBG2 (or the strain-sensing grating, ε-FBG) was sensitive to both strain and temperature. Interrogating both gratings at the same time is the easiest solution to one of the classical problems of FBG cross-sensitivity to temperature, which always occurs when sensing other physical quantities.

The structural material used to construct the patch was ABS as it has better mechanical properties than PLA, another popular filament type used in FDM. The depth of the embedding channel was set to 150 μm, which is the smallest reproducible dimension with the 3D printer used (thickness of one layer). For the sake of robustness, secondarily coated silica fibre was directly integrated into the sensing patch. For this reason, the fibre channel is visibly wider at the fibre inlet to the structure – see the rightmost part of the structure in Figure 6-2(a).

The final design of SOFBG housing patch resulted from multiple design tests and embedding trails that were performed in order to optimise the structure (Figure 6-2(a)). There were two main aspects of investigation:

- appropriate housing structure design, ensuring that the T-FBG was not cross-sensitive to strain
- search for appropriate adhesion strength between fibre and structure.

The former problem was noticed when both gratings were placed in a single channel running through the housing structure (as in Figure 6-2(b)). In this case, the T-FBG was still able to detect about 1/3 of the strain magnitude sensed by the ε-FBG, despite being placed outside the straining region (i.e., the region limited by the perpendicular supports). This was believed to be due to high silica fibre stiffness compared to the sensing patch material, which resulted in strain transfer outside the straining region.

A good solution to that came from one of the distinctive characteristics of 3D-printing techniques, namely the ability to easily incorporate empty cavities in printed designs. An air cavity was placed between the two gratings, and the channel for the T-FBG was offset from the central position. These resulted in a fibre slack, ensuring that any strain transferred by the fibre from the straining region relaxed in the empty cavity. This approach proved to be successful, yielding strain induced in the straining region not being sensed by the T-FBG.

The other main issue related to silica fibre embedding, namely the need for optimising adhesion strength between the fibre and the housing structure, became evident when unfavourable fibre behaviour embedded in the early printouts was noticed. It consisted of apparent hysteresis on quick bending or straining of the structures by hand, which resulted in "zero level shifting" (random changes of Bragg peak wavelength for zero strain after bending or straining the structure for a moment and then releasing the bend or strain). Another symptom of insufficient fibre-structure adhesion was Bragg peak quickly moving back towards the initial wavelength after straining or bending the structure and holding the strain or bend. Finally, on temperature increase, when structure was expanding, abrupt jumps in the Bragg wavelengths were noticed, which were related to fibre relaxing accumulated stress. These effects were believed to be associated with fibre sliding against the housing structure, which was coming from insufficient adhesion strength between the fibre and the structure.

The effects enumerated above were visible with smaller or higher magnitude for all of the following embedding approaches:

- fibre with uncoated SOFBG region embedded directly into the structure without using glue
- fibre with uncoated SOFBG region embedded using ethyl 2-cyanoacrylate + poly(methacrylate-co-ethyl acrylate) (commonly known as Super Glue), deposited on the entire fibre length
- the same as above, but leaving the SOFBG region free from glue
- fibre with uncoated SOFBG region glued with (3-(trimethoxysilyl)propyl)ethylene-diamine, deposited on the entire fibre length; it is a popular elastic glue, which initially bonds in 5 min, and fully cures in 1 hour.

None of the above embedding approaches prove to yield satisfying results from the viewpoint of the sensing applications. In turns, the following embedding methods seemed promising according to the preliminary results:

- fibre without coating along almost the entire housing length, including the SOFBG region, bonded using Super Glue deposited on the entire fibre length

- through-coating-inscribed SOFBGs bonded to the patch using Super Glue

The latter approach was followed in this section. Although the through-coating FBG inscription process is slightly more complex, such gratings were expected to provide some important advantages. First, adhesion strength between the fibre and its primary coating was supposed to be high. Moreover, the bonding strength coming from gluing polymer coating to the material of the housing structure was expected to be higher than when gluing the exposed regions of the glass fibre.

Embedded through-coating-inscribed SOFBGs showed much better characteristics than these yielded by the aforementioned unsuccessful embedding approaches, and none of the previously described issues manifested itself. Interestingly, the Bragg peak position for a relaxed structure moved importantly from the original value before embedding. SOFBG1 (T-FBG) moved from 1535.69 nm before embedding to 1531.73 nm afterwards (for a relaxed structure), giving the change of -3.96 nm. SOFGB2 (ε-FBG) shifted from 1529.39 nm to 1525.00 nm, yielding the difference of -4.39 nm. The changes were probably caused by structure shrinkage after cooling down when the printing was finished. The fact that the fibres stayed under compressive stress after printing and did not relax is an argument supporting the high fibre-structure adhesion strength. Quantitative test results are presented in Section 6.1.4.

POFBGs

The design of the POFBG housing structures is depicted in Figure 6-2(b). The difference between the structure 3D-printed of PLA and ABS was the channel depth, which was influenced by the printing nozzle temperature for both materials (around 210 °C for PLA and 270 °C for ABS). As POFs are thermoplastic materials, they must be protected from excessive temperature not to damage the fibre or the inscribed Bragg gratings. This was achieved by increasing the embedding channel depth. After inserting the fibre to the bottom of the channel, it was covered with a much thicker layer of glue than when embedding SOFBG. The (3-(trimethoxysilyl)propyl)ethylene-diamine elastic glue used acted not only as an adhesive, but also a thermoinsulator.

The glue was deposited at the bottom of the channel and along the POF, which provided optimal glue distribution. The fibre was inserted in the channel and moved forth and back along it multiple times in order to assure that the fibre was at the very bottom of the channel and that it was well surrounded with glue. The fibre was mounted with tape on temporary supports at both fibre inlets. The glue was allowed to cure for some time (see below for details). Subsequently, the printing process was resumed, leading to full development of the sensing patch.

In the case of the PLA housing, the bottom of the embedding channel was set at the neutral axis of the beam, and its depth was fixed at 750 μm. It was found to be enough to protect the POFBG from the nozzle temperature (210 °C). The printing bed temperature was set to 60 °C, but the temperature could have been lower at the level of the embedding channel, into which the PLA-POFBG was inserted. These

thermal settings did not cause any observable change to the POFBG peak shape. After gluing the grating into the channel and before resuming printing, no grating annealing was observed on the timescale of minutes. The response peak moved from 828.2 nm before embedding to 826.5 nm afterwards, which probably came from structure shrinkage after cooling down, similarly to what was described for embedding SOFBGs. Structure shrinkage initially made the peak shape and strength deteriorate, but as the glue was not fully cured at that stage yet, stretching the fibre at both structure inlets helped the PLA-POFBG regain its initial characteristics. Ultimately, it showed a decrease of Bragg peak power of 1 dB compared to before embedding.

Embedding a POFBG in an ABS housing was found to be more challenging due to a higher printing nozzle temperature required for ABS (270 °C). The channel depth was set to 2.3 μm, which resulted in the bottom of the fibre embedding channel being close to the bottom of the sample and no longer at the neutral axis of the beam. Previous embedding trials showed that 1.15 μm deep embedding channel was not deep enough for thermoinsulation from the high nozzle temperature. The typical printing bed temperature used for ABS (105 °C) was found to anneal the fibre on the timescale of minutes. Hence, it was lowered to 60 °C, which prove previously not to cause any adverse effects to this type of POFBG. These printing parameters helped the ABS-POFBG withstand the 3D printing process. The peak shape and strength were unchanged after finishing the printing, but they deteriorated after detaching the structure from the printing bed. This was probably due to structure shrinkage as this phenomenon is particularly pronounced for ABS, which is because thermal expansion of material is proportional to the product of CTE and temperature change. First, CTE of ABS is normally higher than of PLA. Secondly, ABS is printed at a higher temperature than PLA, hence the temperature difference between printing and room conditions is also higher. When the structure was detached from the printing bed, the glue had already cured fully (1 h after deposition) so stretching the fibre at the structure inlets did not help the grating to regain its original characteristics, as it did for the PLA patch above. Nevertheless, this issue is expected to be easily addressable this way in the future. Yet, the peak shape quality was still good enough to be tracked.

6.1.4 Strain response of the sensing patches

Following the embedding process, tests of the strain response of the sensing patches were performed. The structures were fixed at the parts perpendicular to the embedding channel (see Figure 6-2) by clamping one of them to an immobilised support and the other one to a translation stage of 20 μm accuracy. As a result, only the middle beam part of the structure was being strained. For each of the three sensing patches, three straining cycles of gradually increasing and decreasing strain were performed at room temperature. After each step change of strain (increment or decrement), the Bragg peak position was measured at different time intervals: at t = 0 min, 1 min, and 5 min. Time between consecutive strain increments or decrements was about 5-6 min.

The translation stage used in these straining trails was only able to exert tensile force on the sample and not compressive one. The scale of the translation stage was rather coarse, only allowing to tell the point at which strain started building up with 20 μm accuracy. Though, during the measurements, this point was normally observed to lay between two scale bars. The strain graphs were then constructed the following way. The first point of all strain graphs below in each strain increase cycle is the last stage displacement division at which no change to Bragg peak was visible. The second point in each cycle was the first stage displacement division that caused Bragg peak change. Thus, although the strain graphs suggest the first point in each series to be the beginning of strain build-up, in the reality it was somewhere between the first and the second data point. This inaccuracy resulted in a systematic error of up to 0.02 mm, which did not change meaning of the results.

Small but visible length increase from cycle to cycle was noticed for all sensing patches. In order to allow rough assessment of the length increase, all the strain graphs are accompanied by those showing Bragg wavelength position versus stage displacement. Cycles 2 and 3 of all the patches start with a period of no stain response, which is 2-3-point long; this is not visible in the strain graphs.

The strain results discussed below displayed unexpected behaviour as regards non-linearity of the Bragg peak response to strain and inconsistency in strain sensitivity values, strain hysteresis values, and Bragg wavelength change in time after strain increment or decrement. It was only found in the course of further research that these discrepancies came from some imperfections of the testing set-up used (backlash of its elements, some set-up elements being free to bend or slide past each other, and some being mounted loosely). They way these issues affected test results is discussed at the end of this section. Section 6.2 describes how these problems were addressed. Improved design of the strain test set-up and testing procedures are also presented there, along with the test results. However, it was still found informative to discuss the results of the early strain trails. First, it makes it possible to assess the difference between the early and late results and appreciate the importance of the introduced upgrades. This type of strain test set-ups are often used in the optical fibre community as they rely on typical optical-table components. Analysis of the results of the set-up upgrade can provide valuable information on those elements of set-up design and testing procedures that minimise experimental errors, artefacts, and inconsistencies. Secondly, not all embedding experiments reported in this section are replicated in Section 6.2. It focuses on accuracy and repeatability of embedding bare and through-coating SOFBGs and reports on their tensile and compressive strain trials. Dual SOFBG embedding and POFBG embedding is only described in the current section. While their test results are not quantitatively correct, they still allowed formulating some qualitative conclusions.

SOFBGs

During the strain tests of the ε-FBG, the sensing patch was interrogated with the HBM DI110 working at 1 kHz, which allowed precise tracking of the peak position in time. The time intervals between

consecutive straining cycles were about 1 hour. The strain response of the SOFBG sensing patch is shown in Figure 6-3.

In all cycles, a non-linear initial response to strain was observed, which became linear above 0.08 mm stage displacement. This type of non-linearity was caused by imperfection of the strain test set-up. The strain decrease series in cycle 1 overlapped roughly with the strain increase one, whereas the former was slightly below the latter in cycles 2 and 3. The response to increasing and decreasing strain in cycle 3 was linear up from 0.06 mm stage displacement value.

Strain sensitivity of the linear range of all the cycles on strain increase and decrease varied between 0.39 and 0.41 pm/με. This value is visibly lower than a standard strain sensitivity of silica fibres given in the literature, which is ~1.2 pm/με at 1550 nm (see Section 2.7.4). However, another through-coating-inscribed SOFBG sensing patch, which was produced in the preparatory stage, yielded strain sensitivity of 0.95 pm/με. The grating was embedded in a very similar beam-like structure following almost identical procedure. This strain sensitivity value was very close to the standard silica fibre one. These discrepancies were also found to be caused by the strain test set-up, which is discussed later in more detail.

The hysteresis value after cycle 1 of the straining was the biggest and of positive magnitude, yielding 401 pm. The hysteresis after cycle 2 and 3 was negative and of a decreasing magnitude from cycle to cycle, giving the value of -222 pm after cycle 2 and -80 pm after cycle 3.

Bragg wavelength changes in time after a strain increment or decrement had a relatively low magnitude on the timescale on which they were measured. They were negative on strain increase in all the cycles, being the biggest at the highest strain values after 5 min from the strain increment. The highest changes were -42, -25, and -18 pm for cycles 1, 2, and 3, respectively. On strain decrease, the Bragg peak changes in time were mostly positive, being the highest after 5 min at high strain values. The highest values for cycle 1, 2, and 3 were, respectively, 18, 6, and 9 pm.

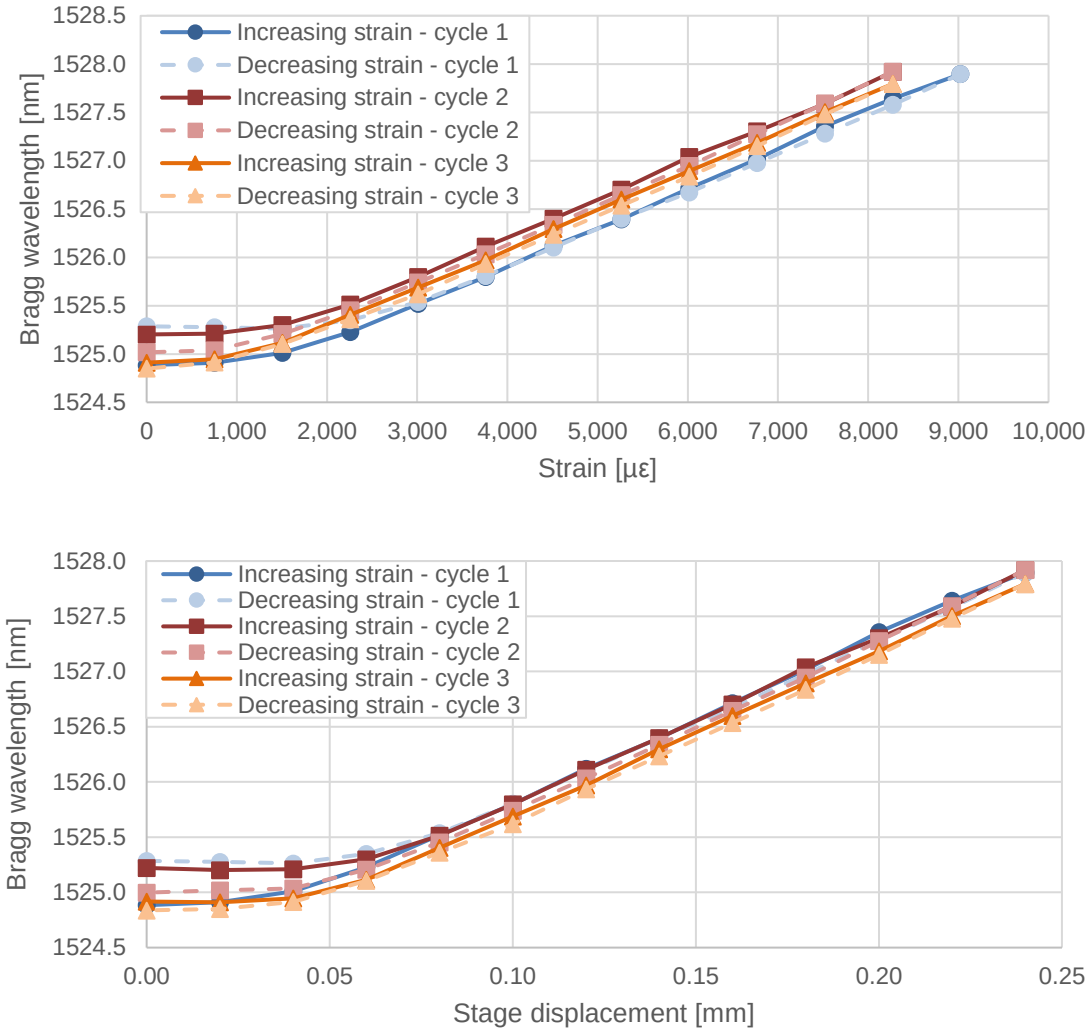

Figure 6-3. ε-FBG (SOFBG) Bragg reflection peak immediately after strain change as a function of strain (top) and testing stage displacement (bottom) for the sensing patch of ABS.

POFBG embedded in the PLA sensing patch

The sample was interrogated as during inscription (see Figure 6-1), i.e., the peak position measurements were taken with an OSA and not with an interrogator. Hence, they could not have been recorded exactly immediately strain change as it was for embedded SOFBGs. Time interval between straining cycle 1 and 2 was over 15 h, while it was around 2 h between cycle 2 and 3. The straining response of the POFBG embedded in PLA has been plotted in Figure 6-4.

From a stage displacement of 0.06-0.08 mm on, the strain increase in cycle 1 showed the lowest linearity of all. This might be attributed to the POF taking optimal position within the housing, compensating for any possible slack that remained from the embedding stage. On strain decrease, a response of good linearity was observed down to 0.10 mm stage displacement. Structure length might have increased from cycle to cycle, because the increase in strain in cycles 2 and 3 started at higher

values of stage displacement. However, such behaviour can also be attributed to the imperfections of the strain test set-up. They are also responsible for non-linear Bragg peak response to stage displacement and strain, which are visible in cycle 2 and 3, and during strain decrease in cycle 1.

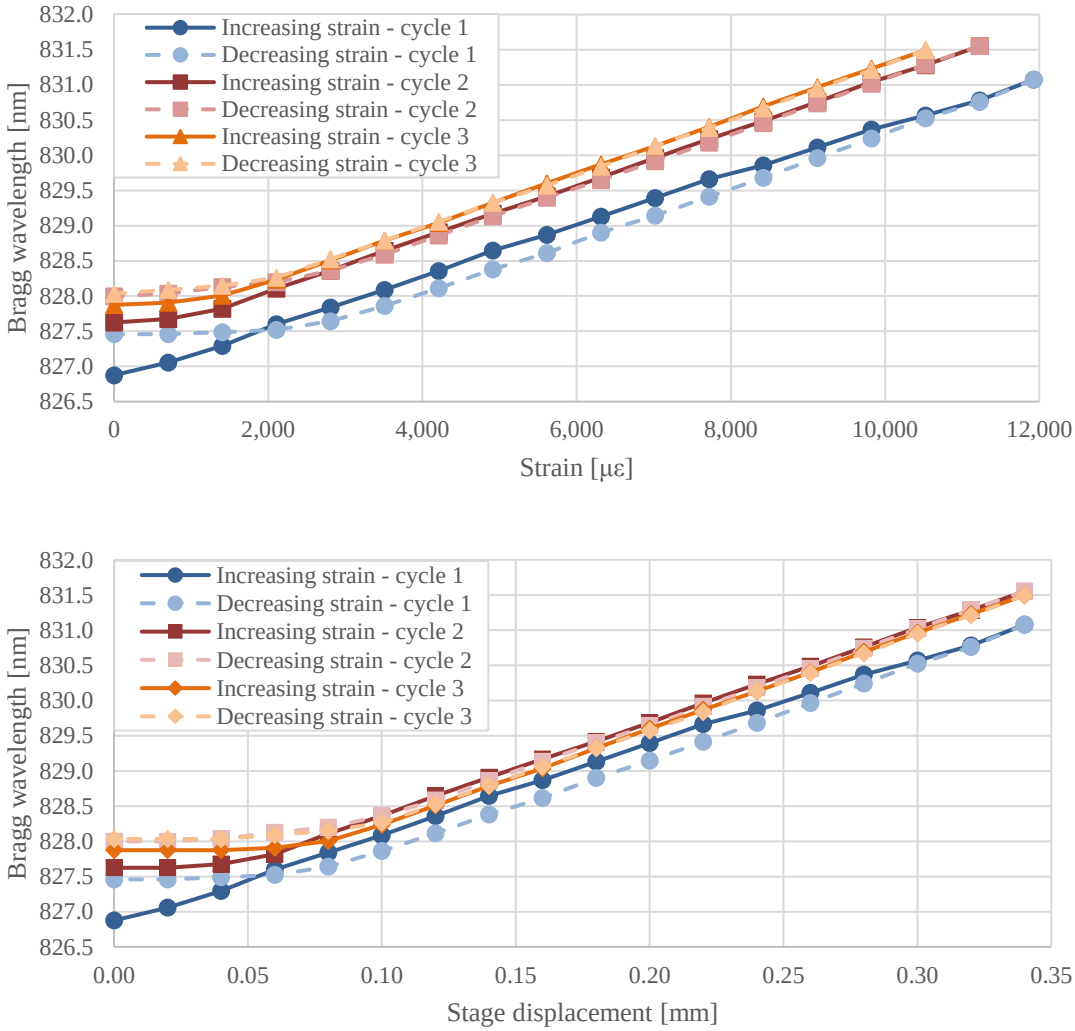

Figure 6-4. Bragg reflection peak from the PLA-POFBG immediately after strain change in the function of strain (top) and testing stage displacement (bottom) for the sensing patch of PLA.

Apart from cycle 1, strain increase and decrease almost exactly overlapped, showing good repeatability of strain response within one cycle. Moreover, in the linear range of cycles 2 and 3, the slope of the increase and decrease of strain showed almost the same value. This confirmed repeatability of strain sensitivity, which is important for sensing applications.

Strain sensitivity, calculated based on the linear strain response ranges (excluding the strain increase in cycle 1), yielded the value of 0.38 pm/με. This is about a half of strain sensitivity of this fibre on its own, reported to be in the range of 0.54-0.77 pm/με [321]. Similarly to embedded SOFBG, this discrepancy was also caused by imperfections of the strain test set-up.

The hysteresis of the strain response was always positive, and its value decreased with increasing cycle, yielding 580 pm, 380 pm and 160 pm, respectively, in cycle 1, 2, and 3. Changes of Bragg wavelength in time after strain increment or decrement were relatively small and rather irregular, being the biggest for measurements taken 5 min after strain change. The maximal positive and negative values for cycles 1, 2, and 3 were, respectively, 22/-47 pm, 1/-58 pm, and 0/-44 pm.

POFBG embedded in the ABS sensing patch

The straining response of the ABS-POFBG sensing patch was tested keeping the same experimental conditions as for the PLA sample above (see the first paragraph of the previous section). The results are shown in Figure 6-5.

There was a notable difference between the absolute Bragg peak positions in cycle 1 and 2/3, which amounted to some 340 pm. This may have been due to longer time elapsed between cycle 1 and 2 than 2 and 3, during which ambient temperature and relative humidity might have changed. However, the same experimental conditions for the PLA patch did not yield similar Bragg peak offset. Consecutive straining cycles show ever lower absolute Bragg wavelength values as opposed to the two previous patches. This might have been caused by the fact that the fibre in the ABS-POFBG structure was not strained to let the grating recover its shape before the glue cures, which was mentioned earlier.

There was a clear offset between the data series for strain increase and decrease in cycle 1 as compared to cycle 2 and 3. Similar behaviour was also observed for the PLA-POFBG sensing patch (see Figure 6-4). This difference between strain increase and decrease in cycle 1 can be perhaps explained by the fibre finding optimal position within the housing structure. Linear strain response manifested itself above 0.06 mm stage displacement value. For lower stage displacements, all straining cycles besides strain increase in cycle 1 showed non-linear Bragg peak response to stage displacement, which was due to flaws in set-up design.

The strain sensitivity in the linear range was calculated to be about 0.14-0.15 pm/με. This was some 4.5 time lower than the values reported for non-embedded fibre, which fall between 0.54 and 0.77 pm/με [321]. As in the case of the other sensing patches, this discrepancy was also caused by imperfections of the strain test set-up.

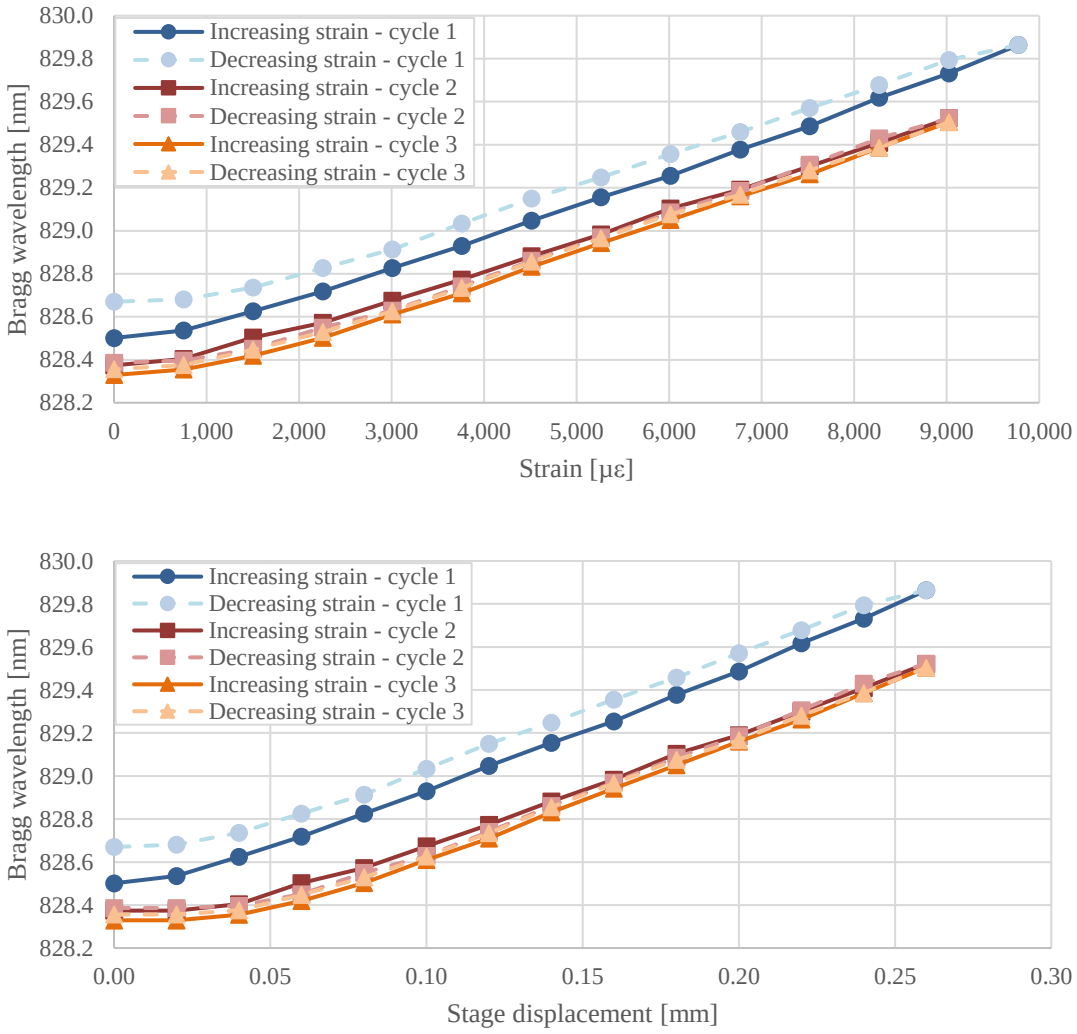

Figure 6-5. Bragg reflection peak for the ABS-POFBG immediately after strain change as a function of strain (top) and testing stage displacement (bottom) for the sensing patch of ABS.

The strain hysteresis was always positive and the biggest in the first strain cycle (169 pm). The other cycles yielded much smaller hysteresis values (12 pm in cycle 2 and 27 pm in cycle 3). Bragg wavelength changes in time after strain increment or decrement were very small in all the cycles. The maximal positive and negative values for cycles 1, 2, and 3 measured after 5 min from strain change were, respectively, 13/-9 pm, 4/-11 pm, and 5/-11 pm.

Comparison of the strain response of the embedded FBGs

Summary of straining characteristics of the three samples (SOFBG embedded in ABS, POFBG in PLA, and POFBG in ABS) has been collated in Table 6-1. Their strain displayed some discrepancies with literature results and experimental artefacts. As was mentioned earlier, much of the unexpected behaviour of the samples during the stain tests was coming from the imperfections of the straining set-up, which was only found after finishing the trails.

First, the same screws in the clamping mechanism of the set-up were responsible for clamping the sample to the set-up and holding some elements of the set-up together. The force holding the elements of the set-up together should be as high as possible not to permit set-up elements being loose and, hence, bending and sliding past each other. However, the clamping force could not be too high not to damage the sample and, so, the screws were not tightened as much as it would be required for the set-up elements to be firmly bound together. This explains the non-linearities observed in the strain test graphs for all the samples for low strain or stage displacement values (up to 0.06-0.08 mm). Moreover, this behaviour of the set-up could have influenced the measured values of strain hysteresis and sample length change. Hence, no conclusion can be drawn from them.

Another unfavourable effect came from screw tightening force changing with each mounted sample. This, in turn, varied also the force binding together the elements of the setup and, hence, dictated how much of sample straining force was effectively absorbed by the set-up elements as described above. That behaviour was found to be behind the large discrepancies between the measured strain sensitivity values and those expected based on the literature.

However, despite the imperfections of the strain test set-up, some conclusions could be drawn from the test results. It could be observed that, after clamping a sample (i.e., fixing the tightening force), the measured strain response was repeatable over the three strain cycles for each sample, yielding stable strain sensitivity value in the linear range. For POFBGs, Bragg peak position for increasing and decreasing strain did not overlap in cycle 1 (as opposed to cycle 2 and 3). As explained, this could have been due to the fibre finding the optimal position in the housing structure after embedding. This effect was not observed for the SOFBG sensing patch, in which case the data series for increasing and decreasing stain virtually overlapped for all the three straining cycles. Finally, it could also be observed that the strain cycles for the same sample did not start at the same Bragg wavelength. Variations of ambient temperature and humidity between the strain cycles could be at the origin of this.

The maximal shifts of Bragg wavelength in time after strain change for all the measurements on the timescale of 5 minutes was -58 pm, while it was usually much lower. It is unsure how much this effect was contributed to by the test set-up imperfections. However, the same effect was observed during the tests with the upgraded strain test set-up and procedures (Section 6.2). Then, it was ascribed to asymmetry of the sample coming from temperature gradient during 3D printing along *z* axis. This resulted in the housing structure being slightly bent along the fibre axis. It is supposed that negative Bragg peak change in time after a strain increment could be associated with the beam-like part of the structure becoming ever more linear (i.e., the bent radius slowly rising), resulting in smaller strain amount sensed by the FBG. This mechanism is discussed in more detail in Section 6.2.

Table 6-1. Summary of straining characteristics for the manufactured sensing patches.

Parameter	SOFBG	PLA-POFBG	ABS-POFBG
Measured strain sensitivity (pm/με)	0.39-0.41 or 0.95	0.38	0.14-0.15
Literature value for unembedded fibre (pm/με)	~1.2 (Table 2-5)	0.54-0.77 (Table 2-6)	0.54-0.77 (Table 2-6)
Hysteresis after cycle 1, 2, and 3 (pm)	401, -222, -80	580, 380, 160	169, 12, 27
Maximal positive Bragg peak change after 5 min from strain change in cycle 1, 2, and 3 (pm)	18, 6, 9	22, 1, 0	13, 4, 5
Maximal negative Bragg peak change after 5 min from strain change in cycle 1, 2, and 3 (pm)	-42, -25, -18	-47, -58, -44	-9, -11, -11

6.1.5 Temperature response of the sensing patches

After strain tests, temperature response of the samples was assessed. They were placed on a hotplate under a specially prepared thermoinsulating cover. It had an opening for a mercury thermometer tip, which was used to control the temperature. The maximum temperature during the test was ~43 °C. This was because POFBG annealing was suspected even at this low temperature, so the patches were not tested at higher temperatures to avoid damaging them. Moreover, fibre slippage was suspected for the silica grating. However, for in-vivo medical use, a temperature of 43 °C can be considered sufficient. It must also be mentioned that the hotplate displayed limited thermal stability in time despite the cover used. The issue was especially visible with the SOFBG patch, as temperature sensitivity was observed to be very high. With this sensing patch, it was clearly visible that the hot plate, attempting to keep stable temperature, displayed cycles of heating up and cooling down at lower temperatures. Hence, it must be borne in mind that the non-linear temperature response of the SOFBG patch was at least partly influenced by the testing set-up.

SOFBGs

The SOFBG patch was interrogated with the HBM DI110. Although the T-FBG was meant to measure the temperature, ε-FBG was found to give a more credible reading. This was because it was placed centrally in the sensing patch, and hence was closer to the central heating region of the hotplate. Because of that, when the central ε-FBG showed the temperature to stabilise or start decreasing, the temperature reading at T-FBG was still rising.

As it has been mentioned above, the hot plate showed cycles of temperature increase (heating) and decrease (cooling) for every temperature setting at lower temperature value. Hence, on increasing temperature, the highest readings for each temperature value were noted, whereas the lowest temperature readings were taken on temperature decrease. The resulting plot is shown in Figure 6-6. It shows roughly linear response to temperature. The non-linearities were later found to be caused at least partly by the testing set-up. Upgrading temperature testing set-up and procedures led to much more linear fibre response to temperature, which is discussed in Section 6.2.4.

Temperature sensitivity for increasing temperature was found to be 146 pm/°C, and for decreasing temperature, 169 pm/°C. These values were 15-17 times higher than temperature sensitivity of unembedded silica grating, which is around 13 pm/°C (see Section 2.7.4). Such an increase in temperature sensitivity comes probably from the fact that the linear CTE of ABS (73.8×10^{-6} °C^{-1} [371]) is over 130 times higher that this of fused silica (0.55×10^{-6} °C^{-1}). As adhesion between the fibre and the structure is high, the fibre is forced to expand with the structure on heating up, which effectively makes it strain. However, temperature sensitivity of silica FBGs is mostly contributed to by thermo-optic coefficient of silica and not its CTE, which is the reason why 130 increase of CTE should not be expected to give an equivalent increase in temperature sensitivity of the embedded grating.

The temperature cycling hysteresis of the temperature response of -526 pm was observed. As it was measured at room temperature, the aforementioned limitations of the testing set-up should not have influenced it. Moreover, it could not have been due to fibre relaxing the compressive strain (under which the fibre was put after embedding) at higher temperature. In this instance, the Bragg peak at room temperature would have increased from ~1524 nm after embedding to get closer to an original wavelength of ~1530 nm. This would have yielded a positive hysteresis value, which was not the case. Furthermore, the hysteresis could not be ascribed to inaccuracy of temperature measurement (±1 °C) because the measured hysteresis value would translate into a temperature difference of over 3 °C (assuming the temperature sensitivity estimated earlier). It is then speculated that the origin of hysteresis could be explained by annealing the plastic housing structure itself, permitting to relax the stress frozen in it. However, further investigation would be necessary to confirm that.

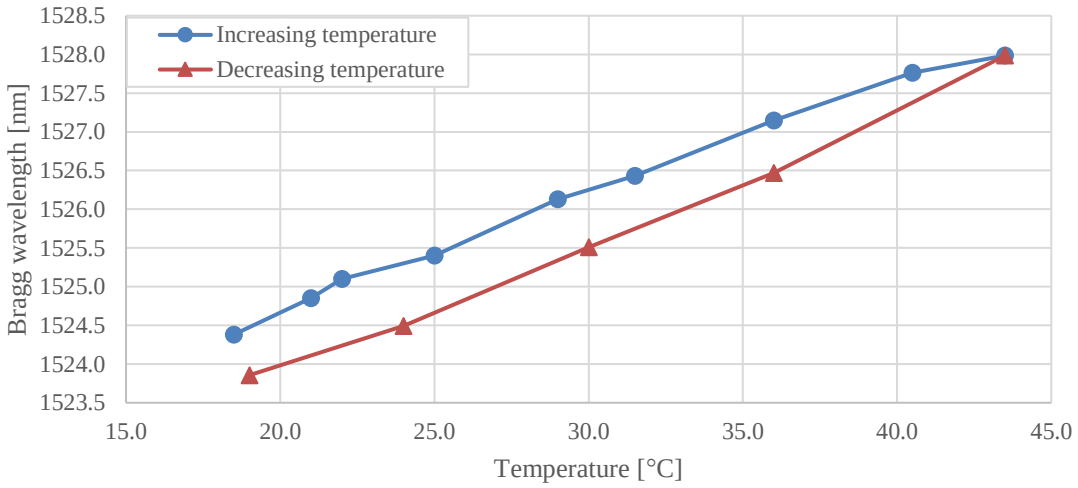

Figure 6-6. Bragg reflection peak of the ε-FBG (SOFBG) immediately after reaching given temperature as a function of temperature (the sensing patch made of ABS).

POFBGs

The temperature response of both POFBG sensing patches was found to be very unstable. The Bragg peak was visibly decreasing with time at temperatures of 30-35 °C, which is at least 15 °C below the annealing temperatures used usually for unembedded POFBGs in this fibre (see Section 3.3.3). It is possible that the phenomenon had to do with annealing of structure material or glue rather than the grating itself, but a definite answer to that would need further investigation. Only the PLA-POFBG structure was managed to be partly thermally stabilised after 3-hour annealing at 55 °C (more than 10 °C above maximal intended temperature of operation and the highest temperature in the temperature test cycle). At the end of the annealing, the Bragg wavelength had decreased by 13.92 nm to 814.08 nm. The thermal response of this grating measured after the annealing was plotted in Figure 6-7.

Thermal hysteresis after cycling was -220 pm. It might be that stabilisation was not complete and the grating, housing structure, or glue annealed further. The resulting temperature sensitivity was 30-40 pm/°C, whereas the usually reported values are of similar magnitude but negative (see Table 2-6). Nevertheless, is has to be noted that the temperature response of POFs made of PMMA is often fibre-dependent and also strongly dependent on humidity [4].

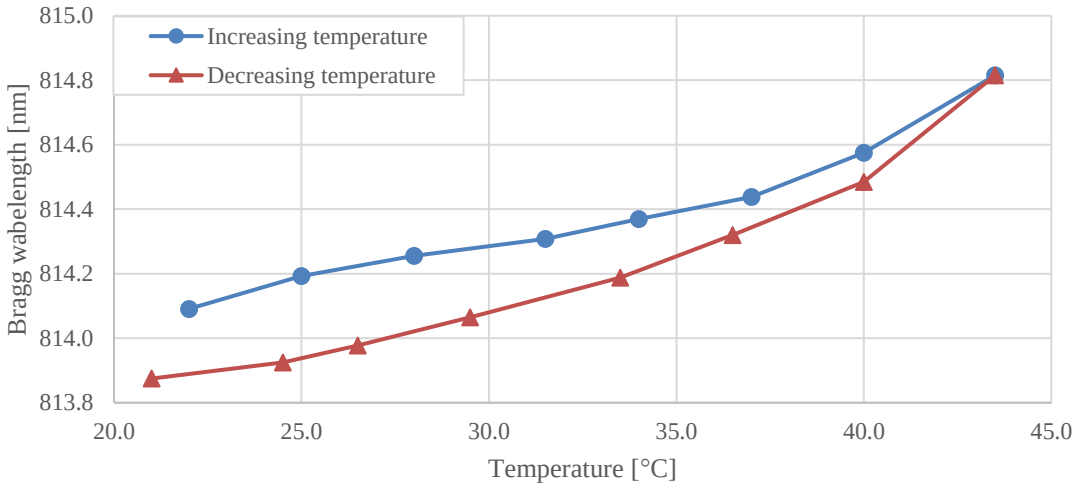

Figure 6-7. Bragg reflection peak of the PLA-POFBG immediately after reaching given temperature as a function of temperature (the sensing patch made of PLA).

6.1.6 Conclusions

In this chapter, an SOFBG embedded in an FDM-3D-printed housing structure yielding a dual-grating temperature-compensated strain sensor is reported. Moreover, the first ever integration of POFBG with a 3D-printed sensing patch for strain or temperature sensing is presented.

Different strain sensitivity figures of the sensing patches were reported: 0.40 and 0.95 pm/με for SOFBG embedded in ABS, 0.38 pm/με for POFBG in PLA and 0.15 pm/με for POFBG in ABS. Strain sensitivity was repeatable and strain response did not change much in time on the timescale of minutes. Strain hysteresis was found to decrease with straining cycles, the smallest value of 12 pm having been measured for the ABS-POFBG patch.

Temperature sensitivity of the SOFBG sensing patch was found to be 146-169 pm/°C, which was up to 17 times higher than the value for an unembedded silica grating. The temperature response of POFBG sensing patches was unstable, yielding 30-40 pm/°C for PLA-POFBG. However, both sensitivity figures have limited credibility due to imperfections of the temperature test set-up.

Many experimental artefacts were observed during both strain and temperature trails, which were later found to be coming from the experimental set-ups and procedures used. The next section discusses the upgrades to them and the results that they yielded.

6.2 Upgraded housing structure and testing procedures

The results of strain and temperature tests of the embedded FBGs presented in Section 6.1 were found very incoherent. Inconsistencies of the strain response were found to be due to some imperfections of the set-ups and procedures used to test the samples. These issues and they ways they were addressed are presented in this section. The focus was put on embedding SOFBGs while embedding POFBGs was

neglected. The reason behind that was to avoid complications related to polymer gratings, especially their possible annealing. Moreover, the technology of silica FBGs is more robust and mature, and hence, they are easier to work with.

6.2.1 Upgraded design of the straining set-up and housing structure

When testing unembedded silica and polymer FBGs, attaching one point of the fibre to a fixed support and the other, to a simple translation stage is enough to achieve linear and repeatable results. This is because the force acting on the straining set-up from the strained fibre is very small, so the mechanical robustness of the set-up is not of paramount importance. However, it was found to be the opposite for embedded FBGs due to considerable force required to strain the 3D-printed housing. For this reason, special care must be taken to ascertain that the experimental artefacts coming from the set-up are eliminated or minimised, which was not recognised during the earlier straining trials.

Furthermore, it was also found important to match the design of the housing structure to the straining set-up used to test it to facilitate measurements (Figure 6-8). A few changes were introduced with respect to the design described Section 6.1. They are discussed in detail below, together with the respective changes in the set-up. The upgraded set-up was also prepared in the software SketchUp Make 2016. The embedding procedure described in the previous section did not change. The grating was also meant to be positioned on the neutral axis of the beam (i.e., along the symmetry axis of the printout in the case of this design). Hence, it was placed along a groove in the central layer of the beam-like part of the structure, having equal number of layers below and above it. The total number of layers in the beam-like part of the structure then had to be uneven. In the upgraded design, this was 17 layers of 0.15-mm height, yielding the beam of a thickness of 2.55 mm. As it was in the previous design, this one also allows embedding fibres with secondary coating on (see the right-hand side fibre inlet in Figure 6-8(b).

The major issue concerning the strain test results presented in Section 6.1 were considerable differences in strain sensitivity of the embedded gratings. In particular, the SOFBG embedded in the ABS housing was tested twice to give the results as different as 0.39 and 0.95 pm/με. Moreover, all embedded gratings showed non-linear response to strain at small strain values: it was initially close to zero and rising gradually over 2-4 strain increments to become linear at higher strains. Both these problems were found to be coming from the straining set-up used to test the samples.

The difference in strain sensitivity was expected to be coming from varying clamping force in the two tests. 3D printouts are more delicate than similar structures produced with conventional methods because of the layered structure of the former. Hence, the clamping force to hold the housing structure for the strain test cannot be too large not to smash the printout. However, the previous straining set-up was constructed so that the clamping screws were also responsible for the strength of the connection between the clamps and the rest of the set-up. Thus, mounting the clamps too loosely gave rise to some backlash in the clamps and the mounting screws, and possibly allowed the elements of the clamping

mechanism move past each other. The loose clamping mechanism, in turn, was absorbing some stain, its particular amount expectedly being proportional to the clamping force used in each test. Moreover, loose clamping was also making it difficult to assess the range of the structure that was being strained because part of the sample below the clamp could also undergo some straining.

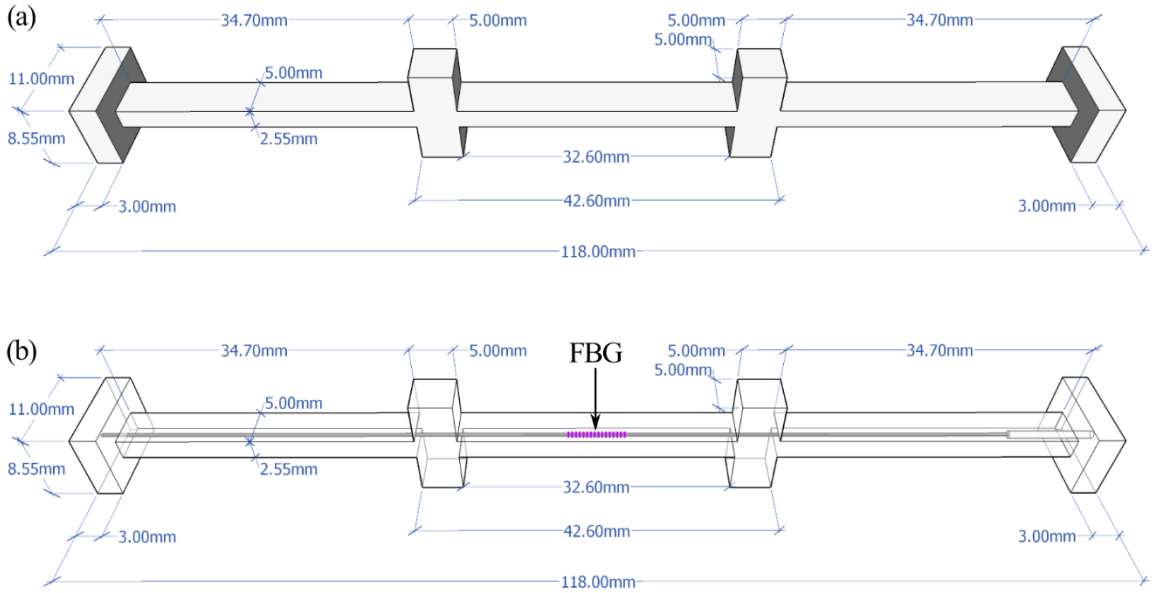

Figure 6-8. Design of the upgraded housing structure used to embed SOFBGs: the view of (a) the outer surfaces only and (b) both the outer and inner structure, showing the channel for fibre embedding and the position of the grating.

The problem of different strain sensitivity among the tests was resolved by changes to the clamping mechanism and design of the housing structure. Spacers were introduced between the upper and lower clamps (marked in violet in Figure 6-9), which allowed firm tightening of the clamping screws without damaging the structure under test. Furthermore, the design of the housing structure was altered. First, mounting legs in the structure were designed so that they fit in the openings of the clamps to press against them during straining. Secondly, the thickness of the beam-like middle part of the structure that were strained (marked in red in Figure 6-9(a)) was set so that it was slightly smaller than the spacing between the upper and lower clamp (2.55 vs 3.15 mm in the previous design). This ensured that the clamps were not pressing against the part of the sample to be strained (see the inset in Figure 6-9(b)). However, this difference was yet small enough not to pose risk of the mounting legs bending during straining, which would interfere with the measurement results. The mounting legs were also made relatively thick (5 x 5 mm in *x*-*y* plane) to minimise this risk further.

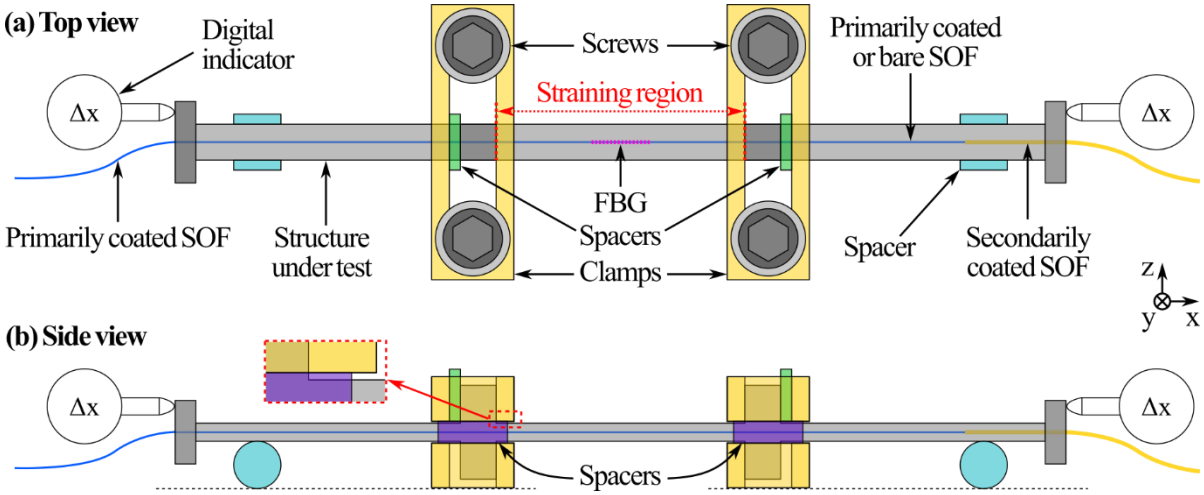

Figure 6-9. (a) Top view and (b) side view of the SOFBG embedded in the housing structure mounted in the straining set-up. One of the clamps was mounted on a fixed support while the other, on a translation stage. Screws are not shown in (b) for clarity.

The initial non-linearity of strain response was found to be coming from mechanical instability of the set-up, including the translation stage, the mounting plates and other elements used to construct it. They were bending or twisting upon the force coming from the strained sample. They were reaching the saturation value around the fourth strain increment, leading to linear strain response at higher strain. In order to minimise the effect of the initial non-linearity of the strain response, different stage and mounting elements were used in the upgraded straining set-up. It was constructed on an optical table, similarly to the previous one. The stage in the upgraded set-up contained crossed-roller bearings of smaller backlash and was composed of elements that were fitted more tightly. The stage was also wider (longer along *y* axis) as were other elements of the upgraded straining set-up. Finally, the sample was placed on the set-up centrally with respect to all the mounting points. All this ensured that the twisting force on the set-up was minimised and that the remaining part of it was having minimal influence. The construction elements that were used were also all based on M6 screws, which – when tightened strongly – bind the elements of the set-up together firmly. This allowed avoiding any backlash and the set-up elements sliding past each other, and it minimised the effect of the set-up elements bending.

In addition to the described changes, the straining set-up was fitted with two digital indicators (Mitutoyo 543-391B, resolution: 1 μm, maximal permissible error of indication: 3 μm, hysteresis and repeatability: 2 μm). They touched the end pads of the housing structure, which were added in the new design to facilitate contact with the probes of the indicators. This ensured that the displacement at each end of the structure was measured directly at the sample end and not at any part of the straining set-up. The two values of displacement were then used to calculate the value of the strain using the distance between the mounting legs (~32.60 mm, measured before each trail; marked in red in Figure 6-9(a)). Relying on direct measurement of displacement at both ends of the sample allowed much more precise

assessment of strain than depending on the micrometric screw of the translation stage. First, the indicators offered higher precision (1 vs 10 μm). Secondly, due to relatively high force from the sample acting on the stage, the elements of the set-up could react to it by slight bending and twisting, due to which the strain that the sample underwent was smaller in the reality than indicated by the micrometric screw of the translation stage. Furthermore, in addition to monitoring the end of the sample clamped to the translation stage, the strain of the fixed sample end was also controlled and used to correct the measurement of the actual displacement. The displacement of the fixed end was found to be about 10% of this at the translated end. This also shows that the reaction of the straining set-up to force coming from the structure during straining was not negligible and had to be gauged.

The changes to the straining set-up and the design of the housing structure described above allowed measuring the strain response of the sensing patches much more accurately and repeatably. Nevertheless, during the initial tensile strain tests with the upgraded set-up and housing structure, further changes prove necessary. First, a close observation revealed that the housing structure was not exactly symmetric along *x* axis after printing despite being so by design. This was ascribed to two factors, the first of them being the temperature gradient along *z* axis during printing. It came from the heated printing bed, which – despite decreasing the problem of printout warping and detaching from the printing bed – also deviated the geometry of the sample after printing. This was caused by uneven contraction of different parts of the printout on cooling down. Those that were kept at the highest temperature during fabrication (i.e., closest to the printing bed) contracted most, while those kept at the lowest temperature (i.e., furthest away from the printing bed) contracted least. To tackle this issue, the upper and lower clamps were slightly shifted with respect to each other. It only offered a partial solution though because the angle between the mounting legs and the central beam-like part of the printout was not exactly right.

The second factor affecting the symmetry pertained to the orientation of the planes building the mounting legs. Instead of being oriented normally or parallel to *xyz* axes, they were slightly skew. This was believed to be due to not taking special care to ensure high quality of reproduction of the corners because the options required for that were missing in the slicer and control software used with the printer. Corners of the sample not being resolved well might be related to the movement of the printing nozzle when drawing the external perimeters of the printout. The nozzle was always drawing them in the same rotational direction. If the printing speed is too high, the thread that has just been deposited shrinks on cooling down, which results in corners being rounded, possibly unevenly. If the same situation is reproduced in consecutive layers in *z* direction, this may lead to the skewness of the entire surfaces. This issue can be tackled by decreasing the printing speed or making the nozzle dwell over the corner for a moment (tens to hundreds of milliseconds) to let the thread being deposited stabilise. In the case of the housing structures used for SOFBG embedding, this skewness was very small but could possibly still influence the results, which is discussed later. To minimise the effect of this asymmetry, the clamps

were positioned slightly skew so that the central beam-like part of the structure was parallel to the translation direction.

In addition to changing the way of clamping, two types of spacers were added to the set-up to facilitate testing. The first one (marked in green in Figure 6-9(a)) stabilised the mounting legs within the clamps and ensured the right angle between the central beam-like part of the sample and the mounting legs. This helped minimise the influence of the asymmetry of the mounting legs coming from the temperature gradient on printing. The other type of spacers (marked in cyan in Figure 6-9(a)) was used to support the ends of the sample. Without these spacers, it was observed that the end pads were changing their position a little on the first strain increment. This was probably caused by the geometrical imperfections of the printout coming from the temperature gradient along *z* axis during printing. Possibly, they could have been further contributed to by other printout and set-up imperfections that were still left despite taking all the aforementioned precautions.

The geometrical imperfections could have also been addressed by machining the surface of the samples. However, both automated and hand machining would be rather difficult and would likely not provide high enough precision. Moreover, the samples could have also been tested in an axial stress-strain testing apparatus, which is typically used to test stress-strain response of the material. This way, some issues pertaining to the mechanical stability of the current straining set-up could have been addressed. Nonetheless, the majority of the problems regarding testing the printouts was related to the clamping part of the set-up, which would also have to be present in the axial stress-strain testing apparatus. Furthermore, it does normally only allow testing the response to strain in tension and not compression, while both are possible with the current set-up.

In addition to the upgraded design for SOFBG embedding, another structure was devised to allow mounting a non-embedded grating in the upgraded strain testing set-up. It was similar to the upgraded design for embedding, the major difference lying in the missing middle beam-like part of structure (Figure 6-10). This permitted measuring the strain sensitivity of a reference grating on the same set-up, to which the results of the embedded gratings could be compared. Moreover, the strain sensitivity of the fibre used was not available in the literature. It should be noted that the straining set-up could behave differently depending on the total force required to strain the sample, which was considerably lower for the non-embedded grating. Still, this was the best reference that could be achieved for this set-up and is further discussed later, being hereinafter referred to as the reference sample or reference grating.

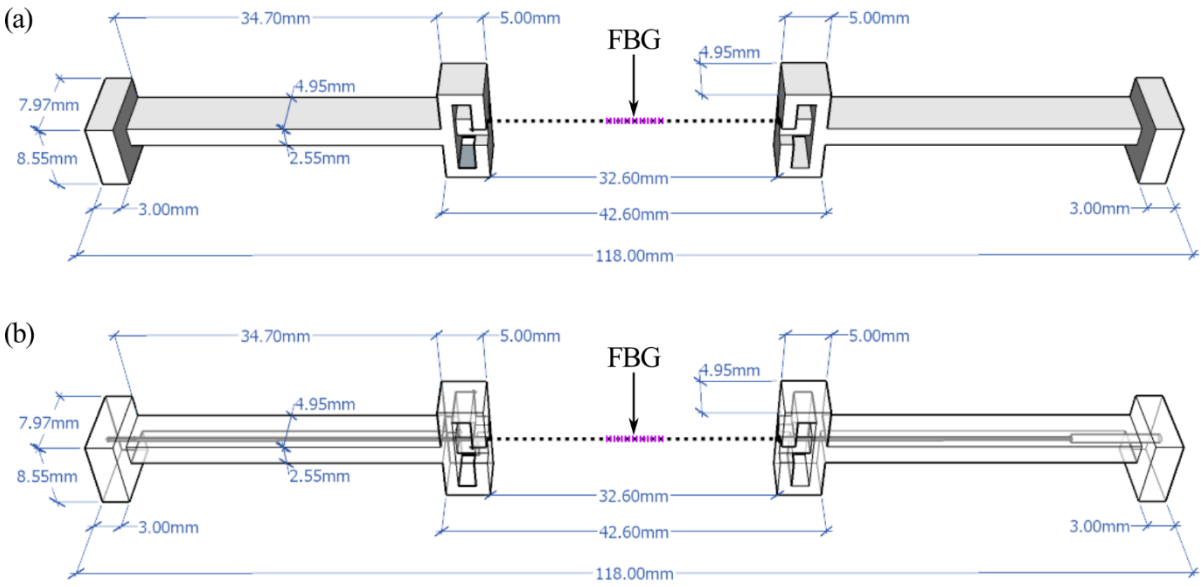

Figure 6-10. Design of the housing structure used for mounting a reference non-embedded SOFBG in the upgraded straining set-up: the view of (a) the outer surfaces only and (b) both outer and inner structure, showing the channel for fibre embedding. The dotted line extrapolates the channels and marks the position in which the fibre with the FBG in was placed.

6.2.2 Fabrication of the sensing patches

This section describes fabrication of the reference sample (see Figure 6-10) and sensing patches using the upgraded design described above (see Figure 6-8). The FBGs that were used were inscribed according to the phase-mask method in the photosensitive fibre PS 1250/1500 from Fibercore with the HeCd 325-nm laser using the phase mask with a period of 1061.18 nm (see Section 3.3). Two grating characteristics were varied: presence or lack of the primary coating on the embedded FBG and the scanning length (point gratings, 1.2-mm long, or scanned gratings, 6-mm long). The rationale behind this was to check the influence of primary coating and grating length on FBG behaviour once embedded. Based on the type of grating that was embedded, the four fabricated samples are referred to as coated point (CP), coated scanned (CS), bare point (BP) and bare scanned (BS). In the case of all the samples, fibre at the inlets had primary or secondary coating on for mechanical robustness. Secondary coating was stripped at ~5-10 mm after the fibre entered the housing. The same applied to the primary coating in the case of the samples with bare FBGs, in which case the fibre was bare for almost entire length of the housing. Exposing only the grating region had previously been found to yield unfavourable characteristics (see Section 6.1.3).

The embedding procedure was similar to this described in Section 6.1 for SOFBG embedding. The printing process was paused midway and acrylic glue (Superglue) was deposited along the entire length of the embedding channel. The fibre was then inserted in the channel and completely covered with the

glue. It was allowed to cure, usually for a few tens of minutes. Finally, the 3D-printing process was resumed to complete the embedding.

Bragg wavelength change in time during manufacturing of the sample CP is shown in Figure 6-11. The graph starts after gluing the grating in the structure and finishes after removing the grating from the printing bed. After inserting the fibre in the structure, depositing the glue, and letting it cure, the Bragg wavelength (λ_B) of the grating CP was at 1535.97 nm (t = 0 in the graph). The printing was then resumed to continue embedding, resulting in multiple peaks in Figure 6-11, whose close view is shown in the inset. These peaks came from the temperature changes sensed by the grating related to movement of the nozzle. After the printing was finished (t = 11 min, λ_B = 1534.65 nm), the sample was left on the printing bed to cool down and stabilise, showing slow and steady fall of the Bragg wavelength. At t = 5 h 20 min, the sample was removed from the printing bed, and the printing raft and support was detached from the printout. This resulted in a step decrease in λ_B to 1531.98 nm. It was related to relaxation of the stress introduced in the sample during cooling after printing. When the printout was still attached firmly to the printing bed, it was preventing the housing from relaxing the stress. After the step decrease in the Bragg peak, it was further falling gradually. This could be ascribed the hysteresis of the plastic, which was expected to appear as the structure was effectively stretched over a few hours after cooling on the printing bed. After being removed from it, the sample was allowed to relax for 18 h (not shown in the graph), yielding a further Bragg peak decrease by 0.53 nm to 1531.45 nm. Very similar Bragg peak falls were observed for all embedded gratings (Table 6-2).

The overall Bragg wavelength decrease with respect to the position after gluing in and before resuming printing was ~4.5 nm. This corresponds to the housing structure contracting by ~3800 με (0.38 %) relative to the size at which it was printed. That value is related to the temperature decrease and was calculated assuming a strain sensitivity of the SOFBG of 1.2 pm/με at ~1550 nm (see Section 2.7.4). It was also assumed that the entire strain of the housing structure was sensed by the embedded FBG. As will be shown in the next section, presenting the response of the samples to strain, complete strain transfer from the housing to the fibre is not the case. Embedded FBGs displayed a clear tendency to sense a higher portion of the housing strain than the coated ones: respectively, ~91-93 % vs. ~71-72 %. However, as will be shown in Section 6.2.4, this tendency was not observed during the temperature and humidity tests. Strain transfer from the housing to the fibre is discussed in more detail in the respective sections. It is then likely that the actual contraction of the housing was higher than gauged by the FBG, but it is difficult to assess the contraction value. For the data collated in Table 6-2, no clear trend for bare and coated gratings can be observed. This could be due to the lack of precise control of temperature, relative humidity, and time after embedding at which the Bragg wavelengths were noted for each sample.

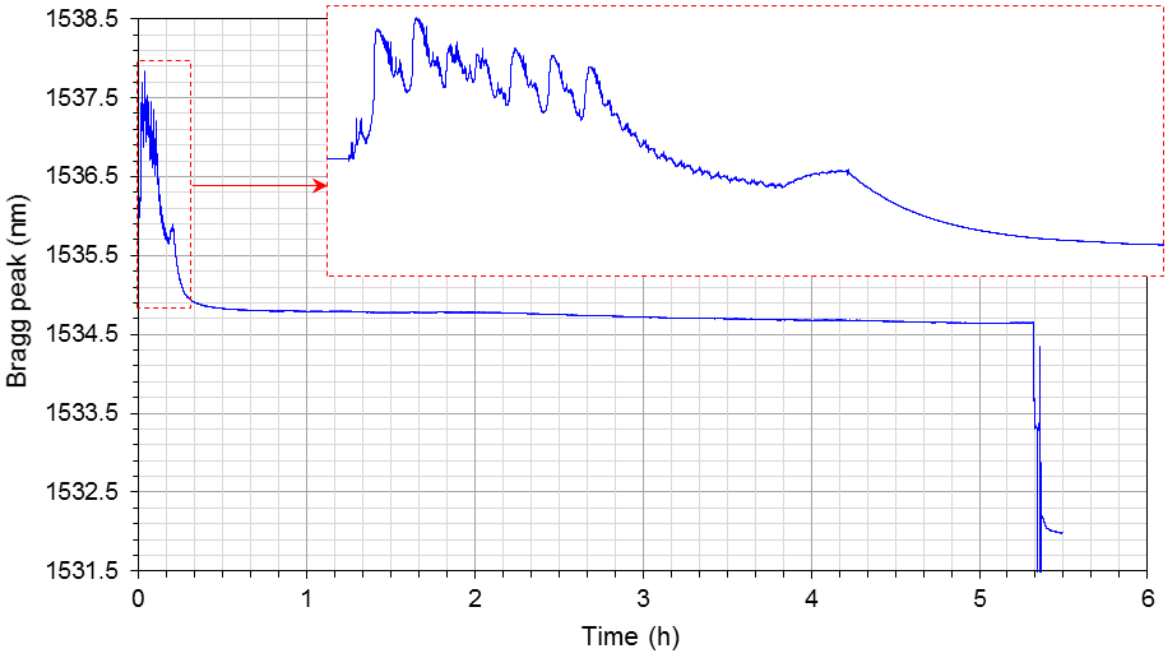

Figure 6-11. Bragg wavelength of the grating CP during embedding (see text for details).

Table 6-2. Comparison of Bragg wavelengths before and after embedding for the four SOFBGs embedded in the upgraded housing structure

	Bragg wavelength (nm)		
Sample	after gluing in, before resuming printing	after embedding[a]	Bragg wavelength difference (nm)
Bare scanned (BS)	1535.81	1531.53	-4.28
Coated scanned (CS)	1536.00	1531.75	-4.25
Bare point (BP)	1536.23	1531.86	-4.37
Coated point (CP)	1535.96	1531.98	-3.98

[a] the values after detaching from the printing bed and removing the printing raft and support; the peak might have decreased further by up to a few hundreds of picometres

6.2.3 Strain response of the sensing patches

This section discusses the strain response of the samples manufactured according to the new design and tested on the upgraded set-up. The samples were interrogated according to the schematic shown in Figure 6-1(a). As it was mentioned earlier, during the initial tensile strain tests it was found that some minor changes still needed to be made to the set-up. Hence, some samples were tested multiple times while the adjustments to the set-up were being made. This repeated loading was found not to deteriorate

their performance, which is described below in more detail. All the samples besides CS were tested both in tension and compression, while the coated scanned sample, only in tension. This was because that sample was used in the temperature and relative humidity tests before the compression trails, for which the set-up had to be rebuilt (the translation stage needed reverting). The sample CS was retested in tension after the temperature and humidity trails to find that its characteristics had changed. The strain tests in compression were then abandoned for this sample since they were not needed for comparison with others, which had not been affected by temperature and humidity cycling. Nevertheless, the lack of data from the compressive strain test for the CS did not have virtually any effect on the conclusions, as it is shown later.

Table 6-3. Number of experiments in tension and compression for all the samples fabricated according to the upgraded design.

	Number of experiments		
Sample	In tension	In compression	Total
Bare scanned (BS)	12	3	15
Coated scanned (CS)	9	–	9
Bare point (BP)	2	2	4
Coated point (CP)	2	1	3
		Total for all the samples:	31

Tensile strain, steps of 1.5 min

Almost all the strain experiments followed the same pattern. Strain was increased in steps up to about 4000 με and then, similarly, decreased in steps. Their size was ~10-15 μm, and the sample was kept at each step for ~1.5 min. The results for all the samples were similar, so each type of graph is shown for only one samples, while the differences among the samples, if any, are discussed in text.

An example of FBG reflection spectra on increasing strain is shown in Figure 6-12. For all the samples, the shape of the Bragg peak remained unchanged during strain change. This proved that embedding did not induce any unusual and undesired grating behaviour.

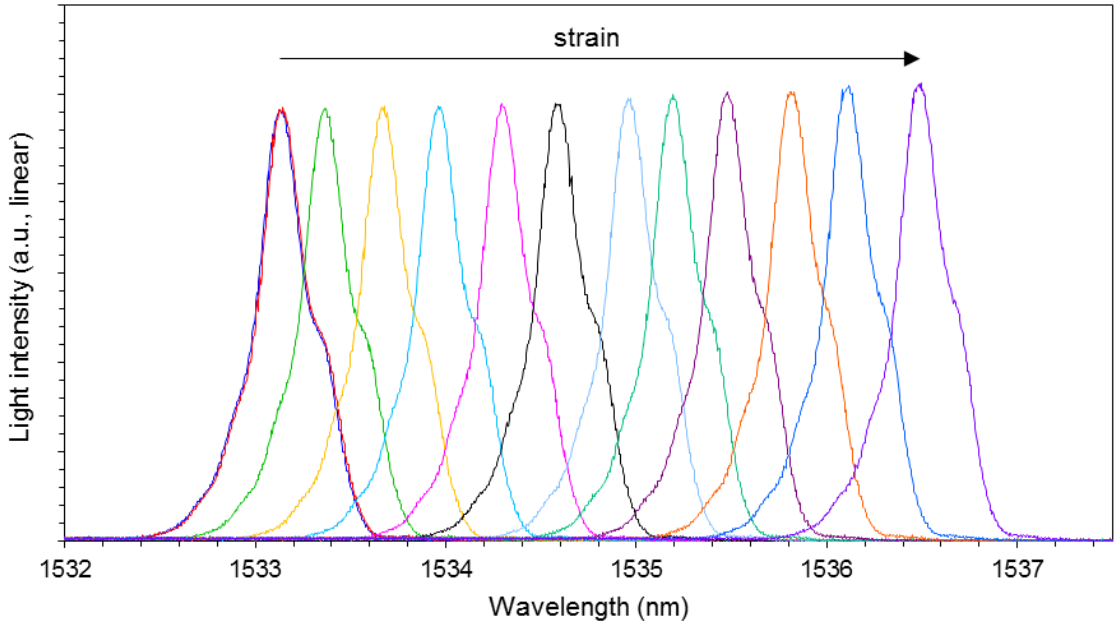

Figure 6-12. Reflection spectra of the sample CS on strain increase (those at strain decrease are not shown for clarity).

Figure 6-13 shows the change of the Bragg peak position in time during a tensile strain experiment for the sample CP. All the following figures related to tensile strain tests will feature this sample for the sake of consistency. The size of the step increment was set to 20 μm according to the scale of the micrometric screw of the translation stage. However, the difference of the readout of the two digital indicators was giving smaller relative displacement values. They were about 50-60% of the translation read from the stage micrometric screw on higher stain, whereas their value during one or two first strain increments was lower. Smaller values coming from the indicators were probably due to bending of the elements of the set-up under relatively high force exerted on it by the strained sample. This is further confirmed by the displacement values measured by the indicator at the fixed end of the sample, amounting to ~10% of this gauged at the translated end. Moreover, for the reference sample, in which case the force acting at the set-up was markedly smaller, the displacement measured at the fixed end was strictly zero throughout the experiment. The huge discrepancy between the readout of the micrometric screw and the indicators allows appreciating the importance of depending on the latter. The translation read from the indicators was considered much more accurate since it was coming from direct measurement of the change of the sample length, and hence, it was used in the calculations. In turn, defining the strain steps based on the micrometric screw of the translation stage made strain steps uneven due to its limited resolution, which can be observed in Figure 6-12 and Figure 6-13.

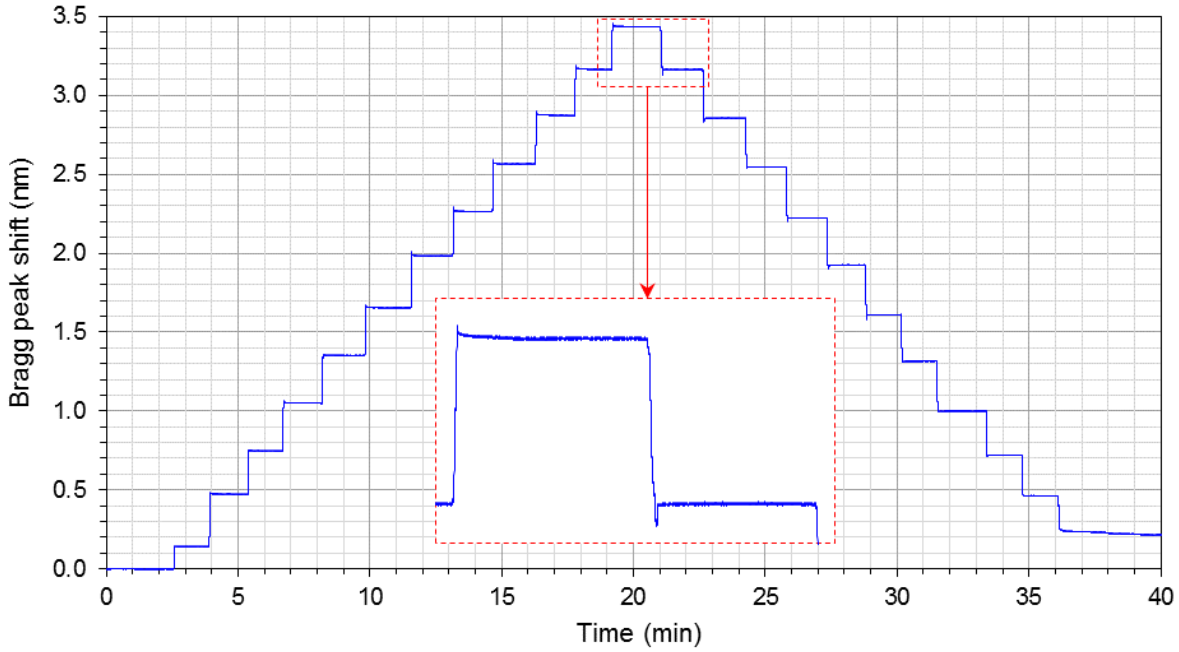

Figure 6-13. Bragg peak shift in time during the discussed tensile strain test of the sample CP with 1.5-min strain steps. The inset shows the close view of the graph at the maximal strain value.

Based on these measurements, Bragg peak shift could be plotted as a function of strain to assess its strain sensitivity (Figure 6-14). It was calculated neglecting the data points when the sample was not at stress, i.e., the very first and a few last data points in Figure 6-14. At the beginning of a strain test, onset of the force coming from the sample and acting on the set-up might have been causing some initial twist and bent in the elements of the set-up (primarily the translation stage mechanism). As a result, the first measurement point was sometimes non-linear with respect to the data captured at higher strain (not well visible in Figure 6-14 but varying from experiment to experiment). On decreasing strain, the force coming from the stress in the sample was observed to vanish before the strain reverted to zero (at 245 με in Figure 6-14). This was the sign of hysteresis of the plastic, which is discussed later. Hence, the data points at no stress were also excluded from calculating the strain sensitivity.

Very similar values of strain sensitivity were achieved during consecutive tests of the same sample. As it was mentioned earlier, in the later trails, the clamps were adjusted to match the slight asymmetries of the structures so that the sample was parallel to the translation direction. This made the strain sensitivity values a little smaller, which are believed to be more accurate, and hence, they are used in the analysis. The sensitivity was usually marginally different on increasing and decreasing strain (up to 0.06 pm/με within the same trial), while there was no tendency as to which one was bigger. It might be coming simply from experimental errors or from imperfections of the testing set-up.

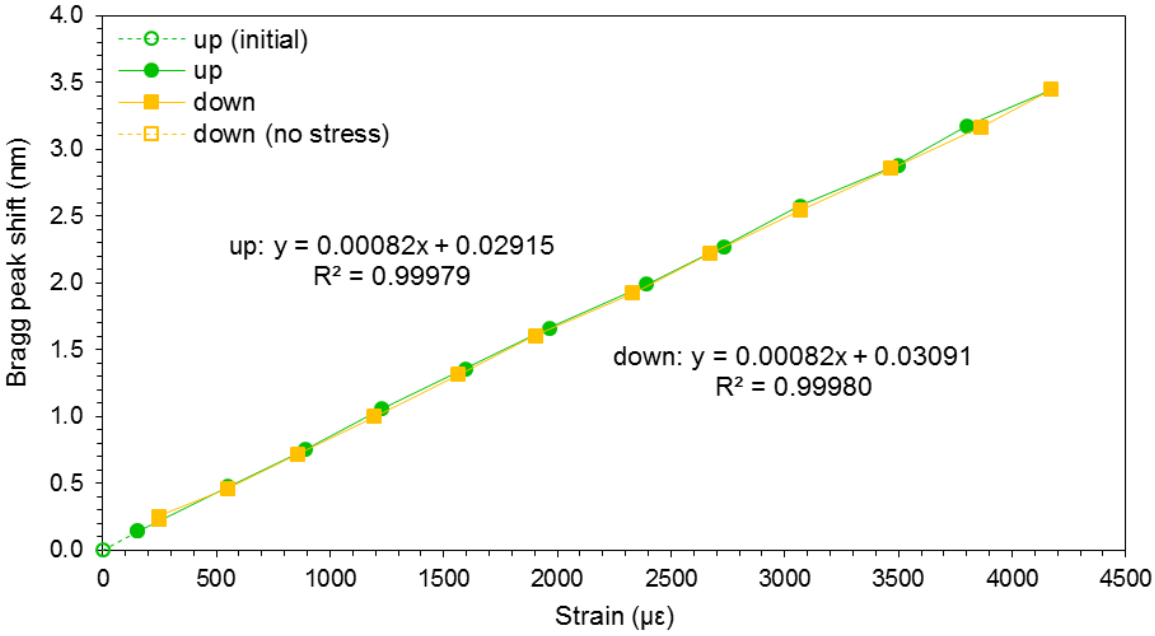

Figure 6-14. Bragg peak shift (right after strain change) as a function of strain during the discussed tensile strain test of the sample CP with 1.5-min strain steps.

Regarding the strain sensitivity among the various samples, a clear difference was observed for bare and coated FBGs. The sensitivity of the former was in a range of 1.025-1.045 pm/με, while of the latter it was 0.795-0.81 pm/με. In turn, the sensitivity of the reference sample was 1.125 pm/με. This means that the difference between the bare samples and the reference one was only 0.08-0.10 pm/με, whereas between the coated samples and the reference is was visibly bigger: 0.315-0.330 pm/με. This can be perhaps explained by the acrylic primary coating shielding a part of stress. In such case, the shielded stress would be proportional to the total stress, which would explain why no non-linearity in the strain response was observed. Finally, no difference in strain sensitivity was observed between point and scanned FBGs.

The lower strain sensitivity for coated gratings could not be explained by fibre moving against the primary coating. As it was mentioned earlier, after embedding, the fibre was at relatively high compression (judging from an FBG peak fall of ~5 nm), putting the fibre at high stress. Despite it, none of the fibres relaxed is since none of the peaks of the embedded gratings was seen to shift back to its original Bragg wavelength. This confirms very good adhesion between the housing structure and the FBGs, which is important from the viewpoint of sensing applications.

Other important characteristics of the embedded gratings to be used as sensors are related to changes of Bragg wavelength on stable strain. In order to test this, the patch was observed for about 1.5 min between the consecutive strain steps. Based on this, changes to Bragg peak over 1 min at each strain step were plotted in Figure 6-15. This graph only considers gradual Bragg wavelength drift in time and neglects the sharp peaks after each strain change (see the inset in Figure 6-13), which are believed to be

due to the mechanics of the straining set-up. It can be seen that the Bragg peak change over 1 min was negative on increasing strain and positive on decreasing strain. These plots for all the samples were very similar, the maximal values of peak shift ranging from -6 to -29 pm for strain increase and from 4 to 15 pm for strain decrease. These values exclude the high peak shift possible at low strain at the beginning or end of each trial. The latter are considered to be related to sample realigning in the test set-up on stress onset at the first measurement point and stress relief at the few last points, respectively. As shown in Figure 6-15, on increasing strain, the magnitude of Bragg peak shift over 1 min was rising with strain, while the tendency on decreasing strain was more complex.

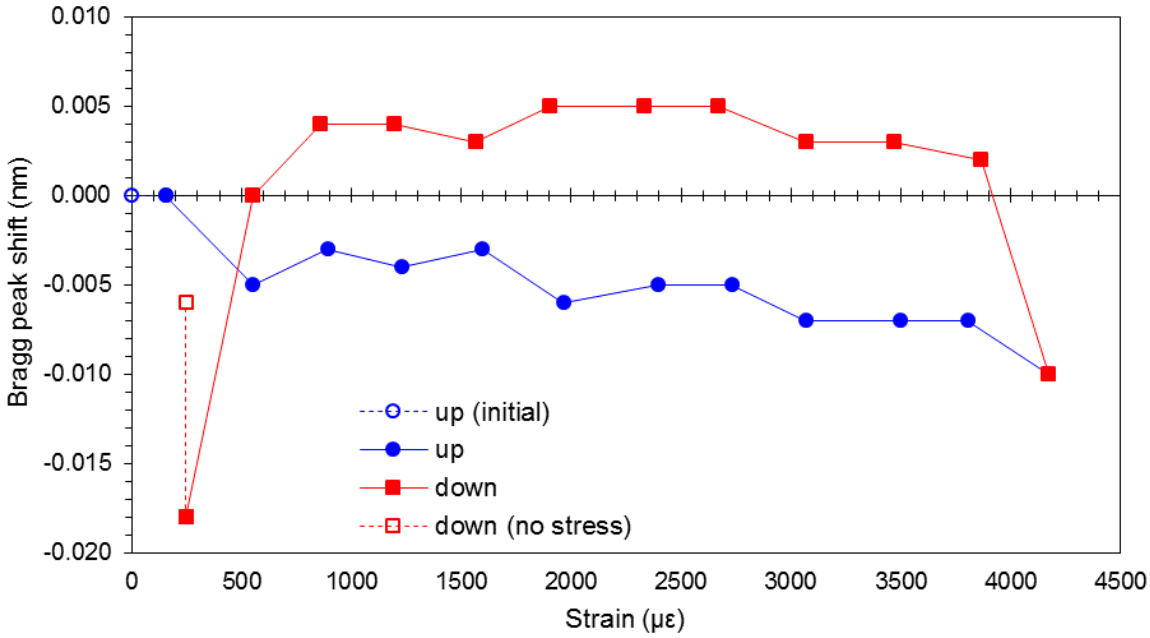

Figure 6-15. Bragg peak shift over 1 min after each strain increment (up) or decrement (down) during the discussed tensile strain test of the sample CP with 1.5-min strain steps.

The origins of the Bragg peak shift over 1 min are by no means obvious. As it was discussed earlier, this shift could not be attributed to movement of the fibre against the primary coating or the glue layer used during embedding. Furthermore, influence of creep of the plastic would also be rather improbable at a relatively low strain and timescale and at room temperature. In addition, creep would be expected to show irreversible changes, resulting in the Bragg peak shift over 1 min being only positive or only negative on both the strain increase and decrease. This is due to creep being proportional to stress, which in both cases was acting in the same direction and not changing sign. For the same reason, imperfections of the experimental set-up are most probably not at the origin of the observed behaviour. It can be perhaps explained by two factors. First, fibre might have not been positioned exactly along the neutral axis of the fibre as the precision of positioning was limited by the accuracy of the printing process, thickness of the glue layer used, and manual handling. The other mechanism would be the asymmetry

of the mounting legs causing the middle beam-like part of the housing structure to be slightly curved after mounting rather than strictly linear along *x* axis. Both described mechanisms would cause uneven stress on the strained region of the sample in *x* direction. The fibre would then be slowly moving to the position that would help relaxing the uneven stress, which would be seen as a slow decrease in Bragg peak. Over the timescale of 1 min, such behaviour would be possibly slowly reaching equilibrium for each stress value. Hence, after stabilising for a stress level resulting from each strain increment, further strain (and stress) increment would result in a further Bragg peak fall over 1 min, whereas strain decrement, in a Bragg peak rise over 1 min.

In general, Bragg wavelength shift on 1 min was very small and had a marginal influence on the value of stain sensitivity. The difference between this calculated based on the measurements made after 1 min and just after strain change was 0.02 pm/με at most (compared to differences of up to 0.06 pm/με on increasing and decreasing strain). Very rarely, Bragg peak shift on time was accompanied by a change in the displacement value given by the indicators. However, the value on increasing strain was always positive while the peak fall on time was negative, while they would be expected to be of the same sign if the peak change over 1 min had been related to the change of the sample length. Moreover, the resolution of the indicators was 1 μm, translating to 32.6 με in the experimental arrangement, which gives a resolution of the Bragg peak shift of ~33 pm at the calculated stain sensitivity of ~1 pm/με. Hence, the observed magnitude of the Bragg peak shift over 1 min was always inferior to the resolution of the strain was always inferior to resolution of the indicators and does not allow systematic verification of whether the peak fall was accompanied by a change in strain.

As it was mentioned earlier, on decreasing strain, the force coming from the stress in the sample was observed to vanish before the strain reverted to zero. This was ascribed to the hysteresis of the plastic of which the housing structure was made since silica FBGs themselves are expected to display no strain hysteresis. Hysteresis of Bragg wavelength was visible for all the samples in all the trials. However, its value was varying from experiment to experiment, without any observable differences between coated and bare or point and scanned FBGs. The average hysteresis value was 229 pm, while the minimal and maximal amounted to 178 and 340 pm, respectively. As to the hysteresis of sample length given by the indicators, the values were even less consistent due to much lower resolution of the indicators. Moreover, after reaching the point on strain decrease where the sample was showing no more internal stress, the length of the sample was not anymore controlled by the micrometric screw of the translation stage – the sample was not under compressive strain. Instead, it was under compressive stress coming from the spring of the translation stage. Furthermore, only a step (of ~10 μm) at which the sample stopped showing internal stress was noted, not allowing precise measurement of the sample length. For all these reasons, the error related to the measurements of the hysteresis is expected to be large. The strain test set-up, however, was not designed to assess the hysteresis of the sensing patches. Its more

accurate analysis would probably require the straining trials to be performed on an axial stress-strain testing apparatus, which continuously monitors stress during the experiment.

Due to the limitations mentioned above, only qualitative description of the sample behaviour after reaching the point of zero internal stress on strain decrease can be provided (Figure 6-16). This point lied at a Bragg shift between ~0.75 and ~0.55 nm in the described trial of sample BS as can be inferred from the inset in Figure 6-16. This is because a strain decrease causing a Bragg peak shift to fall to ~0.75 nm resulted in an abrupt change in Bragg wavelength, which can be seen at a time *t* of ~33.5 min in the inset. Similar behaviour was observed for all points of higher strain (compare also Figure 6-13). In contrast, the following strain decrement (*t* = ~35.0 min) yielded an abrupt change first but then a gradual relaxation of the Bragg wavelength, which stabilised at ~0.50 nm. This could be attributed to relaxing the strain offset coming from the hysteretic behaviour of the plastic, which was additionally aided by the spring of the translation stage as it was discussed earlier. Further decrement of the strain value set at the micrometric screw of the translation stage (*t* = ~36.5 nm) only resulted in minor peak shift. From then on, the sample could be considered to be under a much smaller value of external compressive stress coming from the spring rather than under a high stress value coming from tensile strain. In these conditions, the Bragg peak of the sample was observed to further decrease quasi-exponentially (see the main graph in Figure 6-16), which could be ascribed to further recovery of the strain from the hysteresis. At *t* = ~11 h, the relaxation of the peak shift was probably dominated by the fluctuation of room temperature. This is because the pattern of the wavelength shift aligned well with the expected temperature changes during day and night. The amplitude of peak oscillations after *t* = ~11 h was slightly below 0.1 nm. This corresponds to a temperature change of ~1 °C, which is due to ~10 times higher temperature sensitivity of the embedded FBG compared to non-embedded. The observed sample behaviour seems to confirm that the hysteresis of the plastic of the housing structure was real, despite the problems with quantifying it.

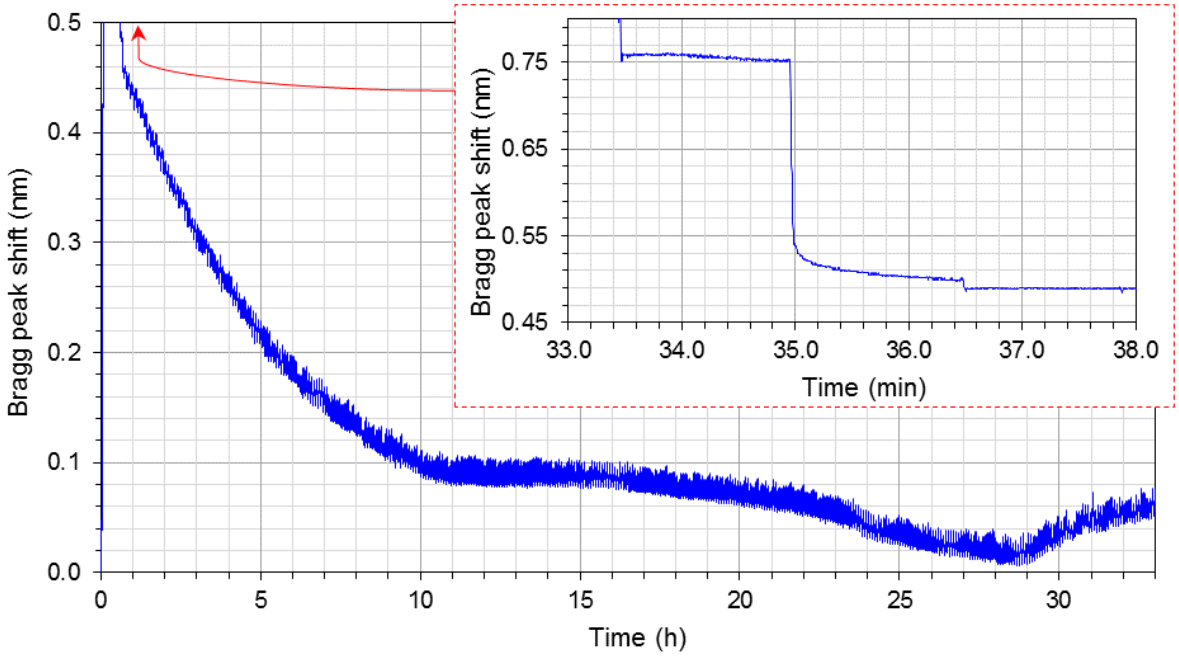

Figure 6-16. Close view of the Bragg peak shift after finishing a straining trail of the sample BS with 1.5-min strain steps. The inset shows a few last steps of the trial.

Compressive strain, steps of 1.5 min

Following the strain tests in tension, the straining set-up was rebuilt to allow trials in compression to test the three following samples: BS, BP, and CP. The methodology of the trails was largely the same as for the tensile strain, hence it is only discussed where it was different. As for the results in tension, the graphs for all the samples in compression were very similar so they are shown only for one sample (CP, for consistency with the graphs for tensile strain). The differences among various samples, if any, are discussed in text.

Bragg peak shift during the compressive strain experiment is shown in Figure 6-17 and the Bragg peak shift as a function of strain, in Figure 6-18. As for the tensile strain trials, no change to peak spectra on was noted. The values of strain sensitivity in tension and compression were very similar, the one in compression being slightly smaller for the presented test (0.795 vs. 0.82 pm/με). However, another trial of this sample in compression showed the same result as in tension (0.795 pm/με). Moreover, very close values of sensitivity to tensile and compressive strain were achieved for the other samples. As with tensile strain, the sensitivity values were higher for the bare FBGs than for the coated. Hence, strain sensitivity in tension and compression can considered equal, which is the expected behaviour.

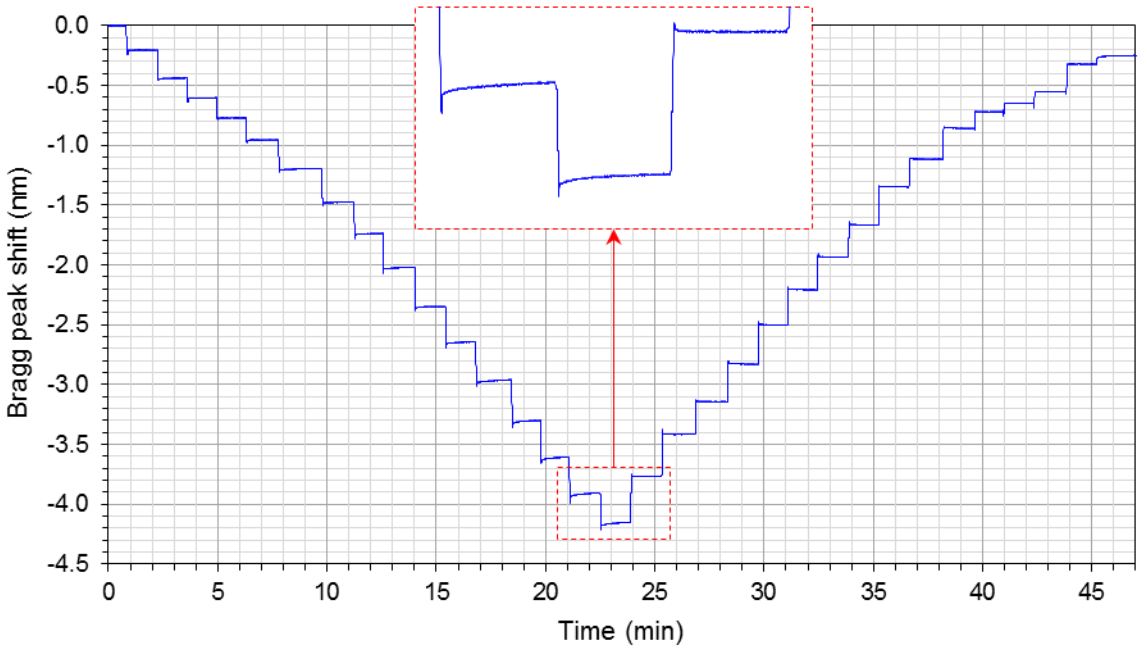

Figure 6-17. Bragg peak shift in time during the discussed compressive strain test of the sample CP with 1.5-min strain steps. The inset shows the close view of the graph at the maximal strain value.

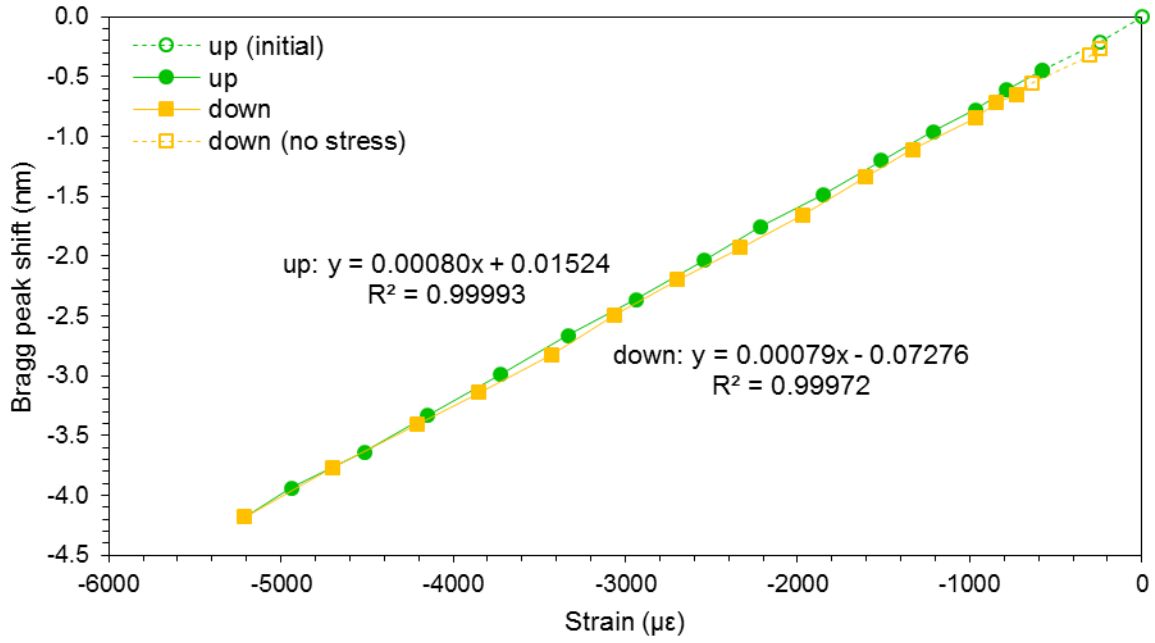

Figure 6-18. Bragg peak shift (right after strain change) as a function of strain during the discussed compressive strain test of the sample CP with 1.5-min strain steps.

Bragg peak shift over 1 min after each strain increment is presented in Figure 6-19. As with the tests in tension, it can be observed that the peak shift over 1 min was reverse to the strain change direction,

i.e., the peak shifted up after a negative strain change and down after a positive change. However, the shift over 1 min was visibly higher compared to the equivalent graph in tension (Figure 6-15). A much sharper peak change in time can also be noted comparing Figure 6-17 and Figure 6-13, particularly their insets. This is believed to be due to the same mechanism as introduced in the discussion on the tensile strain results, i.e., bending of the middle beam-like part of the structure. However, in the case of tensile strain, the bent radius was increasing (the beam profile was ever closer to a line), while it was decreasing during the compressive strain trails (the beam was ever more curved). As the middle beam-like part of the structure was only slightly bent, bend increase could have much higher effect than bend decrease. However, the magnitude of the peak shift over 1 min varied from experiment to experiment for both tensile and compressive trials, even for the same sample, so it is difficult to draw quantitative conclusions from the amplitude of the changes. It could perhaps depend on the way the sample was mounted for each experiment as the changes in mounting could possibly result in higher or lower degree of bend to the middle beam-like part. Finally, as for the tensile strain tests, calculating strain sensitivity from the Bragg peak shift after 1 min was only yielding marginal differences if any (no difference observed for the discussed trail of the sample CP).

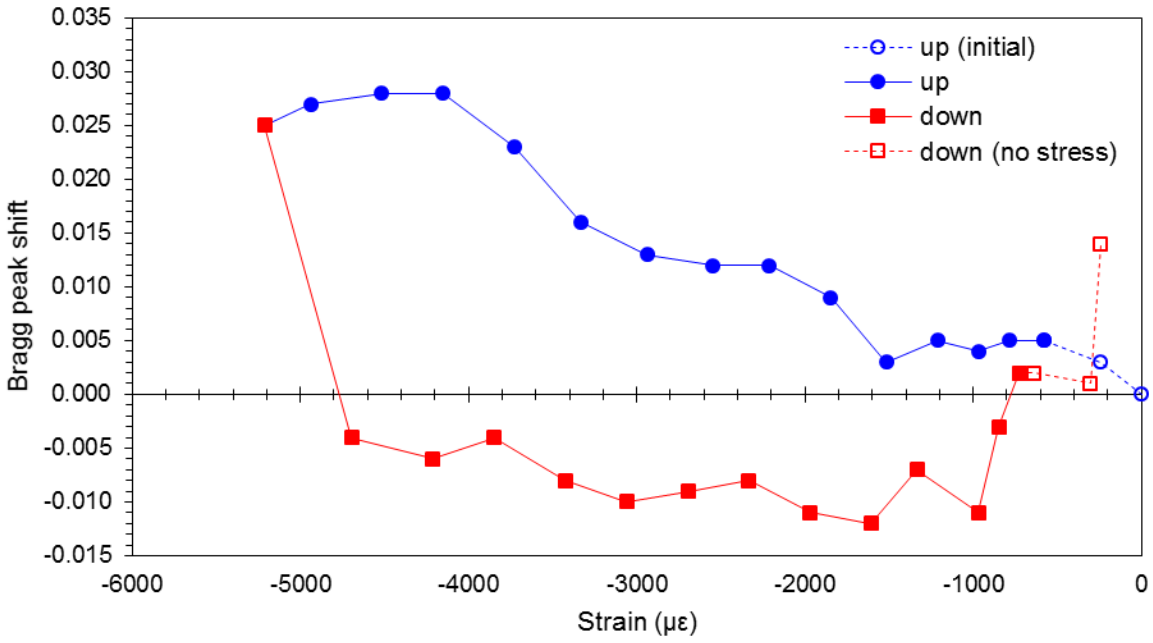

Figure 6-19. Bragg peak shift over 1 min after each (negative) strain increment (up) or decrement (down) during the discussed compressive strain test of the sample CP with 1.5-min strain steps.

Regarding the Bragg peak hysteresis, it was negative and larger in magnitude for the trials in compression than in tension. The average hysteresis value for compressive strain was -399 nm (vs. 0.229 nm for tensile), with the minimal and maximal values yielding, respectively, -0.265 and -0.466 nm (vs. 0.178 and 0.340 nm for tensile). The higher value of the hysteresis could also originate from higher

potential of shape change of the middle beam-like part of the structure on compressive strain than on tensile, as it was discussed with Bragg peak shift over 1 min.

Tensile strain, steps of 20 min

In order to further analyse the hysteresis of the housing structure in more detail, the procedure of one of tensile strain trials was modified. The strain increments were increased (1,000 με), and the strain was kept constant for 20 min after each change instead of 1.5 min.

Bragg peak shift during the experiment has been plotted in Figure 6-20. It can be noted that the peak shifts after each stain change is much more pronounced than during the experiments with a strain step duration of 1.5 min. Hence, the graph showing the Bragg peak shift as a function of strain (Figure 6-21) contains clear discontinuities coming from Bragg wavelength changing while the strain in kept constant. The long delay between consecutive straining steps can be observed in Figure 6-22 to have a clear influence on the calculated strain sensitivity values. On increasing strain, the sensitivity is very close to this calculated previously for the bare FBGs in the trails with a strain step of 1.5 min (1.025-1.045 pm/με). However, the clamps were not twisted and offset with respect to each other in order to accommodate the sample asymmetries discussed earlier because the importance of that was only recognised after this experiment had been performed. In these conditions, larger strain sensitivity values were normally measured on strain increase (1.05-1.14 pm/με), and it is then probable that the strain sensitivity value on strain increase was actually below the average. Moreover, the Bragg peak shift on increasing strain does not overlap with this on decreasing. The latter was much higher (1.18 pm/με), even higher than for the reference sample (1.125 pm/με). This discrepancy can be attributed to the hysteretic behaviour the sample plastic, which is more pronounced in the trial of a strain change step of 20 min. The average strain sensitivity though, amounting to 1.095 pm/με, is close the averages measured during other strain trials of the bare samples. Finally, the sample was relaxing for 12.5 h (under the delicate compressive stress from the translation stage spring). It can be noted in Figure 6-21 and Figure 6-22 that both the Bragg peak and strain values decreased, probably corresponding to the sample recovering the strain from the hysteresis.

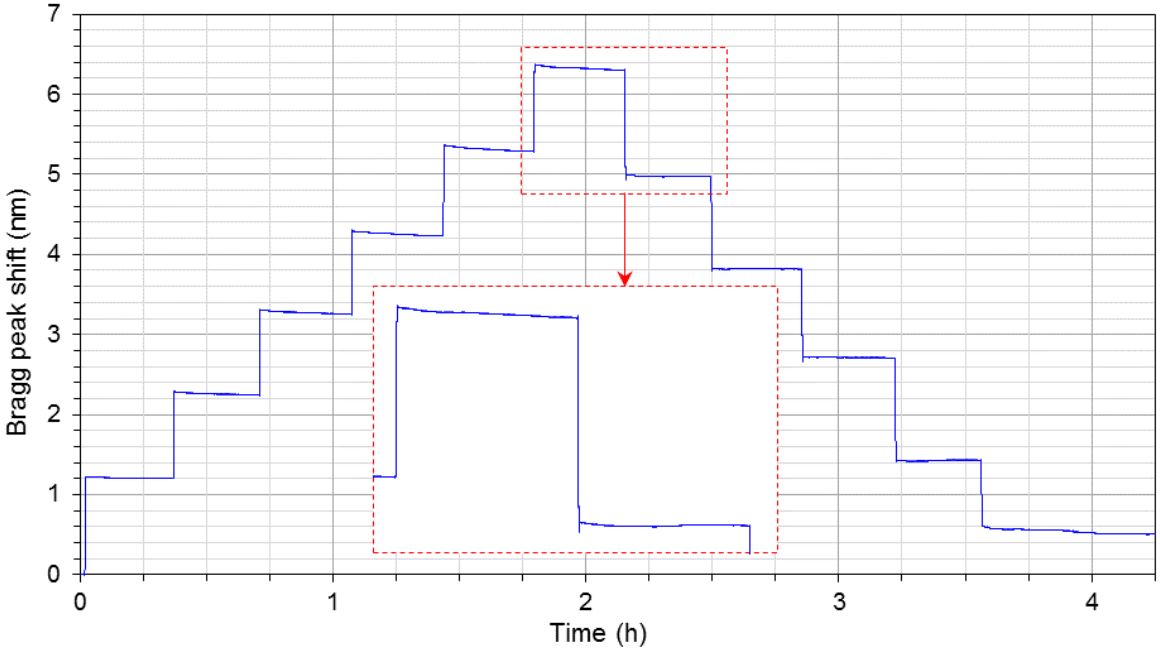

Figure 6-20. Bragg peak shift in time during the discussed tensile strain test of the sample BS with 20-min strain steps. The inset shows the close view of the graph at the maximal strain value.

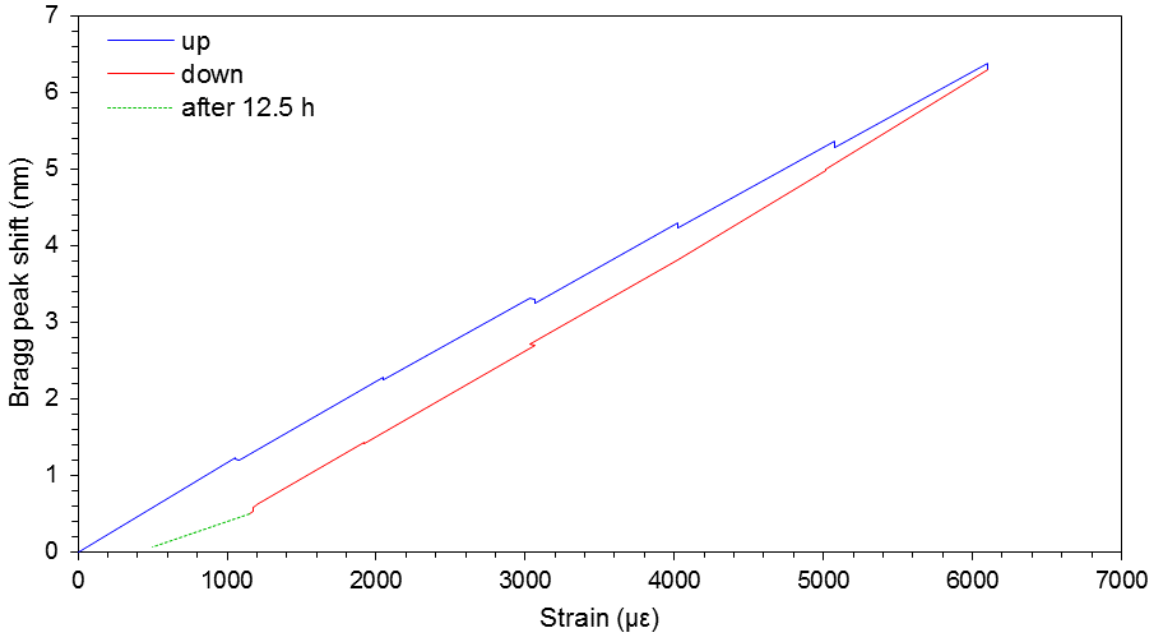

Figure 6-21. Bragg peak shift (right after strain change, 1 min and 20 min after strain changes) as a function of strain during the discussed tensile strain test of the sample BS with 20-min strain steps.

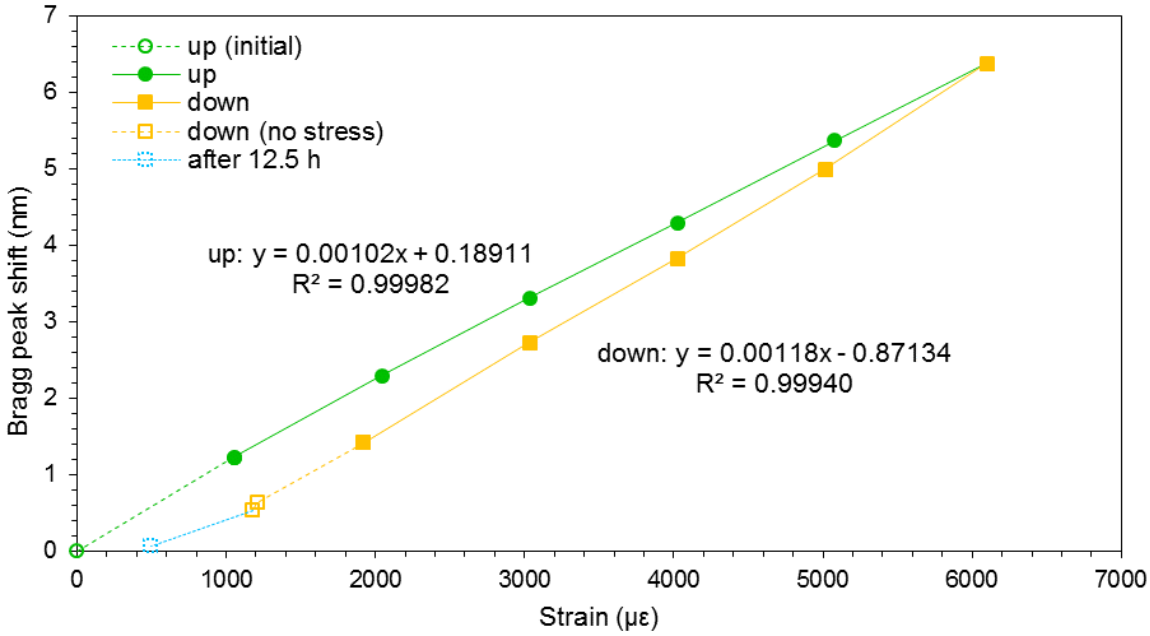

Figure 6-22. Bragg peak shift (right after strain change) as a function of strain during the discussed tensile strain test of the sample BS with 20-min strain steps.

The much higher Bragg peak shift on time (down to -83 pm on strain increase and up to 15 pm on decrease) is also visible in Figure 6-23 when contrasted with the tests of 1.5-min strain change steps (compare Figure 6-15). In the mechanism described earlier, a longer time between the strain steps allowed higher magnitude of bend. This is well visible on increasing strain, where the peak shift over 20 min seems roughly proportional to this over 1 min. However, on decreasing strain, such relationship does not hold anymore, and the behaviour of the sample seems more complex. This can be observed in the inset in Figure 6-20, where the peak in the first strain decrement is first observed to fall and then to rise.

Finally, the value of strain hysteresis was also bigger compared to the tensile straining tests of a strain change step of 1.5 min, amounting to 0.534 nm (vs. 0.340 nm at maximum, 0.218 on average). This difference can also be attributed to a longer total straining time and a higher maximal strain value.

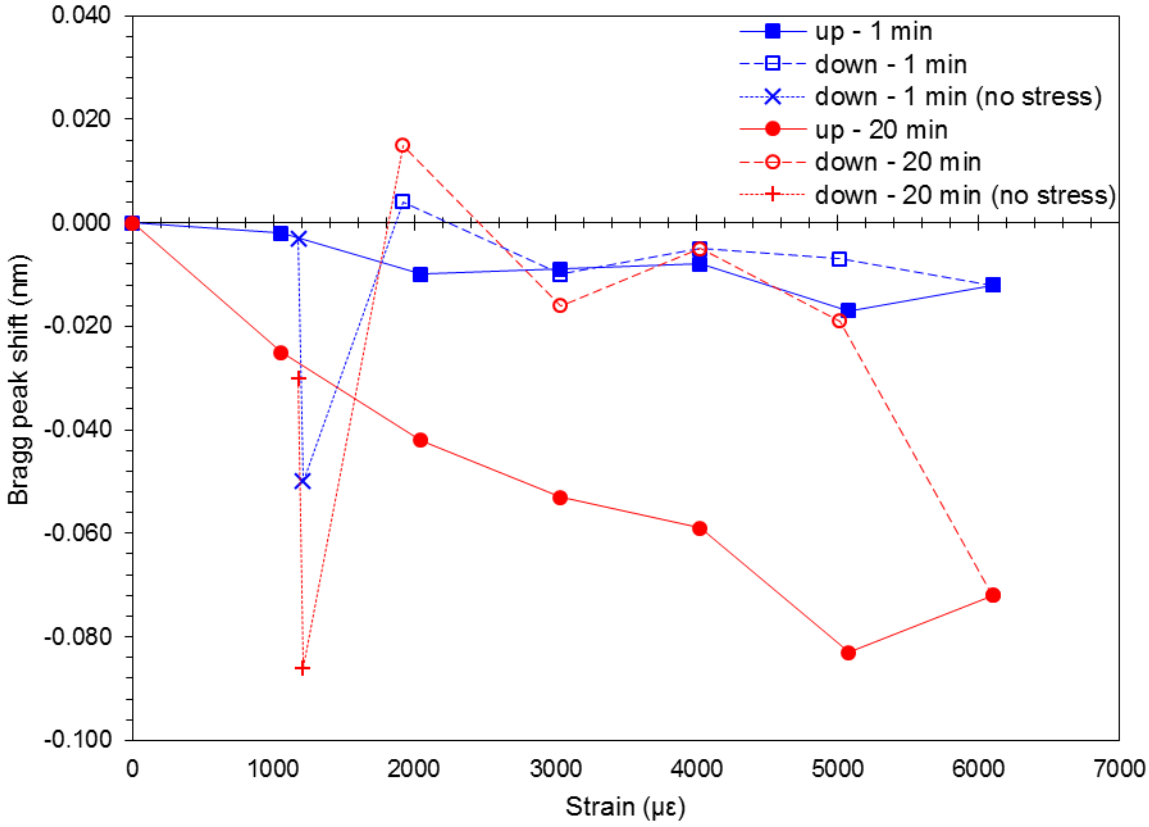

Figure 6-23. Bragg peak shift over 1 and 20 min after each strain increment (up) or decrement (down) during the discussed tensile strain test of the sample BS with 20-min strain steps.

6.2.4 Temperature and humidity response of the sensing patches

This section presents the results of the experiments designed to test the response of the sensing patches to changes of temperature and relative humidity. Out of the samples manufactured according to the upgraded design (see Section 6.2.2), the trials were performed on two, which differed with both characteristic parameters: the coated scanned (CS) and bare point (BP) samples. The former was used in the initial experiments, during which the experimental set-up and routines were optimised. As a result, 11 temperature and humidity trials were performed on the sample CS. After the optimal testing conditions were identified, a single, long test was conducted for the sample BP, allowing to fully test its properties. Moreover, a similar temperature trail was performed on the reference unembedded silica FBG inscribed in the same fibre (see Section 6.2.1 and Figure 6-10). **Error! Reference source not found.** shows the overview of all the temperature and humidity experiments discussed in this section.

Table 6-5 summarises the experiments performed on the sample CS. Rather than describing all of them in detail, this section highlights their most significant parts from the viewpoint of understanding sample behaviour. Special attention is paid to the characteristics that are crucial in sensing applications,

including physical processes occurring in the sensing patch, its sensitivity to measurands, repeatability of sensor response, and its long-term behaviour.

The following part of this section discusses the details of the optimisation of the experimental set-up and procedures, highlighting the rationale of every upgrade. Then, observations concerning the sample CS are presented. They include, first, changes to the reflection spectrum over the experiments 1–5 and their consequences. Secondly, shifts of the peak position of the sample CS in time are discussed, which are ascribed to the embedded fibre sliding against its primary coating. Irregular humidity response of the sample CS is also presented. In the further part of this section, the temperature and humidity experiment for the sample BP is described. Finally, the performance of both samples is contrasted and compared with the results of a similar temperature trail conducted for the reference unembedded silica FBG.

Table 6-4. Overview of the temperature and humidity experiments conducted on the sensing patches fabricated according to the upgraded design.

Sample	Number of experiments	Total duration of experiments
Coated scanned (CS)	11	1813 h ≈ 75.5 days
Bare point (BP)	1	1557 h ≈ 65 days
Reference SOFBG	2	18 h
Total for both samples	12	3388 h ≈ 141 days

Table 6-5. Summary of the temperature and humidity experiments performed on the sample CS.

Experiment	Duration (h)	Dry conditions	Low temperature	Description
1	8	non-stabilised[a]	non-stabilised[c]	dry: low T, high T[e], low T
2	17			dry: low T, high T[e], low T (hold)
3	–			(cancelled)
4	31			dry: low T, high T[e], low T (hold)
5	61			dry: 5 identical cycles of low T and high T[e] | low T (hold)
6	64			wet[f]: low T, high T[e], low T; dry: low T (hold)
7	124			dry: low T, high T[e], low T, high T[e] (hold)
8	472			dry: high T[e]; wet[f]: high T[c]; dry: high T[e]
9	404	stabilised[b]		dry: 5 different periods of low T and high T[e]
10	158			dry: high T[e] (hold)
11	47		stabilised[d]	dry: low T (hold)
12	427			dry: low T, high T[e]; wet[f]: high T[e], low T

[a]dry conditions non-stabilised: low-humidity periods of the experiments performed without humidity stabilisation, i.e., in ambient humidity

[b]dry conditions stabilised: low-humidity periods of the experiments relied on enclosing the sample in a sealed container with silica gel, which was aimed to ensure a stable level of low relative humidity (<10 %RH)

[c]low temperature non-stabilised: low-temperature periods of the experiments performed in room temperature without stabilisation, often reflecting cyclic temperature fluctuations of a few °C in the laboratory between day and night

[d]low temperature stabilised: during low-temperature periods of the experiments, temperature was stabilised to 1 °C by air conditioning (at 21–23 °C)

[e]high temperature stabilised at ~50 °C

[f]wet conditions (highlighted in blue): the sample fully immersed in water, yielding a stable relative humidity of 100 %RH

Evolution of the testing set-up and procedures

Similarly to the strain trails, the sensing patches were interrogated with the HBM DI110 according to the schematic shown in Figure 6-1(a). The peak position was measured four times per second, and the reflection spectrum of the FBG embedded in the sensing patches, approximately once per minute.

All the experiments were performed in a programmable oven (Thermo Scientific Heratherm OGH 100-S). During the trials, the samples were exposed to temperatures ranging from room temperature to ~50 °C. The maximal temperature value varied, and hence, it is often referred to as the high temperature rather than giving its exact figure. On the one hand, this temperature range of almost 30 °C was large enough to reliably assess temperature response of the sensing patches. On the other hand, the maximum temperature was still low enough to expect not to damage the samples. The experiments consisted of periods of stable low and high temperature (respectively, room temperature and ~50 °C). They were separated with periods of temperature change (rise or fall) of varying length (1–10 h).

The oven did not offer high enough accuracy of temperature setting to reliably test the temperature characteristics of the sensing patches in view of their expected high sensitivity (see Section 6.1.5). First, its temperature setting relied on a thermocouple, which was positioned in the top part of the oven chamber, i.e, away from the sample under test. As temperature gradient along the height of the oven chamber was expected, it would be difficult to infer the actual temperature at the level of the sample under test. Secondly, when heating of the oven was turned off, the sample was still under the influence of ambient temperature fluctuations, which would not be impossible to track. To overcome these limitations, the temperature was logged every 10 seconds by a thermologger EasyLog EL-WiFi-DTP+. It features two external (cabled) thermistor probes of a measurement accuracy of 0.2 °C (in the temperature range used in the experiments) and a measurement resolution of 0.01 °C. The former was expected to offer higher accuracy than the thermocouple of the oven. Moreover, the probes could be inserted by the side opening of the oven and positioned exactly next to the sample under test, minimising the influence of temperature gradient in the oven chamber.

Precise temperature logging allowed assessing accuracy and fluctuations of temperature in the oven chamber. It was found that high temperature periods of the experiments were stable to a fraction of a degree Celsius, which was enough for the needs of the experiments. However, low temperature periods of the initial experiments featured temperature fluctuations of about 5 °C (from ~18 to ~23 °C), reflecting the changes of ambient conditions in the laboratory between day and night. To ensure more stable low temperature values, the experimental set-up was moved after the experiment 10 to an air-conditioned space (see Table 6-5, the column *Low temperature*). This permitted stabilising low temperature to 1 °C (at 21-23 °C, depending on the experiment).

In the course of the experiments, a significant influence of relative humidity on the sensing patches was observed (which is described in detail in the following part of this section). The simplest approach to assess this impact was a two-point measurement at the furthest possible parts of the relative humidity

spectrum. That called for stabilising the level of relative humidity at the sample under test and logging its values because relative humidity decreases with increasing ambient temperature (according, e.g., to the psychrometric charts or the Arden-Buck equation [372]). High relative humidity could be easily realised by completely immersing the sample under test in water along with a thermistor probe. Such procedure yielded a stable relative humidity value of 100 %RH irrespective of ambient temperature. In turns, relative humidity stabilisation at low values required a more complex approach. This was achieved by enclosing the sample under test in a sealed container with silica gel, which was aimed to absorb humidity. In this case, relative humidity was temperature-dependent and, thus, had to be tracked. To achieve this, a humidity logger EasyLog EL-WiFi-TH+ was sealed in the container along with the sample under test, silica gel, and one of the thermistor probes. Humidity stabilisation during the dry periods of the experiments (i.e., those of low relative humidity) started from the experiment 9 (see Table 6-5, the column *Dry conditions*). The humidity logger features a build-in temperature and relative humidity sensor. The data from the former was not used as the cabled thermistor probes of the thermologger, first, had a smaller thermal capacity, resulting in little thermal delay between temperature changing and this change being measured by the probe. Secondly, the cabled thermistor probes could be placed at a very short distance from the sample to ensure temperature was measured as close to the sample under test as possible. Hence, using the data from the thermologger minimised the experimental errors. In the temperature range used during the experiments, the humidity logger offered an accuracy of relative humidity measurement of ±1.8 %RH at 10-90 %RH and of ±2.0 %RH at <10 %RH and >90 %RH. Relative humidity was usually <10 %RH during the low humidity periods.

Spectral change of the FBG response of the sample CS during the experiments 1–5

Before embedding, all the FBGs to be embedded showed regular single-peak reflection spectrum with minor side lobes (Figure 6-24(a)). After embedding and during the experiments 1–5, the reflection spectrum of the FBG embedded in the sample CS was observed to change gradually as shown in Figure 6-24. The spectra (b)–(f) in the graph are shifted in wavelength and scaled in intensity to overlap at the position of the original normalised spectral peak of (a). This allows observing the evolution of the original spectral response of the grating.

It was found that the spectrum of the grating did not change due to embedding. It can also be noted from Figure 6-24 that the reflection spectrum deviated from the initial form even before starting the first temperature experiment. This spectral change was found to had appeared between the straining experiments 6 and 7, when the sample was left mounted (unstrained) on the straining set-up for approximately two months. However, the deviated spectrum was found stable during the subsequent straining trial (the experiment 7, see Figure 6-12). In turns, as was mentioned before, the spectrum deviated further from its original shape with every temperature experiment during the experiments 1–5. Supposedly, such behaviour was caused by local chirping (positive or negative) of the 6-mm-long

scanned FBG in the sample CS. The chirping might have been due to local uneven straining of the grating, coming from the temperature and strain acting on the interfaces between the fibre, its primary coating, the glue, and the 3D printout. This is discussed in more detail in the following part of this section.

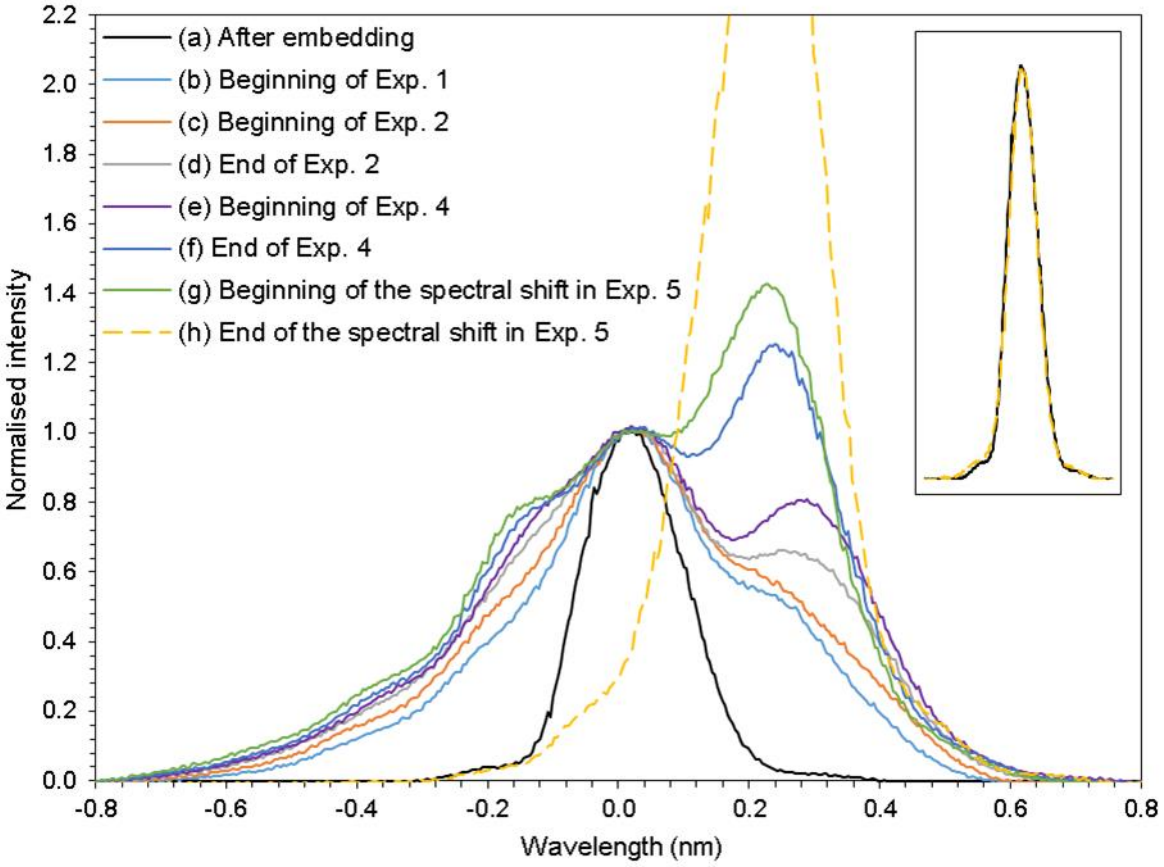

Figure 6-24. Evolution of the reflection spectrum of the sample CS in the experiments 1–5 measured with the HBM DI110 interrogator. The spectrum (a) has been normalised and its peak has been placed at 0 nm. The spectra (b)–(g) have been shifted in wavelength and normalised to overlap at the position of the original spectral peak of (a), which allows observing the evolution of the reflection spectrum and the appearance of the side peak. The maximum of the spectrum (h) overlaps with the corresponding spectral peak of (g), which transformed into the peak in (h). Both (g) and (h) share the same scaling (normalisation) factor to reflect the extent of the intensity change of the reflection peak. The spectrum (h) is above the scale due to abrupt increase of the peak intensity. The inset shows the full normalised spectral shape of the embedded grating measured with the HBM interrogator after the experiment 5 compared with the spectrum (a).

Two distinct shifts in the peak position in time were noted during the experiment 2 on temperature decrease, the first of which was observed at the experimental time $t \approx 8{:}05$ and had a positive magnitude of ~30 pm (Figure 6-25(a)). It was unexpected from the viewpoint of the usual linear response of the sensing patches to temperature change, which is discussed later in more detail. The first peak shift in time (Figure 6-25(a)) was related to the aforementioned evolution of the reflection spectrum (Figure 6-24) and appearance of the side peak. The logged spectral graphs allowed discerning that the wavelength of the original peak was constantly decreasing over the time of the detected peak increase (Figure 6-25(b)). It was supposedly due to the peak tracing algorithm used by the inner circuitry of the HBM interrogator. The algorithm searches for peak position in the spectral ranges above a chosen noise threshold. The peak tracking relies on differentiating the reflection spectrum with respect to wavelength and tracing the position of zero crossings. They correspond to the wavelength where the slope of the peak changes from rising to falling, which marks the top of the peak. The first peak shift in time in the experiment 2 (Figure 6-25(a)) overlaps with the appearance of the side reflection peak, as can be seen in Figure 6-25(b)). The extent of the spectral change is even clearer when comparing the spectra at the beginning and end of the experiment 2 (Figure 6-24(b) and (c), respectively). The appearance of the side peak resulted in formation of two more zero crossings in the differential of the spectrum, both falling above the noise threshold set during the experiment. It was not disclosed by the manufacturer of the interrogator how exactly the algorithm behaves in such a situation. A complex peak tracking approach in such a case can be suspected based on the spectral graph displayed in the software during peak tracing. Then, the detected peak position is marked on the graph with a bar, which – it the case of a bifurcated peak – does not overlap with neither of its differential zero crossings though. Hence, it can be noted that the observed step change in peak position is related – due to the algorithm used – to gradual deviation of the reflection spectrum from its initial shape.

Another change of the reflection spectrum occurred during the experiment 5 (Figure 6-26). It consisted of five cycles of rising and falling temperature, aiming to assess the repeatability of the sensor response. During the rising slope of the temperature cycle 3 (at $t \approx 16{:}05$), a dramatic change of the reflection spectrum occurred (compare Figure 6-24(g) and (h)). The extent of the change was so large that the peak of the spectrum afterwards exceeded the scale of the recorded spectrum. However, in the HBM interrogator, the peak is tracked by its inner circuitry and not tracked based on the recorded spectrum. Thanks to this, the peak was tracked correctly until the end of the experiment. Afterwards, detector sensitivity of the interrogator was readjusted to reveal that the grating regained its original shape (see the comparison of the spectral shape after embedding and after the experiment 5 in the inset in Figure 6-24). This spectral change resulted in the wavelength of the tracked peak falling by ~300 pm, compared to the rise by ~30 pm during the spectral change discussed previously. The recovered FBG shape was preserved during all the following experiments on the sample CS (the experiments 6–12). The evolution of the spectral shape of the sample CS is discussed later.

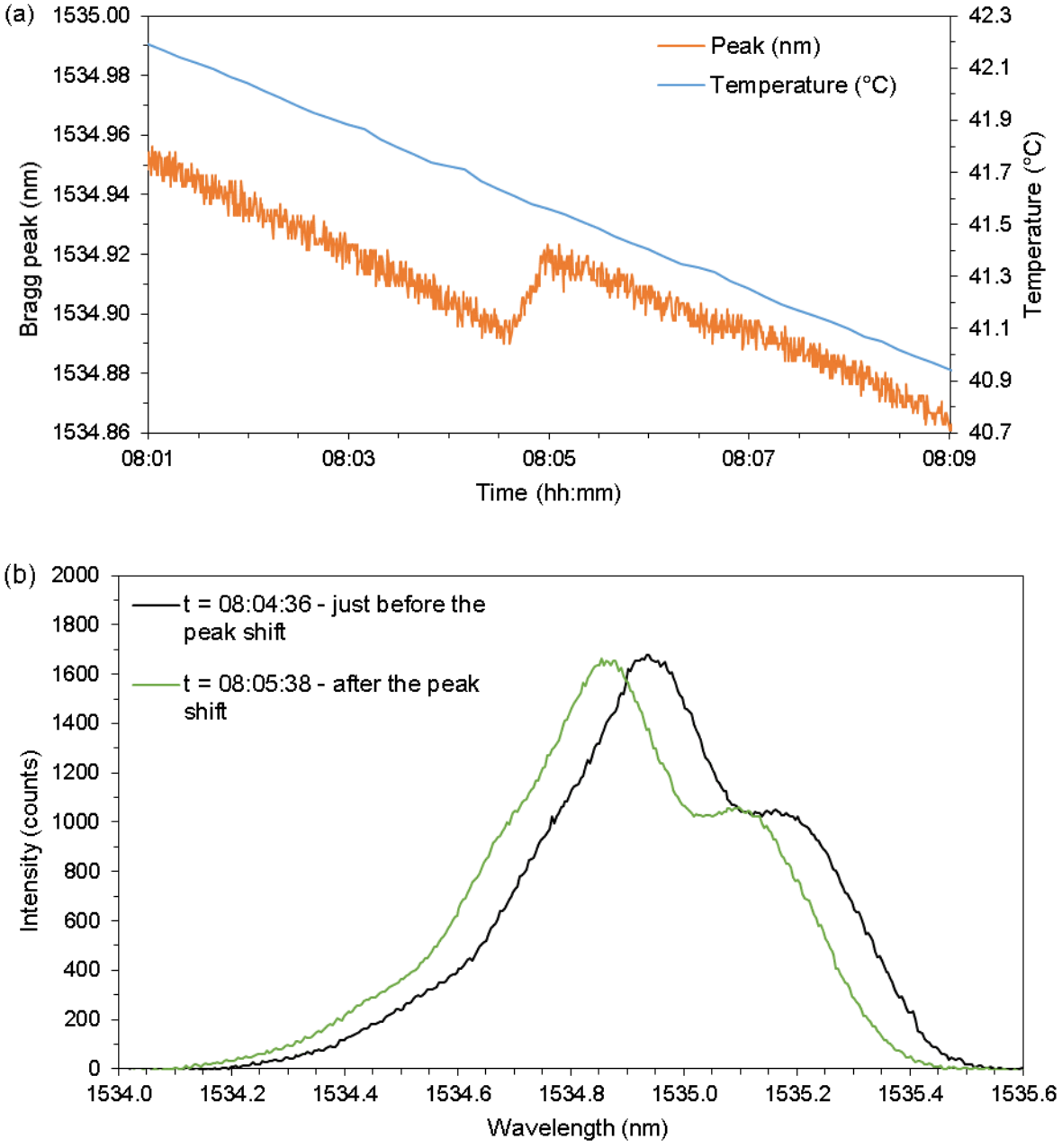

Figure 6-25. (a) 8-min-long time interval of the experiment 2 for the sample CS showing a distinct shift of the peak position in time at $t \approx 8{:}05$ (shift duration ≈ 25 s) along with (b) the corresponding reflection spectra.

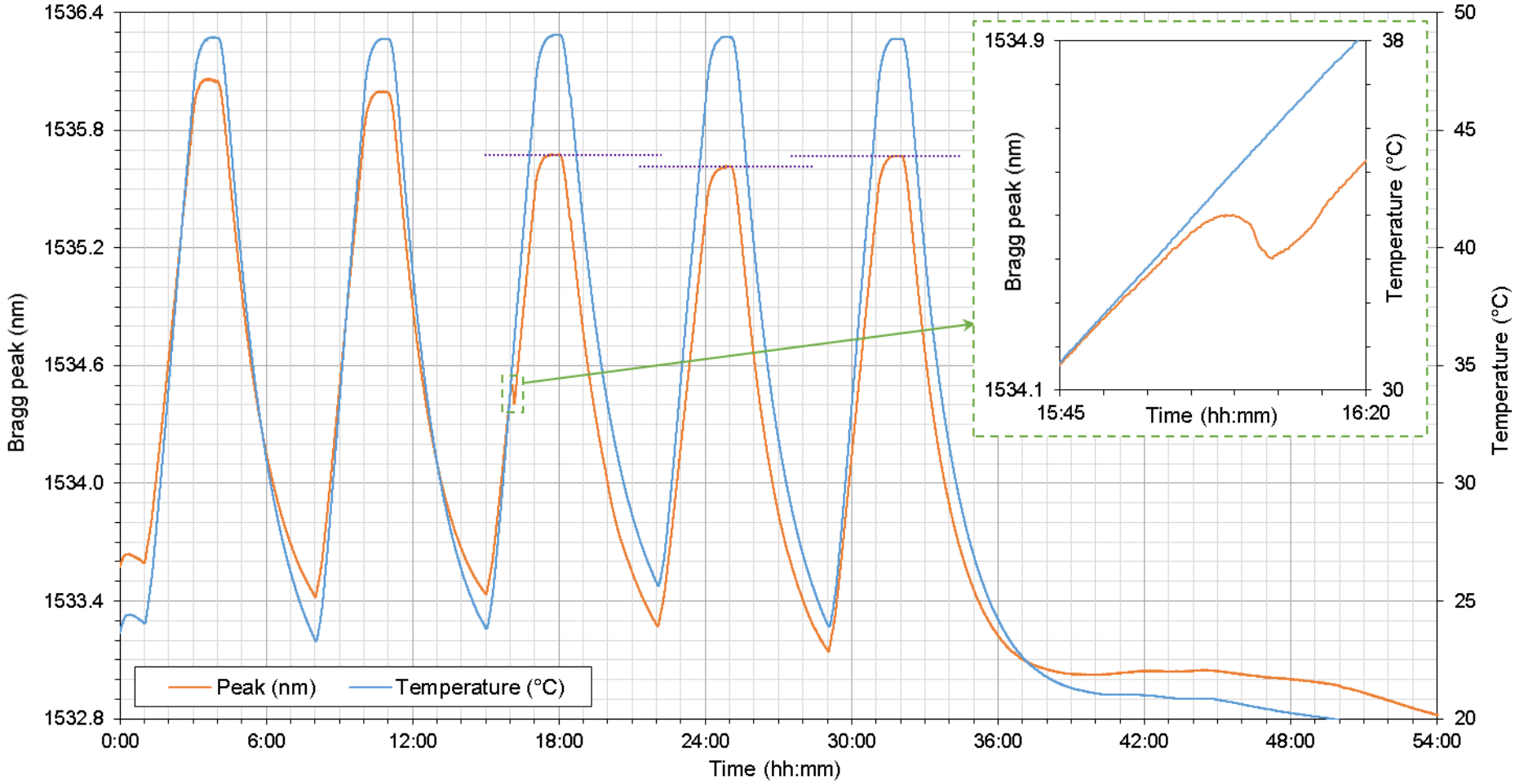

Figure 6-26. Bragg peak and the temperature as a function of time during the experiment 5 for the sample CS. The inset shows the close view of the peak shift at $t \approx$ 16:05. See text for discussion.

Peak shifts of the sample CS in time during the experiment 1–5

Deviation of the reflection spectrum of Sample CS observed during the experiments 1–5, discussed above, was one of the causes of peak shifts in time. Another was probable fibre slippage during the temperature experiments.

Error! Reference source not found.(a) shows the second peak shift in time observed during the experiment 2 (at $t \approx 10{:}26$). Then, the main peak of the reflection spectrum was found to actually redshift (**Error! Reference source not found.**(b)) as opposed to the first peak shift in time during the experiment 2 discussed above (see Figure 6-25).

This effect became even more pronounced after the FBG had regained its original shape in the experiment 5. This can be observed in Figure 6-26 judging from the maximal peak values in time in each temperature cycle. They were not equal, despite the temperature being nearly identical (~49 °C) at the high temperature period of each cycle. The fall of the maximal peak value in time from the cycle 1 to 2 could perhaps be explained by housing structure shrinkage due to its drying as the high temperature periods were also characterised with low humidity. This phenomenon is further discussed in more detail. However, the maximal peak value increased from the cycle 4 to 5, while – if it had been due to drying – the opposite behaviour would have been expected (compare the violet dotted lines in Figure 6-26).

Both the second peak shift in time in the experiment 2 and the differences in the maximal peak position in time at the high temperature in the experiment 5 are believed to be the signs of fibre sliding against its primary coating. Supposedly, this originated form the fibre relaxing the compressive stain under which it was put during embedding. As was mentioned in Section 6.2.2, the housing structures shrank after detaching from the printing bed compared to the size at which they were printed. This was due to thermal contraction of the housing on cooling down as the patches were printed at high temperature. The FBGs, embedded at high temperature, shrank along with their housing structures. For the sample CS, the peak value decreased to 1531.57 nm after embedding from 1536.00 nm after gluing in the structure of the sensing patch and before resuming 3D printing. This fall of -4.25 nm corresponds to the contraction of the housing structure by ~3770 με (assuming a strain sensitivity of 1.127 pm/με for the sample CS, see Section 6.2.2). Thus, the embedded fibres were at relatively high compressive stress, which they were prone to relax by sliding against their primary coatings, if they were present, or alternatively, the housing structure.

The high stress at which the fibre was put during embedding was first observed to partly relax between the tensile strain experiments 6 and 7 for the sample CS. During the experiments, the fibre was left mounted (unstrained) on the strain test set-up for over two months. At the beginning of the strain experiment 7, the reflection spectrum was observed to had changed as it was mentioned above. Along with that, the Bragg wavelength redshifted by +1.55 nm, from 1530.61 nm to 1532.16 nm (at room temperature). Although no longitudinal strain was exerted on the sample, it was possible that the alignment imposed on the sample, leading to non-equilibrium position from the viewpoint of its internal

stress, resulted in deviation of the reflection spectrum and Bragg peak redshifting. The latter could also be related to fibre sliding against its primary coating. Alternatively, this could have been due to creep effects in the housing structure, i.e., slow deformation of sample geometry coming from long-term exposure to stress.

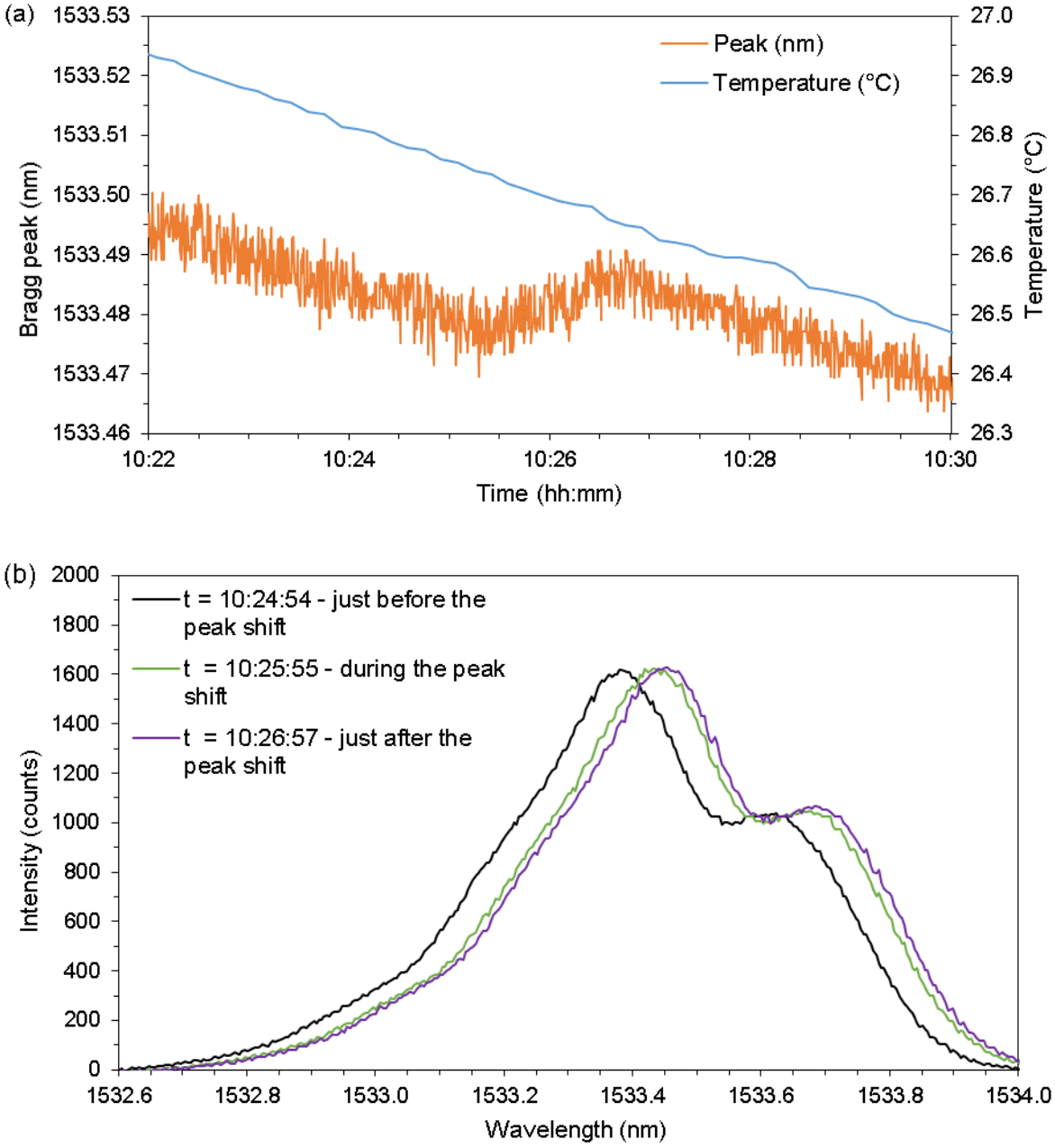

Figure 6-27. (a) 8-min-long time interval of the experiment 2 for the sample CS showing a distinct shift of peak position in time at $t \approx$ 10:26 (shift duration ≈ 1 min 18 s) along with (b) the corresponding reflection spectra.

Performance of the sample CS during the experiments 6–8

To further validate the hypothesis of fibre slippage, the peak value of the sample CS was noted for all the experiments at a constant temperature (**Error! Reference source not found.**). The latter was important to avoid temperature differences among observations interfering with the results due to high temperature sensitivity of the sensing patches. A temperature of 31.0 °C was chosen because it was achieved in all the experiments. Delta denotes the difference between the expected Bragg peak of an unembedded FBG and the sample CS. The former was calculated assuming only the influence of TOC and neglecting CTE (small anyway) for the purpose of comparison with the embedded FBG. This was because the grating embedded in the sample CS was not able to freely change its dimensions according to its material properties described by the CTE for silica (see Section 492.2.4 for details).

In **Error! Reference source not found.**, a slow but constant decrease of the peak during the experiments 1–5 can be noticed. This was despite the fact that these experiments involved relatively short temperature cycles of up to 6 h. The largest increase in Bragg wavelength was observed after the experiment 2, which involved the two peak shifts in time discussed above. The peak value measured in the experiment 6 did not follow the tendency of slow increase and was visibly higher. This was because the peak value was measured in the period when the sample was immersed in water, which caused it to expand due to humidity absorption. During the experiment 6, the sample was exposed to the high temperature in water for 6 h. This did not cause any change to the peak position at 31.0 °C, as measured at the beginning of the experiment 7. The latter experiment, in turns, involved keeping the sample at the high temperature in the dry conditions for ~98 h running. During that period, the peak was observed to slowly fall gradually due to sample drying, which is discussed later. However, similarly to the experiment 6, the Bragg wavelength at 31.0 °C increased only marginally, as evidenced by the measurement at the beginning of the experiment 8.

A dramatic change of the Bragg wavelength at a temperature of 31.0 °C occurred during the experiment 8 though. It involved exposing the sample to the high temperature in water. Hence, during the experiment 9, the wavelength of the sensing patch at 31.0 °C was noted only after over 224 h of drying to avoid the effect of swelling due to humidity absorption. Yet, the peak at 31.0 °C showed a considerable increase of 1.72 nm. The origin of that Bragg wavelength change is discussed below.

The time graph of the experiment 8 (**Error! Reference source not found.**) shows the temperature at the sample, the logged peak value, and the peak value corrected for the influence of temperature (peak T-corr.). Due to relatively high temperature sensitivity of the sensing patches, temperature variations in the oven, even when the temperature was stabilised to <1 °C had predominant influence on the peak value and hindered observation of concurrent phenomena like humidity absorption (or desorption) and fibre slippage. To analyse the behaviour of the peak devoid of temperature influence (i.e., of CTE of the housing structure and TOC of the fibre), the peak value corrected for temperature ($\lambda_{B,\,T\text{-}corr}$, nm) was calculated for every measurement point in time according to the following equation:

$$\lambda_{B,T-corr.} = \lambda_B - S_T\,\Delta T \tag{6-1}$$

where S_T (pm/°C) is the temperature sensitivity of the sensing patch, and $\Delta T = T - T_0$ (°C), T being the temperature at a given point in time and T_0, usually at the beginning of the experiment.

Table 6-6. Peak values at a temperature of 31.0 °C and the maximal attained peak values for the sample CS.

Experiment	Temperature = 31.0 °C			Maximal peak value		
	Peak (nm)	Delta[a] (nm)	Comment	Peak (nm)	Delta[a] (nm)	Comment
1	1533.81	-2.25	dry[b]	1535.63	-0.68	dry[b], high T[d]
2	1533.93	-2.13	dry[b]	1535.73	-0.58	dry[b], high T[d]
4	1534.32	-1.74	dry[b]	1536.10	-0.21	dry[b], high T[d]
5	1534.21	-1.85	dry[b] (increasing slope in the cycle 1)	1536.06	-0.25	dry[b], high T[d]
6	1534.69	-1.37	wet[c]	1536.90	0.59	wet[c], high T[d]
7	1534.26	-1.80	dry[b] (beginning of the experiment)	1536.13	-0.18	dry[b], high T[d]
8	1534.37	-1.69	dry[b] (beginning of the experiment)	1537.04	0.73	wet[c], high T[d]
9	1536.09	0.03	dry[b] (after drying for over 224 h)	1538.00	1.69	dry[b], high T[d]
10	1535.85	-0.21	dry[b]	1537.86	1.55	dry[b], high T[d]
11	1535.88	-0.18	dry[b]	1536.50	0.36	dry[b], 37 °C
12	1535.93	-0.13	dry[b] (beginning of the experiment)	1538.57	2.26	wet[c], high T[d]

[a]delta – the difference between the expected Bragg peak of an unembedded FBG (1536.31 nm at ~50 °C) and the sample CS; the former was calculated assuming only the influence of TOC and neglecting CTE, for the purpose of comparison with the embedded FBG; the grating embedded in the sample CS was not able to freely change its dimensions according to its material properties described by the CTE for silica (see Section 2.2.4 for details)

[b]measured in dry conditions, stabilised or non-stabilised (see for **Error! Reference source not found.** details)

[c]measured in wet conditions: the sample fully immersed in water, yielding a stable relative humidity of 100 %RH; humidity absorption caused the housing structure to swell, yielding an increase of the peak value

[d]high temperature stabilised at ~50 °C

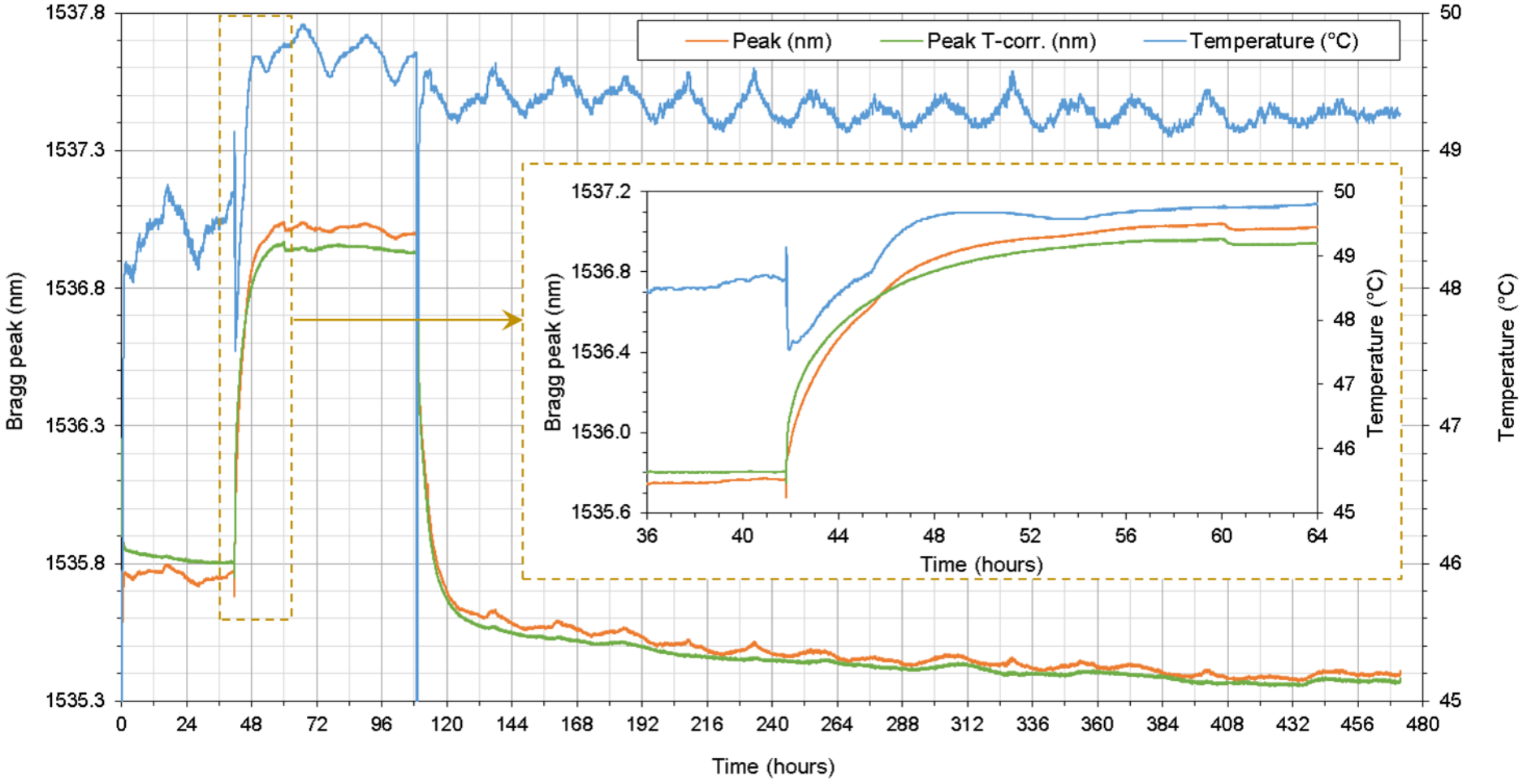

Figure 6-28. Bragg peak, the Bragg peak corrected for the temperature influence (Peak T-corr.) and the temperature as a function of time during the experiment 8 for the sample CS. The inset shows the close view of the beginning of the humidity absorption period. See text for discussion.

The temperature sensitivity was calculated based on the response of the sensing patch to rising or falling temperature measured throughout the experiments, which equalled to 99.2 pm/°C on average (range: 98.1–101.3 pm/°C). The choice of T_0 is arbitrary, as is the value of the peak corrected for temperature. It only conveys relative information and not absolute, and, hence, it can be shifted along the vertical axis by addition or subtraction.

At the beginning of the experiment 8, the temperature quickly increased (over ~1 h) to the high temperature, which was then kept stable throughout the experiment. During the period $t \approx$ 1:00–41:50 h, the peak T-corr. is relatively smooth and shows constant decrease in value (by ~0.5 nm overt the entire period). This was caused by the sample drying at the high temperature and releasing the humidity absorbed during room temperature exposure before the experiment. The value of lower humidity at higher temperature can be assessed from psychrometric charts or the Arden-Buck equation [372], knowing the humidity value at room temperature. In this experiment, humidity at the high temperature ≈ 10 %RH. In the later experiments, humidity was also logged, similarly to temperature. The fall in Bragg wavelength in this experimental period could not be explained by the fibre slippage. This is because, at $\lambda_B \approx$ 1535.85 nm, the fibre was still under slight compressive stress (the delta calculated as in **Error! Reference source not found.** equalled to -0.46 nm). Consequently, the fibre relaxing the compressive stress would translate to a redshift and not blueshift as observed in this experimental period.

At $t \approx$ 41:50, the oven chamber was opened (hence a dip in the temperature in **Error! Reference source not found.**) and the sample was immersed under water along with the thermistor probe. The water temperature had had previously equalised with this in the oven. At $t \approx$ 41:50–56:00 h, the peak T-corr. showed a regular quasi-exponential increase, related to the sample swelling due to humidity absorption (see the inset in **Error! Reference source not found.**). ABS, of which the sample had been made, displays a relatively high water absorption of up to 1 % [373]. However, the peak T-corr. stopped growing exponentially at $t \approx$ 56:00 h, and it started displaying much less regular behaviour after $t \approx$ 60:00 h. Supposedly, this was how the fibre slippage manifested itself. At $t \approx$ 60:00, the peak achieved its highest value during the experiment 8 (1537.04 nm) and was above the value calculated for a non-embedded FBG by 0.72 nm at the high temperature (see **Error! Reference source not found.**). As a result, the fibre was under tensile stress, which it was prone to relax by redshifting towards its equilibrium state, corresponding to a Bragg wavelength of 1536.31 nm. As the sensing patch kept absorbing water, the fibre kept slipping after $t \approx$ 60:00 h. This resulted in the peak T-corr. having irregular, "wavy" form in time, which was not due to ambient temperature fluctuations. A similar phenomenon occurred during the experiment 12 for the sample CS on humidity uptake.

At $t \approx$ 110:00 h, the oven chamber was opened once again (compare the dip in the temperature in **Error! Reference source not found.**), the sensing patch and the thermistor probe were removed from the water and placed on a plastic tray for drying. The high temperature setting of the oven was preserved. It can be seen from **Error! Reference source not found.** that the peak T-corr. displayed a trend to fall

during drying, like during the period $t \approx 1{:}00–41{:}50$ h. However, the form of the peak T-corr. in time was irregular and "wavy", similarly to what was noticed at $t \approx 60{:}00–110{:}00$ h and oppositely to what was observed at $t \approx 1{:}00–41{:}50$. Again, the "wavy" form of the peak T-corr. could not be coming from temperature fluctuations. The fibre slippage during the water immersion period was also confirmed by the fact that the peak T-corr. value after the sample was removed from water decreased markedly below the peak T-corr. value before water immersion. If not for the fibre slippage, the opposite behaviour would have been expected due to the sensing patch swelling on water absorption, which would translate to an increase in the peak T-corr. value.

It is also worth underlining that the sample drying and fibre slippage continued for a prolonged time (over 15 days) after removing the sample from water. At that experimental period, the fibre was under compression (the peak below the equilibrium value at 50 °C, 1536.31 nm). Hence, the fibre could be relaxing compressive stress by slipping, which corresponds to the peak redshifting. Possibly, humidity contained in the fibre primary coating was still at a high enough level to allow the fibre slide against its primary coating. It is speculated that the fibre slippage occurred at the interface between the fibre and its primary coating and not the primary coating and the sample or glue. This is because the acrylic primary coating is not produced to maximise its adhesion to the fibre as this is normally not required in the optical fibre applications. PMMA, of which the primary coating is made, shows a water affinity of up to 2 % [143], which is twice as much as for ABS. Alternatively, the "wavy" form of the peak T-corr. after removing the sample from water could be due to variations of ambient humidity. They would be expected to follow the fluctuations of the ambient temperature related to changes of the environmental conditions between day and night, which seem to be reflected in the forms of the peak and peak T-corr. series. However, similar fluctuations were not observed during the period $t \approx 1{:}00–41{:}50$, when humidity was also non-stabilised. Neither hypothesis could be validated without further research, which is out of the scope of this thesis.

Furthermore, it is worth noting that no fibre slippage on humidity intake at the high temperature was observed during the experiment 6, although it also involved exposure to the high temperature and humidity. Possibly, this was due to the following differences. First, during the experiment 6, the fibre was exposed to the high temperature merely for 6 h, while the fibre slippage in the experiment 8 was observed only after 18 h. The fibre slippage was speculatively dependent on the amount of humidity absorbed by the primary coating. The fibre embedded in the innermost part of the structure is the last to absorb humidity as it must first diffuse through the outer layers of the housing structure. It is then likely that the humidity at the fibre position increased only marginally after 6 h, in view of a much thinner POF (of a 190-μm-diameter) requiring a considerable time of ~30 min for stabilisation of its humidity response (see Section 2.7.4). Secondly, judging from the delta values for the maximal peak (see **Error! Reference source not found.**), which were noted at the high temperature and humidity, the tensile stress on the fibre was slightly smaller in the experiment 6 (delta = 0.62 nm) than experiment 8 (delta = 0.76

nm). This could also decrease the probability of the fibre slippage since it presumably only occurred after exceeding some threshold value of stress on the fibre.

Performance of the sample CS during the experiments 9-12

Before the experiment 9, the experimental set-up was upgraded. The sample was enclosed in a sealed container with silica gel in order to achieve stable low humidity. This change was made to minimise the influence of humidity fluctuations, which occurred when humidity was not stabilised. One of the thermistor probes was put in the container next to the sample, along with the humidity logger. **Error! Reference source not found.**(a) shows the peak and temperature during the experiment 9, while (b), the peak T-corr. and relative humidity values. It must be noted that the psychrometric charts would dictate the opposite relative levels of humidity than what was shown by the humidity logger. That is, lower relative humidity values would be expected at a higher temperature rather than at a lower temperature, while the humidity logger shows the opposite (compare **Error! Reference source not found.**(b)). However, the accuracy of the relative humidity readout is ±2 %RH in the temperature range achieved during the experiment. The differences in the humidity readings of the humidity logger for high and low temperature fall below that threshold of accuracy.

For the temperature characterisation of the sensing patches to be reliable according to the method used, the experimental condition of a quasi-static temperature change had to be conserved (i.e., temperature changing slowly enough to be gauged without delay by the sample). This could be judged from the peak T-corr. series, as they allow appreciating changes to the Bragg wavelength that are not directly related to temperature changes (i.e., other than due to thermal expansion of the housing and TOC of the fibre). The peak T-corr. values in the experiment 9 shows that this could be considered the case for the temperature changes until $t \approx 230$ h. In that interval, the shortest of these rising and falling slopes was 5 h long on temperature changing from room temperature to the high temperature or inversely. The variations of the peak T-corr. were <50 pm then. They were probably also contributed to by the sample shrinking due to drying on heating up or by the sample swelling due to humidity absorption on cooling down. The latter was especially well visible because the temperature decrease was normally slowing down towards the end during all the experiments (see the experiment 9 at, e.g., $t \approx$ 122:00, 182:00, and 220:00 h). However, sharp redshifts of the peak T-corr. of an amplitude of over 100 pm appeared on the rising temperature slopes at $t \approx$ 288:00, 310:00, and 333:00 h, which were all 1 h long. The offset in time between the peak and temperature during these periods was visibly larger than during all the other, leading to a higher degree of non-linearity resulting in the sharp redshifts. However, the temperature sensitivity figures of the sensing patches calculated based on the one-hour-long temperature slopes were very similar to those based on longer temperature slopes, not clearly tending to be bigger or smaller. However, the slopes of a length of 5 h were considered optimal and were normally used during all the temperature and humidity experiments to calculate the temperature

sensitivity and the correction factors for the peak T-corr. data series. One the one hand, they ensured the condition of the quasi-static temperature change, and, on the other, they were less prone to the interference from humidity absorption or desorption.

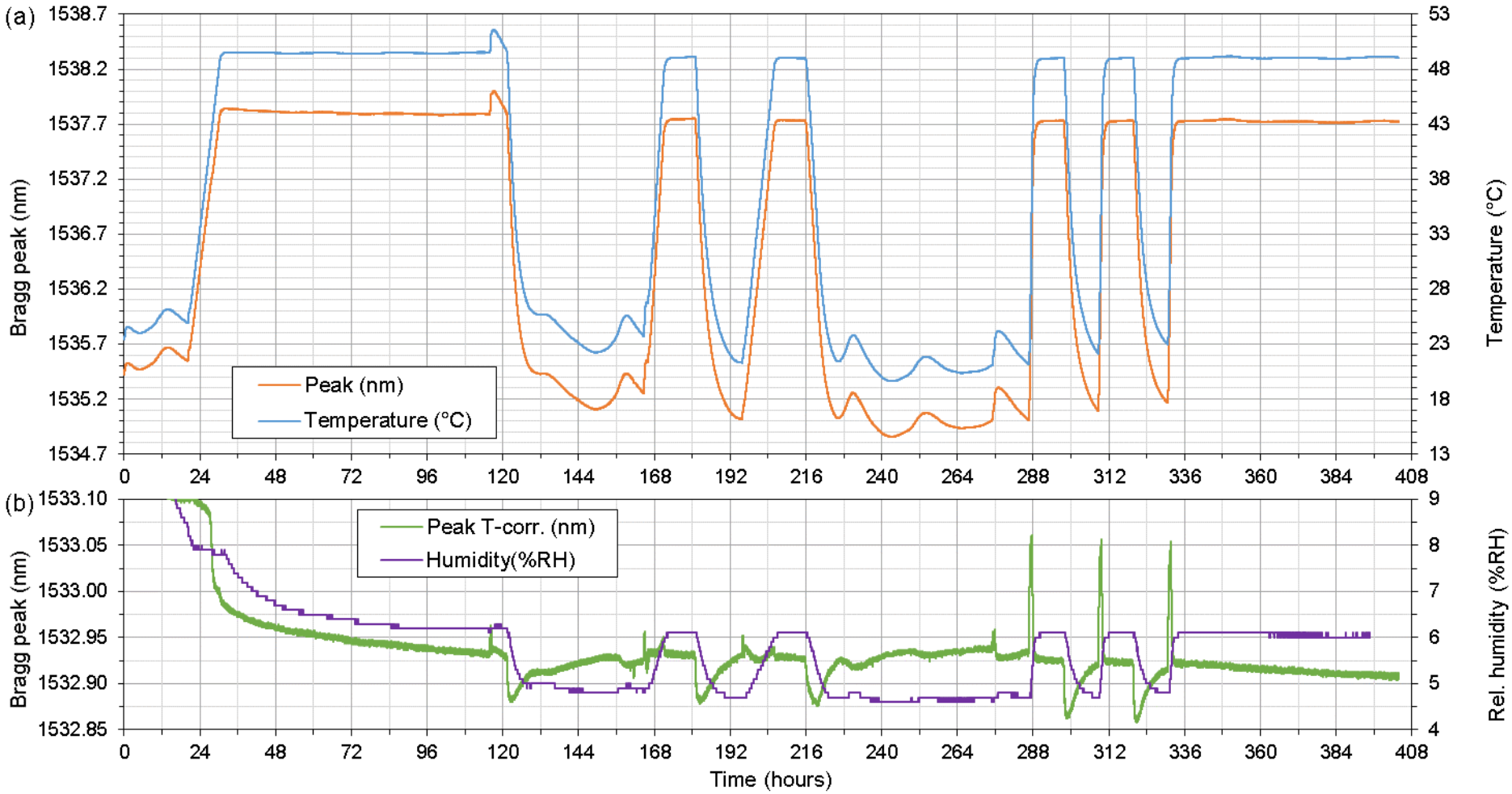

Figure 6-29. (a) Bragg peak and the temperature, (b) the Bragg peak corrected for the temperature influence (Peak T-corr.) and the relative humidity as a function of time during the experiment 9 for the sample CS. See text for discussion.

During the stable low or high temperature intervals, the peak T-corr. allowed observing the sample absorbing or desorbing humidity. The sample drying and shrinking was most apparent at the first high temperature period of the experiment 9 ($t \approx$ 26:00–120:00 h), before which the sample had accumulated relatively much humidity at room temperature. To a lower extent, the sample were shrinking due to drying during all the high temperature experimental periods, the longest of them ($t \approx$ 334:00–404:00 h) displaying this tendency most clearly. Inversely, the low temperature intervals of the experiment 9 after the initial drying (i.e., starting from $t \approx$ 128:00 h) featured the sample reabsorbing humidity at room temperature as the relative humidity increases on a temperature fall. In the case of the experiment 9, such sample behaviour could have theoretically been explained by the fibre slippage. This is due to the fact that, at the high temperature, the fibre was under tensile stress, which it would relax by blueshifting. Inversely, during the low temperature intervals, the fibre was under compressive stress and would tend to relax it by redshifting. However, first, the fibre slippage was characterised by a much less regular, "wavy" form of the peak in time. Secondly, peak slowly and constantly rising during the room temperature periods and falling during the high temperature ones was also observed during the experiment 8 at $t \approx$ 1:00–41:00 h and during the experiments 1–5, 7, 10, and 11, whose full time graphs were not shown. Finally, the values of the peak at 31.0 °C in the experiment 9 and 10 were very similar, while, if the fibre slippage had occurred, the difference between them would have been much larger (compare the fibre slippage during the experiment 8).

Another upgrade of the experimental set-up, i.e., stabilisation of room temperature, was made before the experiments 10–12. They displayed a smoother and more stable level of the temperature, and, thus, the peak. As was mentioned before, the fibre slippage was observed again during the experiment 12 at the high temperature with the sample being immersed in water, similarly to the experiment 8 (compare the maximal peak values in **Error! Reference source not found.** in the experiments 10 and 12 versus 8 and 9, respectively). No fibre slippage was noticed from the experiment 9 to the beginning of the experiment 12, which can be inferred from the relatively stable peak at 31.0 °C during these experiments (see **Error! Reference source not found.**). Nonetheless, the experiments 10–12 confirmed previously described observations and, hence, do not need to be described in detail.

Impact of temperature and humidity trails on the strain sensitivity of the sample CS

After finishing the temperature and humidity experiments, the strain sensitivity of the sample CS was retested. The strain sensitivity was found to have decreased from 0.81–0.85 to 0.675 pm/με. Two strain trials were performed to exclude the risk of error, both of which gave the same result. It is unsure where this change came from. It might be due to fibre detached from the glue and sliding against the housing structure. However, this would supposedly result in a much higher Bragg peak hysteresis, while it was found to be similar to this before the temperature and humidity trials (0.111 and 0.208 nm in two tensile strain tests). Alternatively, the elasticity of the primary coating might have been changed due to the

relaxation of stress on the fibre or temperature and humidity cycling. This, in turn, could have made the coating shield a bigger proportion of stress, resulting in a smaller strain to the fibre sensed by the FBG. However, these explanations are only speculative and further research would be required to understand the behaviour of the sample in more detail.

Summary of the results for the sample CS

In conclusion, it can be noted that the sample CS displayed both temperature and humidity sensitivity, as expected of the ABS plastic of a rather high CTE and showing considerable affinity for water. Temperature sensitivity was repeatable and fell within the range 98.1–101.3 pm/°C, the average value being 99.1 pm/°C. However, the peak position in time showed multiple unexpected blueshifts and redshifts, which were neither related to temperature nor humidity changes and could be considered parasitic from the viewpoint of the use in sensing. As a result, the peak position at a temperature of 31.0 °C, used as a benchmark figure, was evolving from experiment to experiment as shown in **Error! Reference source not found.**. This was unfavourable from the point of view of the sensing applications as they require the transfer function of a sensor to be stable, which was not the case.

Two origins of the parasitic shifts of the peak in time were identified: the fibre slippage and the changes of the reflection spectrum of the embedded FBG. The former might be coming from the creep effect due to the sample CS having been left mounted on the strain test set-up between the tensile strain experiments 6 and 7. Slight deviation of the reflection spectrum was observed afterwards. This uneven chirping of the FBG could have been the first sign of the fibre detaching from its primary coating, which was then boosted during the temperature and humidity response trials. The grating recovering its shape during the experiment 5 could be associated with complete disappearance of the local areas of higher adhesion, which were supposedly responsible for the local positive or negative chirp on the FBG. Alternatively, the fibre slippage could have come from the very presence of the primary coating. As the adhesion force between the fibre and its primary coating does not normally need to be maximised for most optical fibres applications, it is speculated that embedding fibres with their primary coating on would sooner or later result in the development of the fibre slippage. To verify this hypothesis, temperature and humidity response trials will be conducted on a sample with bare embedded fibre.

The evolution of the reflection spectrum was presumably caused by local positive or negative chirps to the embedded scanned grating. This could have also had to do with the detachment of the fibre from its primary coating mentioned above. Possibly, this effect was further contributed to by temperature cycling of the sample. The peak shift in time associated with the spectral evolution came from the algorithm of the HBM interrogator used to monitor the sample. The peak tracking algorithm relied on searching for zero crossings of the differential signal of the reflection spectrum with respect to wavelength. During the spectral evolution, the side lobe in the reflection spectrum kept growing and reached the point when it became a local maximum. It then started being recognised as another peak,

which complicated peak tracking and supposedly resulted in a peak shift in time. The use of a different peak tracking algorithm could allow avoiding the observed peak shift. However, none of the currently available algorithms would perform well with an FBG of a varying spectrum. This includes even the newly proposed dynamic gate algorithm, which was found very efficient for tracing the position of the gratings of an irregular shape [374]. Moreover, the deviation from the idealised FBG reflection spectrum was likely a sign of the grating gradually detaching from its primary coating, which triggered other issues described above. The problem of grating chirping could possibly be addressed using a sensing patch containing a point FBG rather than scanned. Such sensing patch will be tested in the next step.

The sample CS preliminarily showed a quasi-exponential increase of the Bragg wavelength due to humidity absorption after immersion in water. However, the fibre likely detached from the housing structure before the response to humidity stabilised, which was seen twice during the experiments. Hence, the humidity sensitivity figure could not be calculated. It is speculated that increased humidity contributed to the likelihood and extent of the peak shifts in time. This was supposedly because the shifts were a function of unrelaxed stress on the fibre and the friction between the fibre and its primary coating, the latter having likely been decreased by the presence of water. Possibly, the use of a sample containing a bare embedded fibre will permit to address the problem of fibre slippage both at low and high humidity.

Temperature and humidity experiment of the sample BP

The temperature and humidity trails of the sample CS, in which a coated scanned grating was embedded, led to formulating the hypothesis that a superior sensing performance might be achieved by the sample containing a bare rather than coated grating and a point one rather than scanned. To verify this, similar tests of the temperature and humidity response were conducted on the sample BP (bare point).

Similarly to all the embedded FBGs, the one in the sample BP blueshifted after embedding, from 1536.23 nm to 1531.86 nm (see Table 6-2). This was due to thermal contraction of the housing structure on cooling down after having been embedded at high temperature (see Section 6.2.2 for details). The sensing patch likely continued stabilising after manufacturing, which was related to a further decrease of the Bragg peak. This was described for the sample CP in Section 6.2.2. During the tensile and compressive strain experiments performed before the temperature and humidity trails, the Bragg wavelength was found to oscillate between 1530.03 and 1531.54 nm. This span of ~1.5 nm was probably coming from temperature fluctuations among the experiments and from mounting the sample for straining. Before the temperature and humidity trail, the Bragg wavelength of the sample BP was at 1530.94 nm. This suggests that the adhesion between the fibre and the housing was high, not letting the fibre relax the compressive stress under which it had been put during embedding. Moreover, virtually no spectral changes were observed for the sample BP during both the straining experiments and the temperature and humidity trails.

The experiment testing the response of the sample BP to temperature and humidity was conducted using the most mature testing procedures and design of the testing set-up. This involved stabilisation of the dry conditions and low temperature (see Table 6-5, the experiments 11–12). The sample BP was placed in a sealed container along with one of the thermistor probes (T1) and the thermologger. During the dry intervals, silica gel was inserted in the container to yield stable low humidity conditions. A relative humidity of 100 %RH was achieved by removing the silica gel and immersing the sample in water. The reflection of the Bragg peak from the embedded FBG was observed on the HBM interrogator.

The experiment was designed to:

- first, allow the sample to dry at room temperature, later facilitating the process by the high temperature
- secondly, observe the behaviour of the sample after drying, both at room temperature and the high temperature
- then, examine humidity intake at room temperature, its speed being increased later by the high temperature
- finally, study the sample drying at room temperature.

The time graph of the experiment is shown in **Error! Reference source not found.**. It has been annotated on top with the numbers of the experimental periods to facilitate discussion. Two temperature data series are shown: T1, measuring the temperature at the sample, and T2, serving as the temperature reference of the chamber. The former is meant when referring to the temperature of the sample. The offset between T1 and T2 is most likely a systematic error due to a difference in positioning the thermistor probes in the oven and the measurement inaccuracy. The peak data series was found visibly noisier than for the sample CS discussed previously. This is due to the latter being a scanned FBG, characterised with a narrower Bragg peak (see Section 2.7.1), as opposed to the sample BP being a point grating. From the time graph, the experimental error of the peak was assessed to be ±10 pm, which was much higher than the resolution of the HBM interrogator itself. The error of the peak T-corr. was assessed as ±35 pm with the total differential method based on the experimental errors. The temperature correction factor for the peak T-corr. was calculated based on the temperature sensitivity from the rising slope of the period 3. This period began after a prolonged drying time and, thus, displayed minimal interference from humidity. It should then be noted that the peak T-corr. series is much more accurate on temperature change in dry conditions (beginning of the period 2 and 3) than at the points when considerable impact of humidity was expected (beginning of the period 1, 5, and 6). In turns, the peak T-corr. is equally accurate in all the periods of stable temperature. As was mentioned previously, the readout of the thermologger would have been expected to fall at the high temperature compared to room temperature, as the psychrometric charts dictate. In turns, the relative humidity values showed the opposite tendency, which was believed erroneous. However, this readout inaccuracy was below the measurement error, which amounted to ±2 %RH in the temperature range achieved in the experiment.

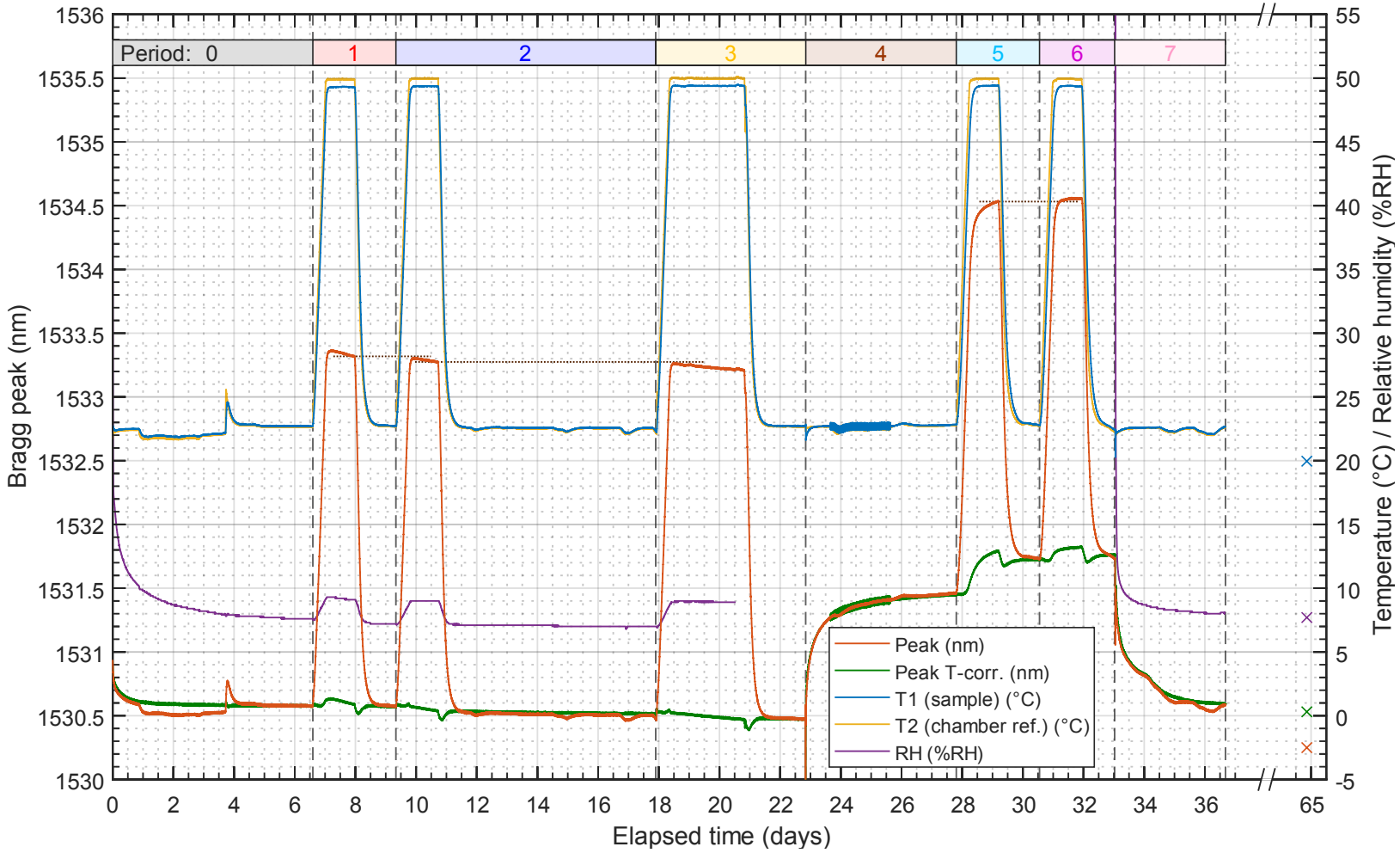

Figure 6-30. Bragg peak, the Bragg peak corrected for the temperature influence (Peak T-corr.), the temperature at the sample (T1) and in the oven (T2), and the relative humidity (RH) as a function of time during the temperature and humidity experiment for the sample BP. See text for discussion.

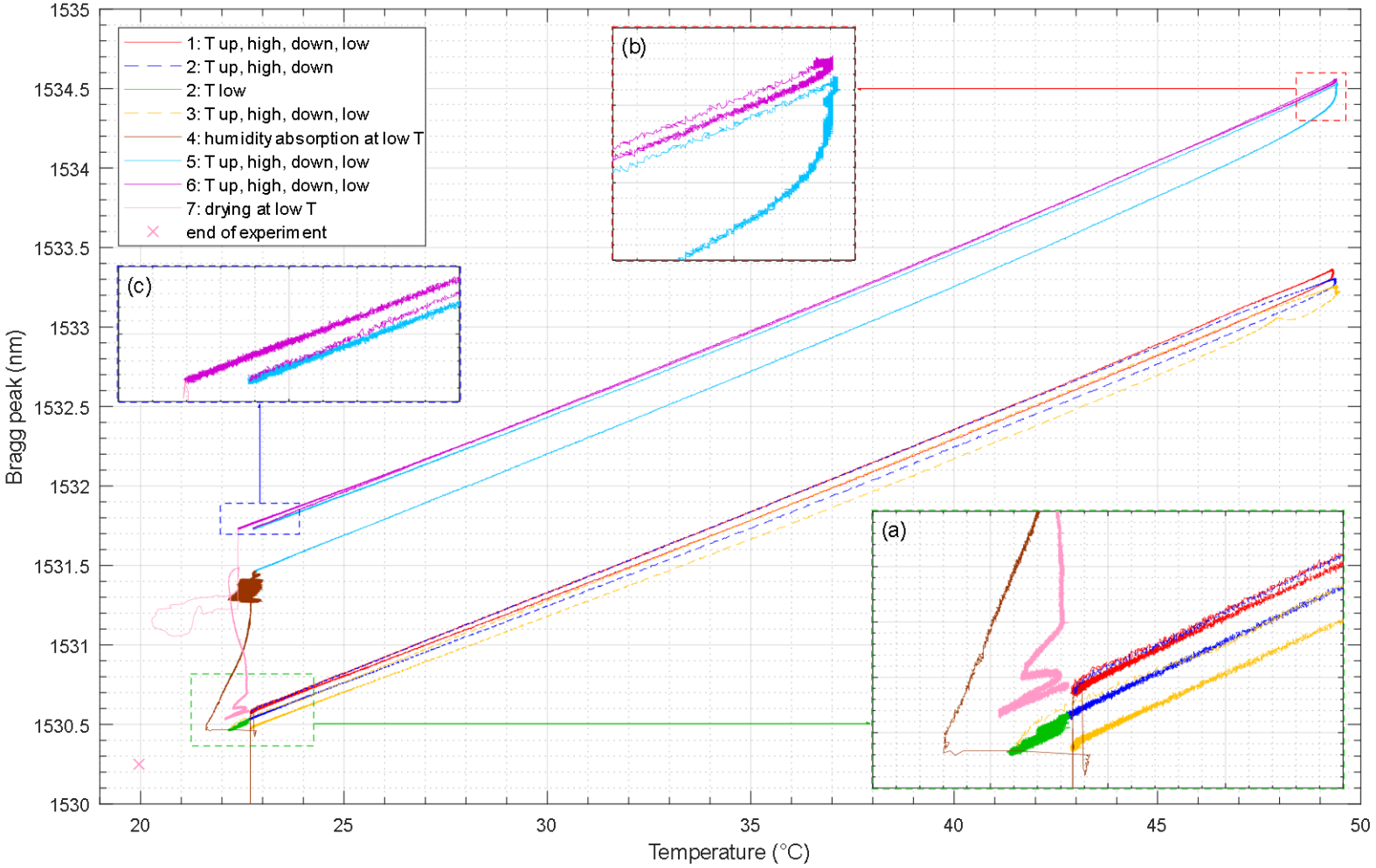
1: T up, high, down, low
2: T up, high, down
2: T low
3: T up, high, down, low
4: humidity absorption at low T
5: T up, high, down, low
6: T up, high, down, low
7: drying at low T
end of experiment
(a)
(b)
(c)
Bragg peak (nm)
Temperature (°C)
1535
1534.5
1534
1533.5
1533
1532.5
1532
1531.5
1531
1530.5
1530
20
25
30
35
40
45
50

Figure 6-31. Bragg peak as a function of temperature during the temperature and humidity experiment for the sample BP. The data series in the legend follow the numbering of the periods in **Error! Reference source not found.**. The insets show magnified views of the important regions of the graph. See text for discussion.

Aside from the time graph (**Error! Reference source not found.**), the graph showing the peak as a function of temperature T1 (the temperature graph, **Error! Reference source not found.**) was produced to facilitate discussion of the experimental results. The data series displayed on it correspond to the numbers of the experimental periods annotated on the time graph.

Before starting the experiment, the sample was kept in water for a prolonged time. This allowed observing drying dynamic of the sensing patch after sealing it in a container with silica get just before starting the experiment, i.e., the period 0. This period is not shown in the temperature graph for clarity. The temperature peak on the time graph at $t \approx 3.75$ days came from the oven turning on. In the time graph, the fall of the peak T-corr. value corresponding to drying was noted. It was relatively quick at the beginning of the period 0 (delta ≈ -310 pm until $t \approx 1$ day) and visibly slower afterwards (delta ≈ 30 pm at $t \approx 1$–6.5 days). From the relative humidity series, it can be observed that the decrease of the humidity value was clearly slower than the fall of the peak during the period 0. This discrepancy might have been caused by the sensor readout stabilisation at low humidity, which was at the edge of the normal range of the sensor.

The relative humidity value in the period 1 had not fully stabilised yet when the temperature was raised to ~49 °C. The gradual fall of the peak T-corr. during the high temperature interval of the period 1 corresponds to the sample drying. This started being noticeable when the sample achieved a temperature of ~45 °C because, from this temperature on, deviation from linearity can be noticed in the temperature graph. However, after reverting to room temperature, the value of the peak T-corr. was almost identical to this at the end of period 0 (delta < -5 pm). That behaviour can also be appreciated from the inset (a) on the temperature graph, in which it is apparent that the period 1 begins and ends virtually at the same point. The sample must then have reabsorbed humidity on temperature decrease, which proves the humidity level in the chamber was still so high that the sample effectively did not dry due to exposure to the high temperature.

The beginning of the period 2 was identical with the period 1, the difference lying in a much longer low temperature interval at the end of the former. After reaching the temperature of ~49 °C in the period 2, the peak value was below this at the end of the high temperature interval in the period 1 (see the brown dotted lines in the time graph). The sample was constantly drying from the beginning of the experiment, so the value of the peak at constant temperature was expected to fall. This proves that no fibre slippage was observed as opposed to, e.g., the experiment 5 of the sample CS (see Figure 6-26).

Compared to the period 1, the response of the sample to humidity changed in the period 2. This time, the peak T-corr. value displayed slightly slower drying dynamics at the high temperature. However, after the temperature reverted to room temperature, the peak T-corr. was not seen to return to the value from the end of the period 1. Instead, it had fallen by ~50 pm, which can also be seen in the inset (a) in the temperature graph. That fall can be associated with shrinkage of the housing structure due to sample drying at the high temperature. The fact that the high temperature boosted drying can be noticed on the

temperature graph, in which the peak visibly deviated from linearity starting from a temperature of ~43 °C on the rising slope. Moreover, the peak value decreased at the stable high temperature due to drying. On cooling down, the sample did not reabsorb humidity, contrarily to what was noticed during the period 1. This could also be seen from the fact that the slope steepness in the temperature graph for rising and falling temperature during the period 2 was almost identical, as opposed to the period 1. Presumably, the sample drying was enabled by humidity in the chamber having stabilised in the period 2 and being smaller than in the period 1.

The interval of low humidity in the period 2 was associated with further humidity decrease as can be seen from the relative humidity data series in the time graph. This allowed the sample to dry further, yielding a peak T-corr. delta of about -10 pm caused by shrinkage of the housing structure (compare the peak T-corr. in the time graph and the low temperature series of the period 2 in the temperature graph). As expected, the drying dynamics at room temperature was markedly lower than at the high temperature of the period 2.

The sample dried further during the period 3, which featured an over two-day-long interval of the high temperature. The relative humidity data was lost starting from $t \approx 20.5$ days due to being overridden in the sensor memory. However, this did not cause any major issue as this data was not decisive for interpreting the sample behaviour and could be inferred from the period 2. The observations of the sample behaviour were similar to those made during the period 2. First, the peak value at a temperature of ~49 °C at the beginning of the period 3 was smaller than at the end of the high temperature interval of the period 2 (see the brown dotted line in the time graph). Again, this confirmed that no fibre slippage occurred between the two high temperature intervals. Secondly, the peak T-corr. decreased much more quickly during the high temperature intervals, probably due to lower relative humidity at the high temperature. This can also be observed in the temperature graph. Thirdly, equal steepness of the slopes on heating up and cooling down was observed in the temperature graph. This yielded a shift in the peak T-corr. of ~20 pm during the high temperature interval, which can be appreciated in both the time and temperature graphs. Moreover, the peak kept decreasing at the ends of the high temperature intervals. Similar slow gradual peak fall at the high temperature was observed during a few experiments for the sample CS to continue for up to 15 days running. The fibre slippage could not be excluded in those cases, although it was considered little probable, as discussed earlier. As the peak fall seen during the experiment of the sample BP was presumably caused by the housing structure shrinking on drying, this would suggest very high water content in the sample. Alternatively, this could stem from very slow drying dynamic, supposedly limited by water diffusion in the sensing patch. Neither explanation could be taken for granted without further research though, which is out of the scope of this thesis.

The rising temperature slope in the period 3 was considered the least affected by the influence of humidity of all the rising temperature slopes as the sample had dried for ~18 days then. In turns, all the falling temperature slopes, including this in the period 3, feature a decrease in their falling speed towards

the end, which makes them more prone to being affected by humidity. Hence, linear regression was applied to the rising temperature slope in the period 3 to assess the temperature sensitivity of the sample as 103±14 pm/°C (CI = 95%, R^2 = 0.9999).

At the beginning of the temperature fall in the period 3, a slight dip in the temperature was observed. It is clearly noticeable in the temperature graph. It is believed to be an experimental artefact coming from instability of the oven on temperature decrease, which has not changed the meaning of the results. After the temperature returned to room temperature, the peak T-corr. fell further by a few pm. As a very slow decrease of the peak T-corr. could continue for a prolonged time without making important difference to the results, its value achieved at the end of the period 3 was considered the saturation value at 6.8 %RH. Hence, it was later used for calculating the relative humidity sensitivity of the sample.

At the beginning of the period 4, the chamber was opened for manipulations: the silica gel and the thermologger were removed from the sealed container, and the sample along with the thermistor probe were fully immersed in water. The water had been kept in the chamber beforehand to avoid temperature difference due to inserting water. These manipulations resulted in some experimental artefacts of a few minutes in the temperature, peak, and peak T-corr. data series at $t \approx 22.8$ days. They were visible both in the time and temperature graphs. The period 4 shows a quasi-exponential profile of the peak T-corr. in the response to a step-change in humidity at room temperature. This is also reflected in the peak rising at room temperature in the temperature graph. No fibre slippage was observed, as opposed to what was noticed at the high temperature during the experiment 8 and 12 for the sample CS. In the period $t \approx$ 23.6–25.6 days, a noisier than usual temperature response was observed, which also transferred to the peak T-corr. data series through the temperature correction factor. The origin of this higher experimental noise is unknown. Speculatively, it might have been linked to the operation of the air conditioning, on which stabilisation of room temperature relied. In any case, this experimental artefact does not influence the interpretation of the results.

In the period 5, the temperature was risen to ~49 °C. This resulted in the peak T-corr. in the time graph started increasing much more quickly compared to the end of the period 4. This is also visible in the temperature graph. The origin of this was supposedly a higher humidity absorption rate. The temperature rise increased the value of saturation water content in the ABS plastic of the housing, on which the absorption rate is dependent. The peak T-corr. was still rising at the end of the one-day-long interval of the high temperature, yielding a total increase in the peak T-corr. of ~350 pm. This prove that the length of the interval was too short for the humidity absorption to finish. During the room temperature interval of the period 5, the peak T-corr. seemed to keep increasing but at a negligibly slow rate. The peak series in the temperature graph did not change at all (see the inset (c) in **Error! Reference source not found.**).

The temperature profile during the period 6 was almost identical to the period 5, the only difference lying in a shorter interval of room temperature in the former. As the sample was expected to constantly

absorb humidity since the beginning of the period 4, the peak value tracked at a constant temperature in time should grow. Indeed, after the temperature reached ~49 °C, the peak was at the level which it had achieved at the end of the high temperature interval in the period 5 (see the brown dotted line in the time graph). This prove again that there was no fibre slippage in the periods of humidity absorption. Judging from the peak T-corr. in the time graph, the rate of humidity intake at the high temperature interval of the period 6 was smaller than in the respective interval of the period 5. However, similarly to the latter, the peak T-corr. grew constantly during the high temperature interval of the period 6 and did not stabilise before the end of the interval. After the temperature reverted to room temperature, the peak T-corr. in time was roughly stable. Furthermore, it was found not to have increased much compared to the end of the period 5 (delta ≈ +20 pm). Finally, it was expected that a slow increase could continue for days, not making important contribution to the achieved peak T-corr. value. Thus, the wavelength achieved at the end of the period 6 was assumed the saturation wavelength at 100 %RH and was then used for calculating the humidity sensitivity of the sample.

The humidity sensitivity of the sample was assessed based on the two measurement points: at the end of the period 3 at 6.8 %RH and at the end of the period 6 at 100 %RH. The sensitivity value was calculated to be 13.8±1.1 pm/%RH, the error having been estimated using the total differential method.

At the beginning of the period 7, the oven chamber was opened once again for manipulation. It relied on removing the water, wiping dry the sample and container, inserting the silica gel along with the thermologger, and resealing the container. Similarly to what was observed at the beginning of the period 4, some experimental artefacts of a few minutes in the temperature, peak, and peak T-corr. data series arose in connection with these manipulations, which are visible both in the time and temperature graphs. Constant fall of the relative humidity and peak T-corr. in time was observed afterwards. Both data series displayed a quasi-exponential decrease. However, the peak T-corr. series featured a “bump” at $t \approx 34$ days, looking as if the exponent of the quasi-exponential decrease had changed. It was checked not to have been related to any kind of manipulation to the experimental set-up. Neither was it caused by a spectral change because the shape of the Bragg peak was stable throughout the experiment, as opposed to this seen in the experiment 2 of the sample CS. Also, the “bump” could not have been related to the fibre slippage. The fibre was under compressive stress at all times during the experiment, so fibre sliding against its primary coating would have resulted in a redshift and not blueshift as was the case. It is speculated that the “bump” could have been related to evaporation of the remains of liquid water, but further research would be required to confirm that.

The period 7 finished at $t \approx 36.6$ days, after which point the sample was not interrogated live anymore. However, it was left in the sealed container in room temperature for almost 30 more days. After that period (at $t \approx 64.9$ days), the temperature, relative humidity, and the peak values were checked again as shown in the time and temperature graphs. It was found that the humidity kept decreasing, but it only reached 7.7 %RH compared to 6.8 %RH at the end of the cycle 2. This discrepancy was below the

thermologger measurement error of ±2 %RH at that temperature range. It might have been also contributed to by the thermal history at the point of measurement. Moreover, drying could have been boosted by the intervals of the high temperature during the periods 1–3, as opposed to the period 7 and later. Alternatively, it is speculated that the discrepancy came from the amount of humidity that silica gel had absorbed, leading to the humidity stabilising at a higher level at the end of the experiment than during the periods 2–3. As to the peak, it blueshifted at the end of the experiment (by ~330 pm, to 1530.25 nm) due to a lower value of temperature at the end of the experiment compared to the end of the period 7 (19.96 °C vs 22.65 °C). However, the peak T-corr. fell only by ~55 pm, accordingly to the relative humidity decrease.

Equation describing the temperature and humidity response of the sample BP

Calculating temperature and humidity sensitivity of the sample allowed formulating the equation describing the change of the Bragg peak of the sample BP on changes of temperature and humidity.

As was mentioned in Section 2.7.4, the combined effect of strain, temperature, and humidity on an FBG, assuming linear additivity, can be expressed as:

$$\frac{\Delta\lambda_B}{\lambda_B} = (1 - P_e)\epsilon + (\alpha + \xi)\Delta T + (\gamma + \eta)\Delta H. \quad (6\text{-}2)$$

However, the sample BP contained a silica FBG, which shows no intrinsic sensitivity to water, and hence, $\gamma = \eta = 0$. Moreover, the embedded grating was not free to expand and contract according to its material characteristics described by its CTE, but it was undergoing strain from the housing structure. Thus, $\alpha = 0$. The effect of humidity and the larger part of the effect of temperature came to the equation through the strain on the FBG from the housing structure (ϵ_{ABS}). It can then be written as:

$$\epsilon_{ABS} = \epsilon_{ABS,T} + \epsilon_{ABS,H} = \alpha_{ABS} \cdot \Delta T + \gamma_{ABS} \cdot \Delta H \quad (6\text{-}3)$$

where $\epsilon_{ABS,T}$ and $\epsilon_{ABS,H}$ are the strain from the ABS housing structure due to, respectively, the change of temperature and humidity; α_{ABS} and γ_{ABS} are, respectively, the CTE and swelling coefficient (coefficient of moisture expansion) of the ABS housing. In the temperature and humidity experiments, ϵ_{ABS} was the only strain acting on the grating as no external stress was put on the housing. Equation (6-2) can then be reformulated as:

$$\frac{\Delta\lambda_B}{\lambda_B} = (1 - P_e)\epsilon_{ABS} + \xi_{SiO_2} \cdot \Delta T = (1 - P_e)(\alpha_{ABS} \cdot \Delta T + \gamma_{ABS} \cdot \Delta H) + \xi_{SiO_2} \cdot \Delta T \quad (6\text{-}4)$$

Assuming the literature values of the Pockels coefficient (P_e = 0.215, see Table 2-4) and TOC (ξ_{SiO_2} = 8.2×10^{-6} °C^{-6}, see Table 2-7) for silica at 1550 nm and knowing the experimental temperature sensitivity of the sample ($\frac{\Delta\lambda_B}{\Delta T} = 103$ pm/°C), the CTE of the ABS housing (α_{ABS}) at stable humidity ($\Delta H = 0$) could be calculated according to the equation:

$$\alpha_{ABS} = \frac{\frac{\Delta\lambda_B}{\Delta T} - \lambda_B \cdot \xi_{SiO_2}}{\lambda_B(1 - P_e)}. \quad (6\text{-}5)$$

The calculated value of the CTE of the ABS housing (α_{ABS}) was found to be 73.9×10^{-6} °C^{-1}, which lies within the range reported in the literature (form 40 to 110×10^{-6} °C^{-1} [373].

Similarly, knowing the experimental humidity sensitivity of the sample ($\frac{\Delta\lambda_B}{\Delta H} = 13.8$ pm/%RH), the swelling coefficient (coefficient of moisture expansion) at stable temperature ($\Delta T = 0$) could be calculated according to the equation:

$$\gamma_{ABS} = \frac{\frac{\Delta\lambda_B}{\Delta H}}{\lambda_B(1 - P_e)}. \quad (6\text{-}6)$$

The calculated value of the swelling coefficient of the ABS housing (γ_{ABS}) was found to be 11.3×10^{-6} %RH^{-1}. No value of the coefficient of moisture expansion of ABS was found in the literature. However, the calculated result falls within the range of values reported for a variety of different plastics (from -2.7 to $+12.6\times10^{-6}$ %RH^{-1} [375]), which confirms the credibility of the figure that was obtained.

Knowing the CTE and swelling coefficient of the ABS housing structure allowed inserting the numerical values to Equation (6-4) to yield the quantitative description of the temperature and humidity response of the sample BP:

$$\frac{\Delta\lambda_B}{\lambda_B} = 0.785\,(73.9 \times 10^{-6} \cdot \Delta T + 11.3 \times 10^{-6} \cdot \Delta H) + 8.2 \times 10^{-6} \cdot \Delta T, \quad (6\text{-}7)$$

where ΔT is expressed in °C and ΔH, in %RH.

Summary of the results for the sample BP

As was speculated based on the results of the temperature and humidity trials for the sample CS, the sample BP showed much more favourable characteristics from the viewpoint of the applications in sensing. The reflection spectrum of the sample BP displayed virtually no changes throughout the experiment. The fibre slippage, observed during many experiments for the sample CS, was not noticed in the case of the sample BP. This means that the compressive stress, under which the sample was put during embedding, did not relax despite numerous strain, temperature, and humidity trials. This, in turns, proves good adhesion between the bare embedded fibre and the housing structure coming from the acrylic glue. However, the sample BP was not left mounted on the straining set-up for over 2 months, as was the case for the sample CS, which could potentially be the origin of the adhesion problems between the fibre and its primary coating. Hence, further research would be required to assess the long-term response of the sample BP to stain.

Very good overlap between the relative humidity values and the peak T-corr. data series was observed, including at $t \approx 64.9$ days. The transfer function of the sensor was stable, with the exception

of the "bump" at $t \approx 34$ days. It was speculatively coming from evaporation of the remains of liquid water contained in the sealed container used for the test. If this had been the case, the "bump" would have not been present during the trials in non-condensing ambient conditions, which are normally required for humidity sensors.

Comparison of the results for the sample CS, BP, and the reference FBG

Table 6-7 shows the comparison of the experimental values of strain and temperature sensitivity of the samples CS and BP measured in the Section 6.2. It can be noted that both the strain and temperature sensitivity for the sample CS is smaller than for BP. However, the difference in the former is much larger than in the latter. The origin of this discrepancy is unclear, but it probably has to do with the influence of temperature.

Table 6-7. Comparison of the experimental values of strain and temperature sensitivity of the samples CS and BP

	Strain sensitivity (pm/με)	Temperature sensitivity (pm/°C)
Sample CS	0.8025	99.2
Sample BP	1.037	103
Sample CS/Sample BP	77.4%	96.3%

It was speculated that the difference in the strain sensitivity between the samples was caused by the primary coating of the sample CS shielding part of the stress, which was then not fully transferred to the fibre. In turns, the sample BP featured no primary coating, and hence, the strain was transferred through the housing structure and the glue directly to the embedded fibre, resulting in a smaller amount of the stress being shielded.

In the case of both samples, their strain sensitivity came from the strain of the housing structure being transferred to the embedded FBG. The strain of the housing structure was due to the external stress acting on it. Similarly, the largest part of temperature sensitivity of the sample came from the FBG sensing the strain coming from the housing structure (apart from the minor influence of TOC of silica, as discussed above). However, in the case of temperature sensitivity, the strain of the housing structure was caused by its thermal expansion and not external stress. The difference relies on the fact that, in the case of the strain of the housing structure due to external stress, it acts only on some of the outer surfaces of the sample (i.e., the mounting support). It is then transferred inside the structure to the position where the fibre is embedded. The stress can be shielded by the intermediate layers of the housing structure itself, the glue, and the primary coating (if present). As a result, it might be that the actual strain on the embedded fibre is smaller than the strain of the external surfaces of the housing structure. On the

contrary, when the housing structure strains due to its thermal expansion, the entire structure (its bulk as well as the outer surface) strains by the same amount. Moreover, although the primary fibre coating (if present) is not free to expand or contract, its CTE is expected to be similar to this of the ABS housing structure, resulting in little stress due to CTE mismatch between the primary coating and the housing. Hence, it is speculated that the primary coating might contribute less to shielding stress in the case of temperature sensing than strain sensing. Thus, when present on the embedded fibre, the primary coating lowers the temperature sensitivity of the sensing patches less than it does for the strain sensitivity. However, this explanation is only hypothetical and further research would be required to fully understand the behaviour of both samples, which is out of the scope of this work. Any speculations are further complicated by the fact that high degree of anisotropy is expected in both the 3D printed housing structure and the thin primary fibre coating.

It was also worth analysing how the embedding influenced the sensitivity of a silica FBG and comparing the result to the competing technology of POFBGs. The sample BP was chosen for comparison because it displayed the best performance and, hence, its strain, temperature, and humidity sensitivity figures could be reliably measured. They were compared with the characteristics measured for the reference silica FBG, which are collated in Table 6-8. Noteworthily, experimental characterisation of the reference SOFBG was important because the measured strain and temperature sensitivity values were visibly different that those usually given in the literature for SOFBGs at 1550 nm (see Table 6-8 for comparison). These discrepancies probably came from the fact that the SOFBGs used in this thesis were fabricated in the photosensitive boron-doped fibre PS1250/1550 from Fibercore, while the literature normally gives the figures for the standard silica fibre (SMF-28).

From Table 6-8, it can be seen that the strain sensitivity of the SOFBG decreased only marginally through embedding. The strain sensitivity of the sample BP was 92% of this of the reference grating. The latter figure was also similar to the strain sensitivity of POFBGs, which tend to be slightly higher. In turns, the temperature sensitivity increased over 12 times due to embedding compared to the reference FBG. Also, the temperature sensitivity of the sample BP was almost two times higher than this of the most sensitive POFBGs. With the majority of POFBGs displaying a temperature sensitivity of 20–30 pm/°C at 1550 nm (see Table 2-6), the embedded SOFBG featured about four times higher temperature sensitivity on average. Finally, the embedding allowed the SOFBG sense humidity as unembedded silica gratings are intrinsically insensitive to it. The humidity sensitivity figure of the sample BP was comparable with this of FBGs inscribed in humidity-sensitive PC (~7.2 pm/°C) and Cytop (10.3–14.7 pm/°C). The humidity sensitivity value of the embedded SOFBG was only clearly exceeded by POFBGs made of PMMA, which excel in humidity sensing (35.2 pm/°C; see Table 2-6).

Table 6-8. Comparison of the experimental values of strain, temperature, and humidity sensitivity of the reference silica FBG (unembedded), the sample BP (embedded), and the literature values for SOFBGs[a] and POFBGs[b] (all values at a spectral range of 1550 nm)

	Strain sensitivity (pm/με)	Temperature sensitivity (pm/°C)	Humidity sensitivity (pm/%RH)
Reference silica FBG (unembedded)	1.1272±0.0081[c]	8.4245±0.0075[c]	0
Sample BP (embedded)	1.037±0.021	103±14 at ~8%RH	13.8±1.1 at 23°C
Embedded/unembedded FBG	0.9200	12.2	–
SOFBGs[a] (literature)	~1.2	~13	–
POFBGs[b] (literature)	from 1.13 to 1.58	from -8.3 to -55	from ~0 to 35.2

[a]usual literature values, see Table 2-5

[b]various kinds of POFBGs, see Table 2-6

[c]error from a linear regression fit, CI=95%

6.2.5 Conclusions

In Section 6.2, an upgraded straining set-up and housing structure design were presented. The modifications to the set-up entailed the changes in its elements (a more robust translation stage and other parts, stronger screw connections), the variations in the clamping mechanism (use of the spacers between the clamps, accommodation of clamps to the asymmetries of the housing structures), the modification to the way of clamping (use of spacers between the sample and the clamps), and the use of indicators. The alterations to the design of the housing structure were made to the support legs in order to fit the clamps. Furthermore, the end pads for indicators were added to the housing structure.

Four types of gratings were embedded (coated point, coated scanned, bare point and bare scanned FBGs). During the straining trails, they were all found to be held firmly in place despite the unrelaxed stress on the fibre coming from embedding. Moreover, no change in the reflection spectra of the gratings were observed, aside from the slight change for the sample CS. It came from the sample being mounted (unstrained) on the strain test set-up for over two months. The response to both tensile and compressive strain displayed very good linearity. The strain sensitivity was different for coated and bare embedded gratings and amounted to 0.795-0.81 and 1.025-1.045 pm/με, respectively. The latter was ~91-93 % of this of the reference unembedded FBG (1.125 pm/με), while the former, ~71-72 %. This discrepancy for the coated embedded FBGs might have been coming from the primary coating shielding a part of

the stress and, hence, decreasing strain gauged by the grating. For both types of embedded gratings, some stress might have also been shielded by the glue and the housing structure itself. Furthermore, the Bragg peak was observed to shift over time despite keeping the strain constant. This was possibly coming from the asymmetries of the housing structure, making the strained region of the sample slightly bent, and the imperfections of the straining set-up. The sample also showed hysteretic behaviour, which was expected of plastic.

Section 6.2 also presented the results of the experiments testing the response of the embedded gratings to temperature and humidity. Two samples were tested: coated scanned (CS) and bare point (BP). The former sample showed some unfavourable characteristics from the point of view of the use in sensing. First, the reflection spectrum of the embedded FBG deviated from the idealised shape of a Bragg grating reflection spectrum during the experiments 1–5. This made the peak position difficult to track for the algorithm used in the HBM interrogator. The evolution of the spectrum was believed to be due to local uneven positive and negative chirps to the fibre due to the influence of glue or the fibre gradually detaching from its primary coating. To address this issue, the use of point rather than scanned FBGs was proposed. Secondly, the embedded fibre was observed to slide against its primary coating to relax stress. Initially, the fibre was relaxing compressive stress under which it had been put during the embedding, but later, the fibre was also seen to relax tensile stress. Using samples containing bare and not coated fibres was proposed to tackle this problem. Both the spectral evolution and fibre slippage might have been contributed to by the fibre having been left mounted on the strain test set-up for over two months during the strain experiment 6 and 7.

The sample BP, containing a bare point FBG, prove to yield much more favourable characteristics from the viewpoint of sensing applications. First, virtually no changes in the reflection spectrum were observed during the strain experiments and the temperature and humidity trial. Secondly, no fibre slippage was observed, leading to a stable sensor transfer function as opposed to the sample CS. The "bump" noticed in the peak in time data series at $t \approx 34$ days was supposedly coming from evaporation of the remains of liquid water. Hence, it should not be present when using the sensing patch in non-condensing ambient conditions, which is the usual requirement for relative humidity sensors. It must also be acknowledged that the sample BP was not left mounted on the strain test set-up for two months, which might have deteriorated the performance of the sample CS. Hence, the long-term behaviour of the sample BP cannot be commented on and may need further investigation.

The samples CS and BP displayed very similar temperature sensitivity values (respectively, 99.2 and 103 pm/°C). The difference between these figures was much smaller than between the values of strain sensitivity. Speculatively, this came from different nature of strain and temperature sensing. Both of them relied on the housing structure transferring the strain to the grating. However, in the case of the sensing patch gauging strain, the housing structure strained due to the external stress acting only on its outer surfaces. It was transferred to the fibre through the bulk of the housing, the glue, and the primary

coating (if present). All of these elements could shield some stress, resulting in its smaller extent acting on the embedded fibre. The primary coating was speculatively mostly responsible for stress shielding. In turns, in the case of the sensing patch gauging temperature, the housing structure expanded due to internal thermal stress in the entire structure and not the external stress acting on the outer surface of the sample. Moreover, the primary coating (if present) was also affected by the temperature change, which was expected to yield little stress due to CTE mismatch between the housing and the primary coating (if present). Hence, its presence did not decrease the temperature sensitivity as much in the case of the strain sensitivity.

When compared to unembedded SOBFG, the sample BP showed slightly smaller sensitivity (92%). It was comparable with this of POFBGs. Nevertheless, embedding yielded a tremendous increase in the temperature sensitivity: this of the sample BP was over 12 times higher compared to the unembedded FBG. The former was also at minimum two times and on average four times higher than the temperature sensitivity of POFBGs. Finally, embedding rendered the SOFBG humidity sensitive. The sensitivity figure was comparable with POFBGs made in PC and Cytop and was markedly exceeded by the sensitivity of PMMA gratings.

Chapter 7 Conclusions and future work

This chapter includes the discussion of the objectives of this thesis. Achievements relating to each of them are underlined, together with the encountered challenges. Further, the chapter discusses potential opportunities to extend the work presented in this thesis.

7.1 Discussion of the thesis objectives

The objective of this thesis was to combine the technology of silica and polymer FBGs with FDM 3D printing to achieve the following aims:

- optimising FDM 3D printing process in terms of printout transparency
- 3D printing solid-core and hollow-core polymer optical fibre preforms
- drawing the 3D-printed POF preforms into fibre
- embedding silica and polymer FBGs in 3D-printed protective housings to be used for strain sensing
- embedding multiple FBGs in 3D-printed sensing patches for temperature-compensated strain sensing
- embedding silica and polymer FBGs in 3D-printed sensing patches to enhance their temperature and humidity sensing capabilities.
- manufacturing moulds for fibre embedding by casting to integrate the fibre with the cast and to protect PMMA POFBGs from the influence of humidity during measurements

- demonstrating 3D-printed application-specific FBG holders that can facilitate FBG handling, with the application in ultrasound sensing
- demonstrating a tailor-made protective phase mask holder with an integrated feedback screen for FBG inscription.

The polymer optical fibre reported in this thesis (3D PC mPOF), manufactured by two-step drawing, exhibited multiple novelties. First, in was the first microstructured fibre drawn from a 3D-printed preform, only fibres of structure lying above the micrometric range having been reported previously. Secondly, this was the first fibre drawn from a 3D-printed preform to show single-mode operation, which was reported at both an operational wavelength of 870 and 1550 nm. Thirdly, 3D PC mPOF displayed the lowest attenuation of all fibres drawn from 3D printed preforms reported so far, including step-index fibres, with a lowest attenuation figure of ~0.27 dB/cm in a few spectral regions (780-785 nm, 820-825 nm, 953-956 nm, 1070-1090 nm). This prove enough for observation of FBG reflection, which is another novelty brought by this work since FBG inscription in a fibre drawing from a 3D-printed perform has not been reported so far. The gratings were inscribed using three different laser systems: a 325-nm continuous-wave helium-cadmium laser, a 248-nm nanosecond krypton-fluoride laser, and a 517-nm femtosecond laser. The latter was used in the plane-by-plane inscription technique, while the two former – in the phase mask method. The HeCd-inscribed grating displayed a temperature sensitivity of -21.3±1.9 pm/^{o}C, which is comparable with this reported for PC mPOFs drawn from drilled preforms.

A number of achievements resulted also from the work on FBG embedding and packaging. The strain sensitivity of the embedded gratings amounted to 92% of the unembedded one, proving only a minimal sensitivity decrease. As for temperature sensitivity, embedding was found to be capable of greatly increase its value. In the case of SOFBG, an increase of over 12 times was reported (from 8.4 to 103 pm/°C). The temperature sensitivity value was almost two times higher than this for the most temperature sensitive POFBGs and about four times higher than the average figure for POFBGs. In addition, embedding in the ABS housing structure allowed SOFBGs gauge humidity. Its sensitivity figure was measured as 13.8±1.1 pm/%RH. It was comparable with humidity sensitivity for POFBGs inscribed in PC and Cytop fibres and clearly smaller only from this for PMMA FBGs, featuring the highest sensitivity to humidity of all POFs.

In the area of manufacturing fibre preforms by means of FDM, five preforms in total were reported in the thesis. These were both solid-core and hollow-core, two designs having been proposed for the latter. The materials used for preform manufacturing were PMMA and polycarbonate.

Several challenges have been encountered in the course of this research. Some of them were successfully addressed, whereas potential solutions have been proposed to others. The first issue pertained to transparency of the printouts. The FDM technique is not well-suited for fabricating transparent structures due to air voids between threads of the printout being created during printing, which is inherent to this technique. Hence, the research started from ascertaining that the basic

requirement for any light transmitting element, good transparency, can be achieved by means of FDM. The amount of air trapped in the printout was minimised thanks to optimisation of printing settings: temperature, feed rate, printing speed, use of heated bed. The following guidelines for setting the printing parameters could be formulated as a result:

- print speed – should be as small as practically achievable (too small printing speeds result in a too long printing time)
- nozzle temperature – should be optimised for every material, both too low and too high values decreasing the printout transparency (PMMA: 280–290 °C, PC: 300 °C at minimum)
- infill – should be optimal, too small and too low values decrease the transparency
- nozzle diameter – should be as small as practically possible (nozzles of a diameter of less than 300 μm suffer from clogging); also, it should be matched to the layer thickness
- layer thickness – should be as small as practically possible (decreasing the layer thickness increases the printing time); it should also be matched to the layer thickness
- bed heating – should be set to maximum to avoid or minimise sample warping and detaching from the printing bed; ideally, a heated printing chamber should be used instead.

The use of low printing speeds and high nozzle temperatures allowed achieving the best transparency. However, in such conditions, water contained in the PMMA filament was observed to boil at the nozzle during printing, which was preventing from producing printouts of high transparency. This was caused by high water absorption of PMMA and was resolved by drying filament before printing or feeding it to the printer directly from an oven. Preforms fabricated using the optimised printing settings displayed some printing imperfections: warping and surface cracks. In general, they did not pose problems in fibre manufacturing. Warping mostly affected the lowermost part of the preform, which was sacrificed during fibre drawing. Surface cracks were not penetrating deep into the printouts, and their surface was machined down to fit with the draw tower oven. Both these issues could be potentially addressed by using a heated printing chamber, which is discussed below.

The solid-core PMMA preform deformed during annealing to the point that it was unsuitable for drawing. This could be caused by some amount of unreacted MMA monomers present in the commercial filament used to fabricate the preform. Alternatively, this could have resulted from still insufficient infill of the printout, i.e., too high amount of air voids. This could potentially be addressed by further optimisation of printing parameters, use of a heated printing chamber, or utilising tailor-made printing filaments of known composition, which is further discussed below.

The hollow-core PMMA preform was successfully drawn into cane, proving material properties being suitable for drawing. However, the structure of the preform deformed from the initial shape, which affected especially the shape and spacing between the cladding capillaries. As with the solid-core PMMA preform, this could have been contributed to by imperfect material properties or still not optimal

printing parameters. Moreover, this could be due to lack of perform pressurisation, which is normally used when drawing silica anti-resonant fibres.

The solid-core PC preform fabricated in this work was successfully drawn to fibre. Its transparency was found to be improved much during annealing with no observable shape deformation. Possibly, the commercial 3D printing filament used was better suited for annealing, or printing parameters were tailored better to the filament used so that the printout comprised fewer air voids. 3D PC mPOF was also found to display an extremely small linear coefficient of thermal expansion (2 order of magnitude lower than for bulk) and a small thermo-optic coefficient (~37% of bulk). Both of these are believed to be due to a very high anisotropy of molecular alignment in the fibre and possibly some stress-induced anisotropy, but further investigation is necessary to fully understand fibre behaviour.

The FDM technique was found to be capable of producing preforms that could be successfully drawn into fibres. Many characteristics of 3D PC mPOF were found much better than reported previously for 3D printed fibres and allowed its practical use. While some issues persist, and the manufacturing process would benefit from resolving them, this approach can yield successful fibre preforms even at its current stage of development. FDM can potentially allow fabricating preforms of very complex shapes, which would be very difficult to fabricate with other methods.

Regarding the work on FBG embedding and packaging, it was shown to provide fibre protection, which is important both for delicate POFs and for the exposed glass regions of SOFBGs. Moreover, it showed high capability of customisation, while not adversely influencing characteristics of the unembedded FBGs. The differences in the strain sensitivity reported for the early designs were found to be coming mostly from the imperfections of the strain testing set-up used, which were subsequently addressed. A repeatable response to strain was observed, yielding virtually identical strain sensitivity between the staining cycles. Moreover, a positive temperature sensitivity for the sensing patches containing POFBGs was observed as opposed to the usual negative value. Further optimisation of the embedding conditions could potentially allow the temperature sensitivity of the POFBGs to be close to zero and, hence, make them temperature-insensitivity, which would be of benefit in various applications. Some strain hysteresis of the packaged gratings was observed, which could be either coming from the housing structure itself or from embedding procedure. Further research would be required to optimise the behaviour of the sensing patches to benefit fully from the potential offered by embedding FBGs in structures printed with FDM. This was demonstrated by one of the manufactured patches, containing two SOFBGs. One was positioned so that it was exposed to strain, whereas the other one was away from the straining region and was used as high-sensitivity temperature compensation. Embedding ensured both gratings were well protected, while not impeding their exposure to measurands.

Finally, FDM 3D printing was successfully used to manufacture tailor-made parts used at different stages of the sensor manufacture and application process. First, this included manufacturing moulds for fibre embedding. This allowed to successfully integrate them with other materials than spooled FDM

filament described above. Secondly, various designs of POF holders were 3D printed, which were used in ultrasound photoacoustic sensing. Finally, FDM allowed fabricating a tailor-made protective phase mask holder with an integrated feedback screen for FBG inscription, which facilitated FBG inscription.

7.2 Future work

In the course of the work presented in this thesis, multiple directions of future research have been identified. Regarding the area of fibre preform manufacture, first, it is expected that printing with tailor-made filaments rather than commercially available ones would allow much better control of the printing process. The custom-made filaments could be fabricated of optical quality plastics, which could result in bringing the loss level of the fibre down. In addition, their chemical composition could be precisely controlled, which could allow avoiding undesired chemical species that can adversely interfere with the POF fabrication process, e.g., hindering preform annealing. Furthermore, some plastics are not available commercially in the form of the spooled FDM filaments as they do not look attractive for the mainstream of the 3D printing consumers, while they would be of much benefit to the optical fibres (e.g., Zeonex, Topas, Cytop). Moreover, filaments could be produced of plastic pairs of slightly different RIs and matched physical properties (e.g., the same polymer but doped and undoped). 3D printers of multiple printing heads, offering the possibility to mix multiple materials within a single printout, are available on the market. Having properly matched filaments mixed within one preform would facilitate drawing fibres of various designs (step-index, graded-index, highly birefringent, multiple-core fibres etc.).

Many potential benefits to printing preforms according to hollow-core designs have also been identified. FDM seems to offer much more flexibility in terms of complexity of the design that can be reproduced, having the potential to simplify the fabrication of, e.g., negative curvature fibres including multiple and oddly shaped nested element. This could be further facilitated by the use of sacrificial material, which could be dissolved away at a later stage. Such approach would allow the printing and drawing a completely solid preform. In this case, the whole drawing process can be expected to be much less complicated than when preform is pressurised for drawing.

Moreover, the two-step preform drawing process involves sleeving fibre canes in tubes, which could also be 3D printed. Their optical properties are normally of much less importance than in the case of the preform, so they can contain a broad range of non-transparent materials. This involves strips running along the sleeving tubes, which could be made of coloured plastics (or even those doped with ferromagnetic materials) to allow control of fibre twist.

Another potential innovation to the manufacturing process entails use of heated printing chambers. Preforms fabricated using a heated bed only suffered from warping and surface cracks. Both these issues come from high temperature differences between the parts of printout that have been manufactured (cool) and are just being manufactured (hot). This could possibly be resolved using a heated printing

chamber, which allows keeping the printout at high temperature (ideally just below its glass transition). This minimises the temperature differences within the printout during its fabrication and allows relaxation of the stress that has been induced. Moreover, a heated printing chamber could potentially permit to increase printing speed and thus decrease the fabrication time, which in this work has been reported to amount to ~323 h for the 3D PC mPOF preform. The low printing speed yielding a high increase in transparency of printout is believed to be due to higher amount of heat being transferred to the printout, allowing its adjacent threads melt together well. If the printout is kept hot during manufacture, it is expected that lower heat transfer from the nozzle would be sufficient, which would allow increasing printing speed. For example, if using the heated printing chamber permit increasing the printing speed from 5 to 40 mm/s without any loss in transparency, the resulting print time would fall from ~323 to ~40 h.

Multiple directions of future work regarding FBG embedding have also emerged. One of them relies on extending the number of measurands that the patches are able to sense. This can rely on, first, mixing materials of different properties (e.g., humidity absorbing and non-absorbing polymers) within one printout. Embedding multiple FBGs in such structure could allow decoupling multiple measurands, such as strain, temperature, and humidity. Secondly, increasing the number of physical quantities to be sensed may come from design. It can involve complex shapes, whose reproduction is one of the biggest advantages of FDM. Some of the examples entail membranes (to gauge pressure), beams (with multiple gratings positioned on and off the neutral axis to sense elongation and bend in different directions), and channels (to be able to use FBGs in microfluidics).

Moreover, some benefit to FBG embedding can come from broadening the range of materials available in 3D printing beyond spooled thermoplastics. Multiple 3D printers relying on tubed materials are commercially available, which could be used to print with, e.g., silicones, whose flexibility is beyond the reach of spooled filaments.

Finally, both preform manufacturing and fibre embedding can benefit from using moulds, which can be readily 3D printed. In the case of the former, preforms could be casted in moulds made of dissolvable materials, which could be dissolved away after the preform is ready. For the use in embedding, moulds can be easily customised to contain inlets for fibre deposition. This could also broaden the range of materials beyond spooled thermoplastics, including embedding fibres in casts made of thermoset plastics and silicones.

Chapter 8 Publications resulting from the work described in the thesis

8.1 Publications

1. **M. G. Zubel**, K. Sugden, D. J. Webb, D. Saez-Rodriguez, K. Nielsen, and O. Bang, "Embedding silica and polymer fibre Bragg gratings (FBG) in plastic 3D-printed sensing patches," in *Micro-Structured and Specialty Optical Fibres IV, SPIE Photonics Europe 2016,* (Brussels, Belgium, 2016).

2. A. Pospori, C. A. F. Marques, **M. G. Zubel**, D. Saez-Rodriguez, K. Nielsen, O. Bang, and D. J. Webb, "Annealing effects on strain and stress sensitivity of polymer optical fibre based sensors," in *Micro-Structured and Specialty Optical Fibres IV, SPIE Photonics Europe 2016,* (Brussels, Belgium, 2016).

3. C. Broadway, D. Gallego, A. Pospori, **M. Zubel**, D. J. Webb, K. Sugden, G. Carpintero, and H. Lamela, "Microstructured polymer optical fibre sensors for opto-acoustic endoscopy," in *Micro-Structured and Specialty Optical Fibres IV, SPIE Photonics Europe 2016,* (Brussels, Belgium, 2016).

4. **M. G. Zubel**, K. Sugden, D. Saez-Rodriguez, K. Nielsen, and O. Bang, "3-D printed sensing patches with embedded polymer optical fibre Bragg gratings," in *Sixth European Workshop on Optical Fibre Sensors (EWOFS'2016),* (Limerick, Ireland, 2016).

5. **M. G. Zubel**, A. Fasano, G. Woyessa, K. Sugden, H. K. Rasmussen, and O. Bang, "3D-printed PMMA preform for hollow-core POF drawing," in *25th International Conference on Plastic Optical Fibres, POF 2016,* P. Scully, K. Sugden, and D. J. Webb, eds. (Aston University, Birmingham, United Kingdom, 2017), pp. 295-300.

6. A. Lacraz, **M. Zubel**, G. Demirci, A. Theodosiou, K. Kalli, K. Sugden, and B. Gawdzik, "Embedding low loss polymer optical fibre Bragg gratings: Two different approaches," in *25th International Conference on Plastic Optical Fibres, POF 2016*, P. Scully, K. Sugden, and D. J. Webb, eds. (Aston University, Birmingham, United Kingdom, 2017), pp. 36-39.
7. C. Broadway, D. Gallego, A. Pospori, **M. Zubel**, D. J. Webb, K. Sugden, G. Carpintero, and H. Lamela, "A Compact Polymer Optical Fibre Ultrasound Detector," in *Photons Plus Ultrasound: Imaging and Sensing 2016, SPIE BiOS,* (San Francisco, California, United States, 2016).
8. C. Broadway, K. Kalli, A. Theodosiou, **M. Zubel**, K. Sugden, P. Mégret, and C. Caucheteur, "L-band CYTOP Bragg gratings for ultrasound sensing," in *Micro-Structured and Specialty Optical Fibres V, SPIE Photonics Europe,* (SPIE, Strasbourg, France, 2018), p. 9.
9. **M. G. Zubel**, A. Fasano, G. Woyessa, R. Min, A. Leal-Junior, A. Theodosiou, C. A. F. Marques, H. K. Rasmussen, O. Bang, B. Ortega, K. Kalli, A. Frizera-Neto, M. J. Pontes, and K. Sugden, "Bragg gratings inscribed in solid-core microstructured single-mode polymer optical fiber drawn from a 3D-printed polycarbonate preform," IEEE Sens J, (In press/early access, 18 June 2020).

8.2 Presentations

The presenter is underlined

1. **M. G. Zubel**, K. Sugden, D. J. Webb, D. Saez-Rodriguez, K. Nielsen, and O. Bang, "Embedding silica and polymer fibre Bragg gratings (FBG) in plastic 3D-printed sensing patches," in *Micro-Structured and Specialty Optical Fibres IV, SPIE Photonics Europe 2016,* (Brussels, Belgium, 2016).
   – *oral presentation*
2. A. Pospori, C. A. F. Marques, **M. G. Zubel**, D. Saez-Rodriguez, K. Nielsen, O. Bang, and D. J. Webb, "Annealing effects on strain and stress sensitivity of polymer optical fibre based sensors," in *Micro-Structured and Specialty Optical Fibres IV, SPIE Photonics Europe 2016*, (Brussels, Belgium, 2016).
3. C. Broadway, D. Gallego, A. Pospori, **M. Zubel**, D. J. Webb, K. Sugden, G. Carpintero, and H. Lamela, "Microstructured polymer optical fibre sensors for opto-acoustic endoscopy," in *Micro-Structured and Specialty Optical Fibres IV, SPIE Photonics Europe 2016*, (Brussels, Belgium, 2016).

4. **M. G. Zubel**, K. Sugden, D. Saez-Rodriguez, K. Nielsen, and O. Bang, "3-D printed sensing patches with embedded polymer optical fibre Bragg gratings," in *Sixth European Workshop on Optical Fibre Sensors (EWOFS'2016)*, (Limerick, Ireland, 2016).
   – *poster presentation*

5. **M. G. Zubel**, A. Fasano, G. Woyessa, K. Sugden, H. K. Rasmussen, and O. Bang, "3D-printed PMMA preform for hollow-core POF drawing," in *25th International Conference on Plastic Optical Fibres, POF 2016*, P. Scully, K. Sugden, and D. J. Webb, eds. (Aston University, Birmingham, United Kingdom, 2017).
   – *poster presentation*

6. A. Lacraz, **M. Zubel**, G. Demirci, A. Theodosiou, K. Kalli, K. Sugden, and B. Gawdzik, "Embedding low loss polymer optical fibre Bragg gratings: Two different approaches," in *25th International Conference on Plastic Optical Fibres, POF 2016*, P. Scully, K. Sugden, and D. J. Webb, eds. (Aston University, Birmingham, United Kingdom, 2017).

7. C. Broadway, D. Gallego, A. Pospori, **M. Zubel**, D. J. Webb, K. Sugden, G. Carpintero, and H. Lamela, "A Compact Polymer Optical Fibre Ultrasound Detector," in *Photons Plus Ultrasound: Imaging and Sensing 2016, SPIE BiOS*, (San Francisco, California, United States, 2016).

8. K. Sugden, **M. G. Zubel**, "3D printing for optical sensing applications", summer school presentation, *COST Action TD1001 - Novel and Reliable Optical Fibre Sensor Systems for Future Security and Safety Applications (OFSeSa)*, Limerick 2017.

9. C. Broadway, K. Kalli, A. Theodosiou, **M. Zubel**, K. Sugden, P. Mégret, and C. Caucheteur, "L-band CYTOP Bragg gratings for ultrasound sensing," *in Micro-Structured and Specialty Optical Fibres V, SPIE Photonics Europe*, (SPIE, Strasbourg, France, 2018).

References

1. S. H. Huang, P. Liu, A. Mokasdar, and L. Hou, "Additive manufacturing and its societal impact: A literature review," Int J Adv Manuf Technol **67**, 1191-1203 (2013).
2. T. J. Horn and O. L. A. Harrysson, "Overview of current additive manufacturing technologies and selected applications," Sci. Prog. **95**, 255-282 (2012).
3. Y. Tamura, H. Sakuma, K. Morita, M. Suzuki, Y. Yamamoto, K. Shimada, Y. Honma, K. Sohma, T. Fujii, and T. Hasegawa, "Lowest-Ever 0.1419-dB/km Loss Optical Fiber," in *Optical Fiber Communication Conference Postdeadline Papers*, OSA Technical Digest (online) (Optical Society of America, 2017), Th5D.1.
4. D. J. Webb, "Polymer Fibre Bragg Grating Sensors and their Applications," in *Optical Fiber Sensors: Advanced Techniques and Applications*, G. Rajan, ed. (CRC Press, United Kingdom, 2015), p. 576.
5. G. F. Fernando, D. J. Webb, and P. Ferdinand, "Optical-Fiber Sensors," MRS Bull **27**, 359-364 (2002).
6. M. G. Kuzyk, U. C. Paek, and C. W. Dirk, "Guest-host polymer fibers for nonlinear optics," Appl Phys Lett **59**, 902-904 (1991).
7. A. Tagaya, Y. Koike, T. Kinoshita, E. Nihei, T. Yamamoto, and K. Sasaki, "Polymer optical fiber amplifier," Appl Phys Lett **63**, 883-884 (1993).
8. F. Baldini and A. G. Mignani, "Optical-Fiber Medical Sensors," MRS Bull **27**, 383-387 (2002).
9. J. Zubia and J. Arrue, "Plastic Optical Fibers: An Introduction to Their Technological Processes and Applications," Opt Fiber Technol **7**, 101-140 (2001).
10. R. F. Cregan, B. J. Mangan, J. C. Knight, T. A. Birks, P. S. J. Russell, P. J. Roberts, and D. C. Allan, "Single-Mode Photonic Band Gap Guidance of Light in Air," Science **285**, 1537-1539 (1999).
11. P. S. J. Russell, "Photonic-Crystal Fibers," J Lightwave Technol **24**, 4729-4749 (2006).
12. J. C. Knight, T. A. Birks, R. F. Cregan, P. S. J. Russell, and P. D. d. Sandro, "Large mode area photonic crystal fibre," Electron Lett **34**, 1347-1348 (1998).
13. L. Michaille, C. R. Bennett, D. M. Taylor, T. J. Shepherd, J. Broeng, H. R. Simonsen, and A. Petersson, "Phase locking and supermode selection in multicore photonic crystal fiber lasers with a large doped area," Opt Lett **30**, 1668-1670 (2005).
14. J. Limpert, T. Schreiber, S. Nolte, H. Zellmer, and A. E. D. Q. G. Tünnermann, "All fiber chirped-pulse amplification system based on compression in air-guiding photonic bandgap fiber," in *Advanced Solid-State Photonics (TOPS)*, OSA Trends in Optics and Photonics (Optical Society of America, 2004), 9.
15. C. J. S. de Matos, J. R. Taylor, T. P. Hansen, K. P. Hansen, and J. Broeng, "All-fiber chirped pulse amplification using highly-dispersive air-core photonic bandgap fiber," Opt Express **11**, 2832-2837 (2003).
16. J. K. Ranka, R. S. Windeler, and A. J. Stentz, "Visible continuum generation in air–silica microstructure optical fibers with anomalous dispersion at 800 nm," Opt Lett **25**, 25-27 (2000).
17. J. M. Dudley, G. Genty, and S. Coen, "Supercontinuum generation in photonic crystal fiber," Reviews of Modern Physics **78**, 1135-1184 (2006).
18. J. E. Sharping, M. Fiorentino, P. Kumar, and R. S. Windeler, "Optical parametric oscillator based on four-wave mixing in microstructure fiber," Opt Lett **27**, 1675-1677 (2002).
19. J. Lasri, P. Devgan, T. Renyong, J. E. Sharping, and P. Kumar, "A microstructure-fiber-based 10-GHz synchronized tunable optical parametric oscillator in the 1550-nm regime," IEEE Photonic Tech L **15**, 1058-1060 (2003).

20. Y. Deng, Q. Lin, F. Lu, G. P. Agrawal, and W. H. Knox, "Broadly tunable femtosecond parametric oscillator using a photonic crystal fiber," Opt Lett **30**, 1234-1236 (2005).

21. P. J. Roberts, B. J. Mangan, H. Sabert, F. Couny, T. A. Birks, J. C. Knight, and P. S. J. Russell, "Control of dispersion in photonic crystal fibers," in *Fiber Based Dispersion Compensation* (Springer New York, New York, NY, 2007), pp. 313-339.

22. W. H. Reeves, J. C. Knight, P. S. J. Russell, and P. J. Roberts, "Demonstration of ultra-flattened dispersion in photonic crystal fibers," Opt Express **10**, 609-613 (2002).

23. F. Poletti, "Advances in Hollow Optical Fiber Technologies and Applications," in *2019 Optical Fiber Communications Conference and Exhibition (OFC)*, 2019), 1-46.

24. F. Poletti, N. Petrovich Marco, and J. Richardson David, "Hollow-core photonic bandgap fibers: technology and applications," in *Nanophotonics*, (2013), p. 315.

25. F. Zolla, G. Renversez, A. Nicolet, B. Kuhlmey, S. Guenneau, D. Felbacq, A. Argyros, and S. Leon-Saval, *Foundations of Photonic Crystal Fibres* (IMPERIAL COLLEGE PRESS, 2011), p. 552.

26. M. C. J. Large, L. Poladian, G. W. Barton, and M. A. Van Eijkelenborg, *Microstructured polymer optical fibres* (Springer US, 2008).

27. C. Wei, R. Joseph Weiblen, C. R. Menyuk, and J. Hu, "Negative curvature fibers," Adv. Opt. Photon. **9**, 504-561 (2017).

28. T. D. Bradley, J. R. Hayes, Y. Chen, G. T. Jasion, S. R. Sandoghchi, R. Slavik, E. N. Fokoua, S. Bawn, H. Sakr, I. A. Davidson, A. Taranta, J. P. Thomas, M. N. Petrovich, D. J. Richardson, and F. Poletti, "Record Low-Loss 1.3dB/km Data Transmitting Antiresonant Hollow Core Fibre," in *2018 European Conference on Optical Communication (ECOC)*, 2018), 1-3.

29. M. A. v. Eijkelenborg, M. C. J. Large, A. Argyros, J. Zagari, S. Manos, N. A. Issa, I. Bassett, S. Fleming, R. C. McPhedran, C. M. d. Sterke, and N. A. P. Nicorovici, "Microstructured polymer optical fibre," Opt Express **9**, 319-327 (2001).

30. K. Cook, J. Canning, S. Leon-Saval, Z. Reid, M. A. Hossain, J. E. Comatti, Y. Luo, and G. D. Peng, "Air-structured optical fiber drawn from a 3D-printed preform," Opt Lett **40**, 3966-3969 (2015).

31. K. Cook, G. Balle, J. Canning, L. Chartier, T. Athanaze, M. A. Hossain, C. Y. Han, J. E. Comatti, Y. H. Luo, and G. D. Peng, "Step-index optical fiber drawn from 3D printed preforms," Opt Lett **41**, 4554-4557 (2016).

32. Q. K. Zhao, F. J. Tian, X. H. Yang, S. Li, J. Z. Zhang, X. L. Zhu, J. Yang, Z. H. Liu, Y. Zhang, T. T. Yuan, and L. B. Yuan, "Optical fibers with special shaped cores drawn from 3D printed preforms," Optik **133**, 60-65 (2017).

33. T. H. R. Marques, B. M. Lima, J. H. Osorio, L. E. da Silva, and C. M. B. Cordeiro, "3D Printed Microstructured Optical Fibers," in *2017 SBMO/IEEE MTT-S International Microwave and Optoelectronics Conference (Imoc)*, (2017).

34. W. Talataisong, R. Ismaeel, T. H. R. Marques, S. A. Mousavi, M. Beresna, M. A. Gouveia, S. R. Sandoghchi, T. Lee, C. M. B. Cordeiro, and G. Brambilla, "Mid-IR Hollow-core microstructured fiber drawn from a 3D printed PETG preform," Sci Rep-Uk **8**(2018).

35. K. O. Hill, Y. Fujii, D. C. Johnson, and B. S. Kawasaki, "Photosensitivity in optical fiber waveguides: Application to reflection filter fabrication," Appl Phys Lett **32**, 647-649 (1978).

36. G. Meltz, W. W. Morey, and W. H. Glenn, "Formation of Bragg gratings in optical fibers by a transverse holographic method," Opt Lett **14**, 823-825 (1989).

37. F. Ouellette, "All-fiber filter for efficient dispersion compensation," Opt Lett **16**, 303-305 (1991).

38. R. M. Jopson, A. H. Gnauck, and R. M. Derosier, "Compensation of fibre chromatic dispersion by spectral inversion," Electron Lett **29**, 576-578 (1993).

39. H. G. Winful, "Pulse compression in optical fiber filters," Appl Phys Lett **46**, 527-529 (1985).

40. J. E. Roman and K. A. Winick, "Waveguide grating filters for dispersion compensation and pulse compression," IEEE J Quantum Elect **29**, 975-982 (1993).

41. F. Ouellette, "Limits of chirped pulse compression with an unchirped Bragg grating filter," Appl Optics **29**, 4826-4829 (1990).

42. I. M. I. Habbab, A. A. M. Saleh, N. J. Frigo, and G. E. Bodeep, "Noise reduction in long-haul lightwave all-amplifier systems," J Lightwave Technol **10**, 1281-1289 (1992).

43. M. C. Farries, C. M. Ragdale, and D. C. J. Reid, "Broadband chirped fibre Bragg filters for pump rejection and recycling in erbium doped fibre amplifiers," Electron Lett **28**, 487-489 (1992).

44. R. Kashyap, R. Wyatt, and R. J. Campbell, "Wideband gain flattened erbium fibre amplifier using a photosensitive fibre blazed grating," Electron Lett **29**, 154-156 (1993).

45. R. P. Davey, R. P. E. Fleming, K. Smith, R. Kashyap, and J. R. Armitage, "Mode-locked erbium fibre laser with wavelength selection by means of fibre Bragg grating reflector," Electron Lett **27**, 2087-2088 (1991).

46. G. A. Ball and W. W. Morey, "Efficient integrated Nd/sup 3+/ fiber laser," IEEE Photonic Tech L **3**, 1077-1078 (1991).

47. V. Lecoeuche, P. Niay, M. Douay, P. Bernage, S. Randoux, and J. Zemmouri, "Bragg grating based Brillouin fibre laser," Opt Commun **177**, 303-306 (2000).

48. H. Y. Liu, H. B. Liu, G. D. Peng, and P. L. Chu, "Polymer optical fibre Bragg gratings based fibre laser," Opt Commun **266**, 132-135 (2006).

49. I. M. Jauncey, L. Reekie, R. J. Mears, D. N. Payne, C. J. Rowe, D. C. J. Reid, I. Bennion, and C. Edge, "Narrow-linewidth fibre laser with integral fibre grating," Electron Lett **22**, 987-988 (1986).

50. T. A. Strasser, P. J. Chandonnet, J. DeMarco, C. E. Soccolich, J. R. Pedrazzani, D. J. DiGiovanni, M. J. Andrejco, and D. S. Shenk, "UV-induced Fiber Grating OADM Devices for Efficient Bandwidth Utilization," in *Optical Fiber Communication Conference*, 1996 OSA Technical Digest Series (Optical Society of America, 1996), PD8.

51. P. Hee Su, Y. Seok Hyun, H. In Kag, L. Sang Bae, and K. Byoung Yoon, "All-fiber add-drop wavelength-division multiplexer based on intermodal coupling," IEEE Photonic Tech L **13**, 460-462 (2001).

52. C. Headley and G. P. Agrawal, *Raman Amplification in Fiber Optical Communication Systems* (Academic Press, Burlington, 2005).

53. S.-K. Liaw, L. Dou, and A. Xu, "Fiber-bragg-grating-based dispersion-compensated and gain-flattened raman fiber amplifier," Opt Express **15**, 12356-12361 (2007).

54. A. Ukil, H. Braendle, and P. Krippner, "Distributed temperature sensing: Review of technology and applications," IEEE Sens J **12**, 885-892 (2012).

55. H.-F. Pei, J. Teng, J.-H. Yin, and R. Chen, "A review of previous studies on the applications of optical fiber sensors in geotechnical health monitoring," Measurement **58**, 207-214 (2014).

56. A. H. Hartog, "Progress in distributed fiber optic temperature sensing," in 2002), 43-52.

57. A. Cusano, A. Cutolo, and J. Albert, *Fiber Bragg grating sensors: research advancements, industrial applications and market exploitation* (Bentham Science Publishers Ltd., Saif Zone, Sharjah, United Arab Emirates, 2011).

58. Y.-J. Rao, "In-fibre Bragg grating sensors," Meas. Sci. Technol. **8**, 355-375 (1997).

59. A. D. Kersey, M. A. Davis, H. J. Patrick, M. LeBlanc, K. P. Koo, C. G. Askins, M. A. Putnam, and E. J. Friebele, "Fiber grating sensors," J Lightwave Technol **15**, 1442-1463 (1997).

60. I. J. Read and P. D. Foote, "Sea and flight trials of optical fibre Bragg grating strain sensing systems," Smart Materials and Structures **10**, 1085-1094 (2001).

61. V. M. Murukeshan, P. Y. Chan, L. S. Ong, and L. K. Seah, "Cure monitoring of smart composites using Fiber Bragg Grating based embedded sensors," Sensors and Actuators A: Physical **79**, 153-161 (2000).

62. Y. Zhao, K. Chen, and J. Yang, "Novel target type flowmeter based on a differential fiber Bragg grating sensor," Measurement **38**, 230-235 (2005).

63. S. Takashima, H. Asanuma, and H. Niitsuma, "A water flowmeter using dual fiber Bragg grating sensors and cross-correlation technique," Sensors and Actuators A: Physical **116**, 66-74 (2004).

64. H. Y. Tam, S. Y. Liu, B. O. Guan, W. H. Chung, T. H. T. Chan, and L. K. Cheng, *Fiber Bragg grating sensors for structural and railway applications*, Photonics Asia (SPIE, 2005), Vol. 5634.

65. I. Read, P. Foote, and S. Murray, "Optical fibre acoustic emission sensor for damage detection in carbon fibre composite structures," Meas. Sci. Technol. **13**, N5-N9 (2001).

66. T. Yamate, *Thermally insensitive pressure measurements up to 300 degree C using fiber Bragg gratings written onto side hole single mode fiber*, Fourteenth International Conference on Optical Fiber Sensors (SPIE, 2000), Vol. 4185.

67. Tomlinso.Wj, I. P. Kaminow, Chandros.Ea, R. L. Fork, and W. T. Silfvast, "Photoinduced Refractive Index Increase in Poly(Methylmethacrylate) and Its Applications," Appl Phys Lett **16**, 486-& (1970).

68. Z. Xiong, G. D. Peng, B. Wu, and P. L. Chu, "Highly tunable Bragg gratings in single-mode polymer optical fibers," IEEE Photonic Tech L **11**, 352-354 (1999).

69. H. Dobb, D. J. Webb, K. Kalli, A. Argyros, M. C. J. Large, and M. a. van Eijkelenborg, "Continuous wave ultraviolet light-induced fiber Bragg gratings in few- and single-mode microstructured polymer optical fibers," Opt Lett **30**, 3296-3298 (2005).

70. G. Woyessa, J. K. M. Pedersen, A. Fasano, K. Nielsen, C. Markos, H. K. Rasmussen, and O. Bang, "Zeonex-PMMA microstructured polymer optical FBGs for simultaneous humidity and temperature sensing," Opt Lett **42**, 1161-1164 (2017).

71. Z. Zhang, P. Zhao, P. Lin, and F. Sun, "Thermo-optic coefficients of polymers for optical waveguide applications," Polymer **47**, 4893-4896 (2006).

72. R. M. Waxler, "The effect of temperature and pressure on the refractive index of some oxide glasses," J. Res. Nat. Bur. Stand. Sect. A **77**, 755-763 (1973).

73. A. Pospori, C. A. F. Marques, D. Sáez-Rodríguez, K. Nielsen, O. Bang, and D. J. Webb, "Thermal and chemical treatment of polymer optical fiber Bragg grating sensors for enhanced mechanical sensitivity," Opt Fiber Technol **36**, 68-74 (2017).

74. C. C. Ye, J. M. Dulieu-Barton, D. J. Webb, C. Zhang, G. D. Peng, A. R. Chambers, F. J. Lennard, and D. D. Eastop, "Applications of polymer optical fibre grating sensors to condition monitoring of textiles," in *20th International Conference on Optical Fibre Sensors*, 2009),

75. C. Broadway, D. Gallego, A. Pospori, M. Zubel, D. J. Webb, K. Sugden, G. Carpintero, and H. Lamela, "Microstructured polymer optical fibre sensors for opto-acoustic endoscopy," in *Micro-Structured and Specialty Optical Fibres IV, SPIE Photonics Europe 2016*, (Brussels, Belgium, 2016).

76. M. F. M. Aressy, "Drawing and mechanical properties of plastic optical fibres," MPhil (University of Birmingham, Department of Metallurgy and Materials, School of Engineering, Birmingham, 2007).

77. G. Woyessa, K. Nielsen, A. Stefani, C. Markos, and O. Bang, "Temperature insensitive hysteresis free highly sensitive polymer optical fiber Bragg grating humidity sensor," Opt Express **24**, 1206-1213 (2016).

78. A. Pospori, C. A. F. Marques, G. Sagias, H. Lamela-Rivera, and D. J. Webb, "Novel thermal annealing methodology for permanent tuning polymer optical fiber Bragg gratings to longer wavelengths," Opt Express **26**, 1411-1421 (2018).

79. C. A. F. Marques, G. D. Peng, and D. J. Webb, "Highly sensitive liquid level monitoring system utilizing polymer fiber Bragg gratings," Opt Express **23**, 6058-6072 (2015).

80. S. L. Philip, C. Francois, W. Ying Ying, V. W. Natalie, P. J. Roberts, and B. Fetah, "Double photonic bandgap hollow-core photonic crystal fiber," Opt. Express **17**, 16238--16243.

81. F. Poletti and D. J. Richardson, "Hollow-core photonic bandgap fibers based on a square lattice cladding," Opt Lett **32**, 2282-2284 (2007).

82. L. Dong, B. K. Thomas, S. Suzuki, and L. Fu, "Extending transmission bandwidth of air-core photonic bandgap fibers," Opt Fiber Technol **16**, 442-448 (2010).

83. F. Poletti, "Hollow core fiber with an octave spanning bandgap," Opt Lett **35**, 2837-2839 (2010).

84. F. Kotz, P. Risch, D. Helmer, and B. E. Rapp, "High-Performance Materials for 3D Printing in Chemical Synthesis Applications," Advanced Materials **31**, 1805982 (2019).

85. J. Klein, M. Stern, G. Franchin, M. Kayser, C. Inamura, S. Dave, J. C. Weaver, P. Houk, P. Colombo, M. Yang, and N. Oxman, "Additive Manufacturing of Optically Transparent Glass," 3D Printing and Additive Manufacturing **2**, 92-105 (2015).

86. J. Luo, H. Pan, and E. C. Kinzel, "Additive Manufacturing of Glass," Journal of Manufacturing Science and Engineering **136**(2014).

87. D. T. Nguyen, C. Meyers, T. D. Yee, N. A. Dudukovic, J. F. Destino, C. Zhu, E. B. Duoss, T. F. Baumann, T. Suratwala, J. E. Smay, and R. Dylla-Spears, "3D-Printed Transparent Glass," Advanced Materials **29**, 1701181 (2017).

88. I. Cooperstein, E. Shukrun, O. Press, A. Kamyshny, and S. Magdassi, "Additive Manufacturing of Transparent Silica Glass from Solutions," ACS Applied Materials & Interfaces **10**, 18879-18885 (2018).

89. F. Kotz, K. Arnold, W. Bauer, D. Schild, N. Keller, K. Sachsenheimer, T. M. Nargang, C. Richter, D. Helmer, and B. E. Rapp, "Three-dimensional printing of transparent fused silica glass," Nature **544**, 337-339 (2017).

90. F. Kotz, K. Plewa, W. Bauer, N. Schneider, N. Keller, T. Nargang, D. Helmer, K. Sachsenheimer, M. Schäfer, M. Worgull, C. Greiner, C. Richter, and B. E. Rapp, "Liquid Glass: A Facile Soft Replication Method for Structuring Glass," Advanced Materials **28**, 4646-4650 (2016).

91. "Glassomer", retrieved 16 Apr 2020, 2020, http://glassomer.com.

92. A. W. Snyder and J. Love, *Optical waveguide theory* (Springer Science & Business Media, 2012).

93. G. P. Agrawal, *Fiber-optic communication systems* (John Wiley & Sons, 2012), Vol. 222.

94. K. Okamoto, *Fundamentals of optical waveguides* (Academic press, 2006).

95. COMSOL v. 4.3, COMSOL AB, Stockholm, Sweden, www.comsol.com.

96. J. Wilson and J. F. Hawkes, "Optoelectronics-an introduction," Optoelectronics-An introduction (2nd edition), by J. Wilson and JFB Hawkes. Englewood Cliffs, NJ, Prentice Hall, 1989, 483 p. (1989).

97. A. Theodosiou, A. Lacraz, A. Stassis, C. Koutsides, M. Komodromos, and K. Kalli, "Plane-by-Plane Femtosecond Laser Inscription Method for Single-Peak Bragg Gratings in Multimode CYTOP Polymer Optical Fiber," J Lightwave Technol **35**, 5404-5410 (2017).

98. L. R. G. Treloar, *The physics of rubber elasticity* (Oxford University Press, USA, 1975).

99. R. M. Waxler, D. Horowitz, and A. Feldman, "Optical and physical parameters of Plexiglas 55 and Lexan," Appl Optics **18**, 101-104 (1979).

100. I. M. Ward and J. Sweeney, *Mechanical properties of solid polymers* (John Wiley & Sons, 2012).

101. G. W. Kaye and T. H. Laby, *Tables of physical and chemical constants*, 16 ed. (Longman, 1995).

102. N. Bansal and R. Doremus, "Handbook of glass properties," (Academic Press, Orlando, FL, 1986).

103. J. Matsuda, "Studies on the Young's modulus of silicate glass as a function of temperature," (1960).

104. A. Stefani, S. Andresen, W. Yuan, and O. Bang, "Dynamic Characterization of Polymer Optical Fibers," IEEE Sens J **12**, 3047-3053 (2012).

105. G. Woyessa, A. Fasano, C. Markos, H. K. Rasmussen, and O. Bang, "Low Loss Polycarbonate Polymer Optical Fiber for High Temperature FBG Humidity Sensing," IEEE Photonic Tech L **29**, 575-578 (2017).

106. K. E. Carroll, C. Zhang, D. J. Webb, K. Kalli, A. Argyros, and M. C. Large, "Thermal response of Bragg gratings in PMMA microstructured optical fibers.," Opt Express **15**, 8844-8850 (2007).

107. A. Fasano, G. Woyessa, P. Stajanca, C. Markos, A. Stefani, K. Nielsen, H. K. Rasmussen, K. Krebber, and O. Bang, "Fabrication and characterization of polycarbonate microstructured polymer optical fibers for high-temperature-resistant fiber Bragg grating strain sensors," Opt Mater Express **6**, 649-659 (2016).

108. K. Makino, T. Kado, A. Inoue, and Y. Koike, "Low loss graded index polymer optical fiber with high stability under damp heat conditions," Opt Express **20**, 12893-12898 (2012).

109. I. P. Johnson, D. J. Webb, K. Kalli, W. Yuan, A. Stefani, K. Nielsen, H. K. Rasmussenc, and O. Bang, "Polymer PCF Bragg grating sensors based on poly(methyl methacrylate) and TOPAS cyclic olefin copolymer," in *Optical Sensors 2011; and Photonic Crystal Fibers V*, 2011),

110. "Materials Data Book" (Cambridge University Engineering Department 2003), retrieved 11 Jul 2018, http://www-mdp.eng.cam.ac.uk/web/library/enginfo/cueddatabooks/materials.pdf.

111. H. K. Rasmussen, A. Fasano, P. Stajanca, G. Woyessa, M. Schukar, and O. Bang, "Mechanical characterization of drawn Zeonex, Topas, polycarbonate and PMMA microstructured polymer optical fibres," Opt Mater Express **8**, 3600-3614 (2018).

112. A. Leal, A. Frizera, M. J. Pontes, A. Fasano, G. Woyessa, O. Bang, and C. A. F. Marques, "Dynamic mechanical characterization with respect to temperature, humidity, frequency and strain in mPOFs made of different materials," Opt Mater Express **8**, 804-815 (2018).

113. "Technical data sheet of TOPAS grade 8007S-04", retrieved 24 Sep 2019, https://topas.com/sites/default/files/TDS_8007S_04_e.pdf.

114. W. Yuan, L. Khan, D. J. Webb, K. Kalli, H. K. Rasmussen, A. Stefani, and O. Bang, "Humidity insensitive TOPAS polymer fiber Bragg grating sensor," Opt Express **19**, 19731-19739 (2011).

115. "Technical data sheet of TOPAS grade 5013S-04", retrieved 24 Sep 2019, https://topas.com/sites/default/files/TDS_5013S_04_e.pdf.

116. C. Markos, A. Stefani, K. Nielsen, H. K. Rasmussen, W. Yuan, and O. Bang, "High-Tg TOPAS microstructured polymer optical fiber for fiber Bragg grating strain sensing at 110 degrees," Opt Express **21**, 4758-4765 (2013).

117. G. Woyessa, A. Fasano, A. Stefani, C. Markos, K. Nielsen, H. K. Rasmussen, and O. Bang, "Single mode step-index polymer optical fiber for humidity insensitive high temperature fiber Bragg grating sensors," Opt Express **24**, 1253-1260 (2016).

118. "Technical data sheet of Cytop", retrieved 29 Sep 2019, http://www.bellexinternational.com/products/cytop/pdf/cytop-catalog.pdf.

119. R. Min, B. Ortega, A. Leal-Junior, and C. Marques, "Fabrication and Characterization of Bragg Grating in CYTOP POF at 600-nm Wavelength," IEEE Sensors Letters **2**, 1-4 (2018).

120. C. Broadway, K. Kalli, A. Theodosiou, M. Zubel, K. Sugden, P. Mégret, and C. Caucheteur, "L-band CYTOP Bragg gratings for ultrasound sensing," in *Micro-Structured and Specialty Optical Fibres V, SPIE Photonics Europe*, (SPIE, Strasbourg, France, 2018), p. 9.

121. "Technical data sheet of Zeonex", retrieved 29 Sep 2019, http://www.zeon.co.jp/content/200323391.pdf.

122. G. Woyessa, A. Fasano, C. Markos, A. Stefani, H. K. Rasmussen, and O. Bang, "Zeonex microstructured polymer optical fiber: fabrication friendly fibers for high temperature and humidity insensitive Bragg grating sensing," Opt Mater Express **7**, 286-295 (2017).

123. C. R. Kurkjian, J. T. Krause, and M. J. Matthewson, "Strength and fatigue of silica optical fibers," J Lightwave Technol **7**, 1360-1370 (1989).

124. P. M. Nellen, P. Mauron, A. Frank, U. Sennhauser, K. Bohnert, P. Pequignot, P. Bodor, and H. Brändle, "Reliability of fiber Bragg grating based sensors for downhole applications," Sens Actuators A Phys **103**, 364-376 (2003).

125. C. Jiang, M. G. Kuzyk, J. L. Ding, W. E. Johns, and D. J. Welker, "Fabrication and mechanical behavior of dye-doped polymer optical fiber," Journal of Applied Physics **92**, 04-Dec (2002).

126. D. J. Webb and K. Kalli, "Polymer Fiber Bragg Gratings," in *Fiber Bragg grating sensors: recent advancements, industrial applications and market exploitation*, A. Cusano, A. Cutolo, and J. Albert, eds. (Bentham Science Publishers Ltd., Saif Zone, Sharjah, United Arab Emirates, 2011).

127. J. Yu, X. Tao, and H. Tam, "Trans-4-stilbenemethanol-doped photosensitive polymer fibers and gratings," Opt Lett **29**, 156--158 (2004).

128. M. G. Kuzyk, U. C. Paek, and C. W. Dirk, "Guest-Host Polymer Fibers for Nonlinear Optics," Appl Phys Lett **59**, 902-904 (1991).

129. G. Emiliyanov, J. B. Jensen, O. Bang, P. E. Hoiby, L. H. Pedersen, E. M. Kjær, and L. Lindvold, "Erratum: Localized biosensing with Topas microstructured polymer optical fiber (Optics Letters (2007) 32 (460))," Opt Lett **32**, 1059 (2007).

130. A. Tagaya, Y. Koike, T. Kinoshita, E. Nihei, T. Yamamoto, and K. Sasaki, "Polymer Optical-Fiber Amplifier," Appl Phys Lett **63**, 883-884 (1993).

131. S. Shirouzu, H. Shikuma, N. Senda, M. Yoshida, S. Sakamoto, K. Shigematsu, T. Nakagawa, and S. Tagami, "Stress-Optical Coefficients in Polycarbonates," Jpn J Appl Phys **29**, 898-901 (1990).

132. Y. Koike and M. Asai, "The future of plastic optical fiber," Npg Asia Mater **1**, 22-28 (2009).

133. M. D. Ediger, C. A. Angell, and S. R. Nagel, "Supercooled Liquids and Glasses," The Journal of Physical Chemistry **100**, 13200-13212 (1996).

134. P. Stajanca, O. Cetinkaya, M. Schukar, P. Mergo, D. J. Webb, and K. Krebber, "Molecular alignment relaxation in polymer optical fibers for sensing applications," Opt Fiber Technol **28**, 11-17 (2016).

135. J. J. Tribone, J. O'reilly, and J. Greener, "Analysis of enthalpy relaxation in poly (methyl methacrylate): effects of tacticity, deuteration, and thermal history," Macromolecules **19**, 1732-1739 (1986).

136. J. T. Bendler, *Handbook of polycarbonate science and technology* (CRC press, 2000).

137. K. Vedam and P. Limsuwan, "Piezo- and elasto-optic properties of liquids under high pressure. II. Refractive index vs density," The Journal of Chemical Physics **69**, 4772-4778 (1978).

138. H. Mueller, "Theory of Photoelasticity in Amorphous Solids," Physics **6**, 179-184 (1935).

139. J. M. Jewell, "Thermooptic Coefficients of Some Standard Reference Material Glasses," Journal of the American Ceramic Society **74**, 1689-1691 (1991).

140. M. B. J. Diemeer, "Polymeric thermo-optic space switches for optical communications," Optical Materials **9**, 192-200 (1998).

141. P. A. Soave, R. A. F. Dau, M. R. Becker, M. B. Pereira, and F. Horowitz, "Refractive index control in bicomponent polymer films for integrated thermo-optical applications," Opt Eng **48**, 1-6 (2009).

142. M. R. Saleem, S. Honkanen, and J. Turunen, "Thermo-optic coefficient of Ormocomp and comparison of polymer materials in athermal replicated subwavelength resonant waveguide gratings," Opt Commun **288**, 56-65 (2013).

143. "MATWEB: Overview of materials for Acrylic, Extruded", retrieved 25 Sep 2019, http://www.matweb.com/search/datasheet.aspx?matguid=632572aeef2a4224b5ac8fbd4f1b6f77.

144. G. Khanarian, "Optical properties of cyclic olefin copolymers," Opt Eng **40**, 1024-1029 (2001).

145. Y. Sato, Y. Yamasaki, S. Takishima, and H. Masuoka, "Precise measurement of the PVT of polypropylene and polycarbonate up to 330°C and 200 MPa," J. Appl. Polym. Sci. **66**, 141-150 (1997).

146. "MATWEB: Overview of materials for Polycarbonate, Extruded", retrieved 4 Apr 2019, http://matweb.com/search/DataSheet.aspx?MatGUID=501acbb63cbc4f748faa7490884cdbca.

147. G. Beadie, M. Brindza, R. A. Flynn, A. Rosenberg, and J. S. Shirk, "Refractive index measurements of poly(methyl methacrylate) (PMMA) from 0.4–1.6 μm," Appl Optics **54**, F139-F143 (2015).

148. L. Prod'homme, "A new approach to the thermal change in the refractive index of glasses," Phys. Chem. Glasses **1**, 119-122 (1960).

149. G. N. Ramachandran, in *Progress in crystal physics*, R. S. Krishnan, ed. (Interscience Publishers, 1960), pp. 139-167.

150. R. Waxler and C. Weir, "Effect of hydrostatic pressure on the refractive indices of some solids," Precision Meas. and Calibration **10**, 61-69 (1965).

151. I. M. Ward, *Structure and properties of oriented polymers* (Springer Science & Business Media, 1975).

152. I. M. Ward, *Structure and properties of oriented polymers* (Springer Science & Business Media, 1997).

153. P. Ji, A. D. Q. Li, and G.-D. Peng, *Transverse birefringence in polymer optical fiber introduced in drawing process*, Optical Science and Technology, SPIE's 48th Annual Meeting (SPIE, 2003), Vol. 5212.

154. H. Wright, C. S. N. Faraday, E. F. T. White, and L. R. G. Treloar, "The elastic constants of oriented glassy polymers," J Phys D **4**, 2002-2014 (1971).

155. W. Zhang and D. J. Webb, "Factors influencing the temperature sensitivity of PMMA based optical fiber Bragg gratings," in *Micro-structured and Specialty Optical Fibres III, SPIE Photonics Europe*, (SPIE, Brussels, Belgium, 2014).

156. I. M. Ward, "The preparation, structure and properties of ultra-high modulus flexible polymers," Advances in Polymer Science, 1-70 (1985).

157. V. B. Gupta, "Nature of the Crystalline and Amorphous Phases in Oriented Polymers and Their Influence on Physical Properties," in *Oriented Polymer Materials*, S. Fakirov, ed. (WILEY-VCH Verlag, 2008).

158. R. Schledjewski and K. Friedrich, "Orientation Effects on the Thermal, Mechanical and Tribological Performance of Neat, Reinforced and Blended Liquid Crystalline Polymers," in *Oriented Polymer Materials*, S. Fakirov, ed. (WILEY-VCH Verlag, 2008).

159. L.-H. Wang, C. L. Choy, and R. S. Porter, "Thermal expansion of oriented poly(methyl methacrylate)," Journal of Polymer Science: Polymer Physics Edition **21**, 657-665 (1983).

160. W. Retting, "Generation and relaxation of the molecular orientation during hot-stretching of amorphous thermoplastics," Colloid and Polymer Science **257**, 689-710 (1979).

161. W. Retting, "The Effect of Molecular Orientation on the Mechanical Properties of Rubber-Modified-Polystyrene," (1978).

162. L.-H. Wang, C. L. Choy, and R. S. Porter, "Thermal expansion of ultradrawn polystyrene," Journal of Polymer Science: Polymer Physics Edition **20**, 633-640 (1982).

163. J. Hennig, "Anisotropy and structure in uniaxially stretched amorphous high polymers," Journal of Polymer Science Part C: Polymer Symposia **16**, 2751-2761 (1967).

164. J. Hennig, "Anisotropie der linearen Kompressibilität in einachsig verstreckten amorphen Hochpolymeren," Kolloid-Zeitschrift und Zeitschrift für Polymere **202**, 127-132 (1965).

165. E. Hecht, *Optics,* 5th global ed. (Pearson Education, 2017).

166. S. Ramo, J. R. Whinnery, and T. Van Duzer, *Fields and waves in communication electronics* (John Wiley & Sons, 1994).

167. M. J. Adams, *An introduction to optical waveguides* (Wiley New York, 1981), Vol. 14.

168. Y. Terui and S. Ando, "Coefficients of molecular packing and intrinsic birefringence of aromatic polyimides estimated using refractive indices and molecular polarizabilities," Journal of Polymer Science Part B: Polymer Physics **42**, 2354-2366 (2004).

169. Y. Hada, H. Shikuma, H. Ito, and T. Kikutani, "Structure and properties of syndiotactic polystyrene fibers prepared in high-speed melt spinning process," Fibers and Polymers **6**, 19-27 (2005).

170. J. Li and S.-T. Wu, "Self-consistency of Vuks equations for liquid-crystal refractive indices," Journal of Applied Physics **96**, 6253-6258 (2004).

171. Y. Terui and S. Ando, "Polarization dependence of thermo-optic coefficients in polyimide films originating from chain orientation and residual thermal stress," Journal of Applied Physics **116**, 053524 (2014).

172. M. K. Szczurowski, L. Khan, D. J. Webb, C. Ye, J. M. Dulieu-Barton, and W. Urbanczyk, "Measurements of stress-optic coefficient and Young's modulus in PMMA fibers drawn under different conditions," (SPIE, Brussels - Photonics Europe, 2010), pp. 13-13.

173. M. K. Szczurowski, T. Martynkien, G. Statkiewicz-Barabach, L. Khan, D. J. Webb, C. Ye, J. Dulieu-Barton, and W. Urbanczyk, "Measurements of stress-optic coefficient and Young's modulus in PMMA fibers drawn under different conditions," in *Photonic Crystal Fibers IV*, 2010),

174. H. J. Kang and J. L. White, "Orientation and Residual Stress Distributions in Thick Melt Spun Polystyrene and Polycarbonate Filaments," International Polymer Processing **1**, 12-18 (1986).

175. R. Wimberger-Friedl and R. D. H. M. Hendriks, "The measurement and calculation of birefringence in quenched polycarbonate specimens," Polymer **30**, 1143-1149 (1989).

176. T. Koyama, Y. Zhu, T. Otsuka, T. Takada, and Y. Murooka, "An automatic measurement system for 2-dimensional birefringence vector distribution," in *ICSD'98. Proceedings of the 1998 IEEE 6th International Conference on Conduction and Breakdown in Solid Dielectrics (Cat. No.98CH36132)*, 1998), 557-560.

177. W. Xu, X. F. Yao, H. Y. Yeh, and G. C. Jin, "Fracture investigation of PMMA specimen using coherent gradient sensing (CGS) technology," Polym Test **24**, 900-908 (2005).

178. H. Ohkita, K. Ishibashi, D. Tsurumoto, A. Tagaya, and Y. Koike, "Compensation of the photoelastic birefringence of a polymer by doping with an anisotropic molecule," Applied Physics A **81**, 617-620 (2005).

179. J. C. Knight, T. A. Birks, P. S. J. Russell, and D. M. Atkin, "All-silica single-mode optical fiber with photonic crystal cladding," Opt Lett **21**, 1547-1549 (1996).

180. P. Yeh, A. Yariv, and E. Marom, "Theory of Bragg fiber," J. Opt. Soc. Am. **68**, 1196-1201 (1978).

181. A. Argyros, "Guided modes and loss in Bragg fibres," Opt Express **10**, 1411-1417 (2002).

182. B. Temelkuran, S. D. Hart, G. Benoit, J. D. Joannopoulos, and Y. Fink, "Wavelength-scalable hollow optical fibres with large photonic bandgaps for CO2 laser transmission," Nature **420**, 650-653 (2002).

183. P. McIsaac, "Symmetry-Induced Modal Characteristics of Uniform Waveguides - I: Summary of Results," IEEE Transactions on Microwave Theory and Techniques **23**, 421-429 (1975).

184. T. A. Birks, J. C. Knight, and P. S. J. Russell, "Endlessly single-mode photonic crystal fiber," Opt Lett **22**, 961-963 (1997).

185. N. A. Mortensen, "Effective area of photonic crystal fibers," Opt Express **10**, 341-348 (2002).

186. J. Broeng, D. Mogilevstev, S. E. Barkou, and A. Bjarklev, "Photonic Crystal Fibers: A New Class of Optical Waveguides," Opt Fiber Technol **5**, 305-330 (1999).

187. B. T. Kuhlmey, R. C. McPhedran, and C. M. de Sterke, "Modal cutoff in microstructured optical fibers," Opt Lett **27**, 1684-1686 (2002).

188. S. G. Leon-Saval, T. A. Birks, W. J. Wadsworth, P. S. J. Russell, and M. W. Mason, "Supercontinuum generation in submicron fibre waveguides," Opt Express **12**, 2864-2869 (2004).

189. W. H. Reeves, D. V. Skryabin, F. Biancalana, J. C. Knight, P. S. J. Russell, F. G. Omenetto, A. Efimov, and A. J. Taylor, "Transformation and control of ultra-short pulses in dispersion-engineered photonic crystal fibres," Nature **424**, 511-515 (2003).

190. W. N. MacPherson, M. J. Gander, R. McBride, J. D. C. Jones, P. M. Blanchard, J. G. Burnett, A. H. Greenaway, B. Mangan, T. A. Birks, J. C. Knight, and P. S. J. Russell, "Remotely addressed optical fibre curvature sensor using multicore photonic crystal fibre," Opt Commun **193**, 97-104 (2001).

191. T. P. White, R. C. McPhedran, C. M. de Sterke, L. C. Botten, and M. J. Steel, "Confinement losses in microstructured optical fibers," Opt Lett **26**, 1660-1662 (2001).

192. T. P. White, B. T. Kuhlmey, R. C. McPhedran, D. Maystre, G. Renversez, C. M. de Sterke, and L. C. Botten, "Multipole method for microstructured optical fibers. I. Formulation," J. Opt. Soc. Am. B **19**, 2322-2330 (2002).

193. B. T. Kuhlmey, T. P. White, G. Renversez, D. Maystre, L. C. Botten, C. M. de Sterke, and R. C. McPhedran, "Multipole method for microstructured optical fibers. II. Implementation and results," J. Opt. Soc. Am. B **19**, 2331-2340 (2002).

194. B. T. Kuhlmey, CUDOS MOF Utilities v. 2.1, http://www.physics.usyd.edu.au/cudos/mofsoftware/index.html.

195. F. Poletti, "Nested antiresonant nodeless hollow core fiber," Opt Express **22**, 23807-23828 (2014).

196. S. G. Johnson, M. Ibanescu, M. Skorobogatiy, O. Weisberg, T. D. Engeness, M. Soljačić, S. A. Jacobs, J. D. Joannopoulos, and Y. Fink, "Low-loss asymptotically single-mode propagation in large-core OmniGuide fibers," Opt Express **9**, 748-779 (2001).

197. Y. Fink, J. N. Winn, S. Fan, C. Chen, J. Michel, J. D. Joannopoulos, and E. L. Thomas, "A Dielectric Omnidirectional Reflector," Science **282**, 1679-1682 (1998).

198. N. A. Mortensen and M. D. Nielsen, "Modeling of realistic cladding structures for air-core photonic bandgap fibers," Opt Lett **29**, 349-351 (2004).

199. J. Broeng, S. E. Barkou, T. Søndergaard, and A. Bjarklev, "Analysis of air-guiding photonic bandgap fibers," Opt Lett **25**, 96-98 (2000).

200. A. A. Maradudin and A. R. McGurn, "Out of Plane Propagation of Electromagnetic Waves in a Two-dimensional Periodic Dielectric Medium," Journal of Modern Optics **41**, 275-284 (1994).

201. K. Saitoh and M. Koshiba, "Leakage loss and group velocity dispersion in air-core photonic bandgap fibers," Opt Express **11**, 3100-3109 (2003).

202. K. Z. Aghaie, S. Fan, and M. J. F. Digonnet, "Birefringence Analysis of Photonic-Bandgap Fibers Using the Hexagonal Yee's Cell," IEEE J Quantum Elect **46**, 920-930 (2010).

203. R. D. Meade, K. D. Brommer, A. M. Rappe, and J. D. Joannopoulos, "Existence of a photonic band gap in two dimensions," Appl Phys Lett **61**, 495-497 (1992).

204. F. Benabid and P. J. Roberts, "Linear and nonlinear optical properties of hollow core photonic crystal fiber," Journal of Modern Optics **58**, 87-124 (2011).

205. T. A. Birks, G. J. Pearce, and D. M. Bird, "Approximate band structure calculation for photonic bandgap fibres," Opt Express **14**, 9483-9490 (2006).

206. F. Couny, F. Benabid, P. J. Roberts, M. T. Burnett, and S. A. Maier, "Identification of Bloch-modes in hollow-core photonic crystal fiber cladding," Opt Express **15**, 325-338 (2007).

207. F. Poletti and E. N. Fokoua, "Understanding the physical origin of surface modes and practical rules for their suppression," in *39th European Conference and Exhibition on Optical Communication (ECOC 2013)*, 2013), 1-3.

208. F. Poletti, N. V. Wheeler, M. N. Petrovich, N. Baddela, E. Numkam Fokoua, J. R. Hayes, D. R. Gray, Z. Li, R. Slavík, and D. J. Richardson, "Towards high-capacity fibre-optic communications at the speed of light in vacuum," Nature Photonics **7**, 279 (2013).

209. F. Benabid, J. C. Knight, G. Antonopoulos, and P. S. J. Russell, "Stimulated Raman Scattering in Hydrogen-Filled Hollow-Core Photonic Crystal Fiber," Science **298**, 399-402 (2002).

210. M. A. Duguay, Y. Kokubun, T. L. Koch, and L. Pfeiffer, "Antiresonant reflecting optical waveguides in SiO2-Si multilayer structures," Appl Phys Lett **49**, 13-15 (1986).

211. A. N. Kolyadin, A. F. Kosolapov, A. D. Pryamikov, A. S. Biriukov, V. G. Plotnichenko, and E. M. Dianov, "Light transmission in negative curvature hollow core fiber in extremely high material loss region," Opt Express **21**, 9514-9519 (2013).

212. W. Belardi and J. C. Knight, "Negative curvature fibers with reduced leakage loss," in *Optical Fiber Communication Conference*, OSA Technical Digest (online) (Optical Society of America, 2014), Th2A.45.

213. S.-f. Gao, Y.-y. Wang, W. Ding, D.-l. Jiang, S. Gu, X. Zhang, and P. Wang, "Hollow-core conjoined-tube negative-curvature fibre with ultralow loss," Nature Communications **9**, 2828 (2018).

214. M. I. Hasan, N. Akhmediev, and W. Chang, "Positive and negative curvatures nested in an antiresonant hollow-core fiber," Opt Lett **42**, 703-706 (2017).

215. S. Chaudhuri, L. D. Van Putten, F. Poletti, and P. J. A. Sazio, "Low Loss Transmission in Negative Curvature Optical Fibers With Elliptical Capillary Tubes," J Lightwave Technol **34**, 4228-4231 (2016).

216. A. Ge, F. Meng, Y. Li, B. Liu, and M. Hu, "Higher-Order Mode Suppression in Antiresonant Nodeless Hollow-Core Fibers," Micromachines **10**, 128 (2019).

217. Y. Han, F. Meng, S. Qiu, T. Dong, W. Zhu, and Y. Qing, *Low loss negative curvature fiber with circular internally tangent nested tube in elliptical tubes*, Tenth International Conference on Information Optics and Photonics (CIOP 2018) (SPIE, 2018), Vol. 10964.

218. M. S. Habib, O. Bang, and M. Bache, "Low-loss single-mode hollow-core fiber with anisotropic anti-resonant elements," Opt Express **24**, 8429-8436 (2016).

219. A. F. Kosolapov, G. K. Alagashev, A. N. Kolyadin, A. D. Pryamikov, A. S. Biryukov, I. A. Bufetov, and E. M. Dianov, "Hollow-core revolver fibre with a double-capillary reflective cladding," Quantum Electronics **46**, 267-270 (2016).

220. F. Meng, B. Liu, Y. Li, C. Wang, and M. Hu, "Low Loss Hollow-Core Antiresonant Fiber With Nested Elliptical Cladding Elements," IEEE Photonics Journal **9**, 1-11 (2017).

221. L. D. v. Putten, E. N. Fokoua, S. M. A. Mousavi, W. Belardi, S. Chaudhuri, J. V. Badding, and F. Poletti, "Exploring the Effect of the Core Boundary Curvature in Hollow Antiresonant Fibers," IEEE Photonic Tech L **29**, 263-266 (2017).

222. T. P. White, R. C. McPhedran, C. M. de Sterke, N. M. Litchinitser, and B. J. Eggleton, "Resonance and scattering in microstructured optical fibers," Opt Lett **27**, 1977-1979 (2002).

223. N. M. Litchinitser, S. C. Dunn, B. Usner, B. J. Eggleton, T. P. White, R. C. McPhedran, and C. M. de Sterke, "Resonances in microstructured optical waveguides," Opt Express **11**, 1243-1251 (2003).

224. Y. Chen, N. V. Wheeler, N. K. Baddela, J. R. Hayes, S. R. Sandoghchi, E. N. Fokoua, M. Li, F. Poletti, M. N. Petrovich, and D. J. Richardson, "Understanding Wavelength Scaling in 19-Cell Core Hollow-Core Photonic Bandgap Fibers," in *Optical Fiber Communication Conference*, OSA Technical Digest (online) (Optical Society of America, 2014), M2F.4.

225. P. Uebel, M. C. Günendi, M. H. Frosz, G. Ahmed, N. N. Edavalath, J.-M. Ménard, and P. S. J. Russell, "Broadband robustly single-mode hollow-core PCF by resonant filtering of higher-order modes," Opt Lett **41**, 1961-1964 (2016).

226. B. J. Mangan, L. Farr, A. Langford, P. J. Roberts, D. P. Williams, F. Couny, M. Lawman, M. Mason, S. Coupland, R. Flea, H. Sabert, T. A. Birks, J. C. Knight, and P. S. J. Russell, "Low loss (1.7 dB/km) hollow core photonic bandgap fiber," in *Optical Fiber Communication Conference*, Technical Digest (CD) (Optical Society of America, 2004), PD24.

227. N. V. Wheeler, M. N. Petrovich, R. Slavík, N. Baddela, E. Numkam, J. R. Hayes, D. R. Gray, F. Poletti, and D. J. Richardson, "Wide-bandwidth, low-loss, 19-cell hollow core photonic band gap fiber and its potential for low latency data transmission," in *National Fiber Optic Engineers Conference*, OSA Technical Digest (Optical Society of America, 2012), PDP5A.2.

228. Y. Y. Wang, N. V. Wheeler, F. Couny, P. J. Roberts, and F. Benabid, "Low loss broadband transmission in hypocycloid-core Kagome hollow-core photonic crystal fiber," Opt Lett **36**, 669-671 (2011).

229. B. Debord, A. Amsanpally, M. Chafer, A. Baz, M. Maurel, J. M. Blondy, E. Hugonnot, F. Scol, L. Vincetti, F. Gérôme, and F. Benabid, "Ultralow transmission loss in inhibited-coupling guiding hollow fibers," Optica **4**, 209-217 (2017).

230. C. Emslie, "Polymer optical fibres," Journal of Materials Science **23**, 2281-2293 (1988).

231. G. Woyessa, "Speciality and microstructured polymer optical FBG sensors," (Ph. D. dissertation, DTU Fotonik, Department of Photonics Engineering …, 2017).

232. Y. Gao, N. Guo, B. Gauvreau, M. Rajabian, O. Skorobogata, E. Pone, O. Zabeida, L. Martinu, C. Dubois, and M. Skorobogatiy, "Consecutive solvent evaporation and co-rolling techniques for polymer multilayer hollow fiber preform fabrication," Journal of Materials Research **21**, 2246-2254 (2006).

233. B.-G. SHIN, J.-H. PARK, and J.-J. KIM, "PLASTIC PHOTONIC CRYSTAL FIBERS DRAWN FROM STACKED CAPILLARIES," Journal of Nonlinear Optical Physics & Materials **13**, 519-523 (2004).

234. X. Feng, A. K. Mairaj, D. W. Hewak, and T. M. Monro, "Nonsilica Glasses for Holey Fibers," J Lightwave Technol **23**, 2046 (2005).

235. M. C. Large, M. A. Van Eijkelenborg, A. Argyros, J. Zagari, S. Manos, N. A. Issa, I. Bassett, S. Fleming, R. C. McPhedran, and C. M. de Sterke, "Microstructured polymer optical fibres: a new approach to POFs," in *POF 2001 Conference, Amsterdam, The Netherlands*, (Citeseer, 2001),

236. J. B. Jensen, P. E. Hoiby, G. Emiliyanov, O. Bang, L. H. Pedersen, and A. Bjarklev, "Selective detection of antibodies in microstructured polymer optical fibers," Opt Express **13**, 5883-5889 (2005).

237. G. Barton, M. A. v. Eijkelenborg, G. Henry, M. C. J. Large, and J. Zagari, "Fabrication of microstructured polymer optical fibres," Opt Fiber Technol **10**, 325-335 (2004).

238. A. Fasano, G. Woyessa, P. Stajanca, C. Markos, A. Stefani, K. Nielsen, H. K. Rasmussen, K. Krebber, and O. Bang, "Production and characterization of polycarbonate microstructured polymer optical fiber Bragg grating sensor," in *The 24th International Conference on Plastic Optical Fibers*, 2015),

239. V. V. Ravi Kanth Kumar, A. K. George, W. H. Reeves, J. C. Knight, P. S. J. Russell, F. G. Omenetto, and A. J. Taylor, "Extruded soft glass photonic crystal fiber for ultrabroad supercontinuum generation," Opt Express **10**, 1520-1525 (2002).

240. K. M. Kiang, K. Frampton, T. M. Monro, R. Moore, J. Tucknott, D. W. Hewak, D. J. Richardson, and H. N. Rutt, "Extruded singlemode non-silica glass holey optical fibres," Electron Lett **38**, 546-547 (2002).

241. H. Ebendorff-Heidepriem and T. M. Monro, "Extrusion of complex preforms for microstructured optical fibers," Opt Express **15**, 15086-15092 (2007).

242. H. Ebendorff-Heidepriem, T. M. Monro, M. A. van Eijkelenborg, and M. C. J. Large, "Extruded high-NA microstructured polymer optical fibre," Opt Commun **273**, 133-137 (2007).

243. R. T. Bise and D. J. Trevor, "Sol-gel Derived Microstructured Fiber: Fabrication and Characterization," in *Optical Fiber Communication Conference and Exposition and The National Fiber Optic Engineers Conference*, Technical Digest (CD) (Optical Society of America, 2005), OWL6.

244. R. T. Bise, R. S. Windeler, K. S. Kranz, C. Kerbage, B. J. Eggleton, and D. J. Trevor, "Tunable photonic band gap fiber," in *Optical Fiber Communication Conference and Exhibit*, 2002), 466-468.

245. Y. Zhang, K. Li, L. Wang, L. Ren, W. Zhao, R. Miao, M. C. J. Large, and M. A. v. Eijkelenborg, "Casting preforms for microstructured polymer optical fibre fabrication," Opt Express **14**, 5541-5547 (2006).

246. M. G. Zubel, A. Fasano, G. Woyessa, K. Sugden, H. K. Rasmussen, and O. Bang, "3D-printed PMMA preform for hollow-core POF drawing," in *25th International Conference on Plastic Optical Fibres, POF 2016*, P. Scully, K. Sugden, and D. J. Webb, eds. (Aston University, Birmingham, United Kingdom, 2017), pp. 295-300.

247. J. Canning, M. A. Hossain, C. Y. Han, L. Chartier, K. Cook, and T. Athanaze, "Drawing optical fibers from three-dimensional printers," Opt Lett **41**, 5551-5554 (2016).

248. S. Li, Z. Dai, Z. Wang, P. Qi, Q. Su, X. Gao, C. Gong, and W. Liu, "A 0.1 THz low-loss 3D printed hollow waveguide," Optik **176**, 611-616 (2019).

249. S. Pandey, B. Gupta, and A. Nahata, "Terahertz plasmonic waveguides created via 3D printing," Opt Express **21**, 24422-24430 (2013).

250. A. L. S. Cruz, C. M. B. Cordeiro, and M. A. R. Franco, "3D Printed Hollow-Core Terahertz Fibers," Fibers **6**, 43 (2018).

251. A. L. S. Cruz, V. A. Serrão, C. L. Barbosa, M. A. R. Franco, C. M. B. Cordeiro, A. Argyros, and X. Tang, "3D printed hollow core fiber with negative curvature for terahertz applications," J. Microwaves Optoelectron. Electromag. Appl. **14**, SI45-SI53 (2015).

252. A. Othonos, K. Kalli, D. Pureur, and A. Mugnier, "Fibre Bragg Gratings," in *Wavelength Filters in Fibre Optics*, H. Venghaus, ed. (Springer, Berlin, 2006).

253. I. Johnson, "Grating Devices in polymer optical fibre," PhD (Aston University, Birmingham, 2011).

254. R. Kashyap, *Fiber bragg gratings* (Academic press, 2009).

255. H. Singh and M. Zippin, "Apodized fiber Bragg gratings for DWDM applications using uniform phase mask," in *24th European Conference on Optical Communication. ECOC '98 (IEEE Cat. No.98TH8398)*, 1998), 189-190 vol.181.

256. A. Pospori, "Fabrication and characterisation of Bragg grating based polymeric optical devices," PHD (Aston University, 2017).

257. D. P. Hand and P. S. J. Russell, "Photoinduced refractive-index changes in germanosilicate fibers," Opt Lett **15**, 102-104 (1990).

258. J. P. Bernardin and N. M. Lawandy, "Dynamics of the formation of Bragg gratings in germanosilicate optical fibers," Opt Commun **79**, 194-199 (1990).

259. M. Sceats, G. Atkins, and S. Poole, "Photolytic index changes in optical fibers," Annual Review of Materials Science **23**, 381-410 (1993).

260. D. L. Williams, B. J. Ainslie, R. Kashyap, G. D. Maxwell, J. R. Armitage, R. J. Campbell, and R. R. Wyatt, *Photosensitive index changes in germania-doped silica glass fibers and waveguides*, Optics Quebec (SPIE, 1993), Vol. 2044.

261. S. J. Grice, "Optical fibre sensors and their applications in the industrial weighing and aerospace industries," PhD (Aston University, 2010).

262. D. Sengupta, "Fiber Bragg Grating Sensors and Interrogation Systems," in *Optical Fiber Sensors: Advanced Techniques and Applications*, G. Rajan, ed. (CRC Press, United Kingdom, 2015), p. 576.

263. S. Ness and P. R. Herman, "157-nm photosensitivity in germanosilicate planar waveguides," in *Technical Digest. Summaries of papers presented at the Conference on Lasers and Electro-Optics. Postconference Edition. CLEO '99. Conference on Lasers and Electro-Optics (IEEE Cat. No.99CH37013)*, 1999), 76-77.

264. J. Albert, B. Malo, F. Bilodeau, D. Johnson, K. Hill, Y. Hibino, and M. Kawachi, "Photosensitivity in Ge-doped silica optical waveguides and fibers with 193-nm light from an ArF excimer laser," Opt Lett **19**, 387-389 (1994).

265. R. M. Atkins and R. P. Espindola, "Photosensitivity and grating writing in hydrogen loaded germanosilicate core optical fibers at 325 and 351 nm," Appl Phys Lett **70**, 1068-1069 (1997).

266. F. Bilodeau, D. C. Johnson, B. Malo, K. A. Vineberg, K. O. Hill, T. F. Morse, A. Kilian, and L. Reinhart, "Ultraviolet-light photosensitivity in Er3+–Ge-doped optical fiber," Opt Lett **15**, 1138-1140 (1990).

267. D. L. Williams, B. J. Ainslie, J. R. Armitage, R. Kashyap, and R. Campbell, "Enhanced UV photosensitivity in boron codoped germanosilicate fibres," in *Electron Lett*, (Institution of Engineering and Technology, 1993), pp. 45-47.

268. L. Dong, J. L. Cruz, L. Reekie, M. G. Xu, and D. N. Payne, "Enhanced photosensitivity in tin-codoped germanosilicate optical fibers," IEEE Photonic Tech L **7**, 1048-1050 (1995).

269. L. Dong, L. Reekie, J. L. Cruz, and D. N. Payne, "Grating formation in a phosphorus-doped germanosilicate fiber," in *Optical Fiber Communications, OFC.*, 1996), 82-83.

270. M. M. Broer, A. J. Bruce, and W. H. Grodkiewicz, "Photoinduced refractive-index changes in several ${\mathrm{Eu}}^{3+}$-, ${\mathrm{Pr}}^{3+}$-, and ${\mathrm{Er}}^{3+}$-doped oxide glasses," Physical Review B **45**, 7077-7083 (1992).

271. K. O. Hill, B. Malo, F. Bilodeau, D. C. Johnson, T. F. Morse, A. Kilian, L. Reinhart, and K. Oh, "Photosensitivity in Eu2+:Al2O3-Doped-Core Fiber: Preliminary Results and Application to Mode Converters," in *Optical Fiber Communication*, 1991 OSA Technical Digest Series (Optical Society of America, 1991), PD3.

272. G. M. Williams, T. Tsung-Ein, C. I. Merzbacher, and E. J. Friebele, "Photosensitivity of rare-earth-doped ZBLAN fluoride glasses," J Lightwave Technol **15**, 1357-1362 (1997).

273. K. Sugden and V. Mezentsev, "Fiber Bragg Gratings: Advances in Fabrication Process and Tools," in *Fiber Bragg grating sensors: research advancements, industrial applications and market exploitation*, A. Cusano, A. Cutolo, and J. Albert, eds. (Bentham Science Publishers Ltd., Saif Zone, Sharjah, United Arab Emirates, 2011).

274. F. Bilodeau, B. Malo, J. Albert, D. C. Johnson, K. O. Hill, Y. Hibino, M. Abe, and M. Kawachi, "Photosensitization of optical fiber and silica-on-silicon/silica waveguides," Opt Lett **18**, 953-955 (1993).

275. C. Wochnowski, S. Metev, and G. Sepold, "UV-laser-assisted modification of the optical properties of polymethylmethacrylate," Appl Surf Sci **154**, 706-711 (2000).

276. C. Wochnowski, M. A. Shams Eldin, and S. Metev, "UV-laser-assisted degradation of poly(methyl methacrylate)," Polymer Degradation and Stability **89**, 252-264 (2005).

277. T. Mitsuoka, A. Torikai, and K. Fueki, "Wavelength Sensitivity of the Photodegradation of Poly(Methyl Methacrylate)," J. Appl. Polym. Sci. **47**, 1027-1032 (1993).

278. D. Sáez-Rodríguez, K. Nielsen, O. Bang, and D. J. Webb, "Photosensitivity mechanism of undoped poly(methyl methacrylate) under UV radiation at 325 nm and its spatial resolution limit," Opt Lett **39**, 3421-3424 (2014).

279. D. R. Tyler, "Mechanistic Aspects of the Effects of Stress on the Rates of Photochemical Degradation Reactions in Polymers," Journal of Macromolecular Science, Part C **44**, 351-388 (2004).

280. R. Oliveira, L. Bilro, and R. Nogueira, "Bragg gratings in a few mode microstructured polymer optical fiber in less than 30 seconds," Opt Express **23**, 10181-10187 (2015).

281. A. Pospori, C. A. F. Marques, O. Bang, D. J. Webb, and P. André, "Polymer optical fiber Bragg grating inscription with a single UV laser pulse," Opt Express **25**, 9028-9038 (2017).

282. L. Pereira, R. Min, X. Hu, C. Caucheteur, O. Bang, B. Ortega, C. Marques, P. Antunes, and J. L. Pinto, "Polymer optical fiber Bragg grating inscription with a single Nd:YAG laser pulse," Opt Express **26**, 18096-18104 (2018).

283. D. Saez-Rodriguez, K. Nielsen, H. K. Rasmussen, O. Bang, and D. J. Webb, "Highly photosensitive polymethyl methacrylate microstructured polymer optical fiber with doped core," Opt Lett **38**, 3769--3772 (2013).

284. Y. Luo, Q. Zhang, H. Y. Liu, and P. Gd, "Gratings fabrication in benzildimethylketal doped photosensitive polymer optical fibers using 355 nm nanosecond pulsed laser," Opt Lett **35**(2010).

285. G. D. Peng, X. Xiong, and P. L. Chu, "Photosensitivity and gratings in dye-doped polymer optical fibers," Opt Fiber Technol **5**, 242-251 (1999).

286. F. P. Laming, "Holographic grating formation in photopolymers—Polymethylmethacrylate," Polymer Engineering & Science **11**, 421-425 (1971).

287. R. Kashyap, J. R. Armitage, R. Wyatt, S. T. Davey, and D. L. Williams, "All-fibre narrowband reflection gratings at 1500 nm," Electron Lett **26**, 730-732 (1990).

288. B. J. Eggleton, P. A. Krug, L. Poladian, K. A. Ahmed, and H. F. Liu, "Experimental demonstration of compression of dispersed optical pulses by reflection from self-chirped optical fiber Bragg gratings," Opt Lett **19**, 877-879 (1994).

289. H. Limberger, P. Fonjallaz, P. Lambelet, C. Zimmer, R. Salathe, and H. Gilgen, "Photosensitivity and self-organization in optical fibers and waveguides," in *Proc. SPIE*, 1993), 272-285.

290. K. O. Hill, B. Malo, F. Bilodeau, D. C. Johnson, and J. Albert, "Bragg gratings fabricated in monomode photosensitive optical fiber by UV exposure through a phase mask," Appl Phys Lett **62**, 1035-1037 (1993).

291. B. Malo, K. O. Hill, F. Bilodeau, D. C. Johnson, and J. Albert, "Point-by-point fabrication of micro-Bragg gratings in photosensitive fibre using single excimer pulse refractive index modification techniques," Electron Lett **29**, 1668-1669 (1993).

292. K. O. Hill, B. Malo, K. A. Vineberg, F. Bilodeau, D. C. Johnson, and I. Skinner, "Efficient mode conversion in telecommunication fibre using externally written gratings," Electron Lett **26**, 1270-1272 (1990).

293. K. O. Hill, F. Bilodeau, B. Malo, and D. C. Johnson, "Birefringent photosensitivity in monomode optical fibre: application to external writing of rocking filters," in *Electron Lett*, (Institution of Engineering and Technology, 1991), pp. 1548-1550.

294. W. H. Loh, M. J. Cole, M. N. Zervas, S. Barcelos, and R. I. Laming, "Complex grating structures with uniform phase masks based on the moving fiber–scanning beam technique," Opt Lett **20**, 2051-2053 (1995).

295. A. Martinez, M. Dubov, I. Khrushchev, and I. Bennion, "Direct writing of fibre Bragg gratings by femtosecond laser," Electron Lett **40**, 1170-1172 (2004).

296. E. Wikszak, J. Burghoff, M. Will, S. Nolte, A. Tünnermann, and T. Gabler, "Recording of fiber Bragg gratings with femtosecond pulses using a "point by point" technique," in *Conference on Lasers and Electro-Optics/International Quantum Electronics Conference and Photonic Applications Systems Technologies*, Technical Digest (CD) (Optical Society of America, 2004), CThM7.

297. A. Cusano, D. Paladino, A. Cutolo, A. Iadicicco, and S. Campopiano, "Photonic Bandgap Engineering in FBGs by Post Processing Fabrication Techniques," in *Fiber Bragg grating sensors: research advancements, industrial applications and market exploitation*, A. Cusano, A. Cutolo, and J. Albert, eds. (Bentham Science Publishers Ltd., Saif Zone, Sharjah, United Arab Emirates, 2011).

298. Z. Qin, D. A. Brown, L. Reinhart, T. F. Morse, J. Q. Wang, and X. Gang, "Tuning Bragg wavelength by writing gratings on prestrained fibers," IEEE Photonic Tech L **6**, 839-841 (1994).

299. G. Sagias, A. Pospori, D. Gallego, D. J. Webb, and H. L. Rivera, *Wavelength tuning of polymer optical fibre Bragg grating at longer wavelengths permanently*, Third International Conference on Applications of Optics and Photonics (SPIE, 2017), Vol. 10453.

300. M. G. Zubel, K. Sugden, D. Saez-Rodriguez, K. Nielsen, and O. Bang, "3-D printed sensing patches with embedded polymer optical fibre Bragg gratings," in *Sixth European Workshop on Optical Fibre Sensors (EWOFS'2016)*, (Limerick, Ireland, 2016).

301. M. G. Zubel, K. Sugden, D. J. Webb, D. Saez-Rodriguez, K. Nielsen, and O. Bang, "Embedding silica and polymer fibre Bragg gratings (FBG) in plastic 3D-printed sensing patches," in *Micro-Structured and Specialty Optical Fibres IV, SPIE Photonics Europe 2016*, (Brussels, Belgium, 2016).

302. A. Pospori, C. A. F. Marques, M. G. Zubel, D. Saez-Rodriguez, K. Nielsen, O. Bang, and D. J. Webb, "Annealing effects on strain and stress sensitivity of polymer optical fibre based sensors," in *Micro-Structured and Specialty Optical Fibres IV, SPIE Photonics Europe 2016*, (Brussels, Belgium, 2016).

303. A. Lacraz, M. Zubel, G. Demirci, A. Theodosiou, K. Kalli, K. Sugden, and B. Gawdzik, "Embedding low loss polymer optical fibre Bragg gratings: Two different approaches," in *25th International Conference on Plastic Optical Fibres, POF 2016*, P. Scully, K. Sugden, and D. J. Webb, eds. (Aston University, Birmingham, United Kingdom, 2017), pp. 36-39.

304. F. Berghmans, H. Thienpont, P. Van Daele, P. Dubruel, W. Urbanczyk, J. Rayss, D. J. Webb, J. Vlekken, K. Kalli, and K. Sugden, "Photonic skins for optical sensing: Highlights of the PHOSFOS Project," in *20th International Conference on Optical Fibre Sensors*, (Edinburgh, United Kingdom, 2009).

305. X. Chen, C. Zhang, D. J. Webb, B. Van Hoe, G. Van Steenberge, K. Kalli, F. Berghmans, H. Thienpont, W. Urbanczyk, K. Sugden, and G. D. Peng, "Polymer photonic sensing skin," in *4th European Workshop on Optical Fibre Sensors*, (Porto, Portugal, 2010).

306. Y. Mizuno, R. Ishikawa, H. Lee, A. Theodosiou, K. Kalli, and K. Nakamura, "Potential of discriminative sensing of strain and temperature using perfluorinated polymer FBG," IEEE Sens J, 1-1 (2019).

307. A. Pospori, C. A. F. Marques, D. Saez-Rodriguez, K. Nielsen, O. Bang, and D. J. Webb, "Sensitivity enhancement using annealed polymer optical fibre based sensors for pressure sensing applications," in *Sixth European Workshop on Optical Fibre Sensors (EWOFS'2016)*, (Limerick, Ireland, 2016).

308. R. Ishikawa, H. Lee, A. Lacraz, A. Theodosiou, K. Kalli, Y. Mizuno, and K. Nakamura, "Pressure Dependence of Fiber Bragg Grating Inscribed in Perfluorinated Polymer Fiber," IEEE Photonic Tech L **29**, 2167-2170 (2017).

309. W. Zhang, D. Webb, and G. Peng, "Polymer optical fiber Bragg grating acting as an intrinsic biochemical concentration sensor," Opt Lett **37**, 1370-1372 (2012).

310. A. Stefani, S. Andresen, W. Yuan, N. Herholdt-Rasmussen, and O. Bang, "High Sensitivity Polymer Optical Fiber-Bragg-Grating-Based Accelerometer," IEEE Photonic Tech L **24**, 763-765 (2012).

311. C. Broadway, D. Gallego, A. Pospori, M. Zubel, D. J. Webb, K. Sugden, G. Carpintero, and H. Lamela, "A Compact Polymer Optical Fibre Ultrasound Detector," in *Photons Plus Ultrasound: Imaging and Sensing 2016, SPIE BiOS*, , (San Francisco, California, United States, 2016).

312. W. Zhang and D. J. Webb, "Polymer optical fiber grating as water activity sensor," in *Micro-Structured and Specialty Optical Fibres III, SPIE Photonics Europe*, (SPIE, 2014),

313. P. Stajanca and K. Krebber, "Radiation-Induced Attenuation of Perfluorinated Polymer Optical Fibers for Radiation Monitoring," Sensors-Basel **17**(2017).

314. G. D. Peng and P. L. Chu, "Polymer optical fiber photosensitivities and highly tunable fiber gratings," Fiber and Integrated Optics **19**, 277-293 (2000).

315. X. Chen, C. Zhang, D. J. Webb, G. D. Peng, and K. Kalli, "Bragg grating in a polymer optical fibre for strain, bend and temperature sensing," Meas. Sci. Technol. **21**, 094005 (2010).

316. T. Wang, Y. Guo, X. Zhan, M. Zhao, and K. Wang, "Simultaneous Measurements of Strain and Temperature with Dual Fiber Bragg Gratings for Pervasive Computing," in *2006 First International Symposium on Pervasive Computing and Applications*, 2006), 786-790.

317. D. D. Raftopoulos, D. Karapanos, and P. S. Theocaris, "Static and dynamic mechanical and optical behaviour of high polymers," J Phys D **9**, 869-877 (1976).

318. I. H. Malitson, "Interspecimen Comparison of the Refractive Index of Fused Silica*,†," J. Opt. Soc. Am. **55**, 1205-1209 (1965).

319. A. Stefani, W. Yuan, C. Markos, and O. Bang, "Narrow Bandwidth 850-nm Fiber Bragg Gratings in Few-Mode Polymer Optical Fibers," IEEE Photonic Tech L **23**, 660-662 (2011).

320. C. Broadway, D. Gallego, G. Woyessa, A. Pospori, G. Carpintero, O. Bang, K. Sugden, and H. Lamela, *Fabry-Perot micro-structured polymer optical fibre sensors for opto-acoustic endoscopy*, SPIE Biophotonics South America (SPIE, 2015), Vol. 9531.

321. A. Pospori, C. A. F. Marques, M. G. Zubel, D. Saez-Rodriguez, F. K. Nielsen, O. Bang, and D. J. Webb, "Annealing effects on strain and stress sensitivity of polymer optical fibre based sensors " in *SPIE Photonics Europe 2016*, Proc. SPIE (SPIE, 2016),

322. Z. F. Zhang and X. M. Tao, "Synergetic Effects of Humidity and Temperature on PMMA Based Fiber Bragg Gratings," J Lightwave Technol **30**, 841-845 (2012).

323. W. Yuan, A. Stefani, M. Bache, T. Jacobsen, B. Rose, N. Herholdt-Rasmussen, F. K. Nielsen, S. Andresen, O. B. Sørensen, K. S. Hansen, and O. Bang, "Improved thermal and strain performance of annealed polymer optical fiber Bragg gratings," Opt Commun **284**, 176-182 (2011).

324. H. Y. Liu, H. B. Liu, and G. D. Peng, "Tensile strain characterization of polymer optical fibre Bragg gratings," Opt Commun **251**, 37-43 (2005).

325. C. Zhang, W. Zhang, D. J. Webb, and G. Peng, "Optical fibre temperature and humidity sensor," Electron Lett **46**, 643-644 (2010).

326. I. P. Johnson, W. Yuan, A. Stefani, K. Nielsen, H. K. Rasmussen, L. Khan, D. J. Webb, K. Kalli, and O. Bang, "Optical fibre Bragg grating recorded in TOPAS cyclic olefin copolymer," Electron Lett **47**, 271-272 (2011).

327. P. Stajanca, A. Lacraz, K. Kalli, M. Schukar, and K. Krebber, *Strain sensing with femtosecond inscribed FBGs in perfluorinated polymer optical fibers*, SPIE Photonics Europe (SPIE, 2016), Vol. 9899.

328. R. Ishikawa, H. Lee, A. Lacraz, A. Theodosiou, K. Kalli, Y. Mizuno, and K. Nakamura, "Strain dependence of perfluorinated polymer optical fiber Bragg grating measured at different wavelengths," Jpn J Appl Phys **57**, 038002 (2018).

329. A. Theodosiou, M. Komodromos, and K. Kalli, "Carbon Cantilever Beam Health Inspection Using a Polymer Fiber Bragg Grating Array," J Lightwave Technol **36**, 986-992 (2018).

330. Y. Zheng, K. Bremer, and B. Roth, "Investigating the Strain, Temperature and Humidity Sensitivity of a Multimode Graded-Index Perfluorinated Polymer Optical Fiber with Bragg Grating," Sensors-Basel **18**, 1436 (2018).

331. H. Y. Liu, G. D. Peng, and P. L. Chu, "Thermal tuning of polymer optical fiber Bragg gratings," IEEE Photonic Tech L **13**, 824-826 (2001).

332. H. B. Liu, H. Y. Liu, G. D. Peng, and P. L. Chu, "Strain and temperature sensor using a combination of polymer and silica fibre Bragg gratings," Opt Commun **219**, 139-142 (2003).

333. N. G. Harbach, "Fiber bragg gratings in polymer optical fibers," PhD (Ecole Polytechnique Federale de Lausanne, Lausanne, 2008).

334. A. Bar-Cohen, B. Han, and K. Joon Kim, "Thermo-Optic Effects in Polymer Bragg Gratings," in *Micro- and Opto-Electronic Materials and Structures: Physics, Mechanics, Design, Reliability, Packaging*, E. Suhir, Y. C. Lee, and C. P. Wong, eds. (Springer US, Boston, MA, 2007), pp. A65-A110.

335. A. Rosenberg, S. H. Lee, J. S. Shirk, and G. Beadie, "Opto-thermal characteristics of amorphous polyimides for optical applications," Opt Mater Express **8**, 2159-2172 (2018).

336. J. M. Cariou, J. Dugas, L. Martin, and P. Michel, "Refractive-index variations with temperature of PMMA and polycarbonate," Appl Optics **25**, 334-336 (1986).

337. R. S. Moshrefzadeh, M. D. Radcliffe, T. C. Lee, and S. K. Mohapatra, "Temperature dependence of index of refraction of polymeric waveguides," J Lightwave Technol **10**, 420-425 (1992).

338. M. Tomiki, N. Kurihara, O. Sugihara, and N. Okamoto, "A New Method for Accurately Measuring Temperature Dependence of Refractive Index," Optical Review **12**, 97-100 (2005).

339. J.-g. Chen, T. Zhang, J.-s. Zhu, X.-y. Zhang, J.-l. Zhou, J.-f. Fan, and G.-h. Hu, "Low-loss planar optical waveguides fabricated from polycarbonate," Polymer Engineering & Science **49**, 2015-2019 (2009).

340. "Technical data sheet of Gehr PMMA (Acrylic)", retrieved 24 Sep 2019, https://en.gehr.de/wp-content/uploads//2019/09/GEHR-PMMA-tech-data-sheet.pdf.

341. J. Brandrup, *Polymer Handbook* (Wiley, 1999), Vol. 1&2.

342. "Technical data sheet of Markolon polycarbonate (Markolon 6265)", retrieved 24 Sep 2019, https://www.plastics.covestro.com/en/products/makrolon/makrolon-6265-x_83439336-05122261.

343. T. Watanabe, N. Ooba, Y. Hida, and M. Hikita, "Influence of humidity on refractive index of polymers for optical waveguide and its temperature dependence," Appl Phys Lett **72**, 1533-1535 (1998).

344. D. T. Turner, "Polymethyl methacrylate plus water: sorption kinetics and volumetric changes," Polymer **23**, 197-202 (1982).

345. W. Zhang, D. J. Webb, and G. D. Peng, "Investigation Into Time Response of Polymer Fiber Bragg Grating Based Humidity Sensors," J Lightwave Technol **30**, 1090-1096 (2012).

346. G. Rajan, Y. M. Noor, B. Liu, E. Ambikairaja, D. J. Webb, and G.-D. Peng, "A fast response intrinsic humidity sensor based on an etched singlemode polymer fiber Bragg grating," Sensors and Actuators A: Physical **203**, 107-111 (2013).

347. J. A. Goff, "Saturation pressure of water on the new Kelvin temperature scale," Transactions of the American society of heating and ventilating engineers, 347-354 (1957).

348. W. Zhang, D. J. Webb, and G.-D. Peng, "Enhancing the sensitivity of poly(methyl methacrylate) based optical fiber Bragg grating temperature sensors," Opt Lett **40**, 4046-4049 (2015).

349. "Dr 3D Filament", retrieved 24 Sep 2019, https://dr3dfilament.com.

350. G. Barton, M. A. van Eijkelenborg, G. Henry, M. C. J. Large, and J. Zagari, "Fabrication of microstructured polymer optical fibres," Opt Fiber Technol **10**, 325-335 (2004).

351. X. Hu, G. Woyessa, D. Kinet, J. Janting, K. Nielsen, O. Bang, and C. Caucheteur, "BDK-doped core microstructured PMMA optical fiber for effective Bragg grating photo-inscription," Opt Lett **42**, 2209-2212 (2017).

352. A. D. Pryamikov, A. S. Biriukov, A. F. Kosolapov, V. G. Plotnichenko, S. L. Semjonov, and E. M. Dianov, "Demonstration of a waveguide regime for a silica hollow - core microstructured optical fiber with a negative curvature of the core boundary in the spectral region > 3.5 μm," Opt Express **19**, 1441-1448 (2011).

353. A. Argyros, R. Lwin, S. G. Leon-Saval, J. Poulin, L. Poladian, and M. C. J. Large, "Low Loss and Temperature Stable Microstructured Polymer Optical Fibers," J Lightwave Technol **30**, 192-197 (2012).

354. A. Kantaros and D. Karalekas, "Fiber Bragg grating based investigation of residual strains in ABS parts fabricated by fused deposition modeling process," Mater. Des. **50**, 44-50 (2013).

355. M. G. Zubel, A. Fasano, G. Woyessa, R. Min, A. Leal-Junior, A. Theodosiou, C. A. F. Marques, H. K. Rasmussen, O. Bang, B. Ortega, K. Kalli, A. Frizera-Neto, M. J. Pontes, and K. Sugden, "Bragg gratings inscribed in solid-core microstructured single-mode polymer optical fiber drawn from a 3D-printed polycarbonate preform," IEEE Sens J, 1-1 (2020).

356. A. Stefani, K. Nielsen, H. K. Rasmussen, and O. Bang, "Cleaving of TOPAS and PMMA microstructured polymer optical fibers: Core-shift and statistical quality optimization," Opt Commun **285**, 1825--1833 (2012).

357. S. H. Law, J. D. Harvey, R. J. Kruhlak, M. Song, E. Wu, G. W. Barton, M. A. van Eijkelenborg, and M. C. J. Large, "Cleaving of microstructured polymer optical fibres," Opt Commun **258**, 193-202 (2006).

358. S. H. Law, M. A. van Eijkelenborg, G. W. Barton, C. Yan, R. Lwin, and J. Gan, "Cleaved end-face quality of microstructured polymer optical fibres," Opt Commun **265**, 513-520 (2006).

359. R. Syms and J. Cozens, *Optical Guided Waves and Devices* (McGraw-Hill Education - Europe, London, United Kingdom, 1992), p. 500.

360. D. Celentano, D. Wimmer, L. Colabella, and A. P. Cisilino, "Viscoelastic mechanical characterization of a short-fiber reinforced polyethylene tube: Experiments and modelling," Int J Pres Ves Pip **134**, 82-91 (2015).

361. S. Ropers, M. Kardos, and T. A. Osswald, "A thermo-viscoelastic approach for the characterization and modeling of the bending behavior of thermoplastic composites," Compos Part a-Appl S **90**, 22-32 (2016).

362. T. C. Henry, C. E. Bakis, and E. C. Smith, "Viscoelastic characterization and self-heating behavior of laminated fiber composite driveshafts," Mater Design **66**, 346-355 (2015).

363. I. K. Lin, K. S. Ou, Y. M. Liao, Y. Liu, K. S. Chen, and X. Zhang, "Viscoelastic Characterization and Modeling of Polymer Transducers for Biological Applications," J Microelectromech S **18**, 1087-1099 (2009).

364. A. G. Leal, C. Marques, A. Frizera, and M. J. Pontes, "Dynamic Mechanical Analysis on a PolyMethyl Methacrylate (PMMA) Polymer Optical Fiber," IEEE Sens J **18**, 2353-2361 (2018).

365. A. Leal, A. Frizera, M. J. Pontes, P. Antunes, N. Alberto, M. F. Domingues, H. Lee, R. Ishikawa, Y. Mizuno, K. Nakamura, P. Andre, and C. Marques, "Dynamic mechanical analysis on fused polymer optical fibers: towards sensor applications," Opt Lett **43**, 1754-1757 (2018).

366. S. P. Timoshenko and J. M. Gere, *Theory of elastic stability*, 2nd ed. (American Society of Mechanical Engineers Digital Collection, 1962).

367. G. Woyessa, "Speciality and microstructured polymer optical FBG sensors," Ph.D. thesis (Technical University of Denmark, Copenhagen, Denmark, 2017).

368. M. Pietralla and T. Pieper, "The problem of intrinsic birefringence and chain conformation in polycarbonate from bisphenol-A," Colloid and Polymer Science **268**, 797-805 (1990).

369. A. Theodosiou, X. H. Hu, C. Caucheteur, and K. Kalli, "Bragg Gratings and Fabry-Perot Cavities in Low-Loss Multimode CYTOP Polymer Fiber," IEEE Photonic Tech L **30**, 857-860 (2018).

370. A. Ioannou, A. Theodosiou, C. Caucheteur, and K. Kalli, "Direct writing of plane-by-plane tilted fiber Bragg gratings using a femtosecond laser," Opt Lett **42**, 5198-5201 (2017).

371. W. E. Forsythe, "Smithsonian Physical Tables (9th Revised Edition)," (Knovel).

372. A. L. Buck, "New Equations for Computing Vapor Pressure and Enhancement Factor," Journal of Applied Meteorology **20**, 1527-1532 (1981).

373. "MATWEB: Overview of materials for Acrylonitrile Butadiene Styrene (ABS), Extruded", retrieved 4 Apr 2019, http://matweb.com/search/DataSheet.aspx?MatGUID=3a8afcddac864d4b8f58d40570d2e5aa&ckck=1.

374. D. Ganziy, O. Jespersen, G. Woyessa, B. Rose, and O. Bang, "Dynamic gate algorithm for multimode fiber Bragg grating sensor systems," Appl Optics **54**, 5657-5661 (2015).

375. T. Ma and B. Bhushan, "Mechanical, hygroscopic, and thermal properties of ultrathin polymeric substrates for magnetic tapes," J. Appl. Polym. Sci. **89**, 3052-3080 (2003).